ABSTRACT

RANDALL, ERIC BENJAMIN. Mathematical Analysis of Autonomic Control of Blood Pressure and Heart Rate. (Under the direction of Mette S. Olufsen.)

Autonomic dysfunction (AD) is characterized by inadequate regulation of the parasympathetic and sympathetic nervous systems hindering the ability of the cardiovascular system to maintain homeostasis. The most prevalent AD conditions of the cardiovascular system cause a wide array of disorders affecting the reflexive control of heart rate and blood pressure, including orthostatic intolerance, postural orthostatic tachycardia syndrome, and orthostatic hypotension. Diagnosis of AD is complicated by the inherent difficulty in measuring neural signals. As a result, AD function is typically assessed indirectly by interpreting measurements of heart rate and blood pressure. One method for assessing AD is the Valslava maneuver (VM), a clinical test where the subject forcibly expires against a resistance while maintaining an open glottis. The VM affects heart rate and blood pressure by imposing an increased intrathoracic pressure, which elicits a signaling cascade modulating the autonomic response. We focus on the mathematical modeling of the parasympathetic and sympathetic outflow in response to the VM.

This study develops a mechanistic open-loop neurological control model taking systolic blood pressure and thoracic pressure as inputs and predicting heart rate. This open-loop formulation provides the basis for a model-based analysis of a cohort of 34 control subjects and 5 patients with AD. The model is a system of ordinary and delay differential equations with 6 states and 26 parameters. Results indicate that modeling the VM is essential in the pathological characterization of AD patients.

The model is analyzed using local and global sensitivity analyses and stability analysis. Local sensitivity analysis (LSA) gives information about the sensitivity of the model output with respect to the parameters evaluated at given parameter values. We conduct LSA to determine a subset of parameters to optimize to determine patient-specific outcomes via the structured correlation method. Global sensitivity analysis (GSA) assesses parameter influence by exploring the physiological parameter space. To conduct this analysis, we develop a new metric for assessing time-dependent model outputs that incorporates fast, transient deviations from baseline behavior, termed *limited-memory Sobol' indices*, which is used to inform a model reduction and selection protocol. Lastly, we use stability analysis to study the behavior of the model solutions. We found that two parameters, the sympathetic delay D_s and the sympathetic time-scale τ_s, are related, and simultaneous adjustment of these parameters can result in unstable modes.

Lastly, we develop a closed-loop model coupling a cardiovascular model to the open-loop neurological model that predicts blood pressure, heart rate, and autonomic responses to the VM. We develop four submodels analyzing the behavior of a control subject and three patients with

AD. The patients exhibit the M, N, and V responses categorized by Palamarchuk *et al.* [94] believed to represent three distinct AD pathophysiologies. The M response is hypothesized to be caused by overactive parasympathetic and sympathetic activity, N by delayed and sustained sympathetic activity, and V by diminished parasympathetic and sympathetic activity.

Mathematical Analysis of Autonomic Control of Blood Pressure and Heart Rate

by
Eric Benjamin Randall

A dissertation submitted to the Graduate Faculty of
North Carolina State University
in partial fulfillment of the
requirements for the Degree of
Doctor of Philosophy

Applied Mathematics

Raleigh, North Carolina

2019

APPROVED BY:

C. Tim Kelley	Pierre Gremaud
Paul Mozdziak	Jesper Mehlsen External Member

Mette S. Olufsen
Chair of Advisory Committee

DEDICATION

To my fur children, Lincoln and Nyx,
for bringing love and joy to my life

BIOGRAPHY

Eric Benjamin Randall was born in Charlotte, NC and grew up in a suburb called Mint Hill. From a young age, Benjamin's parents fostered in him a love of science in all forms, from going to college-level chemistry classes with his mother as a kid, to participating in the Duke Talent Identification Program (TIP) in middle and high school to attending the epitome of "nerd camp" through the Summer Ventures in Science and Mathematics Program in the summer of his junior year of high school. After graduating in the top of his class, he attended the University of North Carolina at Chapel Hill (UNC), where he wrestled with his many and varied interests. In December 2011, he graduated a semester early from UNC Chapel Hill obtaining a Bachelor's of Science in Chemistry - Biochemistry Track and three minors in Biology, Linguistics, and Hispanic Studies. Graduating in the middle of the Great Recession of the U.S. was initially challenging, so he decided to return to school to pursue a second Bachelor's of Science in Mathematics from the University of North Carolina at Charlotte, completing the degree in May 2014.

Science has always been a passion for Benjamin, given his pursuit of chemistry, though mathematics was always a constant in his life. His various degrees and minors, grammarian nature, love of music and languages, and inherent knack for puzzles (especially crosswords) share one overarching motif: these disciplines have a formulaic structure with a defined set of rules that require creative and innovative solutions. In actuality, it isn't surprising that Benjamin's desire to explore, interpret, and analyze complex structures with underlying intrinsic properties lead to his study of math.

In 2014, the Department of Mathematics at North Carolina State University (NCSU) accepted him into their graduate program in mathematics. Much to the chagrin of his fellow Tarheels, he moved to Raleigh, NC and began attending NCSU in August of that year with the intent of becoming a pure mathematician. After his first semester of grad school and some serious soul-searching, he realized that he wanted to combine his extensive biological and chemical knowledge with his mathematical sciences. Switching to Applied Mathematics, he joined the Cardiovascular Dynamics Group under the direction of Dr. Mette Olufsen using mathematical modeling to study and analyze the cardiovascular control system. He received his Master's of Science in Applied Mathematics in December 2016.

Working with Dr. Olufsen throughout his graduate career provided Benjamin with many fortunate opportunities and experiences, including:

- Receiving research support from the Research Training Grant (RTG) in Mathematical Biology.

- Presenting his research in a variety of conferences and workshops.

- Traveling to Copenhagen, Denmark to collaborate with Dr. Jesper Mehlsen, which also spawned his first European jaunt (of hopefully many).

- Participating in the American Mathematical Society's Mathematics Research Communities workshop on *Mathematics in Physiology and Medicine,* which proved to be an extremely fruitful professional and personal endeavor.

- Teaching and mentoring many students to pass on his love for math and science.

These experiences culminated in a successful defense of his thesis in June 2019 obtaining a Doctor of Philosophy in Applied Mathematics with a minor in Physiology. Benjamin has accepted a position at the University of Michigan in the Molecular and Integrative Physiology department as a postdoctoral fellow under the direction of Drs. Daniel Beard and Brian Carlson.

ACKNOWLEDGEMENTS

To my mentee, Nick Randolph, I have had the privilege of being a part of your growth as a researcher. Thank you for producing great work and being open to exploring new avenues. Thank you for continuing on diligently even when I was overwhelmed with completing my degree. I am so excited to see the great work you will do in the future.

To my friends, I am forever indebted to you for the love and support you have given me as I have trudged a whole decade through school, and I plan on dedicating the rest of my life to repaying you emotionally and spiritually (not financially, you fiends).

- To my grad school friends, though too many to name, Ariel Nikas and Anila Yadavalli deserve special mention. Thank you for commiserating with me and providing a unified front against simultaneously teaching, conducting research, applying for jobs, interviewing for jobs, obtaining job offers, making future decisions, writing our theses, and trying to actually live.

- To my kickball team, The Wrecking Balls, I truly am so glad to have become a part of each of your lives. Thank you being my first true set of friends in Raleigh. Thank you for providing me a safe space to be myself. Thank you for accepting me, loving me, and supplying me with ample amounts of alcohol (which may be redundant with the acceptance and love part).

- To the PigPen (alphabetically), Dr. Gregory Downing, Nicholas Johnson, Eric Jones, Dr. Felix Nwogbo, Steven Pius, (future Dr.) Taylor Smith, and Nick Szerszen, you are some of the wittiest, most intelligent, fiercest, lascivious, most incredible humans I know. Thank you for our family dinners and game nights, Game of Thrones memes, The Devil Wears Prada references, and Drag Race viewings. Thank you for helping me maintain my sanity. Thank you for your intellectual conversations and irreverent commentary. Thank you for everything.

- To the MM&FF (chronologically), Danielle Pollman, Lauren Shirkey, Alissa Smith, Nina Willis, Vaughn Pollman, and Jackie Iuliano, I am blessed to have had friendships with you all that have lasted the majority of my life. Thank you for the Mean Girls quotes, Riverdale references, impromptu musical numbers, and cheese platters (#espressocheese). Thank you for our seminal holiday soirées (Friendsgiving, Friendsmas, Halloween, etc.). Thank you for continuing to be steadfastly supportive of my academic and professional endeavors, even as I continue to move further and further away.

- To my bestie, Nina Willis, you get a shoutout twice. Thank you for checking in with me daily to ensure that I am okay and alive. Thank you for always being there when I need you. Thank you for knowing me better than anyone. I am so incredibly fortunate to have met my soulmate so early in life.

To my brother, William Randall, you have been an amazing roommate and co-fur parent throughout my graduate career. Thank you for picking up the slack when my school life got too crazy. Thank you for taking excellent care of Lincoln and Nyx when I couldn't. Lastly, but most importantly, thank you for giving me the opportunity to live safely, decently, and happily these last five years.

To my parents, Kelly and Eric Randall, I know it's cliché but there a no words to describe the depth of my gratitude and love for you. I would not have made it through almost three decades on this earth without you. Thank you both for allowing me the freedom to pursue my interests at every stage of my life. Dad, thank you for always being game to travel, both domestic and abroad. Thank you for your love, support, and vigilant confidence in me. Mom, thank you for being the one person I can always call about anything in my life. Thank you for talking me down when hysteria hits. Thank you for inspiring me daily to strive for and attain more, while also finding happiness and grace in what I have. I am eternally thankful for your unconditional love and I am so lucky to have you.

TABLE OF CONTENTS

LIST OF TABLES

LIST OF FIGURES

CHAPTER

1

INTRODUCTION

Autonomic nervous system dysfunction (AD) is a broad term referring to disorders associated with the regulation of the parasympathetic and sympathetic nervous systems. These systems maintain homeostasis in humans through complex interactions of positive and negative feedback mechanisms. When one or both are impaired, serious complications arise, involving expensive health care costs and decreased quality of life. AD can occur concomitantly with other diseases, such as diabetes mellitus and Parkinson's disease [75, 95], be idiopathic [132], or be induced by other factors, *e.g.,* in young females receiving the human papillomavirus (HPV) vaccine [18]. The most prevalent AD conditions affect the cardiovascular system [40], causing:

- *Orthostatic intolerance* (OI) characterized by decreased fidelity of the cardiovascular control during posture changes [132].

- *Postural orthostatic tachycardia syndrome* (POTS) characterized by a substantial increase in heart rate due to posture changes [139].

- *Orthostatic hypotension* (OH), or in more severe case *pure autonomic failure* (PAF), characterized by a decrease in blood pressure in response to posture changes [19].

Diagnosis of specific AD disorders is difficult clinically due to the myriad of shared symptoms, *e.g.,* fatigue, widespread pain, dizziness, and syncope. Since measuring neural activity directly requires invasive techniques and anesthetization, which impairs autonomic function, AD is commonly studied

and assessed indirectly by analyzing patterns in blood pressure, heart rate, and electrocardiogram measurements.

Pattern recognition [94] and spectral techniques [12, 122] are clinical methods typically used for data analysis. The former provides classifications for patient outcomes but cannot explain why these patterns arise. The latter are useful in assessing frequency-based responses but are unable to characterize signal transduction processes via specific pathways. In this study, we explore a model-based analysis approach to infer the underlying neurological mechanisms and provide hypotheses for the etiologies of patients with AD. We develop simple yet informative models that interrogate hypotheses of how these disorders manifest and compare simulations to data. A major focus of this work is in rendering the models patient-specific as opposed targeting the average individual [64, 69, 91]. While the latter are excellent at understanding population behavior, the former is powerful as it can provide insight into the AD of an individual patient.

Specific tests evaluating the function of the autonomic nervous system include deep breathing, active standing, head-up tilt, and the Valsalva maneuver (VM) [48]. This dissertation primarily focuses on the latter, in which the subject forcibly exhales against a resistance increasing intrathoracic pressure [41]. We choose to analyze the VM because of its unique ability to affect both the parasympathetic and sympathetic nervous systems via the baroreceptor reflex (*baroreflex*) and its reproducibility in the clinical setting [102].

There are many ways to analyze the behavior of a model. In this study, we use local sensitivity analysis to determine parameter influence on the model output and subset selection to determine parameters that can be estimated given the model and data [87, 100]. We perform a global sensitivity analysis on the model assessing the influence of the parameters through exploration of the physiological parameter space. Due to the transient nature of the VM, we develop a new metric termed *limited-memory Sobol' indices* for problems with fast, yet significant, disturbances. Additionally, we employ stability analysis to determine the types of solutions our model can generate, providing constraints on the system to ensure appropriate model behavior.

An overarching theme of this work is the analysis of discrepancies between healthy control subjects and patients with AD. To this end, we have three goals.

1. **Development of physiological models** to analyze the autonomic response to the VM:

    (a) Open-loop neurological model predicting heart rate as a function of systolic blood pressure and thoracic pressure.

    (b) Closed-loop model coupling a cardiovascular model and the open-loop model that predicts heart rate and blood pressure in a control subject and patients with AD exhibiting M, N, and V responses.

2. **Patient-specific modeling** using parameter estimation to predict responses for 34 control subjects and 5 patients with AD exhibiting V responses.

3. **Model analysis** investigating the effects of model components and parameters on the model output via local and global sensitivity analyses and stability analysis.

Overview of dissertation

This work is the culmination of four studies at various stages of preparation.

- Chapter 2 discusses the physiological background focusing on the control mechanisms modulating the cardiovascular system.

- Chapter 3 explains the data acquisition protocol and numerical preprocessing of the data.

- Chapter 4 develops and analyzes a patient-specific open-loop neurological model of the autonomic response to the Valsalva maneuver predicting heart rate as a function of blood pressure and thoracic pressure. This chapter also conducts a local sensitivity analysis and determines a subset of parameters to optimize, which is compared across 34 control subjects and 5 patients with AD. (currently under review)

- Chapter 5 performs a stability analysis on the open-loop model and determines regions of instability.

- Chapter 6 implements a global sensitivity analysis (GSA) using Sobol' indices on the open-loop model. This chapter compares scalar Sobol' indices to the performance of three methods of computing time-varying Sobol' indices: pointwise, generalized, and limited-memory (new). This chapter also describes a GSA-informed model reduction and selection protocol.

- Chapter 7 develops a lumped-parameter cardiovascular model coupled to the open-loop model, predicting the effects of the baroreflex for a control subject and 3 subjects with AD exhibiting the M, N, and V responses, respectively.

CHAPTER

2

PHYSIOLOGICAL BACKGROUND

This chapter provides an overview of the physiological function of the cardiovascular system and its regulation by the autonomic nervous system, focusing on short-term heart rate and blood pressure regulation and its pathophysiology in patients with autonomic dysfunction (AD). Most of the physiological facts discussed here are from the texts by Boron and Boulpaep [16] and Hall [40]. Section 2.1 describes the cardiovascular system. Section 2.2 discusses regulatory mechanisms impacting the cardiovascular system, including the baroreceptor reflex, the cardiopulmonary reflex, and the respiratory sinus arrhythmia. Section 2.3 reviews common autonomic tests in clinical practice. Section 2.4 discusses pathophysiological responses.

2.1 Cardiovascular system

The heart acts as the pump for the cardiovascular system (CVS) bringing blood to the body. The primary function of the CVS is oxygen (O_2) distribution vital for cellular respiration, which gives off carbon dioxide (CO_2) as a waste product.The CVS also transports nutrients used for growth and repair, neurotransmitters and hormones to the muscles and viscera for signal transduction, and immune agents to their target areas for defense purposes. As shown in Figure 2.1, the two branches of the CVS are the systemic circulation, which transports oxygenated blood to the body, and the pulmonary circulation, which transports deoxygenated blood past the lungs for gas exchange.
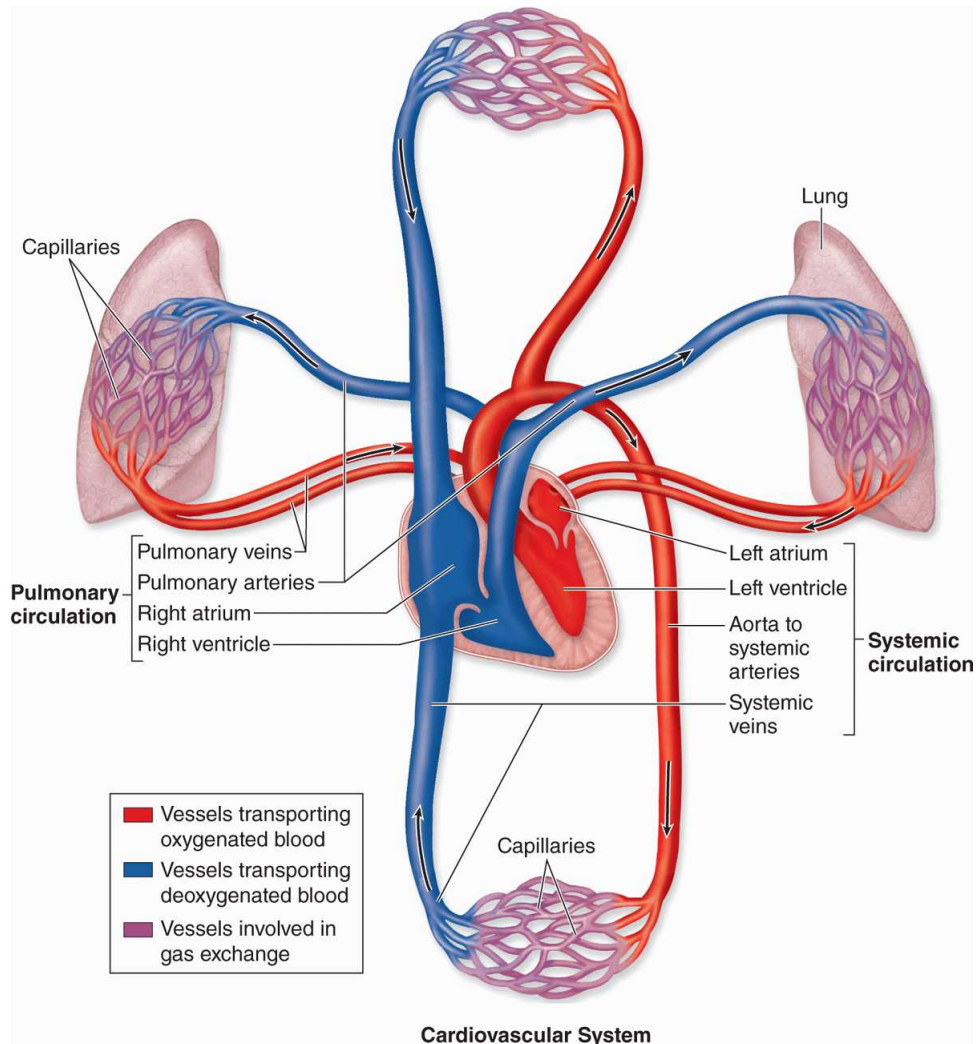
Figure 2.1 The cardiovascular system. The heart pumps oxygenated blood from the left ventricle to the aorta, which branches into the systemic arteries, arterioles, and capillaries where gas exchange occurs. Deoxygenated blood travels through the venules, veins, and superior and inferior vena cava, ultimately draining into the right atrium and ventricle. The right ventricle pumps the blood, albeit at a lower pressure, to the pulmonary circulation via the pulmonary arteries. Gas exchange occurs at the pulmonary capillaries and oxygenated blood travels from the lungs to the left atrium via the pulmonary veins. The left atrium drains into the left ventricle, and the cycle begins again. Reprinted with permission from Basicmedical Key (`https://basicmedicalkey.com/the-circulatory-system-2/`).

Table 2.1 Components of cardiovascular hemodynamics analogous to an electrical circuit.

Cardiovascular System				Electrical Circuit			
Description	Units	Symbol	Relation	Description	Units	Symbol	Relation
Volume	mL	V		Charge	C	Q	
Flow	mL sec^{-1}	F	$F = \dfrac{\mathrm{d}V}{\mathrm{d}t}$	Current	A	I	$I = \dfrac{\mathrm{d}Q}{\mathrm{d}t}$
Pressure	mmHg	P		Voltage	V	V	
Resistance	mmHg sec mL^{-1}	R	$R = \dfrac{\Delta P}{F}$	Resistance	Ω	R	$R = \dfrac{\Delta V}{I}$
Conductance	mL mmHg^{-1} sec^{-1}	G	$G = \dfrac{1}{R}$	Conductance	S	G	$G = \dfrac{1}{R}$
Compliance	mL mmHg^{-1}	C	$C = \dfrac{\mathrm{d}V}{\mathrm{d}P}$	Capacitance	F	C	$C = \dfrac{\mathrm{d}I}{\mathrm{d}V}$
Elastance	mmHg mL^{-1}	E	$E = \dfrac{1}{C}$	Elastance	F^{-1}	E	$E = \dfrac{1}{C}$
Inertance	mmHg sec^2 mL^{-1}	L	$P = -L\dfrac{\mathrm{d}F}{\mathrm{d}t}$	Inductance	V sec A^{-1}	L	$V = -L\dfrac{\mathrm{d}I}{\mathrm{d}t}$

Electrical circuit units: C - coulomb, A - ampere, V - volt, Ω - Ohm, S - siemens, F - farad
The resistance relation is given by Ohm's Law.

The left ventricle contracts, pumping O_2-rich blood to the systemic circulation via the aorta, which branches into the arteries, arterioles, and capillaries. Gas exchange occurs in the capillary beds, transporting O_2 to and receiving CO_2 from the tissues. The venules, veins and vena cava transport the CO_2-rich blood to the right atrium, which drains into the right ventricle. After contraction, the right ventricle pumps CO_2-rich blood to the pulmonary circulation via the main pulmonary artery, which branches rapidly into the small arteries, arterioles, and capillaries surrounding the alveoli of the lungs. At this level, gas exchange occurs and O_2 diffuses into the capillaries and CO_2 diffuses into the alveoli. The oxygenated blood passes through the small veins into the pulmonary veins, which drain into the left atrium. The left atrium drains into the left ventricle, and the cycle starts again.

2.1.1 Arterial and venous hemodynamics

The CVS can be thought of an analog to and electrical RC circuit (summarized in Table 2.1) in which current is analogous to flow (F, mL sec^{-1}), voltage to pressure (P, mmHg), charge to volume (V, mL), and capacitance to compliance (C, ml mmHg^{-1}), while resistance (R, mmHg sec mL^{-1}) is the same in both formulations. Under the steady flow assumption, the CVS obeys Ohm's Law

$$\Delta P = FR, \tag{2.1}$$

P, F, and R vary over time and R changes depending on location in the vasculature. According to Poiseuille's Law for a rigid tube of small diameter, the resistance is related to the radius (r, cm) of the blood vessel via

$$R = \frac{8\eta l}{\pi r^4}, \tag{2.2}$$

where η (mmHg s cm^3 mL^{-1}) is the viscosity and l (cm) is the length of the vessel. To determine overall resistance across a vascular bed (R_{tot}, mmHg sec mL^{-1}), we use electrical circuit theory to condense n resistances in series via

$$R_{tot} = R_1 + R_2 + \cdots + R_n \tag{2.3}$$

and in parallel

$$\frac{1}{R_{tot}} = \frac{1}{R_1} + \frac{1}{R_2} + \cdots + \frac{1}{R_n}. \tag{2.4}$$

This analog forms the basis of the cardiovascular modeling approach discussed in Chapter 7.

The pressure generated to move the blood through the systemic circulation is far greater than that of the pulmonary circulation. The *high-pressure system* is comprised of the contracted left heart, systemic arteries, and arterioles, maintaining a mean arterial blood pressure (MBP) of ~95 mmHg in the large arteries and oscillating between a maximal systolic blood pressure (SBP) of ~120 mmHg and a minimal diastolic blood pressure (DBP) of ~80 mmHg. The MBP decreases

slightly from the aorta to the systemic arteries. When the blood reaches the systemic arterioles, MBP substantially reduces. Clinically, a typical approximation relates these three quantities as

$$\text{MBP} = \frac{1}{3}\text{SBP} + \frac{2}{3}\text{DBP}. \tag{2.5}$$

The arterioles are surrounded by smooth muscle cells that, when stimulated, vasoconstrict and increase vascular resistance and pressure while flow remains constant. Given a total blood volume of ~5 L in a 70 kg man, the system arteries contain ~15% of the total blood volume.

The pulmonary circulation operates under a MBP of ~15 mmHg, ~10 mmHg in the pulmonary capillaries, ~5 mmHg in the pulmonary veins. Similar to the high-pressure system, the *low-pressure system* encompasses the systemic capillaries (~25 mmHg), systemic veins (~3-15 mmHg), pulmonary circulation, left atrium, and a relaxed left ventricle. The low-pressure system contains approximately 80% of the total blood volume with the remaining 5% belonging to the heart. The systemic veins act as a blood reservoir containing ~65% of the total blood volume.

The blood vessels are elastic tubes with three layers: the intimia, media, and adventitia. These layers consist of endothelial cells, elastic fibers (composed of elastin and microfibrils), collagen, and smooth muscle cells. The elastic fibers contribute the most to the distensibility of the vessel. Compliance (C, mL mmHg^{-1}) is a measure of vessel distensibility given as the derivative of the pressure-volume curve

$$C = \frac{dV}{dP} \tag{2.6}$$

as listed in Table 2.1. The compliance of the arteries accommodates large changes in arterial blood pressure as volume increases. In the elastic arteries (*e.g.*, the aorta), an increase in arterial pressure increases vessel radius, which has a negligible effect on the resistance (equation (2.2)). Hence, the arteries approximately have a stable resistance and compliance. The veins are highly compliant as small increases in pressure result in large increases in volume. This is due to the ellipsoidal configuration of the vessel operating at very low pressures. As pressure increases, the ellipsoidal cross-sectional area becomes circular, which is able to receive a large amount of blood. However, the veins are resistant to stretching at high pressures, resulting in a dynamic compliance. In a similar manner equations (2.3) and (2.4), we calculate the total compliance (C_{tot}, mL mmHg^{-1}) of n compliances in series as

$$\frac{1}{C_{tot}} = \frac{1}{C_1} + \frac{1}{C_2} + \cdots + \frac{1}{C_n} \tag{2.7}$$

and in parallel

$$C_{tot} = C_1 + C_2 + \cdots + C_n. \tag{2.8}$$

The volume (V) of a CVS region is related to the P. As the vessels fill with blood, the amount of blood necessary to fill the vessel to achieve a zero pressure ($P = 0$) is the *unstressed volume* (V_u),

which is interpreted as the y-intercept of the line given in the pressure-volume loop (Figure 2.3). The volume needed to increase $P > 0$ is the *stressed volume* (V_{str}). For the arterial regions, V_{str} is ~30% of the total volume [11]. For the venous regions, V_{str} is ~10% of the total volume [11].

The microcirculation is critical to the CVS, serving as the main site for the exchange of gases, nutrients, water, and waste products. However, for the purposes of this dissertation, we will not address the capillaries here. Information regarding these processes can be found in [16, 40].

2.1.2 The heart

The heart is divided into four chambers: the left atrium and ventricle and the right atrium and ventricle (shown in Figure 2.1). The heart has four valves that are at the inlet and outlet of each ventricle designed to prevent the backflow into the preceding chamber. The atrioventricular valves are between the atria and the ventricles, the mitral valve for the left heart and tricuspid valve for the right. The semilunar valves are between the ventricles and the arteries, the aortic valve for the left heart and the pulmonary valve for the right.

2.1.2.1 Cardiac cycle

The heart chambers work together due to excitation-contraction coupling, the excitation of cardiomyocytes resulting in cardiac contraction. The sinoatrial (SA) node is a group of cells in the right atrium that serve as the pacemaker of the heart. As the cytosol of the cells in the SA node becomes progressively less negative, it reaches a threshold and rapidly depolarizes, causing an action potential that is propagated from the SA node through the atrioventicular (AV) node and splits at the bundle of His to the Purkinje fibers of the left and right heart. This depolarization causes an influx of calcium ions, which stimulates atrial contraction and a delayed ventricular contraction due to the action potential passing through the AV ring. Should the SA node fail, the AV node's intrinsic pacemaker ability can take over. Should both the SA and AV nodes fail, the Purkinje fibers can initiate heart beats, though this excitation-contraction coupling mechanism is very slow.

The electrocardiogram (ECG) measures the electrical activity of the heart. An example ECG is shown in Figure 2.2. A typical cardiac cycle as shown in the ECG is comprised of the P-wave, the QRS-complex, and the T-wave. An ECG cannot detect the electrical activity of the conducting fibers themselves, but rather the activity of the atria and ventricles. The P-wave corresponds to atrial depolarization. The QRS-complex marks ventricular depolarization as the upward and downward reflections denote the propagation of the current throughout the ventricles. The T-wave occurs due to repolarization of both the left and right ventricles. Heart rate is measured as the inverse of the timespan between consecutive R-waves. For a healthy individual at rest, a cardiac cycle lasts ~0.8 sec corresponding to ~75 bpm.

The valves dictate four phases of the cardiac cycle, as they depend solely upon the pressure
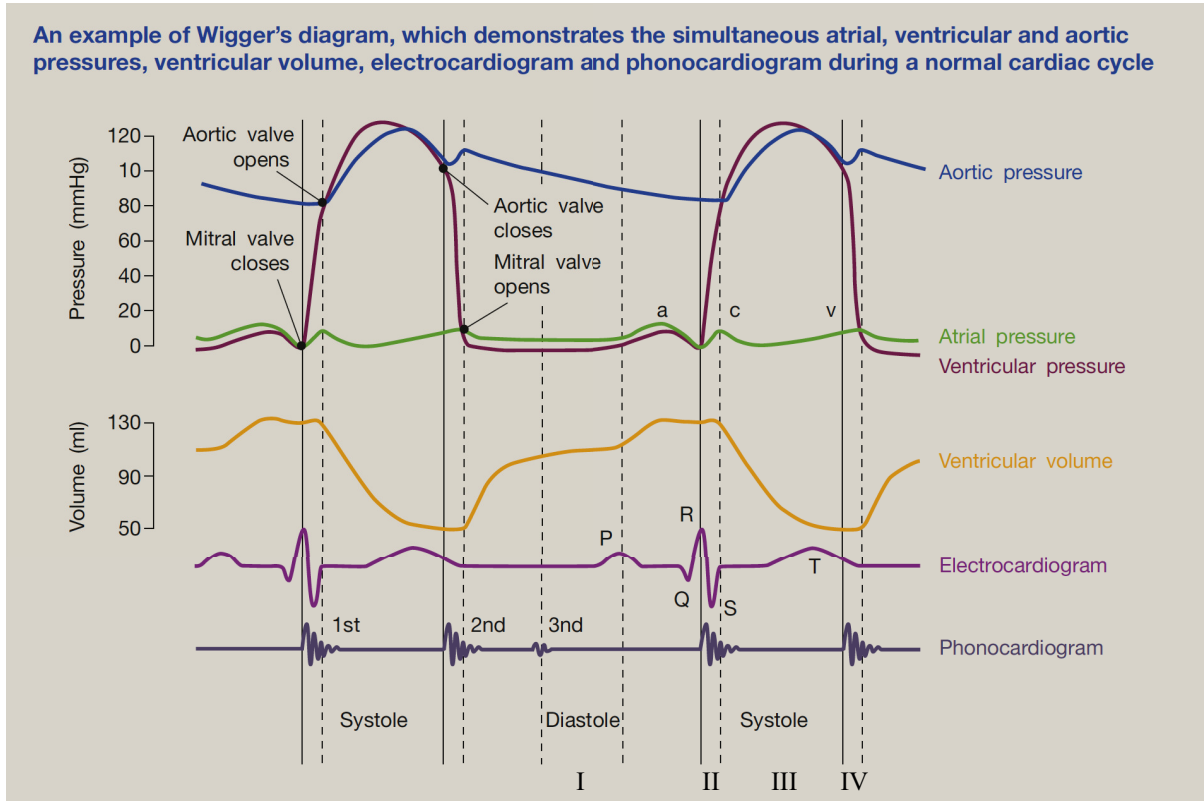
Figure 2.2 An example Wigger's diagram. *First plot:* traces for the aortic pressure (blue), left ventricular pressure (purple), and left atrial pressure (green). Valve openings and closing are indicated with vertical lines. The a-, c-, and v-waves in the left atrial pressure are denoted. *Second plot:* Left ventricular volume. *Third plot:* Electrocardiogram trace with P-wave, QRS complex, and T-waves indicated. *Fourth plot:* Phonocardiogram with first, second and third heart sounds indicated. Reprinted with permission from [76].

gradient across the valve. For a healthy individual, there never occurs a time at which both valves are open simultaneously as shown in the example Wigger's diagram in Figure 2.2, which includes pressure and volume traces, an ECG, and a phonocardiogram. For the purposes of this study, the pressure, volume, and ECG curves will be the primary focus. We will illustrate the four phases of the cardiac cycle with the left heart as follows:

I. *Ventricular filling:* Due to decreased left ventricular pressure, the mitral valve opens and the ventricle fills rapidly. During filling, the aortic valve is closed. As time evolves, ventricular filling slows, a period known as *diastasis*. As pressure between the atrium and ventricle equilibrate with the atrial pressure only slightly higher, atrial excitation results in the P-wave of the ECG. The atrium contracts and fills the left ventricle. The ventricles begin to depolarize (QRS-complex of the ECG) causing ventricular pressure to rise above the atrial pressure. The mitral valve closes.

II. *Isovolumetric contraction:* With both valves closed, the ventricle contracts significantly increasing the pressure in the ventricle, which exceeds the aortic pressure.

III. *Ejection:* The aortic valve opens, and the ventricle rapidly ejects blood into the aorta and ventricular volume decreases. Aortic pressure increases above the ventricular pressure, but the aortic valve remains open for a short time due to the inertia of the blood. Ejection rate decreases, causing a reduction in both the aortic and left ventricular pressures. Blood flow across the aortic valve slows considerably, resulting in negative flow. The left ventricle repolarizes (T-wave of the ECG).

IV. *Isovolumetric relaxation:* The aortic valve closes and blood flow normalizes in the aorta. The result is the dicrotic notch, which propagates through the circulation. The ventricle relaxes while both valves are closes and left ventricular pressure drops dramatically to below the left atrial pressure.

Systolic blood pressure (SBP) is associated with the ventricular contraction and diastolic blood pressure (DBP) is associated with ventricular relaxation and filling. The difference between SBP and DBP is the pulse pressure (PP). Since cardiac output is similar in both the left and right hearts, these phases also apply to the right heart with the associated components.

2.1.2.2 Cardiac output

Cardiac output (CO, $\text{L}\,\text{min}^{-1}$) is the amount of blood pumped by the heart per cardiac cycle given as

$$\text{CO} = H\text{SV}, \tag{2.9}$$

where H (bpm) and SV (mL) are the heart rate and stroke volume, respectively. SV is the difference in end-diastolic volume (EDV), the maximal volume of the ventricle at the end of diastole ($\sim$120 mL), and end-systolic volume, the ventricular volume at the end of systole ($\sim$50mL). EDV and SV are related by the *Frank-Starling mechanism*, an empirical law that states that an increase in ventricular filling causes an increase in the tension of the cadiac myocytes (*preload*), which in turn induces a more forceful contraction of the ventricle. This mechanism functions primarily to maintain the approximately equal CO ($\sim$5 L/min $\approx$ 83 mL/sec) of both the right and left heart though both sides operate under different pressures. As the heart ejects blood, the tension in the contracting myocytes must overcome the opposing arterial pressure (*afterload*).

2.1.2.3 Cardiac contractility

The Frank-Starling mechanism is a nonlinear relationship between myocyte tension and end-diastolic volume. This is most notably evident during an increase in contractility, or the ability of
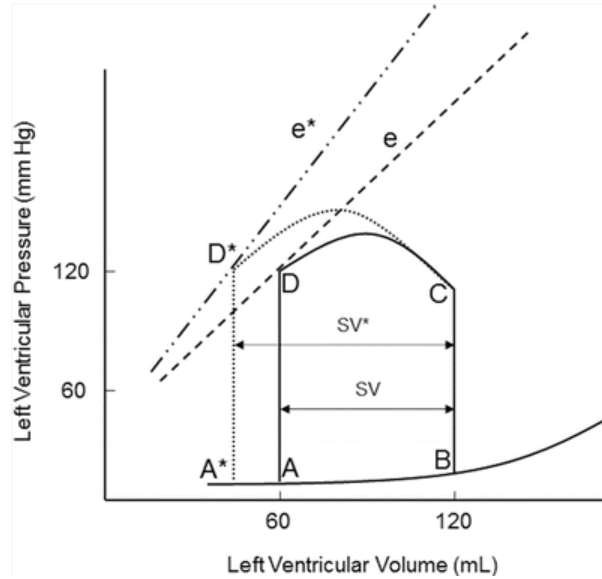
Figure 2.3 Pressure-volume (PV) loop of the effect of increasing contractility while preload and afterload remain constant. The line *e* indicates the end-systolic pressure-volume relation. As contractility increases (from *e* to *e**), stoke volume (SV) increases (from SV to SV*). Reprinted with permission from [68].

the heart muscle to contract. This metric is clinically relevant as it is an intrinsic property of the cardiomyocytes. Contractility is the slope of the line describing the *end-systolic pressure-volume relation* (ESPVR) on a pressure-volume loop plot (Figure 2.3). The ESPVR is the line going through the points of the theoretical maximal isovolumetric pressure (if the valves did not open) and the end-systolic pressure. Increasing contractility results in an increase in stroke volume. The y-intercept of the ESPVR is the unstressed volume (V_u).

2.2 Regulation of the cardiovascular system

This section focuses on describing the regulatory mechanisms impacting the cardiovascular system (CVS). Cardiovascular control is mediated by the autonomic nervous system (ANS) both neurally and hormonally, occurring on several time-scales, which include:

- *Fast:* (seconds or minutes) mediated by the ANS in response to rapid fluctuations in blood pressure and volume.

- *Intermediate:* (hours) mediated by the microcirculation shifting volume to and from the interstitial fluid and by endocrine and paracrine factors regulating local vasomotor control.

- *Slow:* (days or weeks) mediated by the renin-angiotensin-aldosterone system of the kidney to regulate blood volume globally.
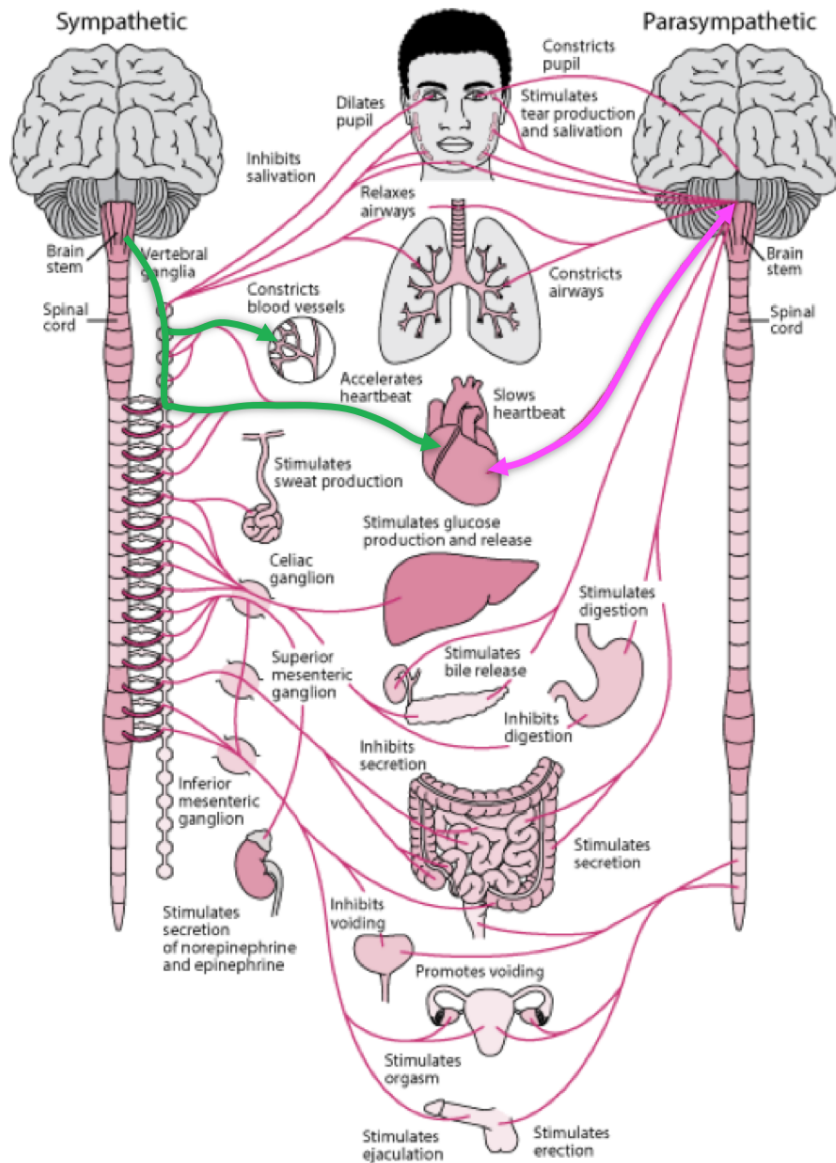
Figure 2.4 Schematic of autonomic nervous system functions. Sympathetic nervous function (left) passes through the sympathetic ganglia chain along the spine, delaying signal transduction. Parasympathetic ganglia are close to the target, resulting in fast responses. Cardiovascular control by the sympathetic (green arrow) and parasympathetic (magenta arrow) nervous systems are indicated. Adapted from the Merck Manual Consumer Version (Known as the Merck Manual in the US and Canada and the MSD Manual in t5he rest of the world), edited by Robert Porter. Copyright (2019) by Merck Sharp & Dohme Corp., a subsidiary of Merck & Co., Inc., Kenilworth, NJ. Available at http://www.merckmanuals.com/home. Accessed (2019).

Figure 2.4 shows a schematic of the ANS target sites. The systems are complex, so here we discuss the effects of short-term regulation via the ANS sensing blood pressure and blood volume via several receptor types. Afferent signals are transmitted to the medulla, where integration of these signals induces the appropriate response. Efferent neural pathways relay the response to the target via a two-neuron pathway, the *pre-ganglionic* and *post-ganglionic* neurons.

The ANS efferents have two main parts, the parasympathetic nervous system (PNS) and sympathetic nervous system (SNS), that work in tandem to maintain homeostasis. The PNS regulates heart and respiratory rates, sexual arousal, salivation, digestion, and excretion. The parasympathetic ganglia (neural clusters) are close to their targets with short post-ganglionic neurons that synapse on the target, secreting acetylcholine (ACh) to bind to muscarinic receptors. The SNS is tonically active at rest but increases in response to various stimuli. Sympathetic pre-ganglionic fibers synapse in the *sympathetic ganglia chain* that runs along the spinal column. Post-ganglionic neurons extend from the sympathetic ganglia chain to the target, secreting norepinephrine (Nor) at the synaptic cleft which binds to adrenergic receptors.

2.2.1 Autonomic control mechanisms

Several control mechanisms affect the CVS, including the baroreceptor reflex (*baroreflex*), the cardiopulmonary reflex, and respiratory sinus arrhythmia (RSA). The baroreflex and cardiopulmonary reflex stabilize changes in blood pressure and blood volume, respectively. The RSA synchronizes heart rate and blood pressure with the respiratory rate inducing heart rate variability [31]. Figure 2.5 summarizes these processes. We note that the ANS also senses and regulates partial pressures of dissolved gases (*e.g.*, O_2 and CO_2) via the chemoreceptors. However, this is not discussed in detail since we focus on the ANS impact on blood pressure and heart rate.

2.2.1.1 Baroreceptor reflex

Baroreceptor neurons are mechanoreceptors embedded in the adventitia of the arterial walls. They respond to stretch of the arterial wall as mechanical distortion of the receptors upon distention opens sodium ion channels and propagates action potentials [16]. The baroreflex modulates heart rate via the PNS and SNS and system-wide vasomotor control via the SNS only. For heart rate at rest, parasympathetic outflow contributes to about 80% percent of the neural control of heart rate and sympathetic contributes 20% [60]. As the arterial wall deforms, the baroreflex maintains mean blood pressure (MBP) by causing vasodilation and bradycardia (decreased heart rate) when MBP increases and vasoconstriction and tachycardia (increased heart rate) when MBP decreases [77].

Afferent stimulation: The primary sites for the high-pressure baroreceptors are in the carotid sinus and the aortic arch, highly distensible arterial regions (Figure 2.5). These bundles of myelinated

Figure 2.5 Schematic of the cardiovascular control mechanisms discussed in this chapter, including the baroreceptor reflex (baroreflex), the Bainbridge reflex, and the respiratory sinus arrhythmia (RSA). High-pressure baroreceptors (HPB) in the aortic arch and carotid sinus sense changes in blood pressure and relay the signal to the medulla. The baroreflex sends a parasympathetic (para) and sympathetic (symp) response controlling heart rate via the sinoatrial node. The sympathetic response also increases cardiac contractility and modulates vasomotor control. Low-pressure baroreceptors (LPB) in the right atrium sense changes in blood volume and relay the signal to the medulla, where the Bainbridge reflex and RSA signals are propagated to the sinoatrial node. Other systemic effects of these reflexes are not shown.

Figure 2.6 Baroreflex effect on (a) heart rate (HR) and (b) renal sympathetic nervous activity (RSNA) as blood pressure increases in rats. Saturation of the signal occurs at excessively high and low pressures. Adapted from [77].

(A-fiber) and unmyelinated (C-fiber) neurons are surrounded by collagen in the adventitia, which causes a viscoelastic deformation of the receptors. Afferent signals from the carotid baroreceptors transduce via the glossopharyngeal nerve and from the aortic baroreceptors via the vagal nerve. These fibers synapse in the nucleus tractus solitarius, which integrates the signals and transmits the appropriate efferent response.

Parasympathetic stimulation: Parasympathetic CVS control is mediated via the nucleus ambiguus and the dorsal motor nucleus in the medulla and signals are propagated through the vagus nerve. The PNS primarily controls heart rate, as denervation of the vagal pathway to the SA node accelerates heart rate to ~100 bpm from a resting rate of ~60-80 bpm. Increased MBP stimulates the baroreceptors and hence the PNS, releasing ACh into the extracellular matrix that binds to muscarinic receptors at the SA node (Figure 2.5). The net effect is bradycardia and vasodilation. The opposite occurs when MBP decreases, inhibiting the PNS and resulting in the fast degradation of extracellular ACh by acetylcholinesterase, which increases heart rate. As MBP decreases or increases excessively, the signal saturates as shown in Figure 2.6a. Since heart rate is primarily controlled by vagal stimulation, Figure 2.6a is assumed to be an assessment of parasympathetic outflow.

Sympathetic stimulation: Sympathetic CVS control is modulated by the rostral ventrolateral medulla, where inhibitory interneurons tonically promote vasoconstriction. These signals are transduced through the sympathetic ganglia chain, causing a delay and synapsing on the heart and blood vessels. The sympathetic delay has been found empirically as 1.7 seconds in dogs [12], 1.06 seconds

in rabbits [14], and 3 seconds in humans [69, 133]. Stimulation of the sympathetic outflow increases extracellular Nor, resulting in an increase in heart rate, cardiac contractility and arteriolar resistance and a decrease in venous compliance (Figure 2.5). Very low or very high MBP causes signal saturation as shown in Figure 2.6b.

2.2.1.2 Cardiopulmonary reflex

The cardiopulmonary reflex relies on the excitation of low-pressure baroreceptors found in the main pulmonary artery, the veno-atrial junctions, the atria, and the ventricles. Since they are baroreceptors, they also respond to stretch of the innervated tissue, which largely depends on distention of the vessels due to venous return to the heart [40]. Therefore, these low-pressure baroreceptors primarily regulate blood volume and cardiac output, which indirectly maintains MBP.

Afferent stimulation: The atrial receptors consist of A- and B-fibers detecting changes in heart rate and central venous pressure, respectively. An increase in blood volume causes an increase in venous blood pressure, which mechanically stretches the vessel walls and deforms the baroreceptors. Afferent signals are sent via the vagus nerve to the nucleus tractus solitarius (Figure 2.5).

Efferent effects: Efferent signals are propagated in a similar manner with a similar time-scale as those mentioned in Section 2.2.1.1. The cardiopulmonary receptors inhibits the PNS, which causes a reflexive increase heart rate (opposite of the baroreflex), which is called the *Bainbridge reflex* (Figure 2.5). Stimulation of the cardiopulmonary receptors results in sympathetic inhibition only in the kidney, causing vasodilation and increasing urine production [78]. Other effects of atrial baroreceptor stimulation include the inhibition of neurons in the hypothalamus that secrete antidiuretic hormone and the release of atrial natriuretic peptide, a vasodilator, from the atrial myocytes that causes diuresis. Overall, the result of stimulation of the low-pressure baroreceptors due to increased central venous pressure (*i.e.*, increased blood volume) is the elimination of fluid to reduce MBP.

Coordination with the baroreflex: When MBP decreases, particularly during respiratory challenges such as the Valsalva maneuver (discussed in Section 2.3), an increase in intrathoracic pressure can cause collapsing of the vena cava. Venous return is diminished and the tonic firing of the cardiopulmonary receptors is greatly reduced. This imposes mild bradycardia but acts against the tachycardia of the stimulated baroreflex. The baroreflex primarily regulates cardiac output (CO) at low volumes, while the Bainbridge reflex regulates CO at high volumes.

2.2.1.3 Respiratory sinus arrhythmia

Respiratory sinus arrhythmia (RSA) is the synchrony of heart rate variability and respiration, causing a shortening of the R-R interval in the ECG during inspiration and a lengthening during expiration [138]. Since the cardiovascular and respiratory control centers are in close proximity in the medulla, these centers interact strongly [40]. RSA has been poorly understood since its discovery, though it seems to play an important physiological role in the effectiveness of gas exchange in the lungs. Many factors influence RSA, including breathing pattern, body position, age, sex, etc. The cardiopulmonary receptors discussed in Section 2.2.1.2 also play a role in modulation of RSA [138]. The response is mediated by the vagal nerve synapsing on the SA node [16] (Figure 2.5). During inspiration, parasympathetic activity is inhibited, causing a natural increase in heart rate. During expiration, parasympathetic activity returns to rest, passively decreasing heart rate. The difference between the maximum heart rate at the end of inspiration and the minimal heart rate at the end of expiration is a clinically significant metric used to assess heart rate variability.

2.3   Autonomic testing

Measuring autonomic activity directly is challenging, as procedures are costly and invasive. Therefore, autonomic dysfunction (AD) is commonly diagnosed via indirect methods analyzing blood pressure and heart rate measurements in response to various autonomic tests assessing the neurological responses to postural and respiratory challenges. Within the last decade, there has been a push to standardize protocols associated with evaluating and diagnosing the various forms of AD through these indirect assessments [83, 132, 139].

This section reviews some typical clinical tests of autonomic cardiovascular control. Heart rate control mechanisms are assessed using deep breathing (DB) in which the subject breathes deeply at a rate of 6 breaths per minute (Figure 2.7a and 2.7b) and the Valsalva maneuver (VM) in which the subject forcefully expires against a resistance for 15 seconds (Figure 2.8a). Blood pressure control mechanisms are assessed via the VM (Figure 2.8b), active standing (AS) in which the subject moves from supine to upright (Figure 2.7c and 2.7d), and head-up tilt (HUT) in which the subject is tilted from supine to 60° (Figure 2.7e and 2.7f). HUT and AS also evaluate the HR response but to a lesser extent than the blood pressure. Tests involving the assessment of HR response to postural change (AS and HUT) versus HR response to respiratory challenges (DB and VM) are not correlated, suggesting these tests stimulate different neurological mechanisms [31]. For each test, clinical indices are discussed and representative data sets are shown.
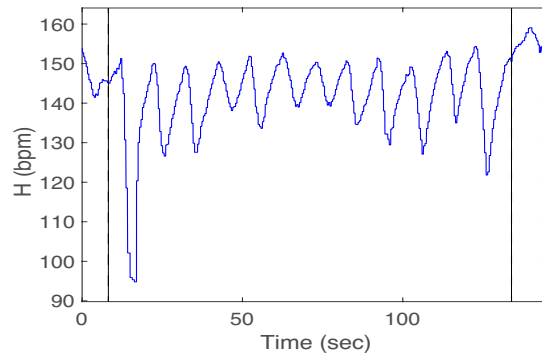
(a)
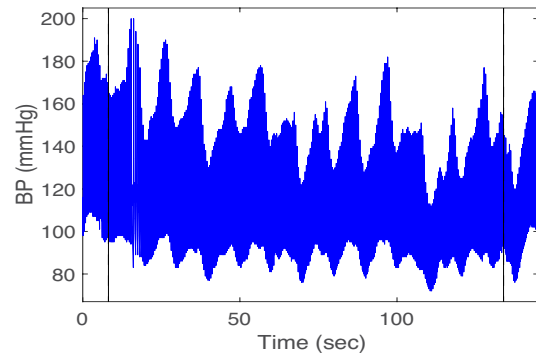
(b)
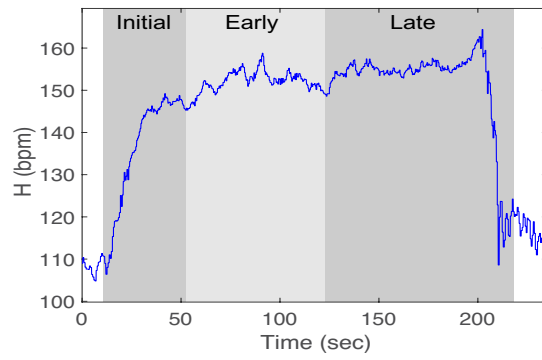
(c)
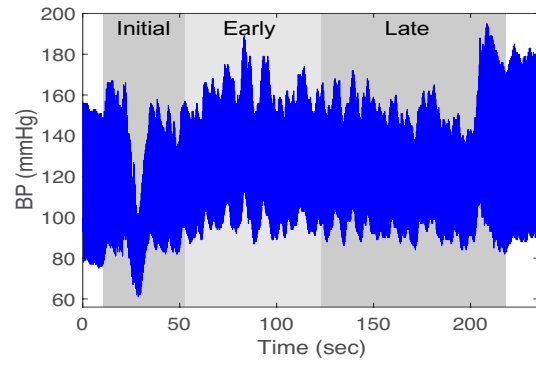
(d)
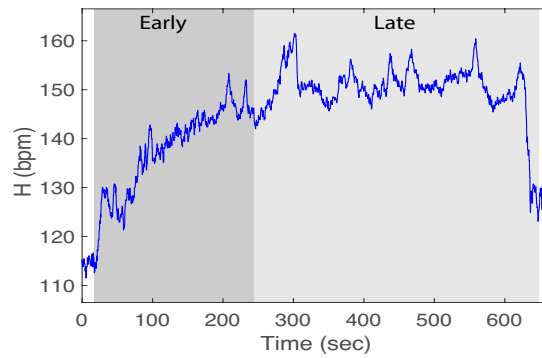
(e)
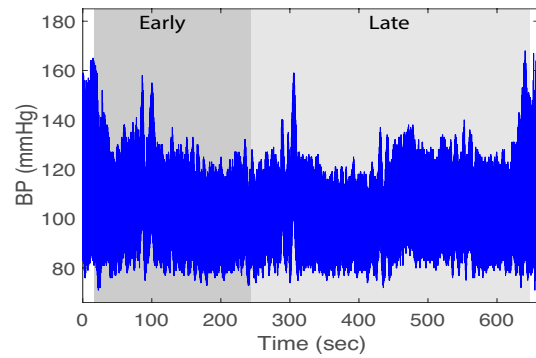
(f)

Figure 2.7 Heart rate (bpm, left column) and blood pressure (mmHg, right column) during deep breathing (DB, top row), active standing (AS, middle row), and head-up tilt (HUT, bottom row). (a) and (b): For DB, the vertical lines denote the beginning and end time of the test. (c) and (d): For AS, the alternating gray and light gray boxes denote the initial, early, and late phases of the test. (e) and (f) For HUT, the gray and light gray boxes denote the early and late phases.

2.3.1 Deep breathing

At rest heart rate is not constant but rather oscillates about a mean value. This relatively simple phenomenon is rooted in complex interactions between the parasympathetic and sympathetic nervous systems, creating a tenuous balance to maintain homeostasis [132]. Fluctuations occur as the result of periodic behavior associated with heart or respiratory rate, circadian rhythm, or even seasonal impulses [16]. As a result, variability in heart rate encodes a bevy of information that is difficult to interpret.

Deep metronomic breathing (DB) assesses RSA discussed in Section 2.2.1.3 [31]. Heart rate accelerates during inspiration and decelerates during expiration under normal conditions [48]. The increase in heart rate during inspiration is primarily due to an inhibition of parasympathetic tone, which passively returns to baseline during expiration [31]. DB is primarily an assessment of parasympathetic function, as stimulation of the vagal nerve modulates RSA and anticholinergic agents blunt the response [132]. The procedure initially requires the patient to breathe normally at rest in supine position for at least one minute. Then, the patient inhales for 5 seconds and exhales for 5 seconds, a cyclical routine of 6 breaths per minute [83]. DB must be performed with caution because prolonged activity can lead to hyperventilation and hypercapnia [132]. It has been found that heart rate variability due to DB declines with age [116]. Figures 2.7a and 2.7b display the heart rate and blood pressure responses, respectively, during DB.

Table 2.2 Ranges for deep breathing

Age (years)	EmI (bpm)		EdI (dimensionless)		Reference
	Normal	**Abnormal**	**Normal**	**Abnormal**	
< 30	~ 15	≤ 10	≥ 1.2	< 1.2	[48, 83, 116, 139]
30-70	~ 10	≤ 5	≥ 1.1	< 1.1	[83, 116]
> 70	~ 7	≤ 5	≥ 1.06	< 1.06	[48, 83, 116]

EdI - expiratory-inspiratory difference. EmI - expiratory-inspiratory ratio.

There are two primary biomarkers calculated during DB [48, 139]:

1. The expiratory-inspiratory difference (EmI), that is,

$$\text{EmI} = H_M - H_m \tag{2.10}$$

   for H_M and H_m the maximal heart rate at the beginning of expiration and the minimal heart rate at the beginning of inspiration, respectively.

2. The expiratory-inspiratory ratio (EdI)

$$\text{EdI} = \frac{H_M}{H_m}. \tag{2.11}$$

Normal and abnormal ranges for DB indices are tabulated in Table 2.2.

DB can also be analyzed in the frequency domain, using spectral analysis methods to split the signal into its many underlying oscillatory components [132]. Clinicians divide these signals in the following manner:

- High frequency (HF) range, 0.15-0.4 Hz, mainly influenced by the parasympathetic system incorporating control from the RSA and blood pressure changes.

- Low frequency (LF) range, 0.04-0.15 Hz, characterized as a combination of both sympathetic and parasympathetic modulation of heart rate incorporating control from the baroreflex.

- Very low frequency (VLF) range, ≤ 0.04 Hz, whose interpretation is unclear but may relate to baroreflex activity over longer time periods.

The ratio LF/HF band power is frequently used to assess "sympatho-vagal balance", as it takes into account effects from both autonomic nervous systems [132]. A healthy individual has a DB frequency of ~0.25 Hz (0.15 - 0.8 Hz) [138].

2.3.2 Active standing

Active standing (AS), also known as the Ewing maneuver, is an orthostatic test assessing the cardio-vascular response from a supine position to a sudden upright position, causing 300-800 milliliters of blood to be redistributed the central compartments to the lower extremities [31]. This blood redistribution results in decreased venous return and stroke volume [139]. AS activates muscle groups in the legs and abdomen most likely causing an "exercise reflex" that initially increases heart rate [31]. AS is very sensitive to whether the patient stands rapidly or in stages, complicating data reproducibility. This orthostatic test can be divided into three phases:

I. Initial phase (30-45 seconds): the subject stands and activation of the abdominal muscles compresses the vessels in the abdomen, increasing venous return and cardiac output. However, this increase does not compensate for the loss of blood volume to the lower extremities, and hence, blood pressure transiently drops, triggering the baroreflex. Heart rate increases abruptly due to parasympathetic withdrawal and muscular activation for ~3 seconds followed by a slower increase in heart rate due to delayed sympathetic activation, peaking ~10 seconds. The rapid reduction in blood volume triggers the cardiopulmonary reflex. Blood pressure declines initially, returns to baseline, and typically overshoots in healthy patients.

II. Early phase (1-2 minutes): this is a stabilization phase marked by an increase in DBP by ∼10 mmHg and sympathetically mediated increase in heart rate by ∼10 bpm.

III. Late phase (5-10 minutes): there is a prolonged response to orthostasis. Heart rate and blood pressure remain stable as sympathetic outflow becomes constant. Humoral mechanisms are triggered to contribute to the regulation of blood pressure.

Figure 2.7c and 2.7d display the heart rate and blood pressure responses, respectively, to AS. Initial, early, and late phases are indicated with alternating gray and light gray boxes. In the initial and early phases, the baroreflex governs heart rate and blood pressure control. The sharp decrease in blood pressure triggers a compensatory tachycardia (due to parasympathetic withdrawal and the subsequent increase in sympathetic outflow), an increase in arteriolar resistance, and decrease in venous compliance [31]. The late phase is characterized by continued sympathetic activation with humoral mechanisms helping to maintain blood pressure [48].

AS is used primarily to assess autonomic issues during the initial phase of the challenge, since the later phases are better assessed via head-up tilt (discussed in the next section) [48]. Clinical indices used for AS are:

1. The 30:15 ratio ($r_{30:15}$):

$$r_{30:15} = \frac{H_{M,15}}{H_{m,30}}, \tag{2.12}$$

where $H_{M,15}$ and $H_{m,30}$ are the the maximum heart rate after 15 seconds and the minimum heart rate after 30 seconds, respectively.

2. The 30-15 difference ($d_{30:15}$):

$$d_{30:15} = H_{M,15} - H_{m,30}. \tag{2.13}$$

For healthy individuals, the $r_{30:15} > 1.04$ is considered normal, though this value is age-dependent [139]. The $d_{30:15}$ should not exceed 20 bpm for young individuals (<15 years) and 11 bpm for elderly individuals (>70 years) [48]. A decrease in SBP >20 mmHg or DBP >10 mmHg is abnormal [139].

2.3.3   Head-up tilt

Head-up tilt (HUT) is a passive postural assessment that monitors blood pressure and heart rate as the patient moves from a supine to an upright position on a moving table. Tilting the table at an angle of 60° over 20 seconds ensures there is no muscle contraction [48], though some methods use a 70° angle [83]. HUT is easily controllable, readily reproducible, and better for patients with suspected autonomic dysfunction [31]. The tilt is maintained for up to 45 minutes, until syncope, or until other "intolerable outcomes" are achieved [97]. HUT can be divided two phases as shown in Figure 2.7e and 2.7f, including:

I. Early phase (1-2 minutes): the gradual change from supine to upright shifts blood from the upper body to the lower body without triggering muscle contraction to resist the pooling. Heart rate and DBP gradually increase while SBP remains relatively constant.

II. Late phase (5-10 minutes): there is a prolonged response to orthostasis. Venous pressure in the lower body increases from ~10 mmHg to ~90 mmHg as blood continues to pool at the feet, decreasing venous return, stroke volume, and cardiac output. Blood pressure decreases, triggering the baroreflex to increase heart rate, which counteracts the reduced cardiac output moderately.

2.3.4   The Valsalva maneuver

The Valsalva maneuver (VM) is the process associated with forced exhalation against an external resistance keeping the glottis open [41]. The subject maintains an expiratory force for 15 seconds, increasing the ITP to 40 mmHg, which in turn reduces venous return to the heart [83, 102]. The reduced filling of the heart decreases stroke volume, decreasing both the blood volume sensed by low-pressure baroreceptors in the veno-atrial junctions, the right atrium, and the pulmonary artery as well as the blood pressure sensed by the aortic and carotid high pressure baroreceptors [131]. The tonic firing of the nerves conducting signals from these receptors to the brain stem is reduced, causing a shift in the output from the cardiovascular control centers. The net effect is a fast withdrawal of parasympathetic activity to the heart and a slower increase in sympathetic activity to the heart and blood vessels. The efferent response induces cardiac acceleration and vasoconstriction. The four distinct phases of the VM marked with alternating gray and light gray boxes in Figure 2.8 are:

I. At the onset of the VM, the subject takes a deep breath and initiates the forced expiration. This increases the ITP, causing a sudden increase in blood pressure due to increased transmural pressure on the heart and large arteries. The deep exhalation and subsequent deep inhalation of the breath results in a transient reduction of ITP just before the maneuver, contributing to a temporary decrease in heart rate.

II. As the breath is held, the respiratory-mediated parasympathetic activity decreases. Increased ITP impedes venous blood return to the heart. Blood pressure falls, triggering the baroreflex, which in turn decreases baroreflex-mediated parasympathetic activity. Heart rate initially rises due to parasympathetic withdrawal (early phase II) and continues to rise as sympathetic outflow increases (late phase II). Despite the decreased stroke volume, blood pressure gradually returns to pretest levels due to increases in peripheral vascular resistance mediated by sympathetic activity.
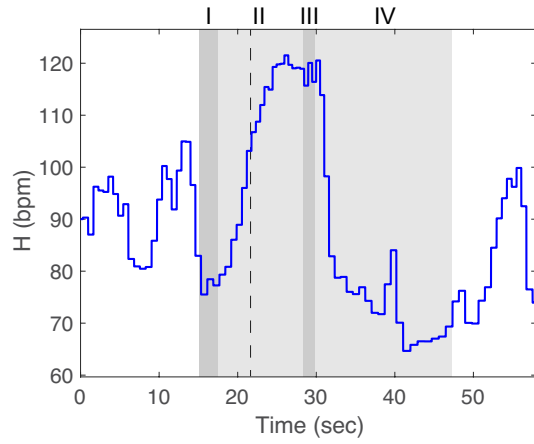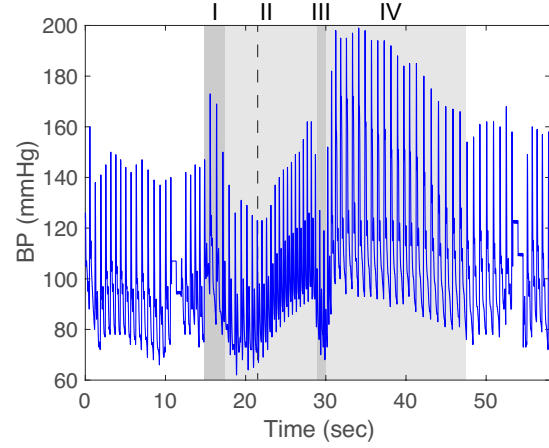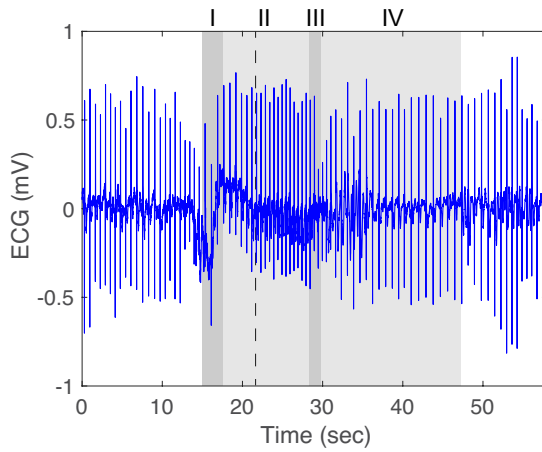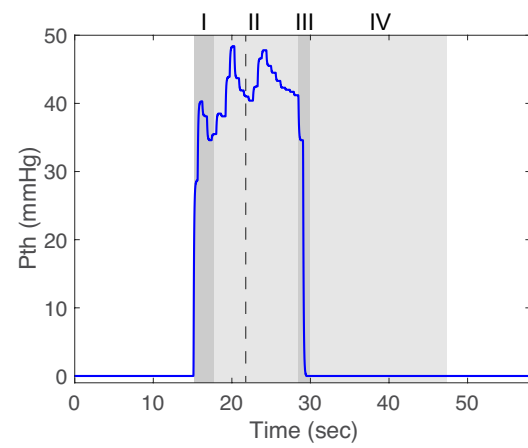
Figure 2.8 (a) Heart rate (H, bpm), (b) blood pressure (BP, mmHg), (c) electrocardiogram (ECG, mV), and (d) thoracic pressure (P_{th}, mmHg) during a Valsalva maneuver. The four phases are indicated with alternating gray (I and III) and light gray (II and IV) boxes. Early and late phase II are designated with the vertical dashed line.
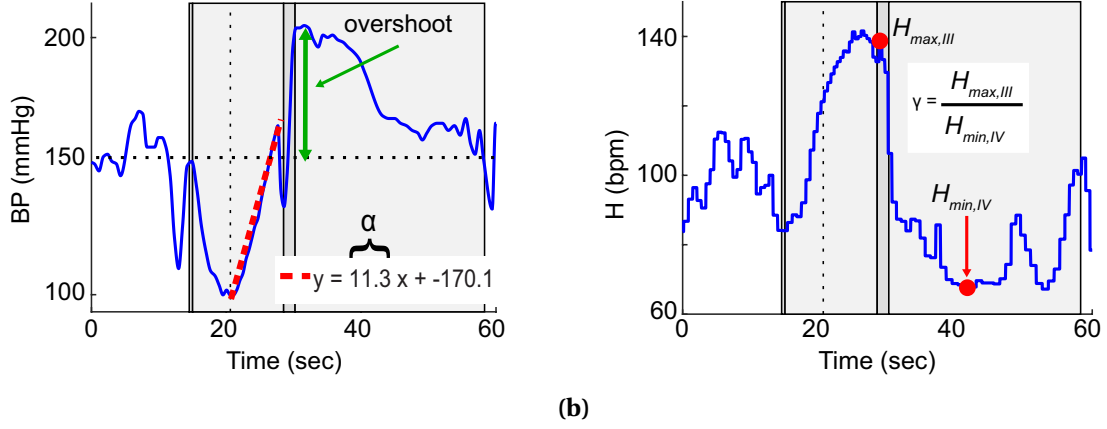
Figure 2.9 Depiction of (a) α as the slope of the line of regression of the systolic blood pressure (SBP) in late phase II and the SBP overshoot in phase IV used to calculated β as in equation (2.15) and (b) γ as the ratio of the maximum heart rate in phase III ($H_{max,III}$) and minimum heart rate in phase IV ($H_{min,IV}$).

III. Upon release of the ITP, the subject typically exhales forcefully. This causes a transient increase in ITP, which further impedes cardiac filling, and hence the preload. The result is a sudden drop in blood pressure. Then, the ITP returns to normal and blood returns to the heart unimpeded.

IV. After normalization of venous return to the heart, the stabilized stroke volume is expelled against an increased vascular resistance causing blood pressure to temporarily overshoot. This overshoot causes a rapid fall in heart rate as the parasympathetic system activates. Breathing returns to normal.

Clinicians extract a number of quantities from the SBP and heart rate to determine "normal ranges" for autonomic function for healthy control subjects [83]:

1. Vasoconstrictive capacity (α) given as

$$\text{SBP} = \alpha t + b, \quad t \in [t_{\text{SBP}_{min,II}}, t_{\text{SBP}_{max,II}}], \tag{2.14}$$

where α and b are the slope and the intercept of the regression, respectively, and $t_{\text{SBP}_{min,II}}$ and $t_{\text{SBP}_{max,II}}$ are the time points for the minimum and maximum SBP in late phase II, respectively. Figure 2.9a depicts the calculation of α. We interpret α as an estimate of the vasoconstrictive capacity of the systemic vasculature. A previous study has hypothesized the that the use of a metric assessing sympathetic function in late phase II of the VM should be considered [93]. To our knowledge, this is the first instance of using α as an approximation of sympathetic nervous function.

2. Baroreflex sensitivity (β) [83, 84, 111] given as

$$\beta = \frac{\text{max R-R} - \text{min R-R}}{\text{max SBP} - \text{baseline SBP}}, \tag{2.15}$$

where the numerator is the difference in maximum and minimum R-R intervals in milliseconds and the denominator describes the extent of the overshoot of the SBP (Figure 2.9a). β is a measure of heart rate change given a change in blood pressure [139]. It should be noted that β does not elucidate how changes in the SBP or R-R interval arise. An increase in β can be contributed to an increase in parasympathetic activity, a decrease in sympathetic activity, or a combination of the two [125].

3. The Valsalva ratio (γ) [83, 111] given as

$$\gamma = \frac{H_{max,III}}{H_{min,IV}}, \tag{2.16}$$

where $H_{max,III}$ is the maximum heart rate in phase III and $H_{min,IV}$ is the minimum heart rate in phase IV (Figure 2.9b). γ is typically interpreted as a measure of vagal function with abnormal values below 1.1 [31].

2.4 Autonomic dysfunction

Disorders associated with autonomic nervous system dysfunction (AD) or failure are prevalent but frequently overlooked or misdiagnosed, especially since the autonomic nervous system affects virtually all organs. Often, autonomic neuropathy is secondary to other more prominent maladies, such as Parkinson's disease and diabetes mellitus, where symptoms emerge concomitantly with disease [75]. However, AD often occurs without an apparent cause [19].

The tests described in the previous section are used to diagnose various forms of AD. Deep breathing (DB) primarily assesses parasympathetic function and AD associated with DB is due to failure of the parasympathetic nervous to induce heart rate variability. Head-up tilt (HUT) and active standing (AS) primarily test sympathetic function, where numerous disorders arise due to either overstimulation or blunting of the sympathetic response. Since the Valsalva maneuver (VM) elicits both parasympathetic and sympathetic responses, we focus on analyzing this test in more detail in the following section.

2.4.1 The Valsalva maneuver and autonomic dysfunction

The VM is used to detect AD in conjunction with the tests discussed above. An interesting observation made by Palamarchuk *et al.* [94] discusses that pathological VM data sets have patterns dictated by

the morphology of the SBP. The data tend to fall into specific categories that are reproducible upon repeated VM trials. Figure 2.10 displays representative patients exhibiting each of the following:

- *M pattern*: characterized by two SBP overshoots, one in late phase II where SBP rises prominently above baseline and the other during phase IV. The overshoot in phase IV rapidly declines to baseline within 5 seconds. It has been hypothesized that the M pattern is result of increased or overactive autonomic (parasympathetic and sympathetic) activity [93, 94] (Figure 2.10a).

- *N pattern*: characterized by a sustained SBP overshoot in phase IV for longer than 10 seconds. It is hypothesized that the N pattern is due to sympathetic hypersensitivity, yielding a delayed response while maintaining a high SBP for an extended period of time [94] (Figure 2.10b).

- *V pattern*: characterized by an absent increase in SBP in late phase II leading to a prolonged decrease in SBP, an altered phase III, and an absent SBP overshoot in phase IV. It has been hypothesized that the V pattern is a result of sympathetic dysfunction, as adrenergic activity contributes to late phase II and phase IV of the VM [94] (Figure 2.10c).

A primary focus of the work in Chapter 4 is the investigation of 5 AD patients exhibiting the V behavior with different diseases in comparison to 34 control subjects, using a model-based analysis of the data to help determine parasympathetic and sympathetic dysfunction. A focus of the work presented in Chapter 7 is modeling a representative control subject and AD patients exhibiting the M, N, and V behaviors. Our goal is to provide mathematical support for the physiological hypotheses of these behaviors given above.
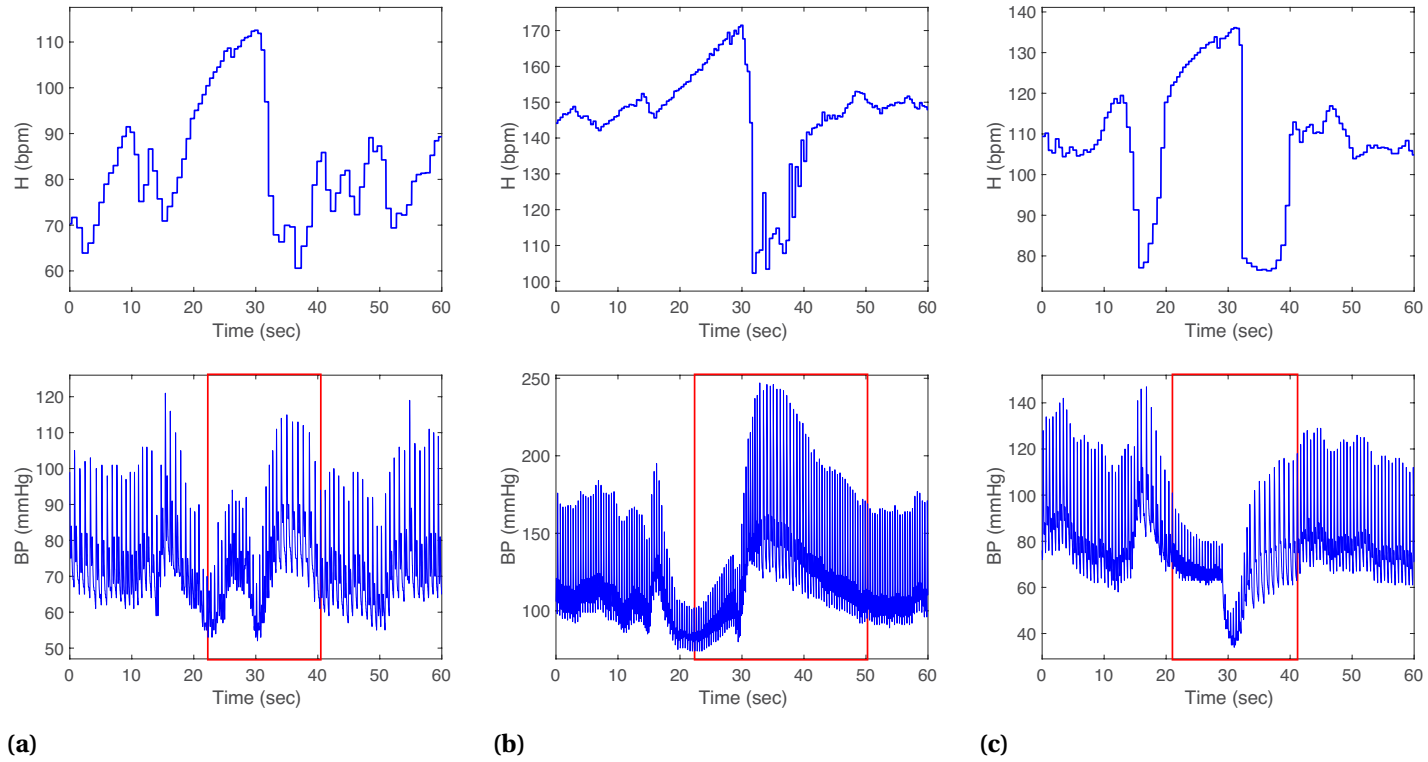
Figure 2.10 Heart rate and blood pressure responses during a Valsalva maneuver for patients with autonomic dysfunction exhibiting (a) an M response, (b) an N response, and (d) a V response. The boxes are assigned in accordance with [94].

CHAPTER

3

DATA

The modeling efforts in this body of work were analyzed and validated against data for control subjects and patients with autonomic dysfunction (AD) conducting multiple iterations of the Valsalva maneuver (VM). Data for the control subjects were collected by Dr. Louise Brinth and Anna Billeschou at the Department of Clinical Physiology and Nuclear Medicine at Bispebjerg Hospital in Frederiksberg, Denmark. The protocol, "Method study in the Valsalva maneuver" (H-16036257), was approved by the Ethics Committee of the Capital Region, Denmark. The measurements from the patients with AD are from a previous experiment with a similar protocol. This chapter discusses the study population (Section 3.1), describes the acquisition of the data (Section 3.2), and provides details about the numerical methods involved in data preprocessing (Section 3.3).

3.1 Study population

The study in Chapter 4 analyzes electrocardiogram (ECG)-derived heart rate and respiratory signals, blood pressure, and intrathoracic pressure (ITP) data from 37 control subjects (24 females and 13 males) and 5 AD patients with different diseases exhibiting the V behavior (1 female and 4 males) as discussed in Section 2.4.1. All subjects gave written consent to participate in the study. Of the 37 control subjects, data from 34 (21 females and 13 males) were analyzed in this study. Two subjects were excluded due to pregnancy and one subject was excluded due to data collection error. Table 3.1 summarizes control subject population statistics. The 5 AD patients exhibiting the V behavior

categorized by Palamarchuk *et al.* have various diseases and broad age range. Patient 1 (16 years old) is diagnosed with postural orthostatic tachycardia syndrome (POTS), Patient 2 (79 years old) is diagnosed with orthostatic hypotension (OH), Patients 3 (71 years old) and 4 (83 years old) have Parkinson's disease (PD), and Patient 5 (75 years old) is diagnosed with pure autonomic failure (PAF). Figure 3.1a - 3.1d shows a VM data set containing ITP, ECG, blood pressure, and heart rate data for a representative control subject. Figure 3.1e - 3.1h shows the VM response from Patient 3. Table 3.2 summarizes the patient descriptions.

The study in Chapter 7 analyzes the blood pressure and heart rate from one control subject and three patients diagnosed with postural orthostatic tachycardia syndrome (POTS), *i.e.*, their heart rate increased more than 30 bpm in response to posture change. While all patients have the same diagnosis, they display different blood pressure responses categorized as the M, N, and V behavior [94]. Figure 3.2 displays the heart rate and blood pressure data for the four subjects of this study. In the figure, the control subject (Figure 3.2a) has resting heart rate (70 bpm) and blood pressure (70 mmHg) values much lower than the POTS patients (∼100 bpm and ∼100 mmHg). Table 3.3 summarizes the subject descriptions.

Table 3.1 Population statistics from the characteristic Valsalva maneuver for 34 control subjects.

Description	Symbol	Units	Population Statistics
Age		years	32 ± 12
Baseline systolic blood pressure	s_w	mmHg	123 ± 20
Baseline heart rate	$\bar{H}$	bpm	79 ± 13
Intrinsic heart rate	H_I	bpm	100 ± 7
Maximal heart rate	H_M	pbm	185 ± 7
Length of breath hold		sec	14 ± 0.7
Max forced expiration		mmHg	37 ± 1

Table 3.2 Descriptions of patients with autonomic dysfunction displaying a V response for the study in Chapter 4.

Patient	Sex	Age	Diagnosis	Abbreviation
1	Female	16	Postural orthostatic tachycardia syndrome	POTS
2	Male	79	Orthostatic hypotension	OH
3	Male	71	Parkinson's disease	PD
4	Male	83	Parkinson's disease	PD
5	Male	75	Pure autonomic failure	PAF
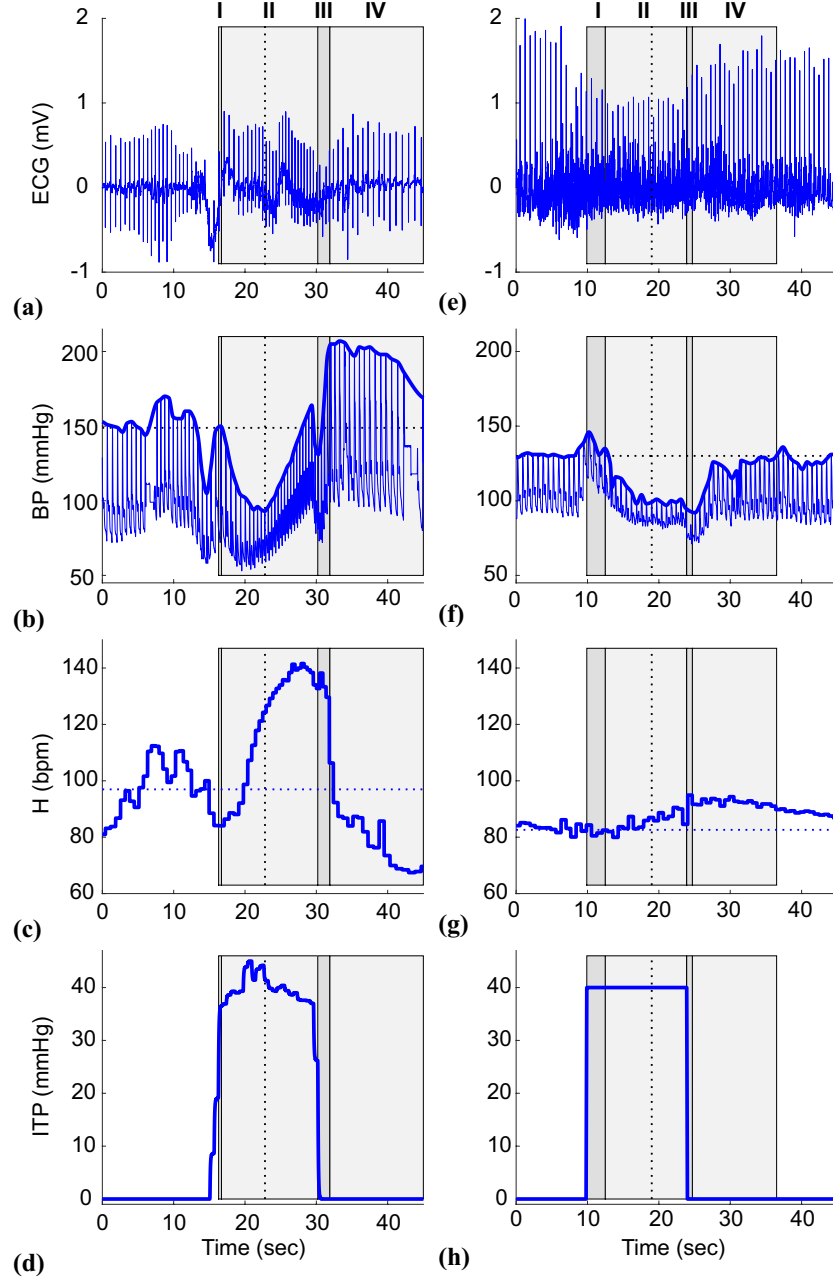
Figure 3.1 Valsalva maneuver (VM) data for the study in Chapter 4 for a representative control subject (a - d) and patient (e - h) with the V behavior as categorized by Palarmarchuk *et al.* [94]. Alternating gray and light gray boxes indicate phases I-IV of the VM. Early and late phases II are divided with a vertical dotted black line. Panels (a) and (e): Electrocardiogram (ECG, mV) trace. Panels (b) and (f): Blood pressure (BP, mmHg) trace with interpolated systolic blood pressure (SBP, thick blue curve) and baseline SBP (dotted blue line). Panels (c) and (g): Heart rate (H, bpm) trace with baseline H (dotted blue line). Panels (d) and (h): Intrathoracic pressure (ITP, mmHg) trace. Panel (d) shows the measured ITP of the control subject from which the VM start and end times, t_s and t_e respectively, were extracted. Panel (h) shows the manufactured ITP calculated in equation (3.1).

31
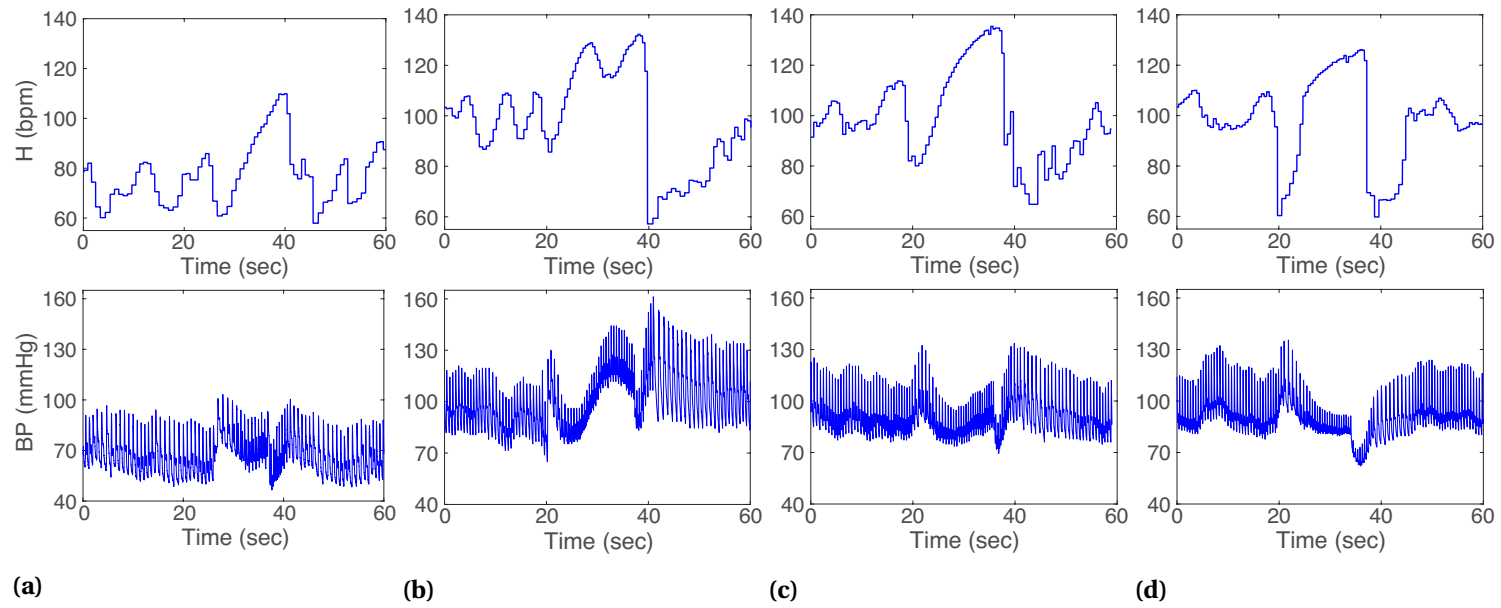
Figure 3.2 Valsalva maneuver (VM) data for the study in Chapter 7. Heart rate (H, top row) and blood pressure (BP, bottom row) for (a) control, (b) M response, (c) N response, (d) V response categorized by Palamarchuk *et al.* [94].

Table 3.3 Descriptions of subjects studied in Chapter 7.

Patient	Sex	Age	Diagnosis	Behavior
1	Female	32	Control	
2	Female	36	POTS	M
3	Female	15	POTS	N
4	Female	39	POTS	V

POTS - postural orthostatic tachycardia syndrome.

3.2 Data acquisition

All tests were performed between 8:00 a.m. and 3:00 p.m. under a non-fasting state at standard room temperature. ECG and blood pressure signals were measured continuously sampled at 1,000 Hz from a precordial ECG-lead and by Finometer equipment (Finapres Medical Systems BV, Amsterdam, The Netherlands), respectively. Analog data acquisition was performed, and data were converted to digital format and stored using the LabChart software (LabChart, AD Instruments Inc., Colorado Springs, CO, USA).

All tests were performed with the subject in sitting position. The subjects were asked to rest for 5 minutes before initiating the VM. A mouthpiece was connected to a mercury manometer by a rubber hose with an intercalated differential pressure transmitter (DTP-7000-R8, HK Instruments, Muurame, Finland). The subjects were asked to take a deep inspiration and then blow into the mouthpiece trying to reach and maintain a steady forced expiration at 40 mmHg for 15 seconds. For the control subjects, ITP was measured continuously. For the AD patients, ITP was measured and verified by visual inspection. We assume the patients maintain a constant expiratory force of 40 mmHg for the duration of the breath hold, given as

$$
\text{ITP}_j = \begin{cases} 40 & t_s \leq t_j \leq t_e \\ 0 & \text{otherwise,} \end{cases}
\tag{3.1}
$$

where ITP_j is the intrathoracic pressure at time t_j, t_s is the start time of the breath hold determined by the sharp increase in SBP in phase I, and t_e is the time the breath hold is released in phase III. Each subject performed multiple repetitions of the VM with 2 minutes between maneuvers. Time-series ECG, blood pressure, ITP, and heart rate signals were extracted from LabChart for all viable VMs, that is, a data set in which the VM was performed correctly (the subject reached approximately 40 mmHg immediately and held that pressure steady with ±5 mmHg). All subjects with the exception of control subject 20 and patients 2 and 4 had more than one VM data set. Heart rate was computed from R-R intervals using LabChart cyclic detection for human ECG.

(a)

(b)
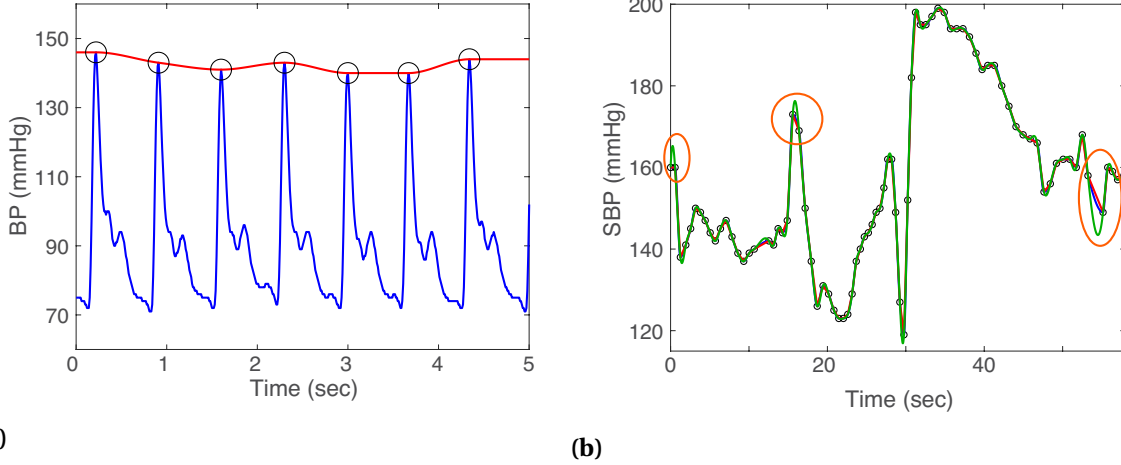
Figure 3.3 Systolic blood pressure (SBP, mmHg). (a) SBP (red) determined from the pulse pressure signal (blue) as the interpolation of the apex of each wave form per cardiac cycle (black circles). (b) Plot of splines through consecutive SBP points (black circles) using piecewise linear splines (red), piecewise cubic Hermite interpolating polynomial (blue), and piecewise cubic splines (green). Red ovals indicate areas of significant variation.

3.3   Data prepocessing

The open-loop model to be discussed in Chapter 4 uses systolic blood pressure (SBP) and thoracic pressure (P_{th}) signals as inputs. SBP and P_{th} distinguish between baroreceptor stimulation of the aortic arch and carotid sinus regions. Since the model is comprised of a system of differential equations, we compute the solutions using a variable-step solver RADAR5 [36], which evaluates the equations at any time point t within the domain. SBP data are sparse in time, which requires an appropriate interpolation method. P_{th} is determined using both the ITP data and an ECG-derived respiratory signal. This section discusses the numerical techniques and algorithms associated with determining these signals.

3.3.1   Systolic blood pressure

Systolic blood pressure (SBP) for one cardiac cycle is the apex of the pulse pressure signal in Figure 3.3a in one heartbeat. To determine a continuous SBP signal, we interpolate consecutive pulse pressure maxima. As shown, the SBP points are sparse in time, and hence, the method of interpolation may change the result. Commonly used splines have certain limitations.

- *Piecewise linear* (PL) splines are not differentiable at every data point [32].

- *Piecewise cubic* (PC) splines are differentiable at the nodes, but for data sparse in time they often induce artificial oscillations, overestimating the activity between nodes [32].

34
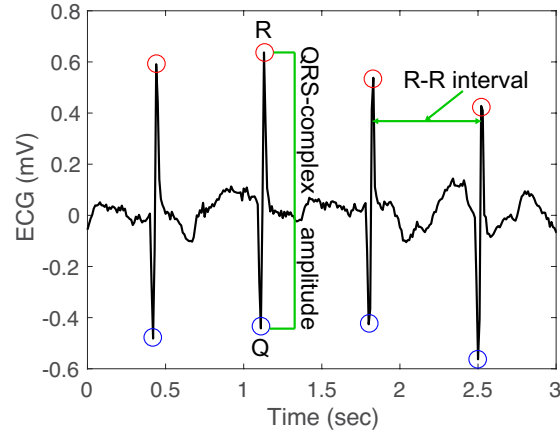
Figure 3.4 Electrocardiogram (ECG, mV) with R- and Q-points indicated with red and blue circles, respectively. A representative QRS-complex amplitude and R-R interval are denoted in green.

- *Piecewise cubit Hermite interpolating polynomial* (PCHIP) splines specify the value and the derivative at the nodes, which ensures differentiability at the nodes, maintains monotonicity, and preserves the shape of the data [32].

Figure 3.3b compares the performance these splines. The PL (red) and PCHIP (blue) splines are indistinguishable for most of the time span, while the PC spline (green) overestimates the behavior between the nodes significantly at the locations circled. The third oval is of particular note, where the PL spline draws a direct line between the nodes, the PCHIP spline curves slightly underneath the PL spline, and the PC spline dramatically fluctuates between the nodes. The PL spline is sufficient between the nodes, but the spline at the nodes themselves is not differentiable. The PC spline does not maintain the monotonic behavior between the two nodes and induces a false minimum. The PCHIP spline does ensure monotonicity and differentiability of the nodes. Therefore, for our purposes, PCHIP is the best interpolation method.

In the open-loop model discussed in Chapter 4, we use the SBP as an input to the model since the clinical ratios for the Valsalva maneuver are computed using the SBP, as shown in Section 2.3.4. However, Arndt *et al.* [5] showed that SBP, diastolic blood pressure, or mean arterial pressure (MAP) contain the similar information in the signals. Therefore, we could have used MAP in place of SBP as the input to this model. In the closed-loop model discussed in Chapter 7, we model the mean arterial blood pressure (MAP) instead of the SBP, since (i) SBP and MAP signals contain the similar information and (iI) MAP is modeled in previous studies [69, 88].
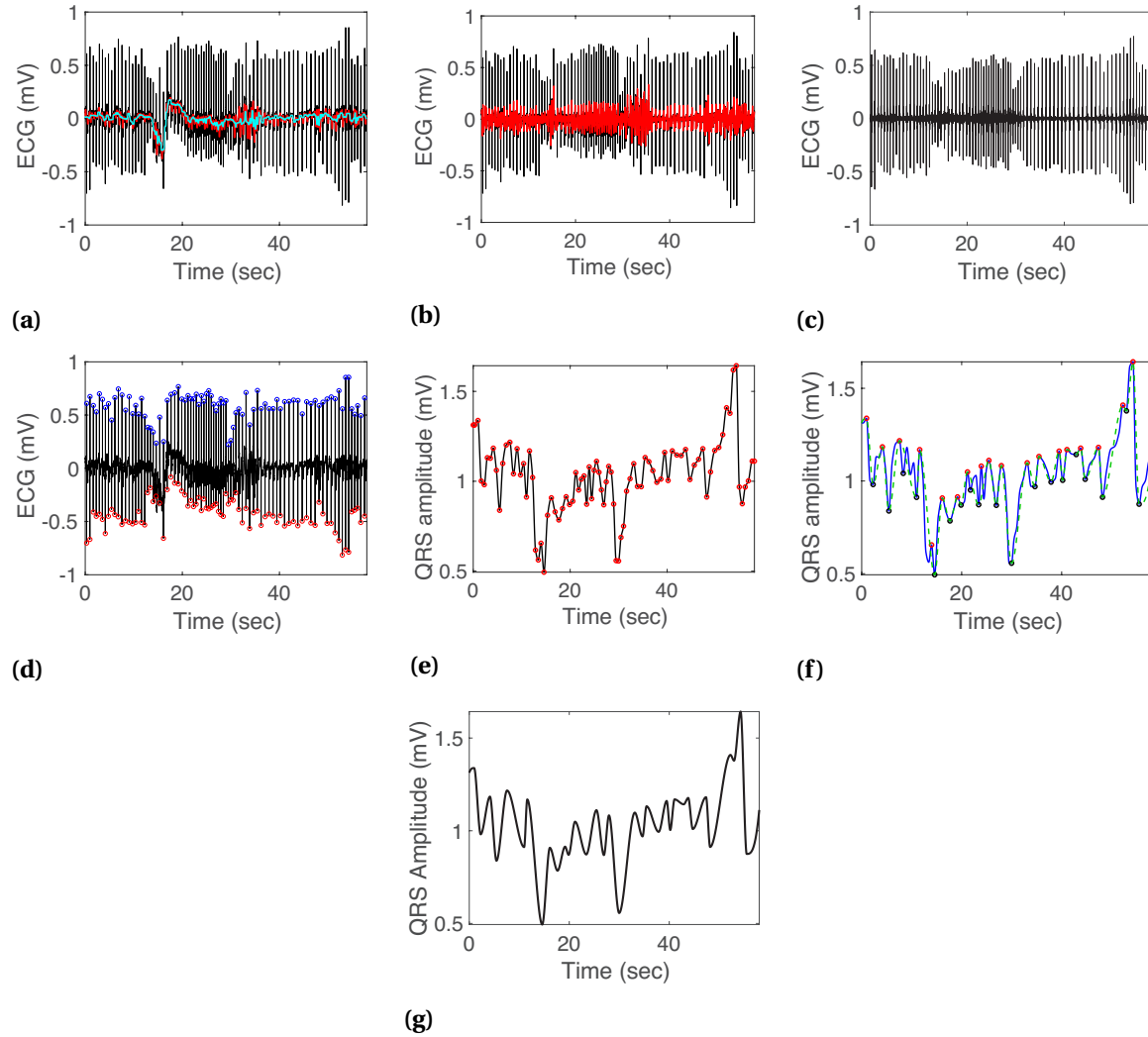
Figure 3.5 Step-by-step depiction of the algorithm deriving the respiration signal from the electrocardiogram (ECG) signal as described in algorithm 1. (a) ECG signal (black) with median filters of 200 ms (red) and 600 ms (blue). (b) Baseline-corrected ECG signal (black) with Savitsky-Golay filter (red). (c) Filtered baseline ECG. (d) Original ECG signal (black) with R- (blue circles) and Q- (red circles) points indicated. (e) Interpolation (black) of QRS-complex amplitude nodes (red circles). (f) Interpolation (black) of end of inspiration (red circles) and end of expiration (blue circles). The interpolation was filtered (green) to disregard false breaths. (e) Final respiration signal.

3.3.2 Effect of respiration on intrathoracic pressure

The amplitude of the ECG gives an indication of the depth of the breath. As the subject inhales, the chest expands and the electrodes on the skin move away from the heart. An ECG-derived respiratory signal can be determined from the interpolation of the amplitude of the QRS-complex in the ECG as shown in Figure 3.4. We developed a protocol employing algorithms from previous studies [105, 128, 134]. Widjaja *et al.* [134] validated this procedure against a measured reference respiratory signal at rest and under mental stress. We found local optima (*i.e.*, the R- and Q-points) to determine the amplitude of each QRS-complex and interpolated the values. Similar to the SBP, the QRS-complex occurs once per cardiac cycle, and the sparsity of the data requires a careful choice in interpolation scheme. Therefore, the only deviation we made from the developed algorithms is using PCHIP splines with a similar justification as given in Section 3.3.1. The resulting interpolated QRS-complex amplitude is assumed to be the mechanical breathing signal. Algorithm 1 gives the details for the algorithm for the processing of the ECG signal to obtain the respiration signal. Figure 3.5 depicts the step-by-step protocol for the algorithm.

Since the ECG-derived respiratory signal may miss obstructive apnea episodes, as in during the VM [46], we combined the respiratory signal at rest and the ITP data as shown in the schematic given in Figure 3.6 during the breath hold to obtain the thoracic pressure (P_{th}). The relationship between respiratory sinus arrhythmia and tidal volume is linear [59]. For simplicity, we assume the tidal volume and ITP are also linear. ITP is typically -4±2 mmHg and breathing amplitudes are typically 3.5-6 mmHg at rest [40]. To avoid sign errors, we scaled P_{th} to oscillate about 4 mmHg (the absolute value of the resting ITP) and incorporated the correct sign in the model. In this study, we combined both the ITP and the respiratory signal, R, to obtain

$$P_{th,j} = \begin{cases} \text{ITP}_j & t_s \le t_j < t_e \\ \dfrac{6-3.5}{\bar{R}_I - \bar{R}_E} R_j + (3.5 - \bar{R}_E) & \text{otherwise,} \end{cases} \qquad (3.2)$$

where $\bar{R}_I$ and $\bar{R}_E$ are the mean amplitudes for end of inspiration and end of expiration, respectively, and t_s and t_e are the start and end times of the VM extracted directly from the ITP signal as the times of greatest increase and decrease in ITP, respectively. This signal was then filtered using the `movmean` command in MATLAB® 2018a, which calculates a moving average over a specified window. For the thoracic pressure, we used a window of one second.

Algorithm 1 Processing of electrocardiogram (ECG) signal to obtain a respiratory signal.

---

1. Remove baseline wander.

   (a) Apply a median filter with a window of 200 milliseconds (ms) to the ECG signal, E, to filter out P-waves and QRS-complexes (Figure 3.5a blue curve) [105]. Then, the filtered signal is

   $$\tilde{E} = \text{ECG} - \text{Median filter of 200 ms.} \qquad (3.3)$$

   (b) Apply a median filter with a window of 600 ms to $\tilde{E}$ to filter out T-waves (Figure 3.3a red curve) [105]. Then, the baseline-corrected signal is

   $$\text{baseline-corrected ECG} = \tilde{E} - \text{Median filter of 600 ms.} \qquad (3.4)$$

   The baseline-corrected signal is shown as the black curve in Figure 3.5b.

2. Filter out extraneous noise by applying a Savitsky-Golay (SG) filter to the baseline-corrected ECG with a window of 150 ms (Figure 3.3b red curve). Then, the filtered baseline signal (Figure 3.5c) is

   $$\text{filtered baseline ECG} = \text{baseline-corrected ECG} - \text{SG filtered signal.} \qquad (3.5)$$

3. Detect the times at which the R- and Q-points occur.

   (a) The R-points are the most accentuated peaks and should be a minimum of 200 ms apart. However, smaller peaks that do not correspond to R-points will be detected. To avoid this, find all local maxima with a minimum peak distance of 200 ms. Then,

      i. Find the mean of peaks, μ_{all}.
      ii. Find all the local maxima again in the filtered baseline ECG signal with a minimum peak height of μ_{all} and a minimum peak distance of 200 ms. These are the R-points.
      iii. Find the mean of the R-points, μ_{R}.
      iv. Remove any of the detected peaks that are $< .25\mu_{\text{R}}$ or $> 2\mu_{\text{R}}$ to remove false R-points.
      v. Save the time points T_{R} at which the R-points occur.

   (b) Repeat for the Q-points with the negative of the filtered baseline ECG signal. Save the time points T_{Q} at which the Q-points occur.

4. Use T_{R} and T_{Q} to locate the R- and Q-points on the *original* ECG signal. Figure 3.5d shows the R- (blue circles) and Q- (red-circles) points on the original ECG signal (black).

5. Find the amplitude of the QRS-complex by subtracting the R- from the Q-points when their times are within 100 ms of each other.

6. Interpolate the QRS-complex amplitudes using a piecewise cubic Hermite interpolating polynomial (PCHIP) spline (Figure 3.5e). This gives the respiratory signal where peaks indicate end of inspiration and valleys indicate end of expiration.

Algorithm 1 Processing of electrocardiogram (ECG) signal to obtain a respiratory signal (continued).

7. Filter out false respiratory cycles.

   (a) Detect the end of inspiration peaks of the QRS-complex amplitude signal and institute a minimum peak distance of 1.5 seconds [134].

   (b) Repeat for the end of expiration valleys with the negative of the respiratory signal.

8. Remove amplitudes that are less than 15% of the difference of the previous and following amplitudes (Figure 3.5f). For an amplitude vector **a** of length n and **i** a vector of indexes,

   1: Let **i** be an empty vector.
   2: **for** $j = 2$ to $n-1$ **do**
   3:     **if** $\mathbf{a}_j \geq 0.85(a_{j+1} - a_{j-1})$ **then**
   4:         $\mathbf{i} \leftarrow [\mathbf{i}\ j]$
   5:     **end if**
   6: **end for**
   7: Concatenate $[a_1\ \mathbf{i}\ a_n]$.
   8: The filtered amplitude vector $\tilde{\mathbf{a}} = \mathbf{a}(\mathbf{i})$.

9. Interpolate $\tilde{\mathbf{a}}$ to obtain the respiratory signal (Figure 3.5g).
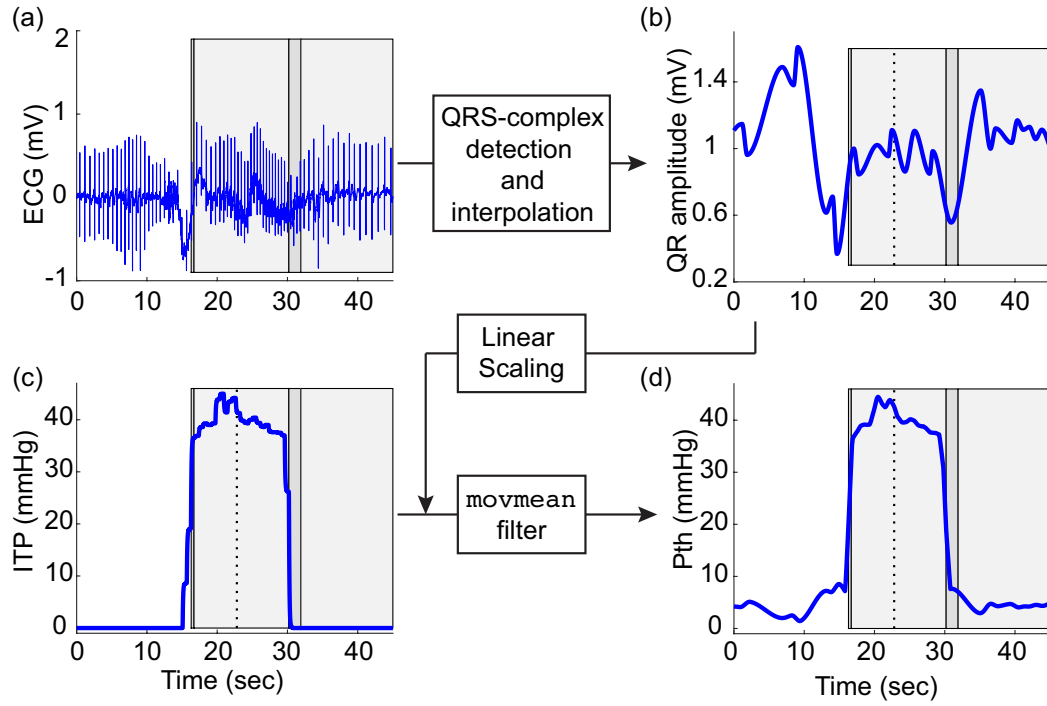
Figure 3.6 Thoracic pressure (P_{th}) input schematic. QRS-complexes are detected in the electrocardiogram (ECG, mV) trace (panel a). Amplitudes of consecutive QRS-complexes are interpolated using a piecewise cubic Hermite interpolating polynomial (PCHIP). This signal is filtered to produce the respiration signal (panel b), which is in turn scaled linearly given in equation (3.2). The intrathoracic pressure (ITP, mmHg) trace (panel c) is combined with the scaled respiration curve and filtered using the `movmean` command in MATLAB® 2018a to produce P_{th} (panel d).

4

NEUROLOGICAL CONTROL MODEL IN RESPONSE TO THE VALSALVA MANEUVER

This chapter is accepted for publication in the Journal of Applied Physiology with the title "A model-based analysis of autonomic nervous function in response to the Valsalva maneuver" with co-authors Anna Billeschou, Louise S. Brinth, Jesper Mehlsen, and Mette S. Olufsen. My contributions included all facets of the work except data collection, conducted by Billeschou and Brinth. Certain sections of this manuscript have been moved to other chapters, including the description of the Valsalva maneuver given in Section 2.3.4, the experimental protocol given in Section 3.2, and the processing of the data given in Section 3.3. All information that is relegated to an appendix in the manuscript has been moved to the body of this chapter.

Abstract

The Valsalva maneuver (VM) is a diagnostic protocol examining sympathetic and parasympathetic activity in patients with autonomic dysfunction (AD) impacting cardiovascular control. Since direct measurement of these signals is costly and invasive, AD is typically assessed indirectly by analyzing heart rate and blood pressure response patterns. This study introduces a mathematical model

that can predict sympathetic and parasympathetic dynamics. Our model-based analysis includes two control mechanisms: respiratory sinus arrhythmia (RSA) and the baroreflex. The RSA model integrates an electrocardiogram-derived respiratory signal with intrathoracic pressure, and the baroreflex model differentiates aortic and carotid baroreceptor regions. Patient-specific afferent and efferent signals are determined for 34 control subjects and 5 AD patients estimating parameters fitting the model output to heart rate data. Results show that inclusion of RSA and distinguishing aortic/carotid regions are necessary to model the heart rate response to the VM. Comparing control subjects to patients shows that RSA and baroreflex responses are significantly diminished. This study compares estimated parameter values from the model-based predictions to indices used in clinical practice. Three indices are computed determining adrenergic function from the slope of the systolic blood pressure in phase II (α - a new index), the baroreceptor sensitivity (β), and the Valsalva ratio (γ). Results show that these indices can distinguish between normal and abnormal states, but model-based analysis is needed to differentiate pathological signals. In summary, the model simulates various VM responses and, by combining indices and model predictions, we study the pathologies for 5 AD patients.

New and noteworthy

We introduce a patient-specific model analyzing heart rate and blood pressure during a Valsalva maneuver (VM). The model predicts autonomic function incorporating the baroreflex and respiratory sinus arrhythmia (RSA) control mechanisms. We introduce a novel index (α) characterizing sympathetic activity, which can distinguish control and abnormal patients. However, we assert that modeling and parameter estimation are necessary to explain pathologies. Finally, we show aortic baroreceptors contribute significantly to the VM and RSA affects early VM.

4.1   Introduction

Patients with autonomic nervous system dysfunction (AD) affecting the cardiovascular control system exhibit a wide array of symptoms including dizziness, syncope, and widespread pain, complicating intervention protocols and potentially leading to incorrect diagnoses [75]. Given the complex interaction of stimuli arising from multiple centers, understanding the mechanisms that cause AD is challenging. Autonomic nervous system (ANS) function is commonly studied indirectly by observing changes in blood pressure and heart rate in a controlled setting in response to postural or respiratory challenges or drug intervention [1, 17, 34, 51, 60, 107]. The objective of this study is to build a mathematical model that can analyze autonomic function for subjects undergoing a Valsalva maneuver (VM), a clinical test used to assess the ability to compensate for acute changes in central blood volume and pressure [60, 114].

In this study, we focus on the VM, which activates both parasympathetic and sympathetic branches of the ANS in sitting patients, inducing short-term changes in autonomic activity [60, 99]. This study develops a new mechanistic mathematical model providing a hypothesis for interactions of both the afferent and efferent neural pathways. Mathematical modeling used in this study and by others [20, 53, 65, 69] is advantageous as it enables us to analyze explicitly the effect of hypothesized pathways and predict responses to interventions by changing parameters or pathways in the model. Another common method for analyzing physiological signals is using signal processing methods [12, 122], which are excellent for determining changes in frequency-based responses but unable to describe signal transmission via specific pathways or predict responses to interventions.

Several deterministic mathematical models have been proposed to explain the autonomic response to the VM. These can be split into two categories: closed-loop models simulating blood pressure and heart rate dynamics simultaneously [53, 64, 69, 101]; and open-loop models that either (a) take blood pressure as an input computing heart rate as an output or (b) take heart rate as an input computing blood pressure as an output [20, 61]. In this study, we pursue the open-loop approach, predicting changes in heart rate in response to the VM. Our model distinguishes between the baroreceptor reflex (baroreflex) and respiratory sinus arrhythmia (RSA) control mechanisms. Others have modeled the interaction between the respiratory and cardiovascular systems [6, 66, 69]. However, these studies have respiratory models that are embedded in closed-loop cardiovascular models and the breathing mechanics are not patient-specific. Our model accounts for individual patient respiration and its effect on heart rate with the incorporation of an electrocardiogram (ECG)-derived respiratory signal, employing algorithms motivated by previous studies [105, 134].

We introduce a novel mathematical model of RSA and baroreflex control mechanisms, modulating heart rate and predicting parasympathetic and sympathetic responses to the VM. The primary objective for this study is to develop a model that can provide a robust description of the varied inter-subject dynamics of 34 control subjects ans 5 patients with AD observed during the VM. Though they have different pathologies, the 5 AD patients exhibit the V behavior as categorized by Palamarchuck *et al.* [94], which we hypothesize is due to diminished parasympathetic and sympathetic activity. We aim to explain the V behavior as it arises in these subjects.

The mathematical techniques used here provide a model-based analysis of the data inferring changes in neurological signaling over time. For patient-specificity, our study uses the subject's intrathoracic pressure (ITP) combined with their ECG-derived respiratory signal to determine thoracic pressure. The thoracic pressure (a) modulates heart rate due to respiration and (b) delineates between the aortic and carotid high-pressure baroreceptor (HPB) regions. To our knowledge, this concept has only been used in one previous study [61]. We estimate a subset of model parameters fitting the model to individual subject heart rate data, determining a patient-specific neural outflow. While the use of subset selection and parameter estimation is not new [87], to our knowledge no previous VM studies have taken advantage of these numerical methods. We also compare model-
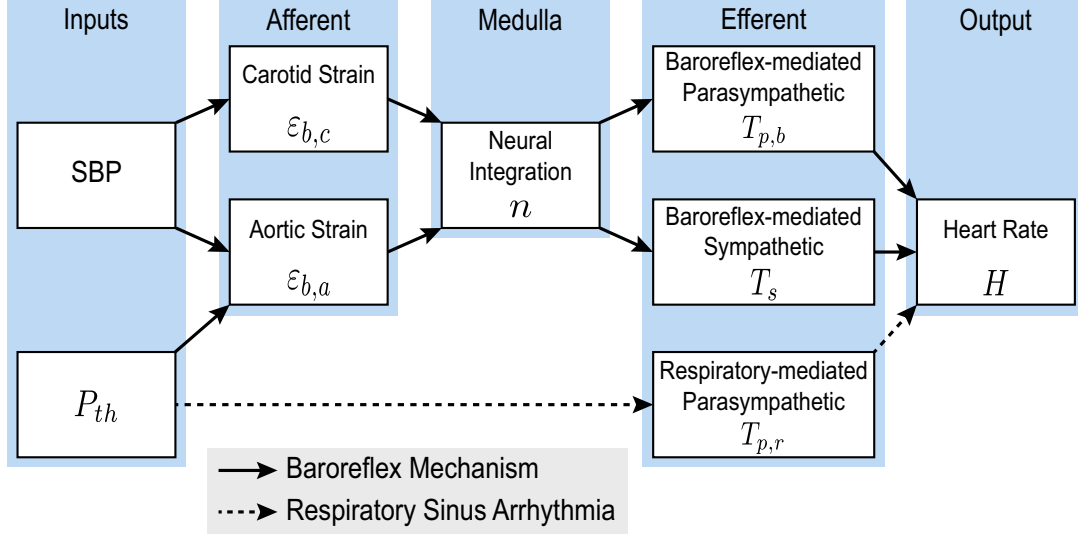
Figure 4.1 Schematic of the model with the systolic blood pressure (SBP, mmHg) and thoracic pressure (P_{th}, mmHg) as inputs. The baroreflex mechanism (solid arrows) and respiratory sinus arrhythmia (RSA, dotted arrows) are shown. Afferent signals are transmitted to the medulla via the carotid baroreceptor strain ($\varepsilon_{b,c}$), stimulated solely by the SBP, and the aortic baroreceptor strain ($\varepsilon_{b,a}$), stimulated by the difference in the SBP and P_{th}. The signals from the carotid sinus and aortic arch are integrated in the medulla via the neural integration, n. The baroreflex activates parasympathetic ($T_{p,b}$) and sympathetic (T_s) efferent signals, which modulate the heart rate output (H). P_{th} also acts modulates H during normal breathing via RSA.

derived quantities with indices extracted directly from the measured systolic blood pressure (SBP) and heart rate data [82, 83], which comprise the baroreceptor sensitivity (β), the Valsalva ratio (γ) [55, 82, 111], and a novel index (α), which we hypothesize is a measure of the subject's sympathetic function. Finally, inspired by previous studies [64, 69, 89], we employ a discrete delay to account for the time it takes to transmit sympathetic signals from the medulla to the effector (heart rate in this case). To our knowledge, this is the first attempt to use this mechanistic modeling approach to analyze autonomic function associated with the VM.

4.2 Materials and methods

This section describes the physiological motivation for the mathematical model and its parameterization. The model takes systolic blood pressure (SBP) and thoracic pressure (P_{th}) as inputs predicting heart rate and parasympathetic and sympathetic signals in response to the Valsalva maneuver (VM). Section 4.2.2 discusses the techniques used to analyze the model, including local sensitivity analysis and subset selection via the structured correlation methods. Moreover, this section describes the method used to determine a characteristic data set for each subject.

44

4.2.1 Model development

The model developed in this study (Figure 4.1) takes SBP and P_{th} as inputs and generates heart rate (H) as the output. The model encoding two control mechanisms, the baroreflex and RSA, has four major components: (a) an afferent baroreflex component, inspired by [72]; (b) a neural integration component, combining aortic and carotid afferent signals; (c) an efferent baroreflex component, encompassing the baroreflex-mediated parasympathetic and sympathetic outflows; and (d) an efferent respiratory component, modulating parasympathetic outflow. These components combine to determine H. The model developed below has 6 interacting state variables with 26 parameters.

4.2.1.1 Pressure signals

Increased ITP and forceful exhalation characterize the VM. Previous studies have posed mathematical models for inducing ITP by using a discrete step function [47, 69] or piecewise-continuous functions [53, 101]. In this study, we use the P_{th} given in equation (3.2). Since the arterial blood pressure data is from the finger (outside the thorax), we assume that it does not account for effects of the fluctuating ITP. Since the model is zero-dimensional (*i.e.*, the equations only depend on time), we neglect the reflected waves, which augment arterial SBP [81]. Therefore, we assign the continuous interpolated SBP to be the blood pressure sensed by the carotid sinus (P_c). We assume the pressure exerted on the tissues as the thoracic cavity inflates is negligible. Conversely, the aortic baroreceptors are inside the thorax and do experience increased ITP. We express the aortic blood pressure (P_a) as the difference between the SBP and P_{th}. These interactions are summarized as

$$P_c = \text{SBP} \quad \text{and} \quad P_a = \text{SBP} - P_{th}, \tag{4.1}$$

where SBP denotes the interpolated SBP and P_{th} is as in equation (3.2).

4.2.1.2 Arterial wall deformation

High pressure baroreceptors (HPBs) are embedded in the tunica externa of the arterial wall surrounded by collagen fibers and supported by elastic laminae [16]. Blood pressure and change in blood pressure deform and distend the arterial wall, causing HPBs to fire. Strain increases as pressure increases [129]. Since HPBs are found in both carotid and aortic regions with little to no variation between cells, we model the arterial wall strain ($\varepsilon_{w,j}$) as

$$\varepsilon_{w,j} = 1 - \sqrt{\frac{1 + e^{-q_w(P_j - s_w)}}{A + e^{-q_w(P_j - s_w)}}}, \tag{4.2}$$
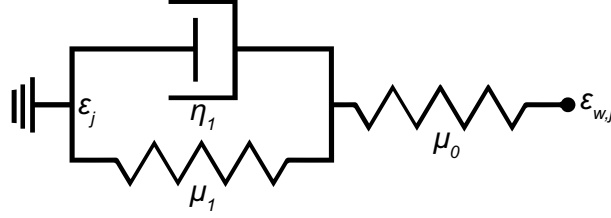
Figure 4.2 Voigt body element of the baroreceptor strain, ε_j, for $j = c$ or a indicating carotid and aortic regions, respectively, as they deform due to the arterial wall strain, $\varepsilon_{w,j}$. The baroreflex strain is predicted using one Voigt body element and a spring in series with spring proportionality constants, μ_0 and μ_1, and dashpot proportionality constant, η_1.

where P_j is the pressure sensed by the arterial wall for $j = a$ or c for aortic or carotid, respectively. The parameters q_w (mmHg^{-1}) and s_w (mmHg) denote the steepness and half-saturation value of the sigmoidal relationship in equation (4.2). A (dimensionless) denotes the maximum to unstressed cross-sectional area ratio [72].

4.2.1.3 High-pressure baroreceptor stimulation

Carotid baroreceptor nerve fibers form bundles of myelinated and unmyelinated fibers embedded in the collagen. As the vessel wall deforms, the HPBs stretch and return to rest. Collagen gives rise to viscoelastic deformation [129]. Given that the baroreceptor nerve endings are embedded in collagen,we hypothesize that baroreceptor deformation exhibits hysteresis, *i.e.*, the baroreceptors respond differently to an increase in wall strain as opposed to a decrease [37].

To model this behavior, we compute baroreceptor strain ($\varepsilon_{b,j}$) using a Voigt body element represented by a dashpot and resistor in parallel, mimicking the viscoelastic properties of the arterial wall [33]. A schematic of one Voigt body element is shown in Figure 4.2, where the Voigt body deforms due to pressure-dependent changes in arterial wall strain $\varepsilon_{w,j}$. Inspired by previous studies [20, 72], we model the stress-strain relationship as

$$\eta_1 \frac{\mathrm{d}\varepsilon_{b,j}}{\mathrm{d}t} + \mu_1 \varepsilon_{b,j} = \mu_0 \varepsilon_{w,j}, \tag{4.3}$$

where μ_0 (dimensionless) is the spring proportionality constant for the spring in series with the Voigt body and η_1 (sec) and μ_1 (dimensionless) are the dashpot and spring proportionality constants, respectively, for $j = c$ or a. Assuming μ_0, μ_1, and η_1 are not region-specific, the baroreceptor nerve fibers are inherently the same in both regions. Similar to previous studies [20, 64, 69], we simplify equation (4.3) by combining parameters and obtaining a linear differential equation predicting $\varepsilon_{b,j}$ as a function of $\varepsilon_{w,j}$ of the form

$$\frac{\mathrm{d}\varepsilon_{b,j}}{\mathrm{d}t} = \frac{-\varepsilon_{b,j} + K_b \varepsilon_{w,j}}{\tau_b}, \tag{4.4}$$

where $K_b = \mu_0/\mu_1$ (dimensionless) and $\tau_b = \eta_1/\mu_1$ (sec) are the gain and time constant of the HPB strain, respectively.

4.2.1.4 Neural integration

Carotid baroreceptors transduce signals via the glossopharyngeal nerve and the aortic baroreceptors via the vagal nerve [16]. The nerves synapse in the nucleus of the solitary tract which integrates and transmits the signals to the appropriate medullary region to elicit an efferent response [16]. Little is known about how the information from various regions of the vasculature are integrated and whether the medulla prefers one signal type to another. We do not model firing of individual neurons, but rather define neural integration (n) as a convex combination of the transduced HPB signals in response to the relative strain of each component, *i.e.*,

$$n = B(\varepsilon_{w,c} - \varepsilon_{b,c}) + (1 - B)(\varepsilon_{w,a} - \varepsilon_{b,a}), \quad B \in [0, 1]. \tag{4.5}$$

If $B = 1$, the model output depends solely on carotid HPB stimulation and aortic for $B = 0$.

4.2.1.5 Efferent baroreflex response

The nucleus ambiguus is the primary determinant of the fast baroreflex-mediated parasympathetic response ($T_{p,b}$), sending efferent signals via the vagal nerve to the heart [16]. The rostral ventrolateral medulla governs the baroreflex-mediated sympathetic response (T_s) via the sympathetic ganglia chain to the heart. Though previous studies have found an empirical sympathetic delay of 1.7 seconds in dogs [12] and 1.06 seconds in rabbits [14], previous modeling studies have used a 3 [69, 133] and 4 [63] second delay for humans. We chose to remain consistent with these modeling studies, using a delay of 3 seconds. $T_{p,b}$ arrives at the sinoatrial node much faster than T_s, and we assume the delay for $T_{p,b}$ is negligible. To maintain the inherent nonlinearity and hysteretic behavior of the neural outflows, we employ sigmoid functions of the form

$$G_{p,b} = \frac{1}{1 + e^{-q_{p,b}(n - s_{p,b})}} \quad \text{and} \quad G_s = \frac{1}{1 + e^{q_s(n - s_s)}}, \tag{4.6}$$

where n (sec^{-1}) is as in equation (4.5) and q_l (sec) and s_l (sec^{-1}) are the steepness parameter and half-saturation value with $l = p, b$ or s for parasympathetic and sympathetic baroreflex effects, respectively. We compute $T_{p,b}$ and T_s as the solutions to the first-order linear differential equations

$$\frac{\mathrm{d}T_{p,b}}{\mathrm{d}t} = \frac{-T_{p,b} + K_{p,b}G_{p,b}}{\tau_{p,b}} \quad \text{and} \quad \frac{\mathrm{d}T_s}{\mathrm{d}t} = \frac{-T_s(t - D_s) + K_s G_s}{\tau_s}, \tag{4.7}$$

where K_j (dimensionless) and τ_j (sec) are the gain and time constants. D_s (sec) is the delay in signal transmission of the sympathetic outflow. $T_{p,b}$ and T_s are dimensionless quantities modeling the outflow of the autonomic nervous activity in response to the afferent baroreflex firing rate.

4.2.1.6 Efferent respiratory pathway

The control centers of the respiratory muscles and heart rate are in close proximity in the brain stem and interact strongly [112]. One such mechanism is *respiratory sinus arrhythmia* (RSA), or heart rate variability in synchrony with respiration [138]. RSA is most prominent at rest, mediated via the vagal nerve synapsing on the sinoatrial node [139]. Many factors influence RSA, one being low-pressure baroreceptors (LPBs) known to modulate heart rate at rest [16]. Note that LPBs do not give rise to RSA but may modify its effects. LPBs deactivate during phases I and II, reactivate in phase III, and help return heart rate to baseline in phase IV. LPBs sense changes in central blood volume in the vena cava and right atrium [16]. However, since these volume measurements are difficult to acquire without performing invasive experiments, we used the ECG-derived respiratory signal in lieu of modeling LPBs explicitly.

The respiratory center receives stimuli from autonomic afferents and from the cerebral cortex. Therefore, respiration can be controlled both voluntarily and involuntarily. Consequently, the model has a solely efferent respiratory-mediated component with P_{th} as the input modeled as a decreasing sigmoid to account for the saturation of the thoracic pressure during large breaths in the form

$$G_{p,r} = \frac{1}{1 + e^{q_{p,r}(P_{th} - s_{p,r})}}, \tag{4.8}$$

where $q_{p,r}$ (mmHg^{-1}) and $s_{p,r}$ (mmHg) are the steepness and half-saturation value of the sigmoid, respectively. The respiratory-mediated parasympathetic outflow ($T_{p,r}$) is the solution of the differential equation

$$\frac{\mathrm{d}T_{p,r}}{\mathrm{d}t} = \frac{-T_{p,r} + K_{p,r}G_{p,r}}{\tau_{p,r}}, \tag{4.9}$$

where $K_{p,r}$ (dimensionless) and $\tau_{p,r}$ (sec) are the gain and time constants, respectively. The respiratory center relays sympathetic signals, but these signals do not synapse on the sinoatrial node [139]. Therefore, a respiratory-mediated sympathetic efferent is not included in this study.

4.2.1.7 Heart rate

Based on our previous studies [87–89], we model the resting heart rate as a linear combination of the efferent responses as

$$\tilde{H} = H_I(1 - H_{p,b}T_{p,b} + H_{p,r}T_{p,r} + H_s T_s), \tag{4.10}$$

where H_I (min^{-1}) is the intrinsic heart rate, $H_{p,b}$ and H_s (dimensionless) are scaling parameters for the baroreflex-mediated parasympathetic and sympathetic heart rate components, respectively, and $H_{p,r}$ (dimensionless) is the scaling parameter for the respiratory-mediated parasympathetic heart rate component. Previous models included a multiplicative term, incorporating the cancellation that occurs with both the parasympathetic and sympathetic baroreflex-mediated signals [69, 92]. However, simulations (not shown) indicate that this term does not affect the model output substantially. The intrinsic heart rate is the natural beating frequency of the denervated heart calculated as a function of age [52]. RSA-mediated parasympathetic activity only acts to increase H, as resting expiration is passive; hence, the positive sign before $H_{p,r}$ in equation (4.10). In response to a stressor, such as the VM, the dynamic heart rate is the solution to the differential equation

$$\frac{\mathrm{d}H}{\mathrm{d}t} = \frac{-H + \tilde{H}}{\tau_H},$$

(4.11)

where τ_H (sec) is the time constant for the response.

In summary, the model defined above is a system of stiff delay differential equations of the form

$$\frac{\mathrm{d}x}{\mathrm{d}t} = f(t, x(t), x(t - D_s); \theta),$$

(4.12)

where $x = [\varepsilon_{b,c}, \varepsilon_{b,a}, T_{p,b}, T_{p,r}, T_s, H]^T$ denotes the vector of 6 model states, D_s denotes the discrete sympathetic delay, and $\theta \in \mathbb{R}^{26}$ denotes the vector of model parameters, including

$$\theta = [A, B, K_b, K_{p,b}, K_{p,r}, K_s, \tau_{p,b}, \tau_b, \tau_{p,r}, \tau_s, \tau_H,$$
$$q_w, q_{p,b}, q_{p,r}, q_s, s_w, s_{p,b}, s_{p,r}, s_s, H_I, H_{p,b}, H_{p,r}, H_s, D_s, t_s, t_e]^T. \quad (4.13)$$

The inputs are the SBP and P_{th} signals and the output is the heart rate state H.

4.2.1.8 Initial conditions

The initial conditions were calculated analytically using the systolic blood pressure (SPB), thoracic pressure (P_{th}), and heart rate data values at the initial time point t_0. The model was parameterized to ensure it began in steady-state conditions. The initial conditions for the arterial wall strain for both the carotid and aortic regions are

$$\varepsilon_{w,c}(t_0) = 1 - \sqrt{\frac{1 + e^{-q_w(P_c(t_0) - s_w)}}{A + e^{-q_w(P_c(t_0) - s_w))}}}$$

(4.14)

and

$$\varepsilon_{w,a}(t_0) = 1 - \sqrt{\frac{1 + e^{-q_w(P_a(t_0) - s_w)}}{A + e^{-q_w(P_a(t_0) - s_w))}}},$$

(4.15)

which yields the initial conditions for the baroreceptors

$$\varepsilon_{b,j}(t_0) = K_b \varepsilon_{w,j}(t_0), \tag{4.16}$$

where $j = c$ or a for carotid and aortic, respectively. The initial neural integration is

$$n(t_0) = B(\varepsilon_{w,c}(t_0) - \varepsilon_{b,c}(t_0)) + (1 - B)(\varepsilon_{w,a}(t_0) - \varepsilon_{b,a}(t_0)). \tag{4.17}$$

The initial condition for the baroreflex-mediated parasympathetic outflow is

$$T_{p,b}(t_0) = K_{p,b} G_{p,b}(t_0) = \frac{K_{p,b}}{1 + e^{-q_{p,b}(n(t_0) - s_{p,b})}} \tag{4.18}$$

and the history for the delayed sympathetic outflow is set constant to the initial condition

$$T_s(t_0) = K_s G_s(t_0) = \frac{K_s}{1 + e^{-q_s(n(t_0) - s_s)}} \tag{4.19}$$

for simplicity. The initial condition for the respiratory-mediated parasympathetic outflow is

$$T_{p,r}(t_0) = K_{p,r} G_{p,r}(t_0) = \frac{K_{p,r}}{1 + e^{q_{p,r}(P_{th}(t_0) - s_{p,r})}}. \tag{4.20}$$

The initial condition for the heart rate ODE is

$$H(t_0) = H_{\text{data}}(t_0). \tag{4.21}$$

Table 4.1 Summary of parameter values and their descriptions, units, source (if any), and nominal values.

Description and Symbol			Units	Source					This Study	
				Mahdi (2013)	Lu (2001)	Ottesen (2000)	Olufsen (2006)	Wesseling (1992)		
Cross-sectional area ratio		A		5					5	
Neural scaling factor		B	sec^{-1}						0.5	
ODE Gains	Afferent baroreceptor	K_b				1*	3.06*		0.1	
	Baroreflex parasympathetic	$K_{p,b}$			0.8*		1*	0.83*	5	
	Respiratory parasympathetic	$K_{p,r}$						1.42	1	
	Baroreflex sympathetic	K_s			1*		1*	0.48*	5	
Heart rate gains	Intrinsic heart rate	H_I	min^{-1}		35*		100		100 ± 7	(4.25)
	Baroreflex parasympathetic	$H_{p,b}$			32*		0.45		0.5 ± 0.2	(4.29)
	Respiratory parasympathetic	$H_{p,r}$							0.3 ± 0.4	(4.28)
	Baroreflex sympathetic	H_s			140*		0.99		0.3 ± 0.4	(4.27)
ODE time constants	Baroreceptor strain	τ_b	sec		1	0.5	0.6		0.9	
	Baroreflex parasympathetic	$\tau_{p,b}$	sec		1.8		1.32	1.8	1.8	
	Respiratory sympathetic	$\tau_{p,r}$	sec					6	6	
	Baroreflex sympathetic	τ_s	sec		10		0.72*	10	10	
	Heart rate	τ_H	sec				1		0.5	
Sigmoid steepness	Arterial wall strain	q_w	mmHg^{-1}	5*					0.04	
	Baroreflex parasympathetic	$q_{p,b}$	sec		0.04*				10	
	Respiratory parasympathetic	$q_{p,r}$	mmHg^{-1}						1	
	Baroreflex sympathetic	q_s	sec		0.09*				10	
Half-saturation values	Arterial wall strain	s_w	mmHg	145					123 ± 20	(4.22)
	Baroreflex parasympathetic	$s_{p,b}$	sec^{-1}		110*				0.54 ± 4e-4	(6.3a)
	Respiratory parasympathetic	$s_{p,r}$	mmHg						4.88 ± 0.21	(4.22)
	Baroreflex sympathetic	s_s	sec^{-1}		100*				0.05 ± 4e-4	(4.24)
Sympathetic delay		D_s	sec		3		6.12	3	3	
Valsalva start time		t_s							data	
Valsalva end time		t_e							data	

 ODE - ordinary differential equation. An empty entry in the Units column indicates the parameter is dimensionless. Some parameters are calculated a priori and the equation reference is provided. Data refers to quantities extracted directly from intrathoracic pressure data.

 * denotes parameter values from models that are scaled differently from the model in this study.

4.2.1.9 Nominal parameter values

Some parameters are calculated a priori to calibrate the model to each individual subject. The half-saturation values of the sigmoidal relationships for the arterial wall strain, s_w, and the efferent respiratory pathway, $s_{p,r}$, can be interpreted as the baseline SBP and baseline P_{th}, respectively, determined as the average value over 15 seconds of rest, *i.e.*,

$$s_w = \bar{P} \quad \text{and} \quad s_{p,r} = \bar{P}_{th}. \tag{4.22}$$

The half-saturation values of the baroreflex-mediated parasympathetic and sympathetic sigmoids, $s_{p,b}$ and s_s, are calculated assuming the parasympathetic activity contributed 80% of the baroreflex control of the heart rate at rest, while the sympathetic activity contributed 20% [25, 107]. The bars in the following calculations indicate average values calculated from the SBP, P_{th}, and heart rate data $(\bar{P}, \bar{P}_{th}, \bar{H})$. The half-saturation values are given by

$$
\begin{aligned}
\bar{P}_c &= \bar{P} \\
\bar{P}_a &= \bar{P} - \bar{P}_{th} \\
\bar{\varepsilon}_{w,j} &= 1 - \sqrt{\frac{1 + e^{-q_w(\bar{P}_j - s_w)}}{A + e^{-q_w(\bar{P}_j - s_w))}}} \\
\bar{\varepsilon}_{b,j} &= K_b \bar{\varepsilon}_{w,j} \\
\bar{n} &= B(\bar{\varepsilon}_{w,c} - \bar{\varepsilon}_{b,c}) + (1 - B)(\bar{\varepsilon}_{w,a} + \bar{\varepsilon}_{b,a}) \\
s_{p,b} &= \bar{n} + \frac{1}{q_{p,b}} \ln\left(\frac{K_{p,b}}{T_{p,b}} - 1\right) & (4.23) \\
s_s &= \bar{n} - \frac{1}{q_s} \ln\left(\frac{K_s}{T_s} - 1\right), & (4.24)
\end{aligned}
$$

where $\bar{T}_{p,b} = 0.8$ and $\bar{T}_s = 0.2$ and $j = c$ or a.

We calculate the intrinsic heart rate, H_I, as a function of age

$$H_I = 118 - 0.57 \text{age} \tag{4.25}$$

[52]. We calculate the sympathetic coefficient for heart rate, H_s, by determining the maximal heart rate possible based on age using the equation from Tanaka *et al.* [127]

$$H_M = 208 - 0.7 \text{age}. \tag{4.26}$$

To attain the maximal heart rate, we assume sympathetic activity should be at its highest value and

parasympathetic activity at its lowest value, *i.e.*, $G_{p,b} = G_{p,r} = 0$ and $G_s = 1$. Then,

$$H_M = H_I(1 + H_s K_s) \quad \Rightarrow \quad H_s = \frac{1}{K_s}\left(\frac{H_M}{H_I} - 1\right). \tag{4.27}$$

The nominal value for the respiratory-mediated parasympathetic scaling factor for heart rate, $H_{p,r}$, is calculated by finding the largest value in the heart rate data due to respiration during rest, $H_{R,M}$, and the lowest value, $H_{R,m}$, *i.e.*,

$$H_{p,r} = \frac{H_{R,M} - H_{R,m}}{H_I}\frac{1}{\bar{T}_{p,r}}, \tag{4.28}$$

where $\bar{T}_{p,r}$ is the steady-state respiratory-mediated parasympathetic outflow set at 0.5 sec^{-1}. The baroreflex-mediated parasympathetic outflow parameter is reverse-engineered from the resting heart rate equation using the baseline heart rate, $\bar{H}$, which yields

$$H_{p,b} = \frac{1 + \dfrac{\bar{H}}{H_I} + H_{p,r}\bar{T}_{p,r} + H_s\bar{T}_s}{\bar{T}_{p,b}}. \tag{4.29}$$

4.2.1.10 Numerical methods

The model was solved using the RADAR5 algorithm, a stiff delay differential equations solver, in Fortran developed by Guglielmi and Hairer [36]. This system is stiff due to the steep, fast changing sigmoidal relationships given in equations (4.2), (4.6), and (4.8) and the time constants (τ_b, $\tau_{p,b}$, $\tau_{p,r}$, τ_s, and τ_H) varying significantly in magnitude. RADAR5 is an extension of Radau IIA methods, which use explicit Runge-Kutta methods that are suitable for stiff delay differential equation systems. This is a variable-step solver, in which the solution is not necessarily computed at the same times as the experimental data. Hence, the model output was numerically interpolated at the time points of the heart rate data.

4.2.2 Model analysis

4.2.2.1 Local sensitivity analysis

We performed a local analysis to determine how the model output H responds to variations in parameter evaluated at their nominal values [28, 30, 71, 72]. To analyze how the model deviates from the data, we compute the sensitivity matrix (**S**) with respect to the residual (**r**) at time t_j given by

$$\mathbf{r}(t_j) = \frac{H(t_j;\theta) - H_{\text{data}}(t_j)}{H_{\text{data}}}\frac{1}{\sqrt{N}}, \tag{4.30}$$
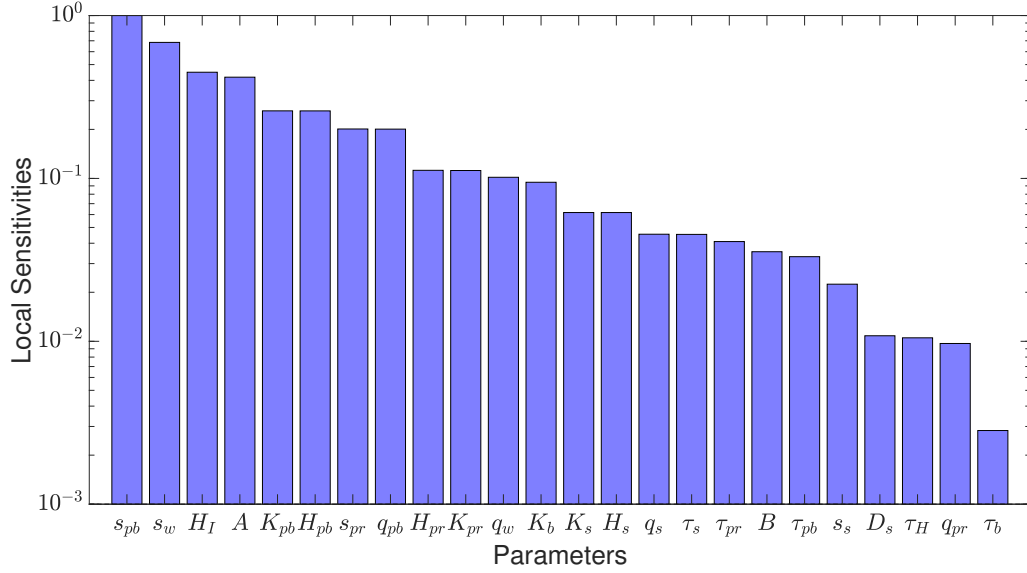
Figure 4.3 Ranked relative sensitivities calculated in equation (4.32) for all parameters excluding the start and end VM times, t_s and t_e, respectively. The most sensitive parameter is on the left and the sensitivities decrease accordingly. All parameters are above the sensitivity threshold of 10^{-3}.

where $H(t_j; \theta)$ and $H_{\text{data}}(t_j)$ denote the heart rate model output and data at time t_j, respectively, and N is the number of data points. Due to the variation in magnitude of the parameters, we compute the sensitivity of the model to the logarithm of parameter θ_i at time t_j as

$$\mathbf{S}_{ij} = \frac{\mathrm{d}\mathbf{r}(t_j)}{\mathrm{d}\log(\theta_i)} = \frac{\mathrm{d}}{\mathrm{d}\theta_i} \frac{H(t_j) - H_{\text{data}}(t_j)}{H_{\text{data}}(t_j)} \theta_i = \frac{\mathrm{d}H(t_j)}{\mathrm{d}\theta_i} \frac{\theta_i}{H_{\text{data}}(t_j)}. \tag{4.31}$$

The columns of $\mathbf{S}$ are vectors with measurements of the model sensitivity to parameter θ_i for all t_j. It is useful to rank the parameters based on their degree of influence. This ranking can help determine whether certain parameters are noninfluential. In this study, we compute the Euclidean norm on each column of the relative sensitivity matrix

$$s_i = \|\mathbf{S}_i\|_2 \tag{4.32}$$

for i the column index. Dividing the column indices by the maximal index yields the most influential parameter with sensitivity 1 and the others decreasing accordingly. The integration tolerance for these models was set to $\phi = 10^{-8}$. The most sensitive parameters are above the sensitivity threshold $10\sqrt{\phi} = 10^{-3}$ [100].

We did not include times extricated from data, t_s and t_e in the sensitivity analysis. Naturally, the model is very sensitive to changes in these parameters, but we set them constant to ensure patient-specificity. Thus, we only consider 24 parameters in the sensitivity analysis. Figure 4.3 displays

the ranked relative sensitivities for these model parameters. All of the parameters were above the sensitivity threshold of 10^{-3}. We determined $s_{p,b}$, s_w, H_I, and A were the most sensitive parameters. Since these parameters are highly sensitive, small fluctuations cause large changes in the model output. Changes in the least sensitive parameters, $q_{p,r}$ and τ_b, show a negligible change in model output.

4.2.2.2 Correlation analysis and subset selection

Many methods exist to perform subset selection to obtain a set of parameters to optimize, including subspace selection [115] and singular value decomposition of $\mathbf{S}$ followed by a Q-R factorization [87]. In this study, we perform a local structured correlation analysis to determine possible pairwise correlations between sensitive parameters [28, 136]. We compute the covariance matrix $\mathbf{C} = (\mathbf{S}^T \mathbf{S})^{-1}$ with corresponding correlation matrix $\mathbf{c}$ as

$$c_{ij} = \frac{C_{ij}}{\sqrt{C_{ii} C_{jj}}}, \tag{4.33}$$

which is symmetric where $|c_{ii}| = 1$ and $|c_{ij}| \leq 1$. For this study, we assumed two parameters were correlated if $|c_{ij}| \geq 0.95$.

We analyzed pairwise correlations between only a subset of parameters. The sigmoid half-saturation values, s_w, $s_{p,r}$, $s_{p,b}$, and s_s, are calculated as shown above. The half-saturation values are difficult to optimize, as the optimized result can force the model to produce a linear relation where nonlinearity occurs physiologically. Estimating the sigmoid steepness parameters, q_w, $q_{p,r}$, $q_{p,b}$, and q_s, pose similar challenges, producing neural signals that are not physiological. Thus, we left these parameters fixed. As with the sensitivity analysis, we excluded the time parameters from the correlation analysis. The new subset of parameters includes

$$\hat{\theta} = [A, B, K_b, K_{p,b}, K_{p,r}, K_s, \tau_b, \tau_{p,b}, \tau_{p,r}, \tau_s, \tau_H, H_I, H_{p,b}, H_{p,r}, H_s, D_s]^T. \tag{4.34}$$

We performed a structured correlation analysis on $\hat{\theta}$. When pairwise correlations arise, we remove the least influential parameter from $\hat{\theta}$ based on the local sensitivity analysis. The resulting subset of parameters to optimize free of pairwise correlations is

$$\tilde{\theta} = [B, \tau_{p,b}, \tau_{p,r}, \tau_s, H_I, H_{p,b}, H_{p,r}, H_s]^T \tag{4.35}$$

in which the parameters are above the sensitivity threshold 10^{-3} and are not pairwise correlated. Furthermore, we confirmed this subset with a global sensitivity analysis using delayed rejection adaptation metropolis (DRAM). DRAM combines the delayed rejection and adaptive metropolis algorithms to improve the efficiency of the Metropolis-Hastings algorithm [39]. While correlation

analysis is significantly less computationally expensive than DRAM, it only calculates a first-order linearization of the parameter interactions, and therefore, does not take into account the higher order parameter interactions. In this regard, DRAM is much more suited for capturing the nuances of nonlinear parameter interactions and ensures our subset was identifiable. Moreover, we conducted a cross-validation of the parameters by altering the nominal parameter values and re-optimizing. We then analyzed 10 re-optimization iterations and found that the coefficient of variation (σ/μ for σ the standard deviation and μ the mean) was $\sigma/\mu < 0.15$ for all parameters in this set.

We estimated $\tilde{\theta}$ using nonlinear least squares optimization, since the problem is nonlinear with respect to the parameters. This method minimizes the cost functional

$$J = \mathbf{r}^T\mathbf{r} + \left(\frac{\max\limits_{j} H(t_j) - \max\limits_{j} H_{\text{data}}(t_j)}{\max\limits_{j} H_{\text{data}}(t_j)}\right)^2, \tag{4.36}$$

where $\mathbf{r}$ is the residual vector given in equation (4.30) and the secdon term ensures that the maximal heart rate attained during the VM is modeled accurately. To account for the wide variation in magnitude of the parameters and to ensure positivity, we optimized the logarithm of the parameters. We used a Levenberg-Marquardt scheme by Kelley [57].

4.2.2.3   Characteristic Valsalva maneuver

Since almost every subject has multiple viable VM data sets, we identify a *characteristic VM* defined as the VM with estimated and calculated parameter values closest to the intra-subject mean for the subject. The following algorithm determines the characteristic VM for each subject:

1. For each viable VM data set j of the ith subject, we consider the subset

    $$\Theta_{i,j} = [\tilde{\theta}^T, s_w, s_{p,r}, \bar{H}]^T = [B, \tau_{p,b}, \tau_{p,r}, \tau_s, H_I, H_{p,b}, H_{p,r}, H_s, s_w, s_{p,r}, \bar{H}]^T, \tag{4.37}$$

    which includes the optimized parameter set $\tilde{\theta}$, the baseline blood pressure and P_{th} values (s_w and $s_{p,r}$), and the baseline heart rate ($\bar{H}$). s_w, $s_{p,r}$, and $\bar{H}$ are used since they are calculated directly from the data and are patient-specific. If an optimized parameter hit a lower or upper bound, that value was excluded. We calculate the intra-subject means of these parameters, $\bar{\Theta}_i$.

2. Since the parameters vary in scale, we compare the logarithm of the parameters. We determine which VM data set is characteristic for that subject by

    $$\min_{j} ||\log\bar{\Theta}_i - \log\Theta_{i,j}||_2. \tag{4.38}$$

3. The viable VM data set with $\Theta_{i,j}$ closest to the mean is the "characteristic VM" for that subject.

56
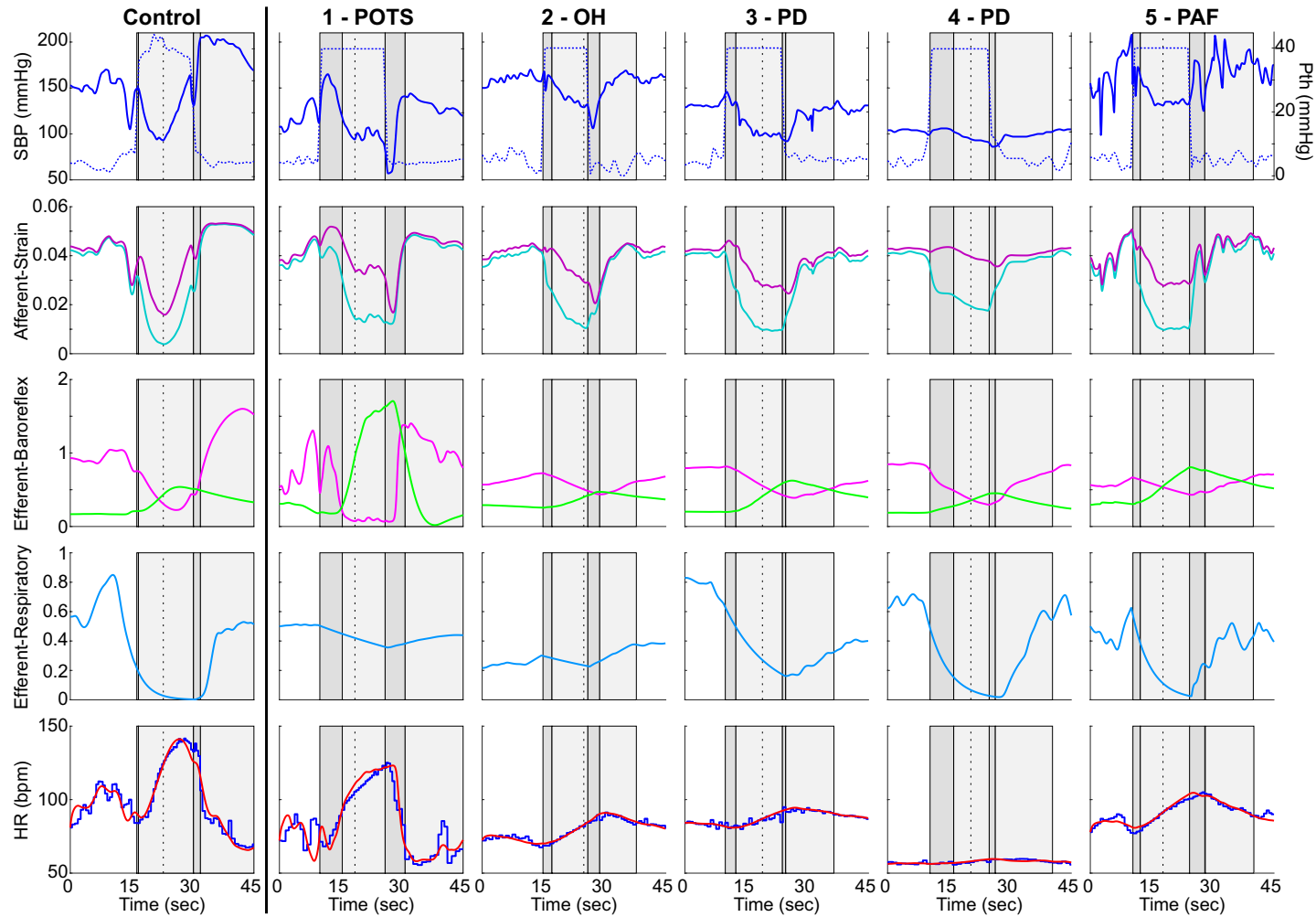
Figure 4.4 Data, model fit, and model predictions for control subject 2 (column 1) and the five patients with autonomic dysfunction (columns 2-6). Each column is designated with their particular pathology: postural orthostatic tachycardia syndrome (POTS), orthostatic hypotension (OH), Parkinson's disease (PD), and pure autonomic failure (PAF). The rows in order: (1) the inputs with the interpolated systolic blood pressure (SBP) plotted from the left y-axis and thoracic pressure (P_{th}) plotted from the right y-axis; (2) predicted baroreceptor strain for the carotid (purple) and aortic (teal) baroreceptors; (3) efferent baroreflex response signals for the parasympathetic ($T_{p,b}$, magenta) and sympathetic (T_s, green) outflows; (4) efferent respiratory response ($T_{p,r}$); (5) and the model fit (red) to heart rate data (blue). The phases of the Valsalva are designated with alternating gray and light gray boxes. The vertical dashed line delineates between early and late sections of phase II.

57

Table 4.2 Clinical ratios for the control group (34 subjects) and for the 5 patients with autonomic dysfunction (pathologies listed in Table 3.2) with means and standard deviations reported.

	Clinical Ratios		
	α	β	γ
Control	5 ± 3	15 ± 13	1.7 ± 0.4
Patient			
1	-0.6*	19	2.8*
2	0*	3	1*
3	0*	13	1.1*
4	0*	18	1*
5	0.5*	3*	1*

* indicates clinical ratio is outside of one standard deviation.

4.3 Results

We have validated our model against 34 control subjects and 5 AD patients with V behavior categorized by Palamarchuk *et al.* [94]. For each subject, we fitted the model to every VM data set and identified a characteristic VM. We used the Levenberg-Marquardt optimization algorithm [57] to estimate the parameter subset $\tilde{\theta}$ given in equation (4.35) minimizing the least squares error given in equation (4.36). Table 4.2 lists the population means and standard deviations of the clinical ratios for the control subjects, calculated from the characteristic VM for each subject, and the clinical ratios for each AD patient. Table 4.3 lists the population means and standard deviations for the estimated parameter values for the control subjects along with the values for the 5 AD patients .

   To test identifiability of the parameters in subset $\tilde{\theta}$, we varied the nominal parameter values in equation (4.35) by ±20% for 10 optimization iterations for control subject 2. The mean (μ) and standard deviations (σ) were calculated across the iterations. The coefficient of variation (σ/μ) for each parameter in subset $\tilde{\theta}$ did not exceed 0.14 . This was performed on the characteristic VM for each subject with similar results, indicating the scheme has reached an individual minimum.

Table 4.3 Means and standard deviations of the cost functional and estimated parameter values for the characteristic Valsalva maneuver for 34 control subjects and 5 patients with autonomic dysfunction (pathologies listed in Table 3.2)

	Cost	Estimated Parameters						
	$J(10^{-3})$	B	$\tau_{p,b}$	$\tau_{p,r}$	τ_s	$H_{p,b}$	$H_{p,r}$	H_s
Control	8 ± 5	0.4 ± 0.3	6.5 ± 5.7	9.6 ± 10.8	14 ± 8	0.5 ± 0.2	0.3 ± 0.2	0.3 ± 0.2
Patient								
1	12	0.04*	0.2*	47*	5	0.4	0.05*	0.1
2	0.5	0.5	17*	41*	36*	0.5	0.4	0.5
3	0.4	0.5	13*	2	16	0.2*	0.07*	0.1
4	0.2	0.5	2	4	13	0.1*	0.09*	0.3
5	0.6	0.09*	23*	4	37*	0.4	0.03*	0.3

* indicates clinical ratio is outside of one standard deviation.

4.3.1 Qualitative behavior

Figures 4.4 displays the model performance (computed with optimized patient-specific parameters) for a representative control subject (subject 2) and all 5 AD patients. Figure 4.4, column 1, panel 1 displays the input signals SPB and P_{th} used to distinguish the afferent HPB strains of the carotid sinus (purple) and aorta (teal) (column 1, panel 2). These signals modulate the efferent baroreflex-mediated parasympathetic ($T_{p,b}$, magenta) and sympathetic (T_s, green) responses (column 1, panel 3). The ordinates of the plot can be interpreted as a percentage of the autonomic outflow. Column 1, panel 4 displays the respiratory-mediated parasympathetic outflow ($T_{p,r}$). The model output H (red) is effectively calibrated to the heart rate data (blue) both at rest and during the VM (column 1, panel 5). The large oscillations in the heart rate data are due to deep inhalations of the subject prior to the VM, which are captured by the respiratory model component. All signals begin in steady-state when the subject is at rest. Since the model output is continuous and the data are discrete, inevitably there will be discrepancies between each individual heart period and the model output.

The 5 AD patients all have different pathologies, noted at the top of columns 2-6, that result in different control responses from the baroreflex and RSA. Patient 1 is diagnosed with POTS, as shown with the substantial increase in heart rate. By comparing column 1 panel 3 (control) to column 2 panel 3 (POTS), the model predicts overactive parasympathetic and sympathetic behavior. $T_{p,b}$ (magenta) oscillates significantly more at steady-state and decreases to zero during the VM. T_s (green) increases substantially during late phase II of the VM, then decreases sharply in phase III,

and undershoots in phase IV. Dynamic regulation from RSA is minimal (column 2, panel 4) as $T_{p,r}$ is a smooth curve with minor fluctuations.

In comparison, patients 2-5 (columns 3-6, panel 3) have a suppressed parasympathetic response to the control subject and patient 1 (column 1-2, panel 3). Since these patients are much older than the control subject and patient 1, they are expected to have decreased $T_{p,b}$ activity [96]. The traces for T_s behave similarly to the control subject. This is surprising, especially for patient 5 as PAF typically displays substantial adrenergic sensitivity [19]. These results suggest that for these patients there is a substantial decrease in parasympathetic, while their sympathetic activity to the sinoatrial is normal.

Similarly, we expect $T_{p,r}$ (the respiratory outflow) to exhibit minimal dynamics. However, for patients 3, 4, and 5, $T_{p,r}$ fluctuates similar to the control subject. The trace for $T_{p,r}$ must be taken in conjunction with the RSA gain for the heart rate $H_{p,r}$ (Table 4.3). Even though $T_{p,r}$ is dynamic for patients 3, 4, and 5, $H_{p,r}$ is 0.02, 0.09, and 0.03, respectively, indicating little to no effect of RSA on heart rate. Hence, the model is able to produce a trace for RSA, which can represent respiratory effects in these patients that are not reflected in the heart rate.

4.3.2   Quantitative results

4.3.2.1   Clinical ratios

Table 4.2 lists the means and standard deviations of the clinical ratios for the characteristic VMs for all 34 control subjects and 5 AD patients. To test if extracted clinical ratios vary with age or sex, we divided the control group by sex (male versus female) and age (≤ 40 years versus >40 years). No statistical differences were detected when accounting for sex, age, or their interactions via a two-way ANOVA (results not included). Thus, the analysis in this study combines all control subjects in one group. The mean value for β agrees with normal baroreceptor sensitivity indices for control subjects in previous studies [55, 84]. The mean value with one standard deviation for the Valsalva ratio γ also agrees with previous standards [83].

All 5 AD patients were chosen because they exhibit V behavior, which we quantify by a value of $\alpha \ll 1$. Since there was no monotonic increase of SBP back to baseline for patient 1, the regression was done over the entire late phase II interval, yielding a negative α value ($\alpha = -0.6$). Patients 2-4 show no change in SBP in late phase II ($\alpha = 0$). For Patient 5, $\alpha = 0.5$ remains below one standard deviation of the mean of the control subjects.

The baroreflex sensitivity index β is within normal range for patients 1, 3, and 4. Patients 2 and 5 are also within normal range but an order of magnitude smaller ($\beta = 3$) than the mean of the control subjects. This is to be expected for patients with OH, as the change in heart rate is small in relation to the change in SBP.

The Valsalva ratio γ for patient 1 was greater than the mean of the control subjects, indicating

Table 4.4 Relative autonomic activity of the 5 patients with autonomic dysfunction exhibiting V behavior compared to the control subject.

Control Mechanism	Pathway	Symbol	Patient				
			1	2	3	4	5
Baroreflex	Parasympathetic	$T_{p,b}$	↑	↓	↓	↓	↓
	Sympathetic	T_s	↑	↓			↓
RSA	Parasympathetic	$T_{p,r}$	↓	↓	↓	↓	↓
Agree with V hypothesis?			N	Y	N	N	Y

Blank spaces indicate no change.
Y - yes. N - no.

a substantial drop in heart rate from phase III to phase IV. This is to be expected for patients with POTS as the heart rate has increased significantly during the VM. Patients 2-5 show $\gamma \approx 1$, indicating abnormal behavior with little to no change in heart rate in the late phases of the VM.

4.3.2.2 Estimated parameter values

Table 4.3 displays the mean and standard deviation of the nonlinear least squares cost and the estimated parameters of the characteristic VM for all 34 control subjects and 5 AD patients. Again, no statistical differences were detected via a two-way ANOVA accounting for sex and age (results not included). No correlations were found between the clinical ratios and the estimated parameters, which is to be expected since the model is not informed by the clinical ratios. Also, no correlations were found between the calculated parameters in Table 4.1 and the clinical ratios. This is surprising since we expected the parameters calculated directly from the data to correlate with the ratios. This could be due to the fact that the clinical ratios reflect transient changes in heart rate and blood pressure, while the calculated model parameters are determined from baseline values. The Valsalva ratio in particular is not dependent on baseline values [31]. The following paragraphs describe the results from the estimated parameters and the predicted autonomic function of each patient. Table 4.4 summarizes these results with arrows signifying either an increase or decrease in function.

For Patient 1 (POTS), the optimized B value is an order of magnitude smaller than the mean of the control subjects, signifying that the aortic baroreceptors contribute the most to the heart rate. The time-scale $\tau_{p,b}$ is an order of magnitude smaller than the mean of the control subjects as well, signifying that the baroreflex-mediated parasympathetic response is overactive. The time-scale τ_s is outside of one standard deviation of the mean of the control subjects, indicating an increased sympathetic outflow, while H_s is within its normal range. The combination of these parameter values implies an increased parasympathetic and sympathetic activity to the sinoatrial node, which contradicts our hypothesis of diminished parasympathetic and sympathetic activity due to the baroreflex. This is surprising since the V behavior is typically seen in subjects with adrenergic failure.

$H_{p,r}$ associated with RSA is approximately zero, signifying the effect from RSA is negligible.

Patients 3 and 4 (PD) have parameter values that fall in similar ranges. The parasympathetic parameters, $H_{p,b}$ and $H_{p,r}$, are outside of one standard deviation off the mean of the control subjects. This is to be expected as PD tends to drastically affect the parasympathetic nervous system, whereas declines in sympathetic activity occur much later. These subjects also do not coincide with the hypothesis for the V behavior, as only the parasympathetic activity has decreased but the sympathetic activity is within normal range.

The parameter values for patient 2 (OH) and patient 5 (PAF) fall in ranges that are indicative of their diagnoses. The B value is an order of magnitude smaller than the mean of the controls, skewing the effect of the baroreceptors on the heart rate to the aortic arch. For patient 5, $H_{p,r}$ is lower than one standard deviation from the mean, indicating little to no effect of the parasympathetic outflow on heart rate from RSA. Furthermore, τ_s is very large for both ($\tau_s > 30$) relative to the control subjects, indicating a much longer effect of the sympathetic control on heart rate. The combination of these parameter values signifies the dysfunction of both the parasympathetic and sympathetic pathways, which agrees with our hypothesis of the V behavior.

4.4   Discussion

This study presents a mathematical model of the autonomic nervous control of heart rate before, during, and after the Valsalva maneuver (VM) through two control mechanisms: respiratory sinus arrhythmia (RSA) and the baroreflex. Since autonomic activity is difficult to measure *in vivo* and, therefore, must be analyzed indirectly, modeling sympathetic and parasympathetic signals yields both a quantitative and qualitative assessment of autonomic function. The model in conjunction with parameter estimation fits many different kinds of heart rate responses to the VM. The model was effectively validated against 34 control subjects and 5 AD patients, varying widely in age and baseline blood pressure and heart rate values. Several other studies have attempted to model the VM [20, 47, 53, 64, 69, 101]. However, our model provides novel facets, such as the (a) inclusion of two input signals SBP and P_{th}; (b) delineation between the aortic and carotid baroreceptor centers; (c) combination of both the ITP and the respiratory signal to determine P_{th}; and (d) incorporation of a sympathetic delay. The estimated parameters can help explain and differentiate etiologies for AD pathologies not captured by the data and/or clinical ratios alone. In summary, the model in conjunction with parameter estimation supplements existing data analysis protocols by providing time-series for various neurological pathways and interpretable parameter values for disease classification.

4.4.1 Neural signals

Since fluctuations in SBP affect the parasympathetic outflow, we expect the baroreflex-mediated parasympathetic outflow ($T_{p,b}$) to oscillate with SBP at rest if large changes in SBP occur. During the VM, $T_{p,b}$ accurately depicts parasympathetic withdrawal in phase II, a second, less dramatic, parasympathetic withdrawal in phase III, and an overshoot in phase IV, known to occur in control subjects [102, 114]. The model captures all of these behaviors for the control subject. The sympathetic outflow should remain relatively constant, or with minor oscillations, at rest. During the VM, the decrease in blood pressure sensed by the HPBs activates the sympathetic nervous system. T_s accurately exhibits a delayed increase in sympathetic activity in phase II and a delayed decrease in activity in phases III and IV. The model in conjunction with parameter estimation depicts all of these behaviors. In Figure 4.4, for patients 2-5 $T_{p,b}$ does not fluctuate as dramatically as the control subject while T_s follows a similar trajectory as the control subject. Since the baseline baroreflex-mediated parasympathetic control and baroreflex-mediated sympathetic activation are known to both decline with age and disease [79], the model distinguishes between these differences. However, since our study does not include data for elderly control subjects, we currently cannot differentiate behavior attributed to age or disease.

4.4.2 Aortic and carotid bodies

Our study supports the hypothesis that the baroreceptors of the aortic body are necessary to calibrate the model for each subject and effectively capture the VM behavior. Though the values vary widely between subjects, the neural scaling factor B has a mean value of 0.4 ± 0.3 sec^{-1} for the control subjects, skewing towards the aortic baroreceptors. Kosinski *et al.* [61] showed that in their model the combined effects of both the carotid and aortic baroreceptor regions is necessary to capture the dynamics of the VM. Our study not only agrees with this finding but emphasizes that the aortic baroreceptors may play a larger role than previously thought in the VM.

4.4.3 Respiratory sinus arrhythmia

Figure 4.5 displays the optimized fit of the model output for the baroreflex-only (black dotted curve) and the joint baroreflex-RSA output (red solid curve). At baseline, the efficacy of the model fit to the heart rate data depends strongly on the RSA, which coincides with previous studies [10, 26]. By incorporating RSA, these oscillations can be effectively captured. During the VM, the baroreflex-only and joint baroreflex-RSA model outputs fit the data well in late phase II and phases III and IV. However, it should be noted that the discrepancy in phase I and early phase II implies the baroreflex-only signal cannot simulate the initial heart rate drop caused primarily by the sharp inspiration. This discrepancy also occurs in the heart rate fits to data in Kosinski *et al.* [61]. With the inclusion of RSA, our model can capture this sudden drop in heart rate.
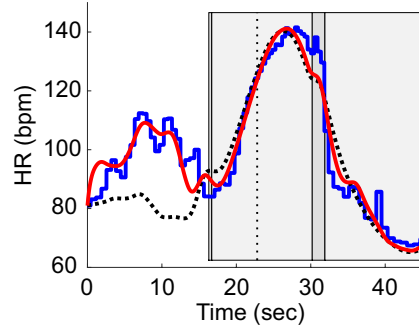
Figure 4.5 Respiratory sinus arrhythmia (RSA) effects on the model output for the baroreflex-only (dotted black curve) and the joint baroreflex-RSA (solid red curve).

4.4.4 Clinical ratios

The clinical ratios α, β, and γ were calculated in this study. A novel component of our analysis is the definition of the index α, the slope of the increase in blood pressure during late phase II, as a measure of sympathetic nervous activity. In the original study by Korner *et al.* [60], it was shown that the late phase II blood pressure increase depended solely on sympathetic activity. To our knowledge, no other studies have used α to approximate sympathetic function. Though α may be affected by an increased cardiac output in late phase II due to the stabilization of stroke volume at a lower level, we propose that α relates to the effectiveness of the sympathetic response to SBP recovery. The 5 AD patients display little to no ability to recover baseline SBP during late phase II ($\alpha \approx 0$ as shown in Table 4.2). Increased arteriolar resistance due to sympathetic activation largely contributes to the return of SBP to baseline in late phase II and the overshoot in phase IV [102]. Thus, in the absence of sympathetic activation, the peripheral resistance does not increase and as a result SBP does not return to baseline, leading to $\alpha \approx 0$. This analysis supports using α to indicate sympathetic function.

The values of β, the baroreceptor sensitivity, for patients 1-4 are within normal range, while patient 5 has a significantly diminished value. Though this index is common [55, 98, 125], interpretation of the ratio is inconclusive. Since this index is a ratio of R-R interval to SBP, various factors can contribute to lower or higher β values. For example, a low β value could be the result of: a marginal change in R-R interval from phase III to phase IV, which could be due to a decrease in parasympathetic activity; a drastic SBP overshoot in phase IV, which could be due to a substantial and sustained increase in sympathetic activity; or a combination of these. Due to the ambiguous nature of this index, we recommend using the parameters estimated from the proposed model in this study to supplement the explanation of β value. We expand upon this notion in the next section.

The Valsalva ratio γ typically associated with vagal function is abnormal when $\gamma \leq 1.1$ [31]. We observe what is traditionally determined as "abnormal" behavior for patients 2-5, but γ is very

high ($\gamma = 2.3$) for patient 1 (POTS) and outside of the normal range. Expanding on the definition of abnormal vagal behavior using this index would be very useful clinically. We propose the following delineation for clarity and ease of use:

- $\gamma \leq 1.1$ - abnormal with diminished parasympathetic activity.

- $1.1 < \gamma \leq 2$ - normal range.

- $\gamma > 2$ - abnormal with overactive parasympathetic activity.

4.4.5   Model-based analysis of autonomic dysfunction

As discussed in the previous section, β only describes the relationship between changes in R-R interval and SBP but does not explain how those changes arise. Abnormally low or high values of β could be the result of many combinations of parasympathetic and sympathetic dysfunction [125]. Furthermore, β could be within the "normal range" but only describes that the compensatory decrease in heart rate is proportional to the overshoot in SBP. Employing the estimated parameters determined by the methods introduced in this study in comparison to the β value would greatly enhance the interpretative power for these patients. The following discusses each AD patient and compares their clinical ratios to the estimated parameters. Table 4.4 tabulates the relative parasympathetic and sympathetic responses of the AD patients to the control subjects.

Patient 1 (POTS) has a large increase in heart rate in relation to the SBP overshoot, yielding a β value within normal range range and a high γ value. POTS is known to occur without orthostatic hypotension, which is not observed in this patient [75]. Though β is normal, this patient clearly has an abnormal VM trace given the V behavior and an increase in heart rate of $\geq$ 30 bpm. To characterize the AD contributing to this abnormal behavior, estimated model parameters show overactive baroreflex-mediated parasympathetic (low $\tau_{p,b}$ and normal $H_{p,b}$ values) and sympathetic (low τ_s and normal H_s values) outflows. Therefore, this patient experiences abnormal changes in the activity of both autonomic sectors to the sinoatrial node, contributing to the substantial increase in heart rate.

Patients 2 (OH) and 5 (PAF) maintain a high blood pressure with a sharp decline during the VM without a substantial compensatory heart rate increase, a key factor in their diagnoses, without a substantial compensatory heart rate increase [75]. Though the β value for these patients is low, it is still within normal range. The estimated parameters for patient 2 show that all time-scales have increased substantially (high $\tau_{p,b}$, $\tau_{p,r}$, and τ_s values) with normal heart rate gains ($H_{p,b}$, $H_{p,r}$, and H_s). These indicate that the baroreflex tone has significantly decreased for this patient for both parasympathetic and sympathetic branches. Patient 5 displays increased $\tau_{p,b}$ and τ_s values, indicating decreased parasympathetic and sympathetic outflow due to the baroreflex, respectively. Furthermore, parameters associated with RSA control are outside of their normal range (high $\tau_{p,r}$

for patient 2 and low $H_{p,r}$ for patient 5) decreasing the effect of $T_{p,r}$ on heart rate, which occurs with age [138]. The etiologies for these patients coincide with the hypothesis of the V behavior.

Patients 3 and 4 (PD) both have normal β values while exhibiting almost no change in heart rate in phase IV ($\gamma = 1$) and the V behavior. In regard to the estimated parameter values, both patients show decreased parasympathetic activity. Patient 3 has a high $\tau_{p,b}$ with low $H_{p,b}$ and $H_{p,r}$, and patient 4 has low values for heart rate gains $H_{p,b}$ and $H_{p,r}$. Therefore, both PD patients exhibit impaired vagal function for both the baroreflex and RSA, while adrenergic function operates normally (τ_s and H_s within normal range). This coincides with PD patients who experience orthostatic hypotension without orthostatic intolerance [95]. Hence, the sympathetic outflow for the PD patients may still affect heart rate but not blood pressure. Further investigation is required to substantiate this hypothesis.

The different causes eliciting the V response for these 5 AD patients leads us to conclude that the hypothesis for the V behavior should be expanded. Pattern recognition alone is not sufficient to explain the etiologies for each of the patients, and therefore, we can develop subcategories which encompass these explanations. Further investigation into this phenomenon with a larger cohort of subjects exhibiting the V behavior is needed to develop these subcategories.

4.4.6   Model limitations

ITP data was not recorded for the 5 AD patients. We used equation (3.1) to obtain an ITP signal, assuming that they maintained an expiratory force of 40 mmHg throughout the breath hold. Moving forward, we suggest the inclusion of time-varying measurements of ITP in all protocols examining the response to the VM. WE computed an ECG-derived respiratory signal in lieu of respiratory data, which was not collected for the subjects. For increased patient-specificity, we recommend measuring respiration in future studies. Since the model uses only the SBP as an input, the Voigt body of equation (4.3) truly responds to the systolic max arterial wall strain, due to the interpolation of the SBP as a continuous input. In actuality, these Voigt bodies respond to the continuous pulse pressure throughout the cardiac cycle. We do not explicitly model action potential generation but rather a collective neural outflow of the baroreceptors in response to the SBP. The model may benefit from a more explicit neuron model, but this may induce unnecessary complexity by significantly increasing the number of model states and parameters.

An important control mechanism activated in response to the VM is the explicit effect of LPBs, which sense changes in central blood volume in the vena cava and right atrium junctions. The effect of these baroreceptors is difficult to model without either (a) available data for right atrial volume/pressure or (b) the use of a closed-loop cardiovascular model coupled to the presented neurological model. We plan to couple these models in Chapter 7.

The conclusions made in this study are limited by the relatively small group of control subjects.

Though these individuals do not exhibit AD in response to the VM, they may experience other conditions not accounted for in this study. We used the patients with AD as a mode of comparison to the control subjects, but we are limited by the availability of patients that exhibit the V behavior. We would benefit from a larger patient cohort to perform a more extensive statistical analysis.

4.5   Conclusions

This study proposes a mathematical model of respiratory sinus arrhythmia and the baroreflex in response to the Valsalva maneuver. The model uses systolic blood pressure and thoracic pressure inputs to delineate the aortic and carotid baroreceptor centers. The model is calibrated to a measured heart rate, simultaneously providing an approximation of respiratory-mediated parasympathetic activity and baroreflex-mediated parasympathetic and sympathetic nervous activity, which cannot be measured noninvasively. Our model performs well, validating it against 34 controls and 5 AD patients. We emphasize the necessity of modeling the two baroreceptor regions to accurately depict the dynamics during the VM, the efferent respiratory pathway to indirectly model effects of low-pressure baroreceptors during the VM, and the delay in sympathetic nervous activity. We have also introduced a new index α, which quantifies the sympathetic gain in late phase II of the VM. Furthermore, our results support the categorization of the V behavior should be divided into subcategories based on the etiology described by the estimated model parameters. We have found no correlation between the clinical ratios studied and the model outputs, indicating the model includes quantities not measured by these clinical ratios. In summary, this model in conjunction with parameter estimation can be used to effectively analyze autonomic cardiovascular control.

CHAPTER

5

TWO-PARAMETER BIFURCATION AND STABILITY ANALYSIS

The model developed in Chapter 4 is formulated using a system of nonlinear ordinary and delay differential equations. This model type can be analyzed with a number of techniques, including stability and sensitivity analyses. In Chapter 4, we used local sensitivity analysis (LSA) to examine parameter influence on the model output at given values and determined a subset of parameters to optimize. In this chapter, we conduct a stability analysis with particular focus on the delay differential equation as delays are known to cause instability in dynamical systems [113]. In chapter 6, we conduct a global sensitivity analysis (GSA) to explore the parameter space (Ω_p) and inform a model reduction protocol.

LSA has the advantage that it is fast and informative but it requires evaluation of the partial derivatives at the nominal parameter values, which only allows us to characterize model behavior in a small neighborhood about the nominal value. GSA, on the other hand, uses sampling methods to explore Ω_p, from the assigned lower to upper bounds. However, GSA is computationally expensive and should be restricted to investigate model dynamics in the region of interest. Moreover, the most popular GSA method (based on Sobol' indices) make assumptions about the parameter interactions (*i.e.*, independence) that are not satisfied in complex nonlinear models. Finally, though not discussed in literature, GSA are derived under the assumption that the model does not change behavior (*i.e.*, that it does not undergo bifurcations) as it explores Ω_p. To investigate this in more detail, we conduct

an analytical and numerical stability analysis of the model developed in Chapter 4. Using this approach, we aim to find constraints on Ω_p to ensure the model does not produce unstable or unphysiological behavior.

5.1 Introduction

Analysis of the dynamics of differential equations models can shed light on the model prediction outcomes reflecting healthy versus disease states. Model predictions of normal and abnormal behavior often require either changes in the nominal parameter values or a change of dynamic pathways. For the former, healthy model predictions can be a result of operating in stable region of the parameter space, while diseased outcomes can be a result of a change to a parameter regime, which is inherently unstable or has a bifurcation to a new stable equilibrium. To explore this further, we conduct a stability analysis to determine if the behavior of the proposed model persists, allowing us to better characterize how to construct a parameter space (Ω_p) over which the model behavior should be explored.

Since the disease state may represent a different part of the parameter space than the healthy state, local sensitivity analysis (LSA) methods are insufficient in quantifying parameter importance [87, 100]. In Chapter 4, we use LSA in the diseased parameter regime and compare the results to the healthy case, yet the usefulness of this approach is unclear as the LSA output are not comparable as the model is evaluated at different parameter values. One way to gain more insight is to sample throughout the entire parameter space, evaluating the model and categorizing its predictions. However, since the upper and lower bounds for each parameter are set by the researcher based on prior knowledge, system intuition, literature, or empirical studies, these ranges may result in parameter regimes that are not physically or biologically sensible for the system. In other words, the physiological parameter regions may contain sub-regions where the predictions change behavior.

The model used in this study is formulated using nonlinear delay differential equations (DDEs), which are common in the study of many real-world systems [8, 56, 80, 130, 135]. DDEs are known to change the dynamical behavior, causing bistability or instability in some systems [15, 27, 106, 113] and broadening the stable region of others [113]. Physically, delays are often used to avoid adding equations describing the process causing the delay. In our case, the process is the transmission of the sympathetic response along the sympathetic ganglia chain. Given DDEs are known to generate instability [113], it is important to analyze whether a delay is critical to model the system and to test alternative formulations, such as *distributed delays*, which impose chains of differential equations with varying time-scales [85]. Often, distributed delays garner a similar effect as a discrete DDE without the added computational expenditure but at the cost of increasing the dimension of the state and parameter spaces. The choice to use distributed versus discrete delays is problem-dependent. We use a discrete delay in the Chapter 4 model to not increase the dimension of the state space.
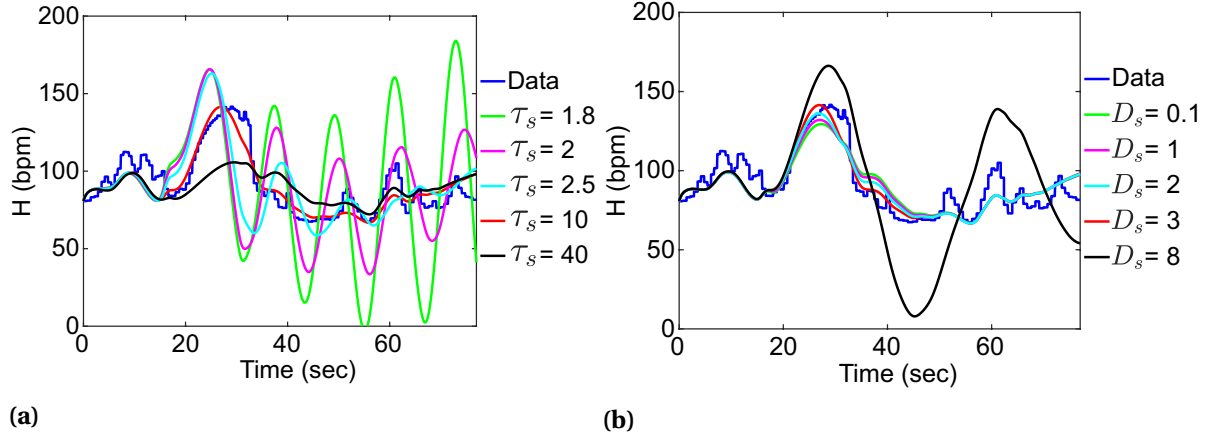
Figure 5.1 Plots of the heart rate model output (H, bpm) for varying values of (a) τ_s, the sympathetic time-scale parameter, and (b) D_s, the delay parameter. All other parameters were held constant at their optimized values.

Numerical tools for bifurcation analysis of DDEs exist, *e.g.*, DDE-Biftool [29] and knut [126]. The former is a powerful collection of MATLAB® routines for autonomous DDEs with constant and state-dependent delays, which has been used in two-parameter bifurcation analyses previously [62, 70, 73]. However, in this study, we analyze a nonautonomous system of DDEs, which DDE-Biftool currently cannot accommodate. Furthermore, our model is a system of stiff DDEs solved with RADAR5 [36], a stiff DDE solver. DDE-Biftool uses the built-in MATLAB delay solver dde23, which does not account for stiff systems with multiple time-scales. knut [108, 126] is a bifurcation analysis package in C++ that allows periodic forcing functions. However, the nonhomogeneous system considered here is not periodic. To remedy this problem, we evaluated the forward model throughout the parameter space and categorized the model output into categories analogous to the harmonic oscillator: critically damped sink, overdamped sink, stable focus, limit cycle, and unstable focus.

Unstable modes arise in many physical and biological systems naturally and avoiding these modes is of particular interest in recent years [15, 24, 106, 135]. In regard to physiological processes, at rest the body is mainly operating via negative feedback mechanisms that maintain homeostasis, *e.g.*, the baroreceptor reflex (*baroreflex*) modulating blood pressure and heart rate. However, it is known that in some disease states the negative feedback mechanisms fail and are overridden by positive feedback mechanisms, *e.g.*, Bezold-Jarisch reflex invoking cardioinhibition during vasovagal syncope, which causes the system to transition to an unstable state (syncope) [40]. The Bezold-Jarisch reflex normally responds as a negative feedback to distention of the ventricular wall causing reflexive bradycardia but can transition to a positive feedback when the left ventricular volume is reduced below a certain threshold, *e.g.*, in response to excessive blood pooling in the legs. This change can cause left ventricular hyperactivity, which results in a reflexive decrease in heart rate,

cardiac contractility, blood pressure, and cardiac output [23, 50]. In this chapter, the objective is to characterize the stability regions important to autonomic dysfunction in patient data (Section 2.4.1). More specifically, we investigate the persistent instability as a result of the baroreflex response to the Valsalva maneuver.

In the model presented in Chapter 4, the sympathetic tone has a discrete delay (D_s) and its interactions with other parameters in the model can lead to unstable modes. As shown in Figure 5.1, when changing parameters τ_s, the sympathetic time-scale (Figure 5.1a), and D_s (Figure 5.1b), we observe oscillatory behavior that emerges. We aim to categorize disease and healthy states based on a two-parameter bifurcation analysis of these parameters. We will show τ_s and D_s are intrinsically linked and certain parameter interactions can cause oscillations and unstable behavior. The use of bifurcation analysis to examine effects of the baroreflex has been done in one other study by Ottesen [90]. This study performed a two-parameter bifurcation analysis and showed that if the time delay is varied over its physiological range, stability switches arise. However, oscillatory modes were not compared to patient data. We compare the sympathetic outflow and heart rate responses of two control subjects and a patient with autonomic dysfunction (AD) exhibiting the M response to the Valsalva maneuver (VM) as categorized by Palamarchuk *et al.* [94] (Figure 5.10), determining parameter regimes where instability occurs. The M behavior is hypothesized as overactive sympathetic and parasympathetic activity. In this study, we analytically determine the locations of the different stability regimes by solving and comparing the homogeneous DDE to numerical simulations of the associated heterogeneous system and discuss the effects of the forcing function on the stability. In addition, we connect these results to physiological data where some instability is seen.

5.2   Model development

This study analyzes the neurological control model of the autonomic nervous response to the Valsalva maneuver (VM) developed in Chapter 4. Utilizing blood pressure, electrocardiogram (ECG), and intrathoracic pressure (ITP) data as inputs, the model predicts heart rate by computing baroreceptor strain and approximating the sympathetic and parasympathetic nervous system responses. Further details can be found in Section 4.2.1. Due to the nature of the sympathetic response, the model incorporates a delay into the differential equation modeling sympathetic tone. Overall, the model consists of 6 differential state equations and 26 parameters with one delay differential equation (DDE). The model has the general form

$$\frac{d\mathbf{x}}{dt} = f(t, \mathbf{x}(t), \mathbf{x}(t - D_s); \theta), \quad \mathbf{x}(t) = \mathbf{x}_0, \ t \in [-D, 0], \tag{5.1}$$

where f is the right hand side of the DDE, $\mathbf{x} \in \mathbb{R}^n$ is a vector of n states, $\mathbf{x}_0 \in \mathbb{R}^n$ is the constant history vector, D_s is the delay, and $\theta \in \Omega_p$ is the parameter vector of length p.

To facilitate the analysis of the effect of the DDE in this chapter, we reduced the model to two states, the baroreflex-mediated sympathetic tone T_s and heart rate H. We make the following simplifications based on the physiology of the system, which is achieved in three steps:

1. We first remove the components of the model associated with the respiratory sinus arrhythmia (RSA). The RSA pathway solely has a parasympathetic efferent in this model with no delay. Moreover, the RSA is not affected by the baroreflex-mediated sympathetic delay D_s. Therefore, we set

$$T_{p,r}(t) = 0 \quad \text{and} \quad \frac{\mathrm{d}T_{p,r}}{\mathrm{d}t}(t) = 0. \tag{5.2}$$

By removing the RSA component, the model solely depends on the contribution from the baroreflex mechanism, which is activated during the Valsalva maneuver. Therefore, we assume the blood pressure is constant at its mean value at rest. We recalibrate the nominal value for $H_{p,b}$ to accommodate this reduced model as

$$H_{p,b} = \frac{1 - \bar{H}/H_I + H_s\,T_s(0)}{T_{p,b}(0)}. \tag{5.3}$$

2. The baroreflex-mediated parasympathetic tone $T_{p,b}$ is also not affected by the sympathetic delay. We reformulate the differential equation as

$$\frac{\mathrm{d}T_{p,b}}{\mathrm{d}t}(t) = \frac{-T_{p,b}(t) + K_{p,b}\,G_{p,b}(t)}{\tau_{p,b}} \quad \Rightarrow \quad \tau_{p,b}\frac{\mathrm{d}T_{p,b}}{\mathrm{d}t}(t) = -T_{p,b}(t) + K_{p,b}\,G_{p,b}(t). \tag{5.4}$$

To remove this differential equation, we take advantage of the fact that the time-scale $\tau_{p,b}$ is small. Setting $\tau_{p,b} = 0$, we solve for $T_{p,b}$ obtaining

$$T_{p,b}(t) = K_{p,b}\,G_{p,b}(t). \tag{5.5}$$

We make a similar simplification of the states modeling the baroreceptor strains ($\varepsilon_{b,j}$), taking advantage of small time-scale τ_b. Thus,

$$\varepsilon_{b,j}(t) = K_b\,\varepsilon_{w,j}(t), \tag{5.6}$$

where $j = c$ or a for carotid or aortic, respectively.

3. The increased thoracic pressure (P_{th}) induces the response to the VM, so we accentuate this effect by eliminating the carotid pathway. Hence, the model depends solely on the effects of

the aortic baroreceptors, that is, we set $B = 0$ and

$$n(t) = \varepsilon_{w,a}(t) - \varepsilon_{b,a}(t) = (1 - K_b)\varepsilon_{w,a}(t) = (1 - K_b)\left(1 - \sqrt{\frac{1 + e^{-q_w(P_a(t) - s_w)}}{A + e^{-q_w(P_a(t) - s_w)}}}\right). \quad (5.7)$$

The resulting model is a system of two states, T_s and H of the form

$$\begin{cases} \dfrac{\mathrm{d}T_s}{\mathrm{d}t} = \dfrac{-T_s(t - D_s) + K_s G_s(t)}{\tau_s}, & T_s(t) = T_0, \ t \in [-D_s, 0] \\[3mm] \dfrac{\mathrm{d}H}{\mathrm{d}t} = \dfrac{-H(t) + H_I(1 - H_{p,b}K_{p,b}G_{p,b}(t) + H_s T_s(t))}{\tau_H}, & H(t) = H_0, \ t \in [-D_s, 0]. \end{cases} \quad (5.8)$$

In this system, the saturation function $G_i(t)$ for $i = p, b$ or s denoting parasympathetic and sympathetic, respectively, is a sigmoidal relation of the form

$$G_i(t) = \frac{1}{1 + e^{q_i(n(t) - s_i)}}, \quad (5.9)$$

where q_i and s_i are the steepness and half-saturation values, respectively, and n is as in equation (5.7). This system is in the form of equation (5.1) where $\mathbf{x} = [T, H]^T$, D_s is a discrete delay, and $\theta \in \mathbb{R}^{14}$ is the vector of parameters

$$\theta = [A, K_{p,b}, K_s, \tau_s, \tau_H, q_w, q_{p,b}, q_s, s_w, s_{p,b}, s_s, H_I, H_{p,b}, H_s]^T. \quad (5.10)$$

A comparison of the model output for the full model (red) discussed in Chapter 4 and the reduced model (black) are shown in Figure 5.2.
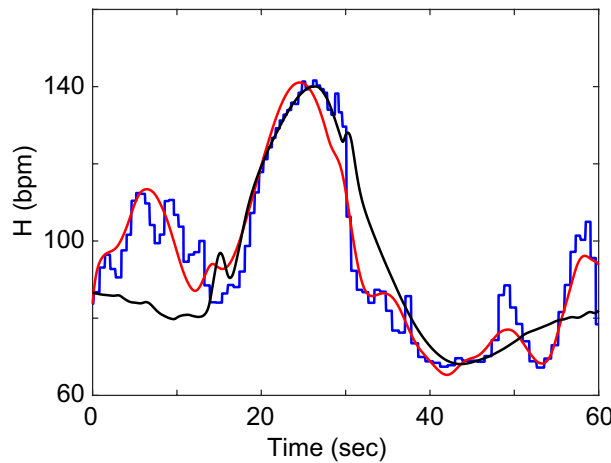
Figure 5.2 Full (red) and reduced two-state (black) model fits to heart rate data (blue).

The model in equation (5.8) is linear with respect to the states. Reformulating the system yields

$$\frac{\mathrm{d}}{\mathrm{d}t}\begin{bmatrix} T_s(t) \\ H(t) \end{bmatrix} = \begin{bmatrix} -\dfrac{1}{\tau_s}T_s(t-D_s)+f(t) \\ -\dfrac{1}{\tau_H}H(t)+\dfrac{H_I H_s}{\tau_H}T_s(t)+g(t) \end{bmatrix} \tag{5.11}$$

with constant initial function vector

$$\begin{bmatrix} T_s(t) \\ H(t) \end{bmatrix} = \begin{bmatrix} T_0 \\ H_0 \end{bmatrix}, \quad t \in [-D_s, 0]. \tag{5.12}$$

The forcing functions $f(t)$ and $g(t)$ for T_s and H, respectively, are given by

$$f(t) = \frac{K_s}{\tau_s}G_s(n(P_a(t))) \tag{5.13}$$

and

$$g(t) = \frac{H_I}{\tau_H}\left(1 - H_{p,b}K_{p,b}\left(G_{p,b}\left(n(P_a(t))\right)\right)\right). \tag{5.14}$$

This is a nonhomogeneous, nonautonomous delay differential equation system. Forcing functions $f(t)$ and $g(t)$ represent the dynamics induced by the blood pressure responses to the VM. Since the forcing functions use blood pressure data as an input, they are not necessarily smooth at every point, complicating the analysis. To ensure smoothness, the data was filtered using a moving mean with a window of one second. Then, we fit a 10th degree polynomial to the filtered signal, that is, the coefficients a_i of a polynomial $P(t) = \sum_{i=0}^{10} a_i x^i$ were optimized to fit the filtered signal. Polynomials of orders >10 produced high frequency oscillatory behavior at the baseline. We artificially extended the baseline blood pressure value before and after the curve to ensure the model began in steady-state. Figure 5.3a compares the original blood pressure data (blue), the moving mean (red), and the fitted polynomial $P(t)$ (yellow). Figures 5.3b and 5.3c display the forcing functions $f(t)$ and $g(t)$, respectively.

In summary, we consider the system

$$\frac{\mathrm{d}\mathbf{x}}{\mathrm{d}t} = \mathbf{A}\mathbf{x} + \mathbf{B}\mathbf{x}_{D_s} + \mathbf{f}, \quad \mathbf{x}(t) = \mathbf{x}_0 \text{ for } t \in [-D_s, 0], \tag{5.15}$$

where $\mathbf{x}_{D_s} = \mathbf{x}(t-D_s)$ is the vector of delayed states, $\mathbf{A}$ and $\mathbf{B}$ are constant matrices given as

$$\mathbf{A} = \begin{bmatrix} 0 & 0 \\ \dfrac{H_I H_s}{\tau_H} & -\dfrac{1}{\tau_H} \end{bmatrix} \tag{5.16}$$
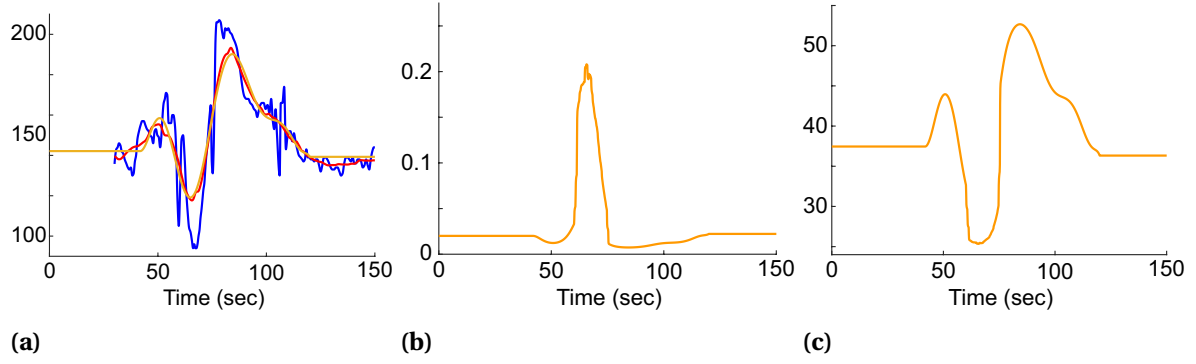
Figure 5.3 Forcing functions. (a) Comparison of the blood pressure data (blue), data filtered with a moving mean (red), and a 10th degree polynomial fitted to the moving mean (yellow). Forcing function (b) $f(t)$ for $T_s(t)$ and (c) $g(t)$ for $H(t)$.

and

$$\mathbf{B} = \begin{bmatrix} -\dfrac{1}{\tau_s} & 0 \\ 0 & 0 \end{bmatrix},$$
(5.17)

and **f** is the forcing vector

$$\mathbf{f} = \begin{bmatrix} f(t) \\ g(t) \end{bmatrix}.$$
(5.18)

5.3 Stability analysis

The stability of the delay differential equation (DDE) system in equation (5.15) depends both the homogeneous solution and the effect of the forcing function. In this section, we analytically explore the homogeneous equation by classifying the roots of the characteristic equation ϕ. We numerically categorize the behavior of the nonhomogeneous, nonautonomous system using an algorithm that takes advantage of the gradient of the solution after the Valsalva maneuver (VM) occurs.

5.3.1 Homogeneous system

To analyze the stability of system (5.11), we follow the typical practice of considering the homogeneous equation

$$\frac{d\mathbf{x}}{dt} = \mathbf{A}\mathbf{x} + \mathbf{B}\mathbf{x}_{D_s}, \quad \mathbf{x}(t) = \mathbf{x}_0 \text{ for } t \in [-D_s, 0].$$
(5.19)

Then, the homogeneous system is

$$\frac{\mathrm{d}T_s}{\mathrm{d}t}(t) = -\frac{1}{\tau_s}T_s(t - D_s), \qquad\qquad T_s(t) = T_0, \ t \in [-D_s, 0] \qquad (5.20)$$

$$\frac{\mathrm{d}H}{\mathrm{d}t}(t) = \frac{1}{\tau_H}\left(-H(t) + H_I H_s T_s(t)\right), \qquad\qquad H(t) = H_0, \ t \in [-D_s, 0]. \qquad (5.21)$$

In this system, the origin is a critical point. If another critical point exists, then from equation (5.21)

$$0 = \frac{1}{\tau_H}(-H(t) + H_I H_s T_s(t)) \quad \Rightarrow \quad H(t) = H_I H_s T_s(t). \qquad (5.22)$$

From (5.20), we have

$$0 = \frac{1}{\tau_s}T_s(t - D_s) \quad \Rightarrow \quad T_s(t) = 0. \qquad (5.23)$$

Therefore, the origin is the only critical point of the system in (5.19).

Since equation (5.20) solely depends on the delayed state $T_s(t - D)$, we assume its solution to be an exponential of the form

$$T_s(t) = c\, e^{\lambda t}, \qquad (5.24)$$

where c is a scaling factor and λ is the growth factor [9, 109]. We make this assumption since the DDE can reduce to an ordinary differential equation (ODE) in steady-state. Hence, we can find an explicit solution to equation (5.21) as

$$\frac{\mathrm{d}H}{\mathrm{d}t} = -\frac{1}{\tau_H}H + \frac{H_I H_s}{\tau_H}T_s$$

$$\Rightarrow \frac{\mathrm{d}H}{\mathrm{d}t} + \frac{1}{\tau_H}H = \frac{H_I H_s}{\tau_H}T_s$$

$$\Rightarrow \int \left(e^{\frac{1}{\tau_H}t}H\right)' \mathrm{d}t = \frac{H_I H_s}{\tau_H}\int T_s e^{\frac{1}{\tau_H}t}\mathrm{d}t$$

$$\Rightarrow e^{\frac{1}{\tau_H}t}H = \frac{H_I H_s}{\tau_H}\int c\, e^{\lambda t}e^{\frac{1}{\tau_H}t}\mathrm{d}t$$

$$= \frac{H_I H_s}{\tau_H}\int c\, e^{(\lambda + \frac{1}{\tau_H})t}\mathrm{d}t$$

$$= \frac{H_I H_s}{\tau_H(\lambda + \frac{1}{\tau_H})}c\, e^{(\lambda + \frac{1}{\tau_H})t} + k$$

$$= \frac{H_I H_s}{\tau_H \lambda + 1}T_s(t)e^{\frac{1}{\tau_H}t} + k \qquad (5.25)$$

for integration constant k. When $t = 0$, we can solve for k as

$$k = H_0 - \frac{H_I H_s}{\tau_H \lambda + 1}T_0. \qquad (5.26)$$

Then,

$$H(t) = \frac{H_I H_s}{\tau_H \lambda + 1} T_s(t) + \left(H_0 - \frac{H_I H_s}{\tau_H \lambda + 1} T_0\right) e^{-\frac{1}{\tau_H} t}. \tag{5.27}$$

Therefore, H linearly related to T_s. As $t \to \infty$, the exponential goes to zero, that is, for large t, H is proportional to T_s, *i.e.*, the stability of H depends explicitly on the stability of T_s. Thus, by analyzing T_s, we inherently know the behavior of H. By substituting equation (5.24) into equation (5.20), we obtain

$$\lambda c e^{\lambda t} = -\frac{1}{\tau_s} c e^{\lambda(t - D_s)} \quad \Rightarrow \quad c e^{\lambda t} (\tau_s \lambda + e^{-\lambda D_s}) = 0. \tag{5.28}$$

Trivially, if $c = 0$, then $T_s(t) = 0$ is a solution to equation (5.28). Considering the portion of (5.28) in parentheses, we obtain the characteristic equation

$$\phi(\lambda) = \tau_s \lambda + e^{-\lambda D_s} = 0. \tag{5.29}$$

Note that $D_s > 0$ and $\tau_s > 0$. Several curves plotted for ϕ in Figure 5.4. ϕ can have 2 real roots (yellow curve), 1 real root (red curve), or infinitely many complex roots. Plotted are examples of solutions with complex roots, that is, for $\lambda \in \mathbb{C}$, $\lambda = \alpha \pm \beta i$ for $\beta > 0$. When $\alpha < 0$ (green curve), the solutions are stable. For $\alpha = 0$ (orange curve), a limit cycle emerges about the origin. When $\alpha > 0$, solutions are unstable.
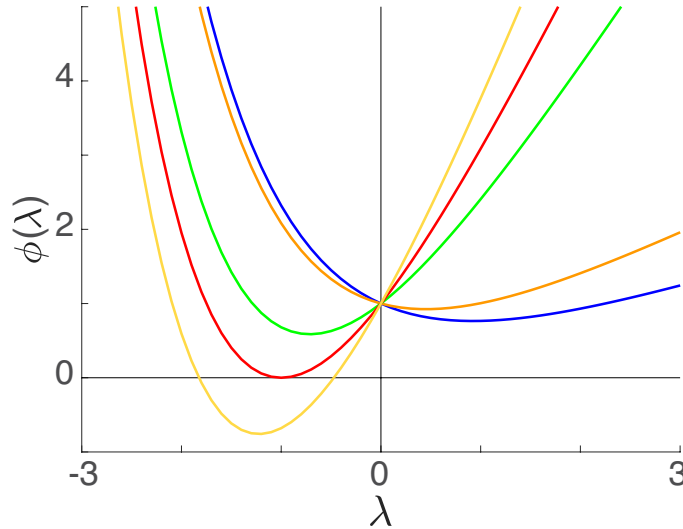
Figure 5.4 The characteristic equation $\phi(\lambda)$ given in equation (5.29) with several curves plotted showing the various types of solutions. Real solutions: $\lambda_1, \lambda_2 \in \mathbb{R}$ where $\lambda_1 \neq \lambda_2$ (yellow) and $\lambda_1 = \lambda_2 = \lambda \in \mathbb{R}$ (red). Infinitely many solutions: $\lambda = \alpha \pm \beta i \in \mathbb{C}$ for $\beta \in \mathbb{R}, \beta > 0$ where $\alpha < 0$ (green), $\alpha = 0$ (orange), and $\alpha > 0$ (blue).

Case 1: Real Roots. We consider the case where the characteristic equation $\phi(\lambda)$ in equation (5.29) has real roots, *i.e.*,

$$\lambda = \lambda_1, \lambda_2 \in \mathbb{R}. \tag{5.30}$$

Observing the behavior of ϕ in Figure 5.4, ϕ has real roots if and only if the absolute minimum of ϕ is less than or equal to zero, that is, for a minimizer λ^* of ϕ, $\phi(\lambda^*) \leq 0 \iff \phi$ has real roots. Taking the derivative and setting it to zero, we obtain

$$\phi'(\lambda) = \tau_s - D_s e^{-\lambda D_s} = 0, \tag{5.31}$$

which yields the minimizer

$$\lambda^* = -\frac{1}{D_s} \ln\left(\frac{\tau_s}{D_s}\right).$$

Substituting λ^* into equation (5.29) and setting $\phi(\lambda) \leq 0$ yields

$$\phi(\lambda^*) = \frac{\tau_s}{D_s}\left(-\ln\left(\frac{\tau_s}{D_s}\right) + 1\right) \leq 0.$$

Since parameters $\tau_s, D_s > 0$, we have

$$-\ln\left(\frac{\tau_s}{D_s}\right) + 1 \leq 0 \tag{5.32}$$

and

$$e D_s \leq \tau_s. \tag{5.33}$$

When equation (5.33) is an equality, $\phi(\lambda)$ has one real root and solutions to the DDE are critically damped, analogous to the harmonic oscillator. Otherwise, there are two real solutions to ϕ that are overdamped. Hence, the solutions that obey the constraint given in equation (5.33) are stable.

Case 2: Complex Roots. We consider $\lambda = \alpha \pm \beta i$ for $\alpha, \beta \in \mathbb{R}$ and $\beta > 0$. Without loss of generality, we consider $\lambda = \alpha + \beta i$. Then,

$$
\begin{aligned}
0 &= \phi(\lambda) \\
&= \tau_s(\alpha + \beta i) + e^{-D_s(\alpha + \beta i)} \\
&= \left(\alpha \tau_s + e^{-D_s \alpha} \cos(D_s \beta)\right) + i\left(\beta \tau_s - e^{-D_s \alpha} \sin(D_s \beta)\right).
\end{aligned}
\tag{5.34}
$$

Since $\phi(\lambda) = 0$, both the real and imaginary parts of $\phi(\lambda)$ must also equal to 0. Thus,

$$0 = \mathrm{Re}(\phi(\lambda)) = \alpha \tau_s + e^{-D_s \alpha} \cos(D_s \beta) \tag{5.35}$$

and

$$0 = \operatorname{Im}(\phi(\lambda)) = \beta \tau_s - e^{-D_s \alpha} \sin(D_s \beta). \tag{5.36}$$

Dividing Equation (5.35) by Equation (5.36), yields

$$\alpha = -\beta \cot(D_s \beta). \tag{5.37}$$

Therefore, it is guaranteed that $\alpha < 0$ as long as $0 + k\pi < D_s \beta \leq \frac{\pi}{2} + k\pi$ for $k \in \mathbb{Z}$. For $\alpha < 0$, the solutions are asymptotically stable and the solutions spiral into the origin.

When $\alpha = 0$, we have from equation (5.35)

$$\cos(D_s \beta) = 0 \tag{5.38}$$

and, therefore,

$$D_s \beta = \frac{\pi}{2} + k\pi \quad \text{for } k \in \mathbb{Z}. \tag{5.39}$$

Since $D_s > 0$ and $\beta > 0$,

$$0 < D_s \beta = \frac{\pi}{2} + k\pi \quad \Rightarrow \quad k > -\frac{1}{2}. \tag{5.40}$$

Hence, $k \in \mathbb{W}$. Moreover, substituting equation (5.39) into equation (5.36) yields,

$$\begin{aligned} 0 &= \beta \tau_s - \sin(D_s \beta) \\ &= \frac{\pi}{2D_s} \tau_s - \sin\left(\frac{\pi}{2} + k\pi\right) \\ \Rightarrow \frac{\pi}{2D_s} \tau_s &= \sin\left(\frac{\pi}{2} + k\pi\right), \end{aligned} \tag{5.41}$$

which only has a solution when k is even since $D_s > 0$ and $\tau_s > 0$. Therefore, $k = 2(l-1)$ for $l \in \mathbb{N}$

When $k = 0$, $D_s \beta = \pi/2$. Substituting this relation into equation (5.36) and solving for D_s, we obtain

$$D_s = \frac{\pi}{2} \tau_s. \tag{5.42}$$

This line is where λ crosses the imaginary axis, resulting in a limit cycle. Therefore, theoretically we observe a Hopf bifurcation about the origin in the states. We restrict our analysis to only the solutions when $k = 0$, even though there are more roots for increasing values of β; however, these result in highly unstable modes which are not seen physiologically. Figure 5.5 shows a plot of several complex roots to $\phi(\lambda)$.

In conclusion, we have shown that for the homogeneous system in equation (5.19) there exist two lines across which the behavior of the solutions changes: one at $e D_s = \tau_s$ where the solutions to the characteristic equation change from real to imaginary, and one at $D_s = \tau_s \pi/2$ where the the imaginary roots cross the imaginary axis. These lines are shown in Figure 5.8a. The former results in
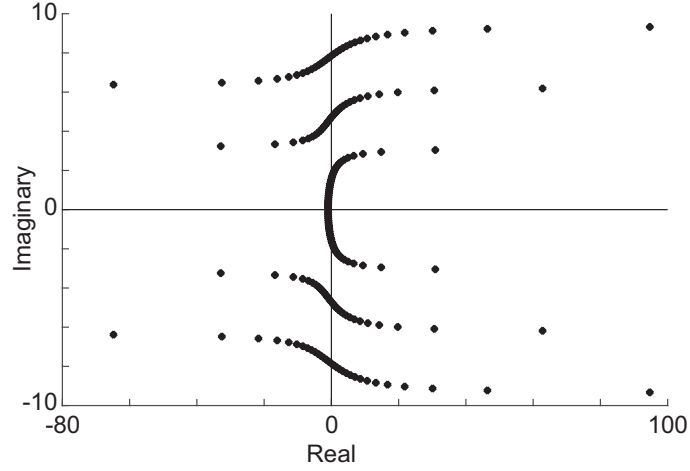
Figure 5.5 Complex roots of the characteristic equation $\phi(\lambda)$ in equation (5.29).

a change in the origin (which is a critical point) from a sink to a stable focus and the latter results in a Hopf bifurcation, producing a limit cycle about the origin, as shown in Figure 5.6a. We classify each each solution as one of the following types with the corresponding color from the contour in Figure 5.8a:

- *Sink - overdamped* (yellow): when $e D_s < \tau_s$, ϕ has two real solutions $\lambda_1, \lambda_2 < 0$.

- *Sink - critically damped* (red): when $e D_s = \tau_s$, ϕ has one real solution $\lambda < 0$.

- *Stable focus* (green): when

$$\frac{1}{e}\tau_s < D_s < \frac{\pi}{2}\tau_s, \tag{5.43}$$

  ϕ has complex solutions $\lambda = \alpha \pm \beta i$ and $\alpha < 0$.

- *Limit cycle* (orange): when

$$D_s = \frac{\pi}{2}\tau_s, \tag{5.44}$$

  ϕ has complex solutions $\lambda = \pm \beta i$ (*i.e.*, $\alpha = 0$) and a limit cycle emerges due a Hopf bifurcation about the critical point.

- *Unstable* (blue): when

$$D_s > \frac{\pi}{2}\tau_s, \tag{5.45}$$

  ϕ has complex solutions $\lambda = \alpha \pm \beta i$ for $\alpha > 0$ and solutions grow exponentially.
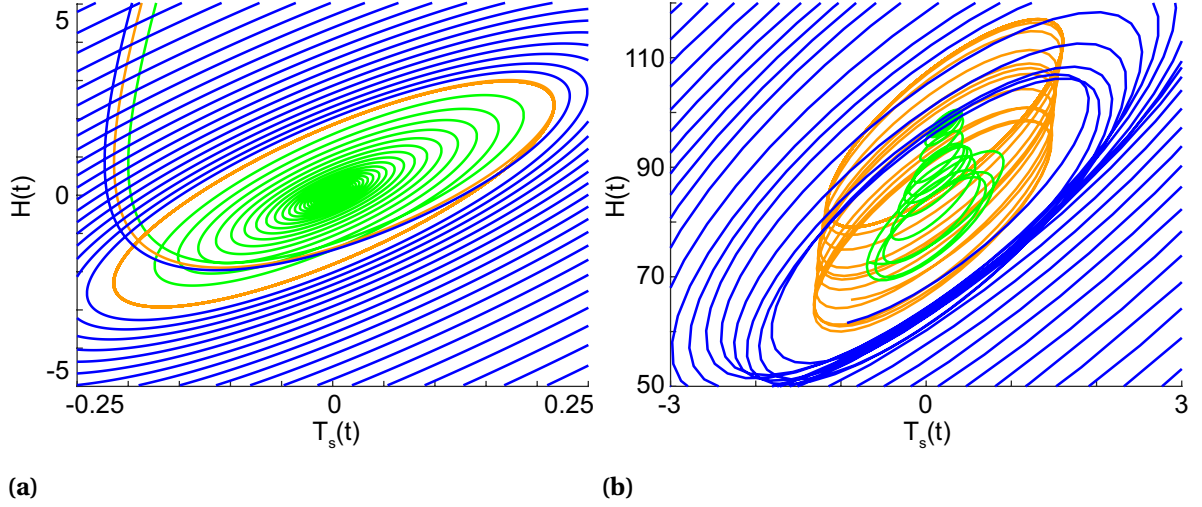
Figure 5.6 Hopf bifurcation observed in (a) the homogeneous system in equation (5.19) and (b) the non-homogeneous system in equation (5.15). Limit cycle (orange) with solutions spiraling out from the critical point (green) and into the critical point (blue).

5.3.2 Nonhomogeneous system

The inclusion of the forcing function, **f**, complicates the analysis, and as discussed in Section 5.1, tools such as DDE-Biftool [29] and knut [126] are not suitable for the nonautonomous, stiff system given in equation (5.15). As shown in Figures 5.3b and 5.3c, **f** is a polynomial fitted to blood pressure data with baseline extended before and after the dynamic behavior. This forcing function ensures that at rest the system is stable. A disturbance caused by this function, such as by the Valsalva maneuver, can result in undesirable model behavior and instability. Moreover, the perturbation of this control system may cause *persistent instability*, that is, instability caused by a disturbance of a forcing function resulting in oscillatory behavior that either remains unstable, oscillates with constant amplitude, or takes a long time to dampen in relation to the stimulus.

In the previous section, we determined regions of the parameter space where the five different behaviors arise for the homogeneous solution. We do not expect these regions to be the same for the nonhomogeneous solutions, especially since forcing functions can stabilize and destabilize systems [113]. However, we do expect analogous regions corresponding to the behaviors given above.

This numerical experiment explores the effects of sudden, transient effects of the forcing function on the stability of the system in (5.15) given a specified parameter range. For this analysis we consider only the effects of the interactions between D_s and τ_s. We chose these parameters to investigate based on the analysis of the homogeneous system, which created stability subregions in the parameter space (equations (5.33) and (5.42)). We assume changing these parameters will also cause instability in the nonhomogeneous system. The parameter space for τ_s and D_s is $[0.1, 10] \times$
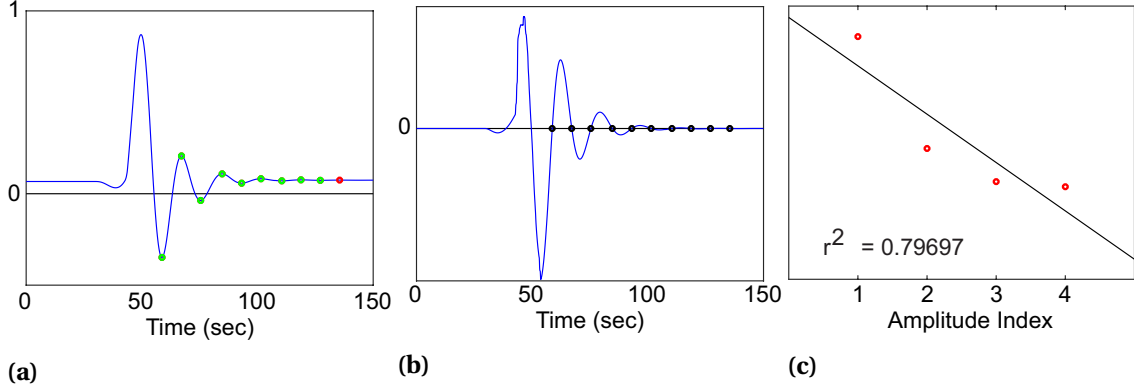
Figure 5.7 Plots denoting different stages in algorithm 2. (a) Representative solution of T_s exhibiting a stable focus with local extrema occurring after the Valsalva maneuver (green circles). The red circle indicates an excluded point if the difference between it and the preceding extremum is $\leq 10^{-8}$. (b) ∇T_s with zeros indicating local extrema (black circles). (c) Consecutive amplitudes (red dots) and a line of regression (black line) with the r^2 value indicated.

[0.1, 10] with a discretized mesh of step-size $h = 10^{-1}$ with all other parameters remaining constant at their nominal values. The model was evaluated iteratively at every point in the mesh. Since the instability is most prominent after the maneuver and during the recovery, we only consider the stability of the signal after the breath hold of the VM was over.

Numerically, we have developed an algorithm to determine the type of solution summarized in Algorithm 2. Of particular note are the thresholds η_1, η_2 and μ. $\eta_1 = 0.5$ is the maximum threshold and $\eta_2 = -10^{-2}$ is the minimum threshold for the slope of the regression line to determine a limit cycle. $\mu = 0.8$ is a threshold for the r^2 value determining the goodness of fit of the regression line to determine a limit cycle. These thresholds ensure that the amplitudes of the limit cycle are approximately equal, the slope of the regression line of consecutive amplitudes is approximately zero, and the regression line fits well ($r^2 \approx 1$).

Solutions for the homogeneous and nonhomogeneous equations were calculated using the stiff, delay differential equation solver RADAR5 [36]. This is a variable-step solver that employs collocation methods to calculate the history of the delayed states. All initial conditions were assigned such that the system begins in steady-state.

5.4   Results and discussion

Stability analysis is important for understanding the kinds of outputs the model can produce. Moreover, bifurcation analysis explores where changes in parameter values impact the system. In this study, we have analyzed a system of nonautonomous, stiff, delay differential equations (DDEs) that can be written as the sum of a homogeneous system (equation (5.19)) and its associated

Algorithm 2 Determine the type of solution behavior for T_s.

1. Calculate ∇T_s (Figure 5.7b). Only consider the behavior of ∇T_s after the Valsalva maneuver end time t_e.

2. Determine where ∇T_s crosses the x-axis (Figure 5.7b).

3. Filter out local extrema if the distance between consecutive points is < 0.1 sec.

4.
   1: Let M_i and m_i be a local maximum and minimum, respectively, at index i and N be the number of maxima.
   2: **for** $i = 1$ to N **do**
   3:    **if** $|M_i - m_i| < 10^{-8}$ **then**
   4:       Remove M_i and m_i.
   5:    **end if**
   6: **end for**

5. Determine the amplitude vector **a** by finding the difference in maxima and minima.

6. Assign solution behavior.
   1: **if a** is empty **then**
   2:    T_s is a sink.
   3: **else if a** has 1 entry **then**
   4:    T_s spirals in.
   5: **else**
   6:    Fit a regression line through the entries of **a**, $y = b_0 + b_1 x$, for b_0 the y-intercept and
   7:    b_1 the slope (Figure 5.7c).
   8:    Calculate the r^2 value of the regression line.
   9:    **if** $\eta_2 \leq b_1 \leq \eta_1$ **then**
   10:       **if** $r^2 > \mu$ **then**
   11:          T_s is a limit cycle.
   12:       **else**
   13:          T_s spirals in.
   14:       **end if**
   15:    **else if** $b_1 > \eta_1$ **then**
   16:       T_s spirals out.
   17:    **else**
   18:       T_s spirals in.
   19:    **end if**
   20: **end if**
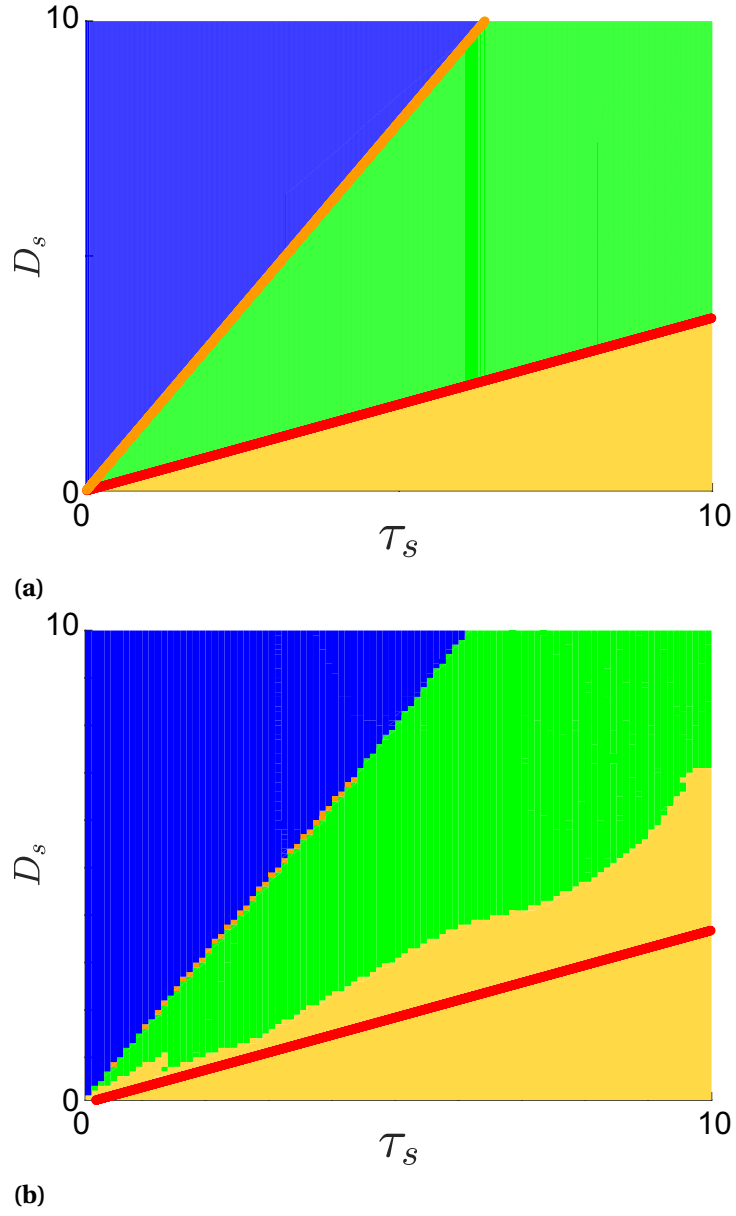
Figure 5.8 Bifurcation diagrams of the behavior of T_s for varying values of $D_s \in [0.1, 10]$ and $\tau_s \in [0.1, 10]$ evaluating the (a) homogeneous system (5.20) and (b) nonhomogeneous system (5.8). Solutions types are denoted as overdamped (yellow), critically damped (red line), stable focus (green), limit cycle (orange line), and unstable (blue). The red line indicated in panel (b) denotes the analytically derived line $\tau_s = e D_s$ for comparison to show the increased sink region (yellow).
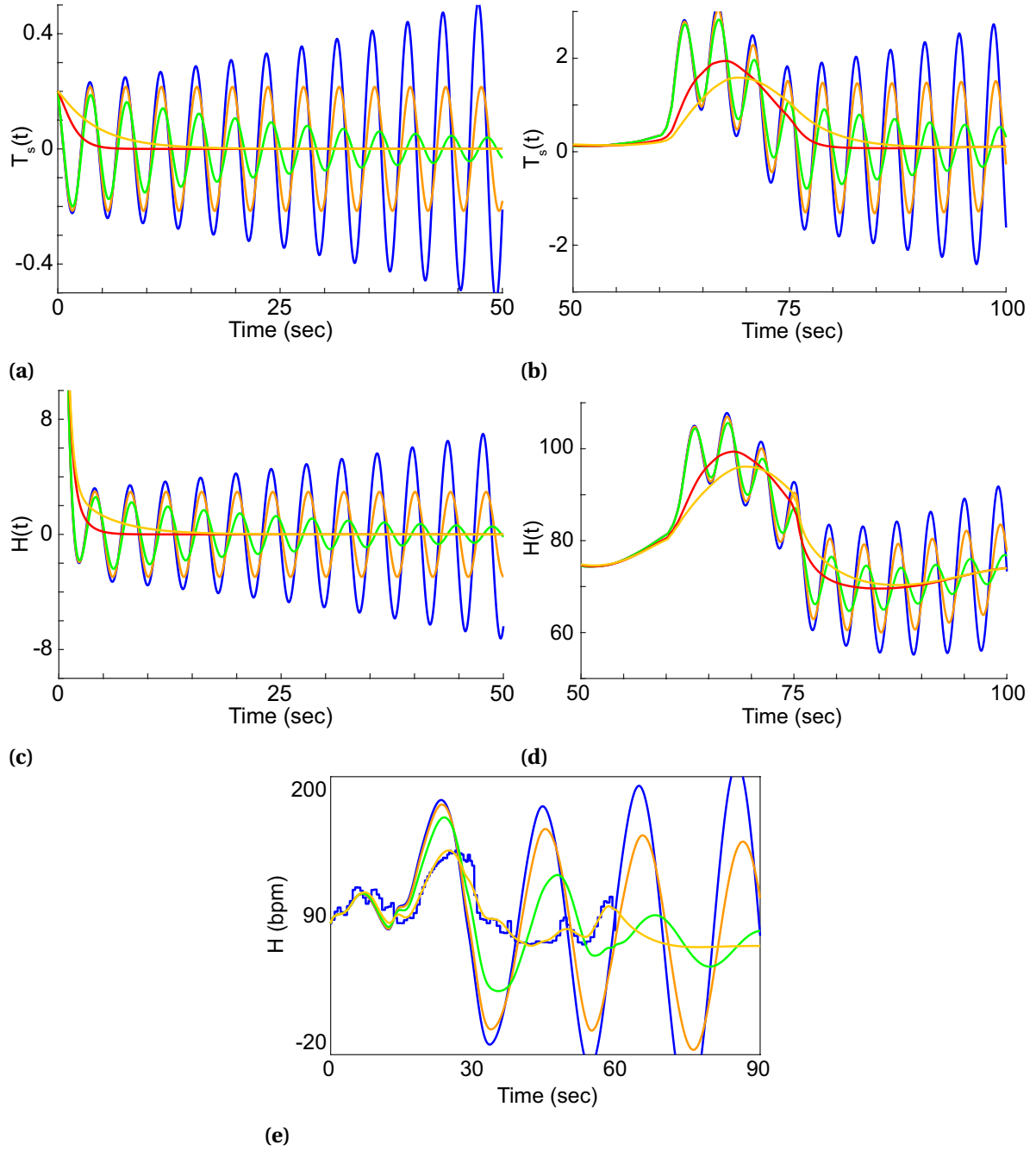
Figure 5.9 Representative solutions of T_s ((a) and (b)) and H ((c) and (d)) for the homogeneous equation (5.20) ((a) and (c)) and nonhomogeneous system (5.8) ((b) and (d)) from each of the different stability regions given in Figure 5.8 with corresponding colors: overdamped (yellow), critically damped (red line), stable focus (green), limit cycle (orange line), and unstable (blue). (e) Simulations of heart rate from the full model in Chapter 4 for a control subject varying τ_s and holding $D_s = 3$ constant. Colors correspond to the contour plot in Figure 5.8b. Sink (yellow) $\tau_s = 7.5$. Stable focus (green) $\tau_s = 4$. Limit cycle (orange) $\tau = 1.9$. Unstable (blue) $\tau = 1.8$.

nonhomogeneous component including the forcing function **f** given in equation (5.18). Figure 5.8 displays the results of the stability analysis with a two-parameter bifurcation diagram plotted for both the homogeneous system (Figure 5.8a) and the nonhomogeneous system (Figure 5.8b in equation (5.8)) denoted with the following colors:

- *Sink - overdamped* (yellow): The inclusion of the forcing function **f** increases the range of the stable region within the parameter space, that is, the yellow region extends beyond the red line in Figure 5.8b.

- *Sink - critically damped* (red): There is a shift in the red line denoting critical dampening from the homogeneous contour to the nonhomogeneous contour, as the sink region expands. This relation is no longer a line but a curve between the sink and stable focus regions.

- *Stable focus* (green): The stable focus region shrinks with the inclusion of the forcing function, resulting in an oscillatory contour that is steeper than the red line predicted in the homogeneous system.

- *Limit cycle* (orange): The limit cycle occurs in the same location in both the homogeneous and the nonhomogeneous bifurcation contours. This is most likely due to the fact that the large amplitude oscillations begin dominate the signal.

- *Unstable* (blue): The unstable region is the same in both the homogeneous and nonhomogeneous contours. This is to be expected as the complex roots to the characteristic equation (5.29) have positive real part and solutions diverge.

Figure 5.9 displays representative curves from each region mentioned above for both T_s (Figure 5.9a and 5.9b) and H (Figure 5.9c and 5.9d). For the nonhomogeneous system (Figures 5.9b and 5.9d), the solutions begin in steady-state and the forcing function **f** induces the Valsalva maneuver (VM), causing some of the responses to have oscillatory behavior. Figure 5.9e shows similar simulations of the full model from Chapter 4 with the systolic blood pressure data as the input. Holding D_s constant at its nominal value, we varied τ_s showing that as τ_s decreases, we see a shift in the behavior of the model output from sink (yellow) to stable focus (green) to limit cycle (orange) to unstable (blue). Hence, the simplifications in Section 5.2 were able to still categorize the behavior of the system appropriately. Furthermore, with the data as an input, we observe that though D_s and τ_s are within their individual physiological ranges, their interactions cause persistent instability for decreasing values of τ_s. Therefore, to ensure that the model produces physiologically relevant results, restricting the parameter space to remain in the sink and stable focus regions is necessary.

Bifurcation packages, *e.g.,* `DDE-Biftool` [29], are insufficient in the analysis of the nonautonomous, stiff system of delay differential equations discussed here. Moreover, the forcing function

Table 5.1 Parameter values for control subjects and AD patient with M behavior.

Subject	D_s	τ_s	Stability region	Color
Control	5.5	8	Sink	Yellow
Control	6	5	Stable focus	Green
AD patient	8.5	8	Stable focus	Green

AD - autonomic dysfunction

is not periodic, so packages, such as `knut` [126], cannot be utilized to analyze equation (5.8). Therefore, we developed our own algorithm to qualitatively assess the behavior of the solutions propagated after the implementation of the Valsala maneuver (VM). This algorithm uses the gradient of the solutions to classify the behavior starting after the transient VM stimulus. With this algorithm, we were able to effectively categorize the solutions and determine the boundary between the sink and stable focus regions.

Figure 5.10 shows blood pressure and heart rate data for control subjects exhibiting sink and stable focus behaviors in the T_s state given the model fit to the heart rate data. The bottom row shows the model fit for a patient with autonomic dysfunction (AD) exhibiting the M behavior as categorized by Palamarchuk *et al.* [94]. The last blood pressure point of the data was repeated for 30 seconds to extend the signal. Parameter values and where they fall in the bifurcation diagram are given in Table 5.1. As shown in Figures 5.10c and 5.10f, control subjects can have both sink and stable focus behavior. This could be due to the fact that some subjects have naturally higher baseline sympathetic activity or due to undiagnosed autonomic dysfunction. Though both signals are stable, the oscillatory behavior of the stable focus control subject attains a slightly negative outflow, which could be interpreted as a switch in behavior from a negative feedback to positive feedback mechanism. The AD patient also exhibits this slightly negative outflow.

As described in Chapter 2, the M behavior is hypothesized to be the result of overactive sympathetic and parasympathetic activity. Figure 5.10f demonstrates that the baroreflex control mechanism is very sensitive for this subject, causing oscillatory dynamics that are generally not seen in control subjects. In Chapter 4, we showed that the model can distinguish between control and patients with the V behavior. In the stability analysis conducted in this chapter, we are able to characterize the dynamics of the M behavior as well and support that the M behavior may be due to instability in the negative feedback control of the baroreflex stimulating a sympathetic response. This concept is important for the assumptions made in Chapter 7 regarding modeling patients with M behavior.

We do not see limit cycles or unstable modes in practice. This is most likely due to the fact that when one system becomes inordinately overactive, there are many other redundancies in place
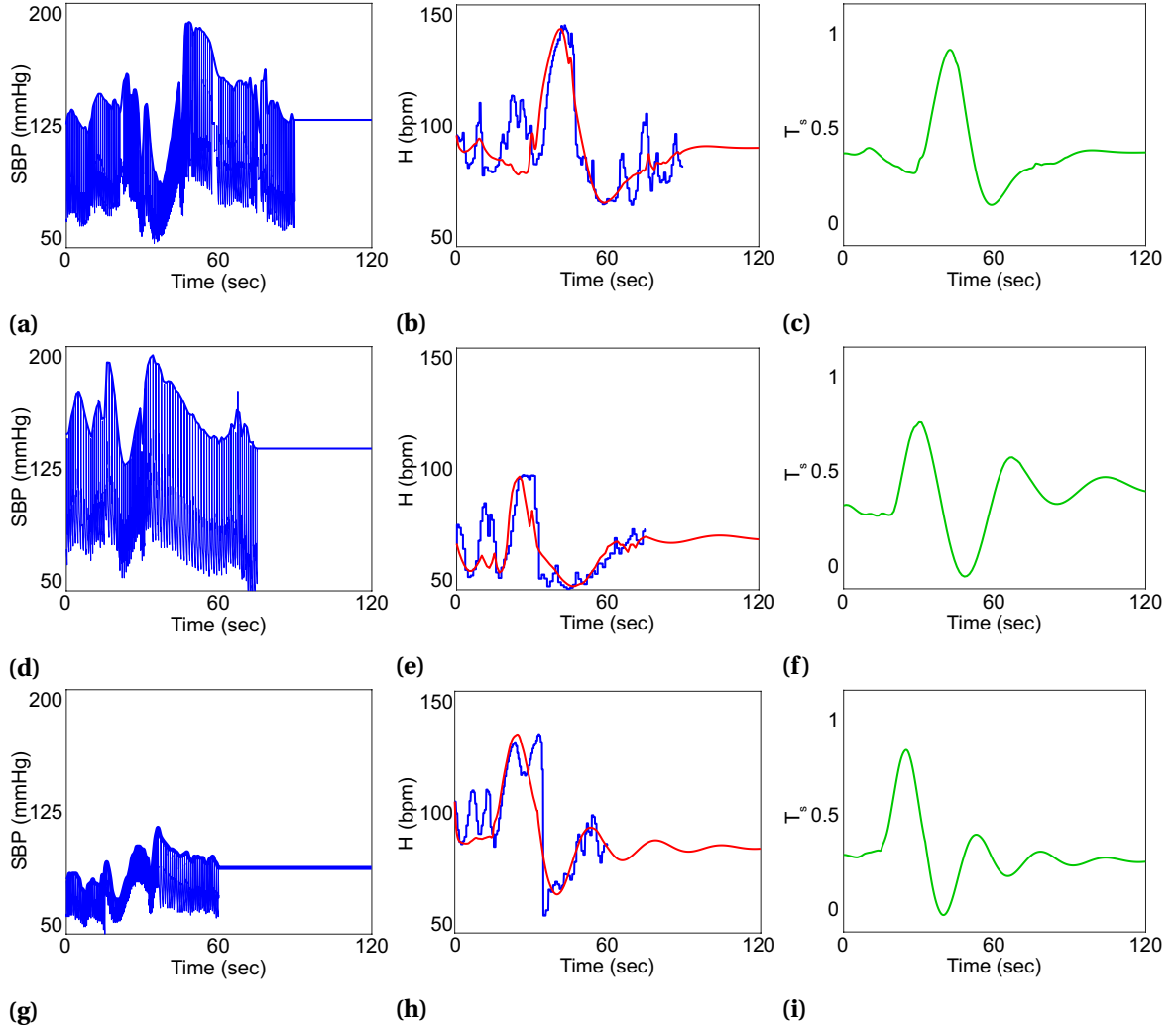
Figure 5.10 Control subjects exhibiting sink (top row) and stable focus (middle row) behaviors and a patient with autonomic dysfunction with M behavior (bottom row). Left column: systolic blood pressure (SBP, mmHg). Middle column: heart rate data (blue) and model fit (red). Right column: baroreflex-mediated sympathetic tone (T_s, green). Solutions are calculated using the two-dimensional nonhomogeneous system (5.8). The end pressure is extended artificially to show dynamic behavior.

88

to reset the body, such as inducing syncope [16]. However, we can classify each of these stability regions not only on the basis of their mathematical properties but of their clinical relevance. These categories are:

- *Sink*: Healthy/control behavior within the "normal" range.

- *Stable focus*: Potential dysfunction caused by overactive sympathetic behavior.

- *Limit cycle*: Unphysiological steady pulsation of sympathetic activity.

- *Unstable*: Sympathetic positive feedback that may be unphysiological (or if it is physiological, it may be corrected via other regulatory mechanisms or, in a worst case scenario, cause death).

In this study, we physiologically reduced the full model to a system of two differential equations that can be solved analytically. This simplified both the model and the analysis and proved to be a reasonable reduction of the system (Figure 5.2). However, numerically, we could have analyzed the full model as opposed to the reduced two-state model. We considered the two-state model for both the homogeneous and nonhomogeneous analyses to facilitate interpretability and comparison.

5.5   Conclusions

In this chapter, we analyzed the effect of the delay differential equation system and categorized the various types of behavior that can result from the interaction of the delay parameter D_s and the time-scale τ_s. Moreover, we classified regions both mathematically and physiologically in a two-parameter bifurcation contour. Motivated by oscillatory behavior that arises in the data, we have determined a numerical relationship between parameters D_s and τ_s. The model supports part of the hypothesis for the M behavior, as we have shown that oscillatory behavior in T_s gives rise to overactive sympathetic activity.

In Chapter 6, we discuss global sensitivity analysis, which uses sampling-based methods that explore the entire parameter space. However, as shown in this analysis, if the parameter space includes regions where unstable modes arise, the analysis is skewed. Therefore, we restrict the parameter space in the global sensitivity analysis to ensure the solutions are in the stable region.

CHAPTER

6

GLOBAL SENSITIVITY ANALYSIS FOR MODEL REDUCTION AND SELECTION

This study develops a methodology for model reduction and selection using global sensitivity analysis. We apply this protocol to the open-loop neurological control model described in Chapter 4 that takes blood pressure and intrathoracic pressure data as an input and predicts heart rate in response to the Valsalva maneuver (VM), a clinical test characterized by forced expiration against a closed airway. In this study, we Sobol' indices to quantify the parameter influence of the model output heart rate. There is a need for GSA methods that take into account transient disturbances from rest, *e.g.,* when analyzing models of the VM. We develop limited-memory Sobol' indices to quantify time correlations and incorporate the history of the variance of the model output via a moving integration window approach, which inform a model reduction study reducing the original model from 6 states and 26 parameters to 4 states and 24 parameters. We also analyze the necessity of modeling both the aortic and carotid baroreceptor regions in response to the VM. The three analytically reduced models considered are (i) aortic-only, (ii) carotid-only, or (iii) both aortic and carotid models. Model selection using the Akaike Information Criterion with correction and the Bayesian Information Criterion in conjunction with a qualitative analysis determined that the aortic-only model is sufficient to model the VM.

6.1 Introduction

Mathematical models of human physiological processes are becoming increasingly more prevalent, simulating functions that are either impossible to perform clinically or difficult to measure without costly and invasive methods. These models clearly have many advantages, but as they become more complex, the number of parameters rises. A versatile model with many components may indeed capture the behavior of a quantity of interest (QoI), but a similar result might be achieved with a simpler model. This begs the question: is it necessary to use a more complex mathematical model for a physiological system when a simpler one may suffice? Can we ensure that this simpler model still produces the same behavior as the original without losing its dynamics and predictive capabilities? If so, does removing or fixing the components that do not affect the QoI change the interpretation of the model predictions? The answer to these questions is problem-dependent, requiring careful analysis of how model components affect the QoI.

Most physiological models are nonlinear and may have parameter interactions not easily determined analytically. To analyze the effects of the parameters on the QoI, many studies use *local sensitivity analysis* (LSA) [28, 74, 87], calculating partial derivatives of the model states with respect to the parameters. These derivatives are typically computed using sensitivity equations [115], finite differences [136], automatic differentiation [104], or the complex-step method [7]. The parameter values are perturbed one at a time, quantifying the effect of each parameter individually on the QoI, without accounting for parameter interactions. On the other hand, *global sensitivity analysis* (GSA) [115] takes into account both the effect of an individual parameter and its interactions on the QoI, computed using Sobol' indices [119], Morris screening [115], generalized sensitivity functions [54], active subspaces [115], and moment-independent importance measures [49]. These methods examine the behavior over a "global" region of interest, that is, each parameter is assigned an upper and lower bound set by the researcher typically based on physiological intuition, empirical studies, or literature. Morris screening is computationally feasible but results are first-order approximations that do not take into account higher order interactions [86]. Generalized sensitivity functions restrict the time-varying influence trajectories to have an end value of one, assuming every parameter has the same influence at that point [54]. Moment-independent importance measures are intractable for larger systems [49].

In this study, we perform a variance-based GSA using Sobol' indices [110, 119], which apportion relative contributions of the overall effect on the QoI to each parameter. This method is widely used to quantify influence of model parameters to the variance of the model outputs [22, 58, 67, 124]. Sobol' indices were developed to study models with scalar outputs [119] and we shall refer to them as *scalar Sobol' indices*. For time-dependent model outputs, *pointwise Sobol' indices* are traditionally computed at every time point individually to assess model sensitivity to the parameters over time [3, 58]. However, this approach neglects the time correlation structure. To remedy this limitation,

Alexandarian *et al.* [4] proposed a method incorporating time dependence via *generalized Sobol'* *indices*, which calculate the ratio of the integral of the variance due to both the parameter and the model output over the entire time interval. Though this method has many applications for models with time-dependent outputs, integrating over the entire time interval averages the effects of parameters that influence the model output over a relatively short time frame. In this study, we propose a modification to this approach, termed *limited-memory Sobol' indices*, that incorporates the effects of transient disturbances in the model behavior. This approach accounts for parameter interactions, time correlations, and the history of the variance within a moving integration window of width Δ.

The limited-memory Sobol' indices are used to inform a model reduction and selection protocol. By analyzing parameter influence, we can select parameters that are noninfluential for the entire time interval and remove the associated model components. "Remove" in this case refers to one of two processes: (i) analytical excision of the mathematical equations associated with the noninfluential parameter [28]; or (ii) fixing the noninfluential parameters at their nominal value [119]. We will make use of both approaches in this model reduction. This process generates a set of reduced models, upon which we can perform a model selection protocol. Metrics, such as the Akaike Information Criterion with correction (AICc) and Bayesian Information Criterion (BIC), are popular choices [137]. In this study, we analyze the behavior of the reduced models using both these criteria and a qualitative approach. To our knowledge, this is the first study using GSA to inform a model reduction and selection protocol for physiological modeling.

Since the acquisition of neural data is difficult, clinicians use the Valsalva maneuver (VM) to indirectly assess autonomic nervous system integrity by analyzing patterns in easily obtainable blood pressure and heart rate data [139]. To supplement these protocols, mathematical modeling can provide time series predictions of parasympathetic and sympathetic nervous function based on the data available. The VM stimulates the baroreceptor reflex (*baroreflex*) triggered by the deformation of baroreceptors in the aortic arch and carotid sinus sensing changes in blood pressure [132]. These signals are integrated in the medulla, eliciting parasympathetic and sympathetic nervous system responses that modulate heart rate and blood pressure. The physiological importance of modeling both the aortic and carotid baroreceptors has been supported in Chapter 4 and Kosinski *et al.* [61]. In this study, we consider modeling both regions from a sensitivity analysis point of view, determining mathematically whether both model components are necessary. We hypothesize that the aortic and carotid baroreceptors are both necessary to model the VM.

This chapter is organized as follows: Section 6.2 presents the mathematical methods, including the limited-memory Sobol' indices, the GSA-informed model reduction protocol, and the model selection; Section 6.3 compiles the results of the GSA and the application of the model reduction and selection protocol; Section 6.4 discusses key findings; and, finally, Section 6.5 states our conclusions.
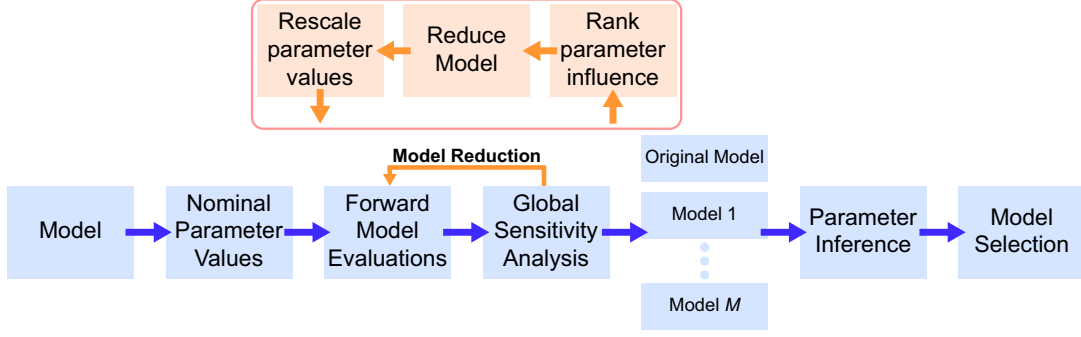
Figure 6.1 Workflow diagram illustrating the steps in this procedure. From left to right: A model is developed and nominal parameter values are set from literature or knowledge of the system. Forward model evaluations produce outputs, which are analyzed via a chosen global sensitivity analysis (GSA) method. The results from the GSA are used to reduce the model (orange arrow) iteratively, which produces an array of M reduced models. For each model, a subset of parameters is estimated to fit data. Finally, the reduced model that captures the aspects of the original model both qualitatively and quantitatively is selected. *Iterative Model Reduction Step* (orange insert): From the GSA, parameters are ranked based on their influence on the model output. The components of the model associated with the noninfluential parameters are removed or fixed. Nominal parameter values are recomputed and rescaled appropriately. Forward model evaluations are conducted and a GSA is performed again.

6.2 Methods

We develop methodology for model selection and reduction motivated by a global sensitivity analysis (GSA). We apply this procedure to a first-order delay differential equation model of autonomic function and heart rate dynamics in response to the Valsalva maneuver (VM). This model has 6 states and 26 parameters. Figure 6.1 shows the workflow used in this study. Main components include:

1. *Forward model analysis*: Determine nominal parameter values and evaluate the scalar or time-varying quantity of interest (QoI) using forward simulations. In this study, the QoI is the residual of the model output to the data $\mathbf{r}(t_j; \theta)$ given in equation (4.30) dependent upon a parameter vector $\theta \in \Omega_p \subseteq \mathbb{R}^p$ and the heart rate data at time t_j, respectively. Ω_p is the prescribed parameter space of dimension p.

2. *Global sensitivity analysis*: Determine the effect of the input parameters on the QoI using the desired GSA method. We compute scalar Sobol' indices with respect to the Euclidean norm of the residual ($\|\mathbf{r}\|_2$.) and time-varying (pointwise, generalized, and limited-memory) Sobol' indices with respect to $\mathbf{r}$.

    (a) *Parameter influence*: Rank the parameters from most to least influential in relation to the prescribed QoI. Noninfluential parameters are below a preset threshold.

(b) *Model reduction*: Test noninfluential parameters to ensure that changing them does not affect the QoI significantly. Remove or fix the least influential parameter from system. This step is inherently problem-dependent, as it may not be feasible to remove certain model components from highly complex systems.

(c) *Model recalibration*: Recompute or rescale model parameters appropriately, ensuring that the reduced model produces a similar result as the original. Again, this step is problem-dependent.

(d) *Global sensitivity analysis*: Conduct the GSA again on the reduced model to test that all parameters are above the threshold. The removal of model components can enhance interactions between the remaining parameters. Repeat this iteratively until the desired set of reduced models is achieved.

3. *Reduced models*: Create a space of models $\mathcal{M} = \{m_0, m_1, \ldots m_M\}$, where m_0 is the original model and m_k are the reduced models for $k = 1, \ldots, M$.

4. *Parameter estimation of reduced models*: Fit the reduced models to data using a desired optimization method. We determine a subset of parameters ($\hat{\theta}$) to optimize by computing a Fisher Information Matrix and analyzing parameter correlations via structured correlation analysis [86, 87, 100]. A limitation of this method is that it is local in nature, since it evaluates the model at specific parameter values.

5. *Model selection*: Select the reduced model that best fits the data and predicts other model outputs. We use the Akaike Information Criterion with correction (AICc) and Bayesian Information Criterion (BIC) to perform model selection and also compare the behavior of the predicted signals from a qualitative standpoint to ensure the reduced models produce similar outputs within physiologically acceptable ranges to the original model.

The remainder of this section discusses first-order and total effect limited-memory Sobol' indices (Section 6.2.2.2), compares their effectiveness against other common methods [4, 110] (Sections 6.2.2.1 and 6.2.2.2), reduces the original model (Section 6.2.4.2), and develops and assesses a set of reduced models, both statistically and qualitatively (Section 6.2.4.3). The summary of the model, local sensitivity analysis methods, and parameter subset selection estimation techniques can be found in Chapter 4. The data analyzed in this chapter are from a 21-year-old female healthy volunteer who gave consent to participate. The experimental protocol follows that described in Section 3.2.

6.2.1 Model overview

The model used in this study (summarized in detail in Chapter 4) is a system of ordinary and delay differential equations of the form

$$\frac{d\mathbf{x}}{dt} = f(t, \mathbf{x}(t), \mathbf{x}(t - D_s); \theta), \quad \mathbf{x}(0) = \mathbf{x}_0, \tag{6.1}$$

where $\mathbf{x} = [\varepsilon_{b,c}, \varepsilon_{b,a}, T_{p,b}, T_{p,r}, T_s, H]^T$ is the vector of states, f is the right hand side of the system, D_s is the discrete delay, and $\theta \in \mathbb{R}^{26}$ is a vector of parameters, including

$$\theta = [A, B, K_b, K_{p,b}, K_{p,r}, K_s, \tau_b, \tau_{p,b}, \tau_{p,r}, \tau_s, \tau_H, q_w, q_{p,b}, q_{p,r}, q_s,$$
$$s_{p,b}, s_{p,r}, s_s, H_I, H_{p,b}, H_{p,r}, H_s, D_s, t_s, t_e]^T. \tag{6.2}$$

Upper and lower parameter bounds were assigned as shown in Table 6.1. For parameters that are calculated from the data, the bounds were set to the mean value ± 2 standard deviations with the exception of τ_s, which interacts with the delay parameter D_s and causes instability (as shown in Chapter 5). For parameters found in literature, the bounds were set to encompass all possible literature values, given in Table 4.1. Parameter B is the convex combination parameter and varies from zero to one. The remaining parameters were varied by $\pm50\%$ of their nominal values. Due to the large variation in the magnitude of the parameter values, the GSA and the parameter estimation methods act on the logarithm of the parameters. Therefore, we enforce positivity by setting the lower bounds that became negative to 0.01.

Table 6.1 Parameter bounds.

Parameter		Nominal value	Physiological range (Mean ± SD)	Lower bound	Upper bound	Description
Description	Symbol					
Cross-sectional ratio	A	5		2.5	7.5	Nominal ± 50%
Convex combination	B	0.5		0.01	1	
Gains	K_b	0.1		0.01	10	Allowed to vary to contain literature values
	$K_{p,b}$	5		0.01	10	Allowed to vary to contain literature values
	$K_{p,r}$	1		0.01	10	Allowed to vary to contain literature values
	K_s	5		0.01	10	Allowed to vary to contain literature values
Time-scales	τ_b	0.9		0.1	1.5	Allowed to vary to contain literature values
	$\tau_{p,b}$	1.8	6.5 ± 5.7*	0.01	17.9	Mean ± 2 SD
	$\tau_{p,r}$	6	9.6 ± 10.8*	0.01	31.2	Mean ± 2 SD
	τ_s	10	14 ± 8*	5	15	Nominal ± 50%**
	τ_H	0.5		0.01	10	Allowed to vary to contain literature values
Sigmoid	q_w	0.04		0.02	0.06	Nominal ± 50%
Steepnesses	$q_{p,b}$	10		5	15	Nominal ± 50%
	$q_{p,r}$	1		0.5	1.5	Nominal ± 50%
	q_s	10		5	15	Nominal ± 50%
Half-saturation	s_w		123 ± 20	83	163	Mean ± 2 SD
Values	$s_{p,b}$		0.54 ± 0.005	0.53	0.55	Mean ± 2 SD
	$s_{p,r}$		4.88 ± 0.21	4.46	5.3	Mean ± 2 SD
	s_s		0.05 ± 0.005	0.04	0.06	Mean ± 2 SD
Heart rate	H_I		100 ± 7	86	114	Mean ± 2 SD
Gains	$H_{p,b}$		0.5 ± 0.2	0.1	0.9	Mean ± 2 SD
	$H_{p,r}$		0.3 ± 0.4	0.01	1.1	Mean ± 2 SD
	H_s		0.3 ± 0.4	0.01	1.1	Mean ± 2 SD
Delay	D_s	3		1	5	Allowed to vary to contain literature values

SD - standard deviation.

* denotes parameter range from optimized parameter values from Chapter 4.

** Bounds restricted to remain in the stable region as determined in Chapter 5.

6.2.2 Global sensitivity analysis

We use the variance-based Sobol' indices for our GSA [110, 119]. This section discusses four different methods of computing Sobol' indices: scalar [110], pointwise [3], generalized [4], and limited-memory (new) Sobol' indices.

6.2.2.1 Scalar Sobol' indices

Consider a mathematical model f with a scalar output y and dependent on $\theta \in \Omega_p \subseteq \mathbb{R}^p$, a vector of p uncertain model parameters with a prescribed parameter space Ω_p; that is,

$$y = f(\theta). \tag{6.3}$$

We can allocate to each θ_i for $i = 1 \ldots p$ its contribution to the variance of y [118, 119]. Assuming that the parameters θ_i are independent, the first-order effect of varying θ_i on f is

$$\mathscr{S}_i(f) = \frac{\mathbb{V}_{\theta_i}(\mathbb{E}_{\theta_{\sim i}}[f|\theta_i])}{\mathbb{V}(f)}, \tag{6.4}$$

where $\mathbb{V}(\cdot)$ and $\mathbb{E}[\cdot]$ denote the variance and expectation operators and $\theta_{\sim i}$ is the vector θ without parameter θ_i, that is,

$$\theta_{\sim i} = [\theta_1, \theta_2, \ldots, \theta_{i-1}, \theta_{i+1}, \ldots, \theta_p]^T. \tag{6.5}$$

The total effect index, which takes into account first and higher order effects of θ_i, is

$$\mathscr{T}_i(f) = \frac{\mathbb{E}_{\theta_{\sim i}}[\mathbb{V}_{\theta_i}(f|\theta_{\sim i})]}{\mathbb{V}(f)} = 1 - \frac{\mathbb{V}_{\theta_{\sim i}}(\mathbb{E}_{\theta_i}[f|\theta_{\sim i}])}{\mathbb{V}(f)}. \tag{6.6}$$

6.2.2.2 Time-varying Sobol' indices

Equations (6.4) and (6.6) give the classically defined *scalar Sobol' indices*, useful when the model output is a scalar value, time-independent, or time-dependent but in steady-state. A limitation of this formulation however is that it may average or neglect changes in parameter influence over time. The following formulations are attempts at accounting for this discrepancy.

Pointwise Sobol indices: One method to compute Sobol' indices for models with time-varying outputs is to compute the Sobol' indices at every time point, which we call *pointwise* Sobol' indices [3]. Consider a model f with time-varying output $y(t)$ on an interval $I_T = [0, T]$ for an end time $T > 0$, that is

$$y(t) = f(t; \theta), \quad t \in I_T. \tag{6.7}$$

We define the first-order pointwise Sobol' index of f at time t as

$$\mathscr{S}_i(f;t) = \frac{\mathbb{V}_{\theta_i}(\mathbb{E}_{\theta_{\sim i}}[f(t;\cdot)|\theta_i])}{\mathbb{V}(f(t;\cdot))}, \quad t \in I_T \tag{6.8}$$

and the total effect pointwise Sobol' index of f at time t as

$$\mathscr{T}_i(f;t) = \frac{\mathbb{E}_{\theta_{\sim i}}[\mathbb{V}_{\theta_i}(f(t;\cdot)|\theta_{\sim i})]}{\mathbb{V}(f(t;\cdot))}, \quad t \in I_T. \tag{6.9}$$

Though the indices in equations (6.8) and (6.9) give a sense of a parameter's influence at a particular time point, they ignore time correlations and the history of the time-dependent signal.

Generalized Sobol' indices: This method proposed by Alexandarian *et al.* [4] takes into account correlations with respect to time by integrating the numerators and denominators of equations (6.8) and (6.9) over time. Let $I_t^0 = [0, t]$ be a time-varying interval. Then, the generalized Sobol' index for the main effect of parameter θ_i on f over the interval I_t^0 is

$$\mathscr{S}_i(f;I_t^0) = \frac{\displaystyle\int_0^t \mathbb{V}_{\theta_i}(\mathbb{E}_{\theta_{\sim i}}[f(\tau;\cdot)|\theta_i])\, d\tau}{\displaystyle\int_0^t \mathbb{V}(f(\tau;\cdot))\, d\tau}, \quad t \in I_T. \tag{6.10}$$

Similarly, the generalized Sobol' index for the total effect of θ_i on f over the interval I_t^0 is

$$\mathscr{T}_i(f;I_t^0) = \frac{\displaystyle\int_0^t \mathbb{E}_{\theta_{\sim i}}[\mathbb{V}_{\theta_i}(f(\tau;\cdot)|\theta_{\sim i})]\, d\tau}{\displaystyle\int_0^t \mathbb{V}(f(\tau;\cdot))\, d\tau}, \quad t \in I_T. \tag{6.11}$$

The denominator of equations (6.10) and (6.11) is the integral of the total variance, which is monotonically increasing and strictly positive. However, by integrating over I_t^0, these integrals effectively the effects of dynamic, transient processes over time, especially for problems where an extended baseline is necessary to obtain steady-state conditions.

Limited-memory Sobol' indices: We propose the *limited-memory* Sobol' indices to analyze parameter influence as the QoI responds to fast, significant disturbances in its steady-state behavior. To do so, we introduce the novel concept of using a moving integration window Δ centered at time t, that is, $t \in I_t^{\Delta} = [t - \Delta/2, t + \Delta/2]$ at every time $t \in I_{T-\Delta} = [\Delta/2, T - \Delta/2]$. By implementing an integration window, the domain of t necessarily decreases by $\Delta/2$ at the upper and lower bound of I_T. However,

if the model is in steady-state on the intervals $[0, \Delta/2)$ and $(T - \Delta/2, T]$, the change in parameter influence over these intervals is negligible. The size of the moving window is problem-specific. The limited-memory Sobol' index for the main effect of parameter θ_i on f over the interval I_t^Δ is

$$\mathscr{S}_i(f; I_t^\Delta) = \frac{\displaystyle\int_{t-\Delta/2}^{t+\Delta/2} \mathbb{V}_{\theta_i}(\mathbb{E}_{\theta_{\sim i}}[f(\tau; \cdot)|\theta_i]) \, \mathrm{d}\tau}{\displaystyle\int_{t-\Delta/2}^{t+\Delta/2} \mathbb{V}(f(\tau; \cdot)) \, \mathrm{d}\tau}, \quad t \in I_{T-\Delta}. \tag{6.12}$$

Similarly, the limited-memory Sobol' index for the total effect of θ_i on f over the interval I_t^Δ is

$$\mathscr{T}_i(f; I_t^\Delta) = \frac{\displaystyle\int_{t-\Delta/2}^{t+\Delta/2} \mathbb{E}_{\theta_{\sim i}}[\mathbb{V}_{\theta_i}(f(\tau; \cdot)|\theta_{\sim i})] \, \mathrm{d}\tau}{\displaystyle\int_{t-\Delta/2}^{t+\Delta/2} \mathbb{V}(f(\tau; \cdot)) \, \mathrm{d}\tau}, \quad t \in I_{T-\Delta}. \tag{6.13}$$

This method reduces the window of integration from I_t^0 in the generalized Sobol' indices to I_t^Δ, and therefore, the denominator in equations (6.12) and (6.13) is not necessarily monotonically increasing but is strictly positive. By integrating the variances within a window about t, we can capture the transient changes in parameter influence (as in the pointwise Sobol' indices) but avoid averaging the signal over time (as in the generalized Sobol' indices).

We compute a uniform integration window centered around time t_j as shown in Figure 6.5a. For comparison, we also assess the performance of using a Gaussian window. Let N^Δ be the number of discretized time points in I_t^Δ. A uniform (rectangular) window treat each point as an equal contributor to the integration window by assigning unity to the entire observational interval I_t^Δ with weights

$$w(n) = 1, \quad -\frac{N^\Delta - 1}{2} \leq n \leq \frac{N^\Delta - 1}{2} \tag{6.14}$$

[43]. Figure 6.5a illustrates the moving window over the variance of the output (red) and the variance due to the parameter (blue). A Gaussian window applies a bell curve to I_t^Δ localizing greater contribution about the central node with weights

$$w(n) = e^{-\frac{1}{2}\left(\frac{\alpha n}{(N^\Delta - 1)/2}\right)^2}, \quad -\frac{N^\Delta - 1}{2} \leq n \leq \frac{N^\Delta - 1}{2}, \tag{6.15}$$

where $\alpha = 2.5$ is the default value [43] .

99

6.2.3 Numerical methods

The GSA was performed on all model parameters except t_s and t_e (taken directly from the data) via Monte Carlo integration, that is, $p = 24$. We computed $L_1 = 10^3(p + 2)$ resulting in 26,000 function evaluations [44, 67] and tested for convergence using $L_2 = 10^4(p + 2)$ with 260,000 function evaluations, which produced similar results. For the reduced models, we computed L_1 evaluations. To approximate the integrals, we used the weights from the trapezoid quadrature scheme.

To approximate the integrands in equations (6.10)–(6.13), we employed estimators proposed by Saltelli *et al.* [110]. Let t_j be a time point where $j = 1,\dots,N$ for N the total number of discretized time points; $t_1 = 0$ and $t_N = T$. Let $l = 1,\dots,L_1$ be the index of model function evaluations. We approximate the numerator for equation (6.8) and the integrands for the numerators of equations (6.10) and (6.12) as

$$\mathbb{V}_{\theta_i}(\mathbb{E}_{\theta_{\sim i}}[f(t_j;\cdot)|\theta_i]) \approx \frac{1}{L}\sum_{j=1}^{L} f(t_j, \mathbf{B})_l(f(t_j, \mathbf{A}_{\mathbf{B}}^{(i)})_l - f(t_j, \mathbf{A})_l) \tag{6.16}$$

and the numerator for equation (6.9) and the integrands for the numerators of equations (6.11) and (6.13) as

$$\mathbb{E}_{\theta_{\sim i}}(\mathbb{V}_{\theta_i}(f(t_j;\cdot)|\theta_{\sim i})) \approx \frac{1}{2L}\sum_{l=1}^{L} f(t_j, \mathbf{A})_l(f(t_j, \mathbf{A})_l - f(t_j, \mathbf{A}_{\mathbf{B}}^{(i)})_l)^2, \tag{6.17}$$

where $\mathbf{A}$ and $\mathbf{B}$ are two independent sampling matrices determined quasi-randomly using Sobol' sets with generic elements a_{li} and b_{li} for $l = 1,\dots,L_1$ and $i = 1,\dots,p$. The matrix $\mathbf{A}_{\mathbf{B}}^{(i)}$ denotes a matrix that contains all of the columns of $\mathbf{A}$ except the ith column, which is swapped with the ith column of $\mathbf{B}$. The denominators for equations (6.8) and (6.9) and the integrands of the denominators of (6.10)-(6.13) were approximated using the variance function `var` in MATLAB® 2018a. Further information on these computational methods can be found in Saltelli *et al.* [110].

6.2.4 GSA-informed model reduction

We compare the performance of each of the four indices discussed in Section 6.2.2. The scalar Sobol' indices are calculated with respect to the Euclidean norm of the residual $\mathbf{r}$, that is,

$$\mathscr{S}_i(\|\mathbf{r}\|_2) \quad \text{and} \quad \mathscr{T}_i(\|\mathbf{r}\|_2), \tag{6.18}$$

where $\mathbf{r}$ is as in equation (4.30). Using $\|\mathbf{r}\|_2$ as the scalar model output gives a decent indication of the sensitivity of the $\mathbf{r}$ to the parameters at steady-state, since the Euclidean norm can be considered an average of the signal over time. However, this disregards the changes in parameter influence as fast disturbances occur in the model output. Therefore, we simultaneously compute the pointwise,

generalized and limited-memory Sobol' indices in response to time-varying $\mathbf{r}$, that is

$$\mathscr{S}_i(\mathbf{r};\cdot) \quad \text{and} \quad \mathscr{T}_i(\mathbf{r};\cdot) \qquad (6.19)$$

pointwise, over the interval I_t^0, and over the interval I_t^Δ, respectively. We also consider several sizes of the moving window Δ at $\Delta = 5, 10,$ and 15 seconds.

6.2.4.1   Sensitivity ranking

To identify parameters that do not influence the model output, we use the fact that a parameter θ_i is noninfluential if $\mathscr{T}_i(f) = 0$ [119] and rank the total effect scalar Sobol' indices $\mathscr{T}_i(\|\mathbf{r}\|_2)$ from most to least influential. The parameters are grouped into three categories: most influential, moderately influential, and noninfluential. Threshold cutoffs are assigned as $\eta_1 = 10^{-1}$ and $\eta_2 = 10^{-4}$ for moderately influential and noninfluential, respectively. η_1 is assigned based on the clear separation in parameter influence values shown in Figure 6.2. η_2 is assigned as $\eta_2 = \sqrt{\psi}$, where $\psi = 10^{-8}$ is the integration tolerance. The parameter groups designated by the scalar indices motivated the grouping used for the time-varying indices (piecewise, generalized, and limited-memory Sobol' indices). Moreover, analysis of the time-varying indices can show if a parameter shifts to a different group as time evolves.

Of particular note are the noninfluential parameters determined by this analysis. We define a parameter θ_i as noninfluential if

$$\mathscr{T}_i(\mathbf{r};\cdot) < \eta_2 \quad \forall t. \qquad (6.20)$$

Hence, the model components associated with a noninfluential parameter may not affect the model output in the given physiological range Ω_p and should be either analytically removed or fixed at its nominal value. The former is inherently problem-dependent, as removing model equations may not be feasible. When equation removal becomes intractable, the latter may be more appropriate. In this study, we use both techniques with a goal to obtain the simplest model.

6.2.4.2   Model reduction

Using the sensitivity ranking, we inform a systematic model reduction methodology as shown in Algorithm 3. We would like to stress that this is an iterative and model-specific process, as there are many instances where removing model components can be detrimental. Some changes must happen simultaneously, which we will exemplify in the next section. Alternatively, if model components cannot be removed, we set the noninfluential parameters fixed at their nominal values [4, 121].

Algorithm 3 Global sensitivity analysis for model reduction.

Compute $\mathcal{T}_i(f; I_t^\Delta)$.

Let **j** be an empty vector.

for $i = 1$ to p **do**

    if Parameter i satisfies $\mathcal{T}_i(f; I_t^\Delta) \leq \eta_2 \; \forall \; t \in I_T$ **then**

        $\mathbf{j} \leftarrow [\mathbf{j} \; i]$.

    end if

end for

for $k = 1$ to the length of **j** **do**

    if The model components associated with $\theta_{\mathbf{j}(k)}$ can be algebraically removed **then**

        Remove model components associated with $\theta_{\mathbf{j}(k)}$ analytically to obtain the reduced model f^*.

        Recalibrate parameter values to obtain new parameter vector θ^*.

        Repeat global sensitivity analysis for $f^*(t; \theta^*)$.

        Model $m_j = f^*$.

    else

        Leave $\theta_{\mathbf{j}(k)}$ fixed at its nominal value.

        Repeat global sensitivity analysis for $f^*(t; \theta^*)$.

        Model $m_j = f^*$.

    end if

end for

Generate space of models $\mathcal{M}$.

6.2.4.3 Model selection

To compare model performance between the full and reduced models, we use a statistical measure that calculates a trade off between how well the model fits the data (goodness of fit) with how complex the model is (number of estimated parameters) [103]. We compute the Akaike Information Criterion with correction (AICc) and the Bayesian Information Criterion (BIC) to quantify this comparison. These criteria calculate a regression between the model output and the data [137]. We assume that the residual errors are independent and identically distributed (iid) with mean zero and finite variance. Therefore, we determine these criteria by predicting the maximum likelihood estimate, which is equivalent to minimizing the least squares error J (equation (4.36)), as

$$\text{AICc} = N \log\left(\frac{J}{N}\right) + 2(\hat{p} + 2)\left(\frac{N}{N - (\hat{p} + 2) - 1}\right) \quad \text{and} \tag{6.21}$$

$$\text{BIC} = N \log\left(\frac{J}{N}\right) + (\hat{p} + 2)\log(N), \tag{6.22}$$

where N is the number of data points and $\hat{p}$ the length of the parameter subset vector $\hat{\theta}$ (equation (4.35)) [21]. We add 2 to $\hat{p}$ to include the intercept of the regression and the variance of the model fit.

This statistical technique is useful when determining the goodness of fit to data. However, there are other predicted model outputs, such as $T_{p,b}$ and T_s, that are of clinical importance since they cannot be measured without costly and invasive procedures that blunt the signals with anesthetization. We must also assess the performance qualitatively by assuming the original model predictions as the true signal. Therefore, our model selection protocol accounts for both model fits to data and predicted model signals.

6.3   Results

This section presents results from the global sensitivity analysis (GSA), model reduction, and model selection protocols. We discuss the outcomes from the four Sobol' indices given in Section 6.2: scalar, pointwise, generalized and limited-memory Sobol' indices. The latter is computed using a moving integration window of width Δ. We compare several window widths for this model. Using outcomes from the limited-memory Sobol' indices, we inform a systematic model reduction. Lastly, we conduct a model selection by computing the Akaike Information Criterion with correction (AICc) and the Bayesian Information Criterion (BIC) from equations (6.21) and (6.22) (Table 6.4) and by qualitatively examining the predicted model outputs $T_{p,b}$ and T_s to ensure the reduced models maintained physiologically interpretable results (Figure 6.6).

6.3.1   Sobol indices

Section 6.2.2 discusses four computations of Sobol' indices. In this section, we analyze their effectiveness and compare the results of the established Sobol' indices (scalar, pointwise, and generalized) to the limited-memory Sobol' indices proposed in this study. The scalar indices are shown in Figure 6.2. We compare the various ways to calculate time-varying Sobol' indices in Figure 6.4. The parameters are divided into three influence groups: most influential, moderately influential, and noninfluential.

6.3.1.1   Scalar Sobol' indices

Figure 6.2 shows the ranking of the total effect scalar Sobol' indices in relation to the Euclidean norm of the model output residual $\|\mathbf{r}\|_2$, that is, $\mathcal{T}_i(\|\mathbf{r}\|_2)$. The indices are scaled from 0 to 1 by the value of the most influential parameter K_s.

Most influential parameters: Figure 6.2 shows the five most influential parameters (K_s, H_s, K_b, $H_{p,r}$, and $K_{p,r}$) with indices above the threshold η_1. The upper insert in the figure shows the first order Sobol' indices ($\mathcal{S}_i(\|\mathbf{r}\|_2)$) overlaid atop $\mathcal{T}_i(\|\mathbf{r}\|_2)$. Since $\mathcal{S}_i(\|\mathbf{r}\|_2)$ (white) does not account for much of the influence of $\mathcal{T}_i(\|\mathbf{r}\|_2)$ (blue), this indicates that there are many parameter interactions.
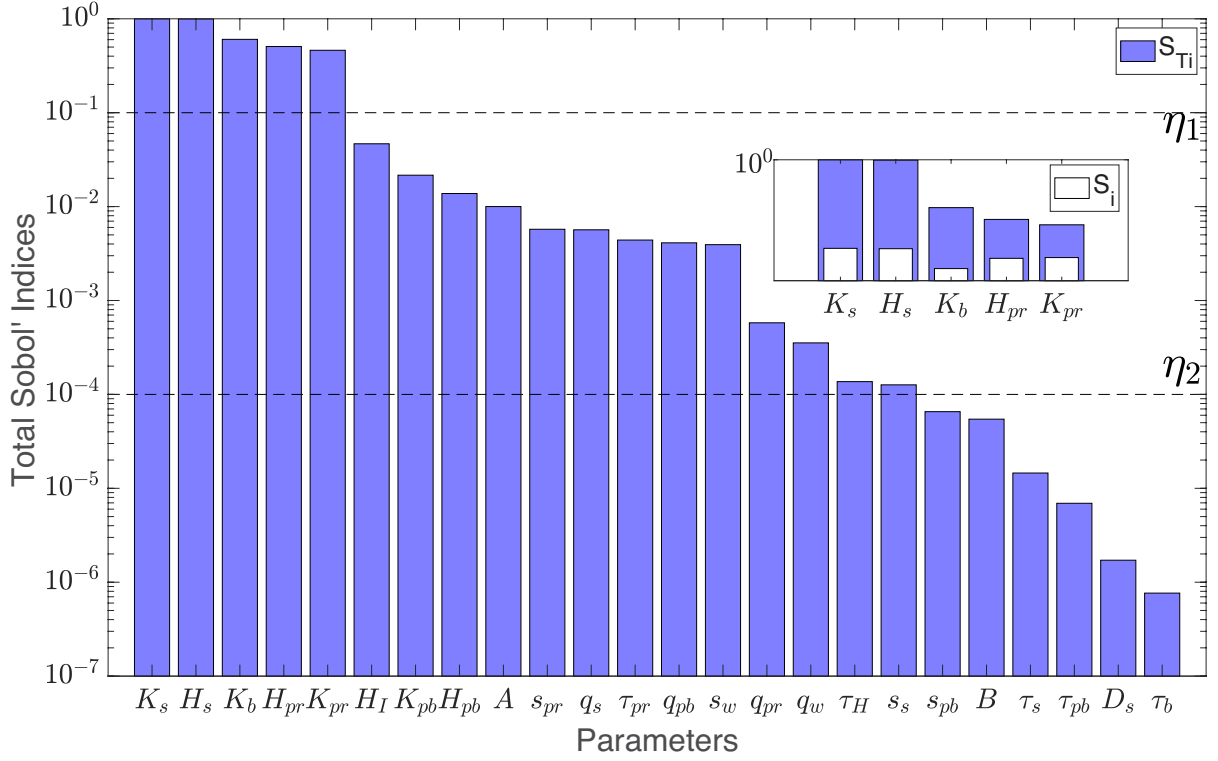
Figure 6.2 Total effect scalar Sobol' indices ($\mathcal{T}_i(\|\mathbf{r}\|_2)$, blue) given in equation (6.6) scaled from 0 to 1 by the most influential parameter K_s. The influence thresholds are indicated with horizontal dashed lines ($\eta_1 = 10^{-1}$ and $\eta_2 = 10^{-4}$). *Insert*: Most influential parameters plotted with their respective first-order Sobol' index ($\mathcal{S}_i(\|\mathbf{r}\|_2)$, white) given in equation (6.4). The remaining parameter indices have similar results (not shown).

This is to be expected since the model is highly nonlinear.

Moderately influential parameters: The moderately influential set of parameters between the influence thresholds $\eta_1 = 10^{-1}$ and $\eta_2 = 10^{-4}$ encompasses H_I, $K_{p,b}$, $H_{p,b}$, A, $s_{p,r}$, q_s, $\tau_{p,r}$, $q_{p,b}$, s_w, $q_{p,r}$, q_w, τ_H, and s_s. This group contributes to the heart rate to a lesser extent than the most influential parameters.

Noninfluential parameters: Six noninfluential parameters are below the threshold η_2, that is, the subset of noninfluential parameters such the $\mathcal{T}_i(\|\mathbf{r}\|_2)$ is

$$\theta_{NI,sca} = \{s_{p,b}, B, \tau_s, \tau_{p,b}, D_s, \tau_b\}. \tag{6.23}$$

In this analysis, τ_b is the least influential parameter on $\mathbf{r}$.

We evaluated the model for each noninfluential parameter at several points within their upper and lower bounds as shown in Figure 6.3. Even though the scalar Sobol' indices determined that these parameters are noninfluential, we observe that they still have a substantial effect on the model output but in certain time frames. Most notably, varying τ_b shows almost no variation across the time interval. It is important to note that the one-at-at-time parameter adjustments are inherently local in nature, though they do provide useful insight. At rest, most of the noninfluential parameters show very little effect on the heart rate output, except $s_{p,b}$ which varies the baseline heart rate. During the VM, B, τ_s, $\tau_{p,b}$, and D_s do have a significant effect the heart rate. After the VM, the parameters exhibit little variation in the heart rate. These results illustrate the need to develop improved metrics that incorporate time dependencies to determine not only if but *when* the parameter is influential.

(a) $s_{p,b}$

(b) B

(c) τ_s

(d) $\tau_{p,b}$

(e) D_s

(f) τ_b
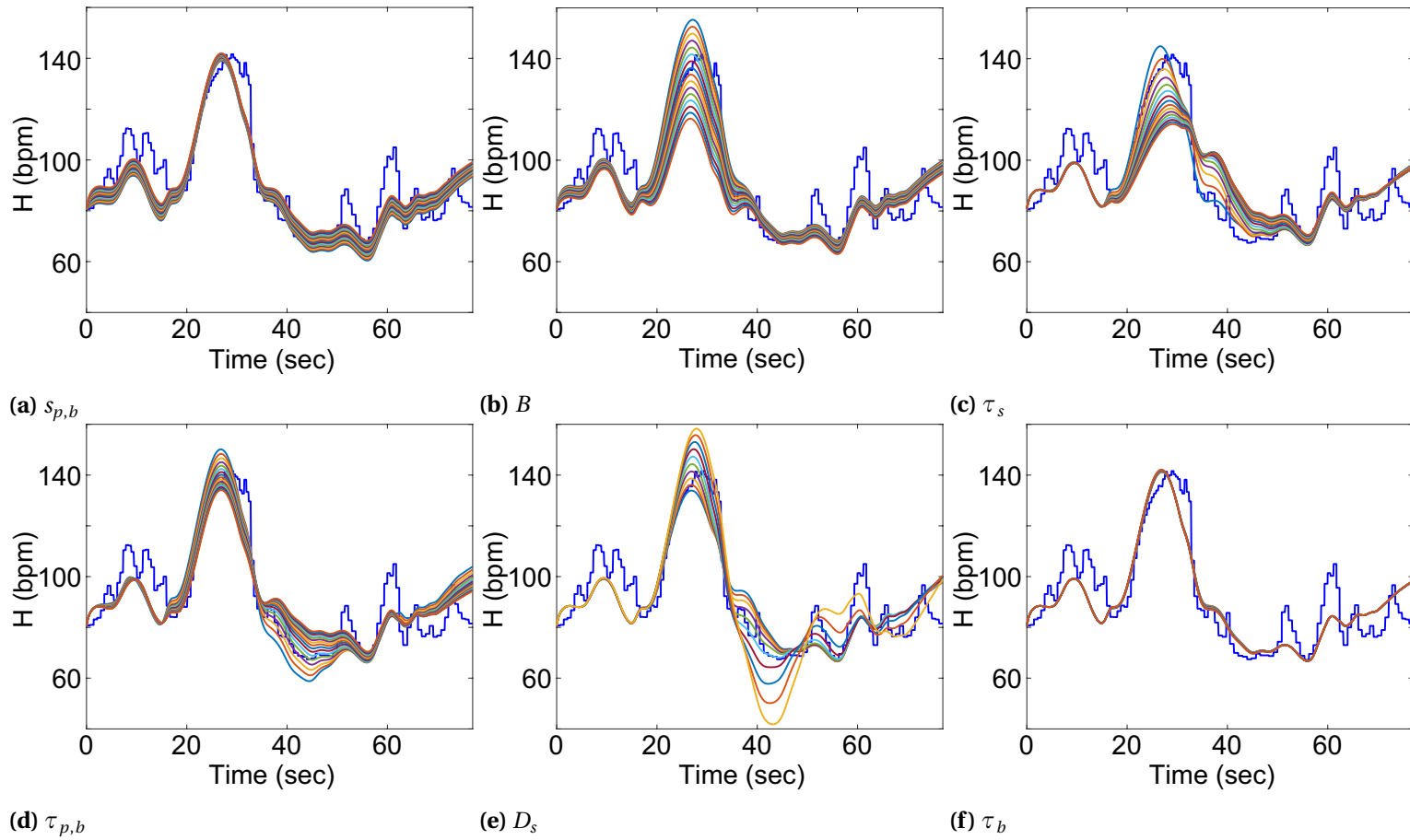
Figure 6.3 Noninfluential parameters as determined by the total effect scalar Sobol' indices in Figure 6.2 evaluated throughout the physiological range given in Table 6.1.
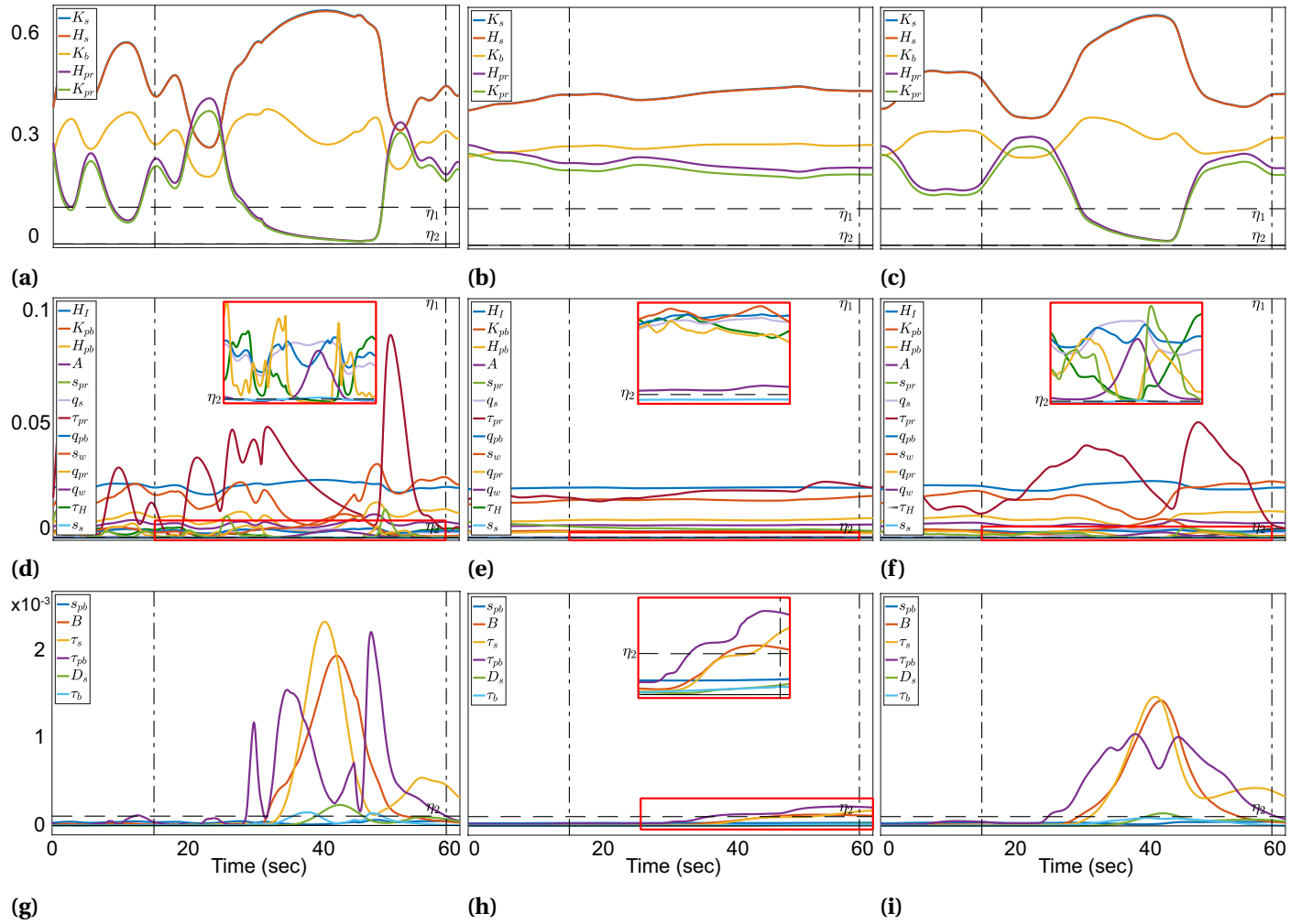
Figure 6.4 Time-varying Sobol' indices for the most influential (top row), moderately influential (middle row), and noninfluential (bottom row) as determined by the scalar Sobol' indices in Figure 6.4 for the pointwise Sobol indices (left column), generalized Sobol' indices (middle column), and limited-memory Sobol' indices (right column). Thresholds $\eta_1 = 10^{-1}$ and $\eta_2 = 10^{-4}$ are indicated with horizontal dashed black lines. The region of the Valsalva maneuver is indicated with vertical dash-dotted black lines. Inserts (red boxes) indicate zooms of the boxed region.

6.3.1.2 Pointwise Sobol' indices

Figures 6.4a, 6.4d, and 6.4g show results from the pointwise Sobol' indices, for the most, moderately, and least influential parameters. The total effect pointwise Sobol' indices ($\mathscr{T}_i(\mathbf{r};t)$) have rapid fluctuations, which are most likely due to their calculation at every time point.

Most influential parameters: The 5 most influential parameters as determined by the scalar Sobol' indices remain influential over the entire time span, though $K_{p,r}$ and $H_{p,r}$ dip into the moderately influential range during the VM (Figure 6.4a).

Moderately influential parameters: The moderately influential parameters show highly oscillatory behavior at baseline, especially the less influential parameters shown in the insert.

Noninfluential parameters: The noninfluential group from the scalar Sobol' indices are inconclusive, as their highly oscillatory behavior complicates their analysis (Figure 6.4g). Note that parameters τ_s, B, $\tau_{p,b}$, D_s and τ_b increase in influence above the threshold during the VM while $s_{p,b}$ remains below η_2 for the entire time interval. In particular, the influence of B, the convex combination parameter designating the effect from the aortic and carotid regions, is below η_2 before and after the VM but increases into the moderately influential range during the VM.

Many parameters (*e.g.*, $H_{p,r}$, $K_{p,r}$, and B) change their level of influence as the VM occurs. In comparison to the scalar indices, the pointwise indices show that there are large fluctuations in parameter influence as time evolves.

6.3.1.3 Generalized Sobol' indices

The total effect generalized Sobol' indices (Figures 6.4c, 6.4e, and 6.4h) remain almost constant with small fluctuations over the entire time interval, I_T. As $\mathscr{T}_i(\mathbf{r};I_t^0)$ integrates to each subsequent time point, the result is an effective averaging of the behavior for all $t \in I_T$. Though there are some minor fluctuations, the parameter ranking over I_T remains relatively constant and generally coincides the ranking produced by the scalar Sobol' indices in Figure 6.2 with a couple minor adjustments.

Most influential parameters: All 5 most influential parameters maintain their ranking throughout the time span.

Moderately influential parameters: This set of parameters maintain a relatively constant ranking as well with some minor switches in the ranking. Of particular note is the parameter s_s, which remains below η_2 for the entire time span, becoming noninfluential.

Noninfluential parameters: For the noninfluential parameters determined by the scalar Sobol' indices, this method indicates that over time, parameters $\tau_{p,b}$, τ_s, and B become moderately influential towards the end of the time period. For these three parameters, $\mathscr{T}(\mathbf{r}; I_t^0)$ shows that they are only important after the VM has completed. The noninfluential parameters such that $\mathscr{T}(\mathbf{r}; I_t^0) < \eta_2$ for all time t is

$$\theta_{NI,gen} = \{s_s, s_{p,b}, D_s, \tau_b\}. \tag{6.24}$$

Since the model has control mechanisms that are activated at different times, it is natural to hypothesize that the parameters associated with those controls should have a greater influence during the time that the control is active. However, these indices do not support this hypothesis. Computing the generalized Sobol' indices provide approximately the same parameter influence at every time point as the scalar Sobol' indices over the whole time interval. Notable exceptions are $\tau_{p,b}$, τ_s, and B in Figure 6.4h, which have a delayed increase in influence. This is counterintuitive, as this analysis shows the parameters associated with activating and deactivating the control pathways are not influential when the VM occurs but after the VM has concluded.

In comparison to the scalar indices, $\mathscr{T}_{s_s}(\mathbf{r}; I_t^0) < \eta_2$ for all time $t \in I_T$, which moves s_s to the noninfluential set. The differences between the pointwise and generalized Sobol' indices are evident. The former provides one case where the parameter influence oscillates significantly during dynamic changes. It does not take into account the history of the variance, and without this history even the baseline results are difficult to interpret. The latter places too much emphasis on the time-dependence, and hence, averages the signal over extended periods of baseline activity, washing out any of the potential transient changes in parameter influence on the model output.

6.3.1.4   Limited-memory Sobol' indices

The most influential (Figure 6.4c), moderately influential (Figure 6.4f), and noninfluential (Figure 6.4i) total effect limited-memory Sobol' indices with a window $\Delta = 10$ are shown. The choice of $\Delta = 10$ is motivated in the next section. These indices provide a balance between these two computation schemes above by smoothing out the highly oscillatory pointwise index signal, facilitating analysis and incorporating time correlations, yet retaining some modulation due to the transient nature of the process. This provides distinct changes in parameter influence rankings from before, during, and after the VM.

Most influential parameters: As with the other indices, the limited-memory Sobol' indices maintain the most influential parameters throughout the time span, which is to be expected. Similar to the pointwise indices, $K_{p,r}$ and $H_{p,r}$ dip below η_1.

Moderately influential parameters: These parameters show a substantial change in parameter ranking from before, during, and after the VM. Moreover, a collective increase in influence is seen in the parameters associated with sympathetic function during the VM (q_s, and s_s) and a decrease in parameters associated with the respiratory component ($q_{p,r}$ and $s_{p,r}$).

Noninfluential parameters: Parameters $\tau_{p,b}$, τ_s, B and D_s become moderately influential during the VM and $\tau_{p,b}$ displays bimodal behavior. Parameters $s_{p,b}$ and τ_b remain noninfluential for the entire time span, that is, the subset of noninfluential parameters such that $\mathcal{T}_i(\mathbf{r}; I_t^\Delta) < \eta_2$ for all time t is

$$\theta_{NI,LM} = \{s_{p,b}, \tau_b\}. \tag{6.25}$$

Fluctuations in parameter influence correspond to different control mechanisms that activate and deactivate during the VM. We expect to observe the change in importance of parameters associated with activated control mechanisms that affect the heart rate dynamically. Before and after the VM, the limited-memory indices remain relatively constant. During the VM, they illuminate a dynamic change in the ranking of the parameter influence over time. We conclude that if the QoI is operating in steady-state, computing the scalar Sobol' indices would suffice for the analysis. However, during a transient disturbance from baseline, limited-memory Sobol' indices provide a more informative parameter ranking.

The addition of the moving window increases interpretability of change in parameter influence over time over the pointwise Sobol' indices. They take into account some of the history of the variance over time, as opposed to the generalized Sobol' indices, which account for changes in the variance from the initial time point. A major difference between the generalized and limited-memory Sobol' indices is that the generalized indices have a denominator that increases monotonically while the this is not necessarily true for the limited-memory indices. This is evident in the increase in influence of the parameters $\tau_{p,b}$, τ_s, B towards the end of the time interval. For the limited-memory indices, centering the integration window Δ about time t considers the variance about that time point, and therefore, provides results that correspond to both the mathematical formulation and the physiology of the system.

Table 6.2 summarizes the subset of noninfluential parameters from the scalar (equation (6.23)), generalized (equation (6.24)), and limited-memory (equation (6.25)) Sobol' indices. The pointwise Sobol indices were not included as their results were inconclusive. The limited-memory indices determined the smallest subset of noninfluential parameters for the entire time interval with 2. These 2 parameters, $s_{p,b}$ and τ_b, are considered in the model reduction in Section 6.3.2.

(a)

(b)

(c)
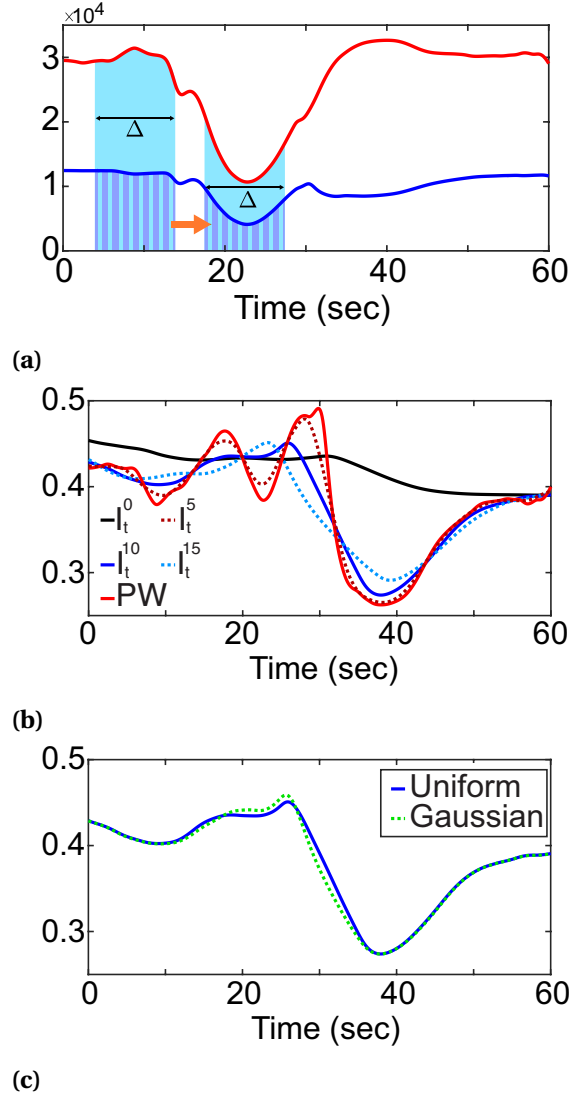
Figure 6.5 Moving window of integration Δ for a generic parameter θ_i. (a) Calculation of the total effect limited-memory Sobol' index in equation (6.13). Integrands of the numerator (red) and denominator (blue) are plotted. Integrals are approximated with using the trapezoid rule with a moving window of width Δ for the denominator (light blue) and numerator (striped purple and light blue). As t moves forward in time, so does the window, *i.e.*, $I_t^\Delta = [t - \Delta/2, t + \Delta/2]$. (b) Comparison of total effect pointwise Sobol' index ($\mathcal{T}_i(\mathbf{r}; t)$) as in equation (6.9) (red), the total effect generalized Sobol' index ($\mathcal{T}_i(\mathbf{r}; I_t^0)$) where $I_t^0 = [0, t]$ as in equation (6.11) (black), and total effect limited-memory Sobol' indices with moving window Δ ($\mathcal{T}_i(\mathbf{r}; I_t^\Delta)$) as in equation (6.13) with $\Delta = 5$ seconds (dotted red), $\Delta = 10$ seconds (blue), and $\Delta = 15$ seconds (dotted blue). These windows were chosen since the breath hold of the Valsalva maneuver occurs over 15 seconds. (c) Comparison of the using a uniform window (solid) and a Gaussian window (dotted).

Table 6.2 Noninfluential parameters from Sobol' index methods.

Parameter	Sobol' indices		
	Scalar $\theta_{NI,sca}$	**Generalized** $\theta_{NI,gen}$	**Limited-memory** $\theta_{NI,LM}$
s_s		✓	
$s_{p,b}$	✓	✓	✓
B	✓		
τ_s	✓		
$\tau_{p,b}$	✓		
D_s	✓	✓	
τ_b	✓	✓	✓

Moving window: In Figure 6.5, we show the time-varying total effect limited-memory Sobol' index for a parameter θ_i with respect to the time-varying model output $\mathbf{r}$, that is, $\mathscr{T}_i(\mathbf{r}; I_t^\Delta)$ where $I_t^\Delta = [t - \Delta/2, t + \Delta/2]$. Figure 6.5a depicts limited-memory Sobol' indices with a uniform moving window of width Δ. Since the choice of window width is problem-dependent, it is prudent to test Δ appropriately. This model predicts heart rate in response to the Valsalva maneuver, which is induced for 15 seconds. Hence, we compare values of $\Delta = 5, 10$, and 15 seconds to determine an appropriate window width.

Figure 6.5b displays the trajectories for $\mathscr{T}_i(\mathbf{r}; I_t^5)$ (dotted red curve), $\mathscr{T}_i(\mathbf{r}; I_t^{10})$ (solid blue curve), and $\mathscr{T}_i(\mathbf{r}; I_t^{15})$ (dotted blue curve). For reference, the pointwise Sobol' index $\mathscr{T}_i(\mathbf{r}; t)$ (solid red curve) and the generalized Sobol' index $\mathscr{T}_i(\mathbf{r}; I_t^0)$ (solid black curve) are shown. In comparison to the pointwise indices, $\mathscr{T}_i(\mathbf{r}; I_t^5)$ is slightly smoother than and retains almost all of the dynamics of $\mathscr{T}_i(\mathbf{r}; t)$. $\mathscr{T}_i(\mathbf{r}; I_t^{10})$ also exhibits similar modulations as $\mathscr{T}_i(\mathbf{r}; t)$, but is much smoother, averaging the wide oscillations in the interval $[10, 30]$ and maintaining the dramatic drop around $t = 35$. $\mathscr{T}_i(\mathbf{r}; I_t^{15})$ begins to dramatically lose the fluctuations of the pointwise indices around $t = 20$ seconds and does not drop as significantly around $t = 35$. As Δ increases, $\mathscr{T}_i(\mathbf{r}; I_t^\Delta) \to \mathscr{T}_i(\mathbf{r}; I_t^0)$, which is to be expected since the integration window will widen until it encapsulates the entire time span. From these results, we determine that $\mathscr{T}_i(\mathbf{r}; I_t^{10})$ is sufficiently smooth while retaining the general morphology of the pointwise indices and incorporating the history of the variance.

Figure 6.5c displays a comparison between a uniform window (solid) and a Gaussian window (dotted) of width $\Delta = 10$ for the chosen index $\mathscr{T}_i(\mathbf{r}; I_t^{10})$. The weights for the uniform and Gaussian windows are given in equations (6.14) and (6.15), respectively. We observe a negligible difference between the two window types, and hence, choose a uniform window for simplicity.

6.3.2 Model reduction

The limited-memory Sobol' indices display gradual changes in the ranking of parameter influence. The two noninfluential parameters determined by this analysis are $s_{p,b}$ and τ_b. We begin by considering the least influential parameter τ_b for all $t \in I_{T-\Delta}$. Removing the least influential parameter and its associated components in the model analytically should have little to no change in the model outputs. However, this removal causes a fundamental change the model equations. Therefore, we expect some of the preexisting parameter independences to become more pronounced while others may diminish. Therefore, we have to redo subset selection for each model to determine the a new identifiable subset of parameters to optimize. We used the method of structured correlation analysis given in Section 4.2.1. One limitation of this method is that it is inherently local. Therefore, the structured correlation analysis should be tested at several locations throughout the parameter space.

Removal of τ_b: Since $0.1 \leq \tau_b \leq 1.5$, the domain of τ_b is small and it is feasible to remove the differential equations associated with this parameter and then rescale the model parameters. This should have a negligible effect on the model output, especially given the fact that $\mathcal{T}_{\tau_b}(\mathbf{r}; I_t^\Delta) < \eta_2$ for all time t and adjusting between its upper and lower bounds showed little to no effect (Figure 6.3f). Therefore, we have

$$\frac{\mathrm{d}\varepsilon_{b,j}}{\mathrm{d}t} = \frac{-\varepsilon_{b,j} + K_b \varepsilon_{w,j}}{\tau_b} \quad \Rightarrow \quad \tau_b \frac{\mathrm{d}\varepsilon_{b,j}}{\mathrm{d}t} + \varepsilon_{b,j} = K_b \varepsilon_{b,j}. \tag{6.26}$$

$\mathcal{T}_{\tau_b}(\mathbf{r}; I_t^\Delta) < \eta_2$ for all time t implies that we can set τ_b to be any value within its domain. Moreover, we assume $\tau_b = 0$ since its lower bound $0.1 \ll 1$ and τ_b is noninfluential. Then,

$$\varepsilon_{b,j}^* = K_b \varepsilon_{w,j}, \tag{6.27}$$

where the asterisk denotes the new equation for $\varepsilon_{b,j}$. Since this parameter is a time-scale for two differential equations, we are able to reduce the number of states of the model by two. Furthermore, since the parameter K_b is now just a scaling factor as shown in equation (6.27), we can rescale the nominal parameter values. Substituting the previous equation into equation (4.5) yields

$$\begin{aligned}
n^* &= B(\varepsilon_{w,c} - \varepsilon_{b,c}^*) + (1-B)(\varepsilon_{w,a} - \varepsilon_{b,a}^*) \\
&= B(\varepsilon_{w,c} - K_b \varepsilon_{w,c}) + (1-B)(\varepsilon_{w,a} - K_b \varepsilon_{w,a}) \\
&= (1-K_b)\Big(B\varepsilon_{w,c} + (1-B)\varepsilon_{w,a}\Big) \\
&= (1-K_b)n, \tag{6.28}
\end{aligned}$$

which can be propagated through to

$$G_{p,b}^* = \frac{1}{1+e^{-q_{p,b}(n^*-s_{p,b})}} = \frac{1}{1+e^{-q_{p,b}((1-K_b)n-s_{p,b})}} = \frac{1}{1+e^{-q_{p,b}^*(n-s_{p,b}^*)}} \tag{6.29}$$

for rescaled parameters

$$q_{p,b}^* = q_{p,b}(1-K_b) \quad \text{and} \quad s_{p,b}^* = n + \frac{1}{q_{p,b}^*}\ln\Big(\frac{K_{p,b}}{\bar{T}_{p,b}} - 1\Big), \tag{6.30}$$

where $\bar{T}_{p,b}$ is the steady-state value. For the sympathetic sigmoidal parameters, we similarly obtain

$$q_s^* = q_s(1-K_b) \quad \text{and} \quad s_s^* = n - \frac{1}{q_s^*}\ln\Big(\frac{K_s}{\bar{T}_s} - 1\Big). \tag{6.31}$$

Therefore, the new system of equations without the baroreceptor strain differential equations is

$$\varepsilon_{w,j} = 1 - \sqrt{\frac{1+e^{-q_w(\bar{P}_j-s_w)}}{A+e^{-q_w(\bar{P}_j-s_w)}}} \quad \text{for} \ \ j = c \ \text{or} \ a \tag{6.32}$$

$$n = B\varepsilon_{w,c} + (1-B)\varepsilon_{w,a} \tag{6.33}$$

$$G_{p,b} = \frac{1}{1+e^{-q_{p,b}^*(n-s_{p,b}^*)}} \quad \text{and} \quad \frac{\mathrm{d}T_{p,b}}{\mathrm{d}t} = \frac{1}{\tau_{p,b}}(-T_{p,b} + K_{p,b}G_{p,b}) \tag{6.34}$$

$$G_s = \frac{1}{1+e^{q_s^*(n-s_s^*)}} \quad \text{and} \quad \frac{\mathrm{d}T_s}{\mathrm{d}t} = \frac{1}{\tau_s}(-T_s(t-D_s) + K_s G_s) \tag{6.35}$$

$$G_{p,r} = \frac{1}{1+e^{-q_{p,r}(P_{th}-s_{p,r})}} \quad \text{and} \quad \frac{\mathrm{d}T_{p,r}}{\mathrm{d}t} = \frac{1}{\tau_{p,r}}(-T_{p,r} + K_{p,r}G_{p,r}) \tag{6.36}$$

$$\frac{\mathrm{d}H}{\mathrm{d}t} = \frac{1}{\tau_H}\Big(-H + H_I(1 - H_{p,b}T_{p,b} + H_{p,r}T_{p,r} + H_s T_s)\Big). \tag{6.37}$$

This is a new system ordinary and delay differential equations consisting of 4 states and 24 parameters. By letting $\cdot^*$ denote the reduced system, we have

$$\frac{\mathrm{d}\mathbf{x}^*}{\mathrm{d}t} = f^*(t,\mathbf{x}^*(t),\mathbf{x}^*(t-D_s);\theta^*), \tag{6.38}$$

where f^* is the right hand side, $\mathbf{x}^* = [T_{p,b}, T_{p,r}, T_s, H]^T \in \mathbb{R}^4$, and

$$\theta^* = [A, B, K_{p,b}, K_{p,r}, K_s, \tau_{p,b}, \tau_{p,r}, \tau_s, \tau_H, q_w, q_{p,b}^*, q_{p,r}, q_s^*,$$
$$s_{p,b}^*, s_{p,r}, s_s^*, H_I, H_{p,b}, H_{p,r}, H_s, D_s, t_s, t_e]^T \in \mathbb{R}^{24}. \tag{6.39}$$

We shall refer to this reduced model as m_1 from this point forward.

To determine a subset of parameters to optimize for m_1, we perform subset selection using

structured correlation analysis and obtain

$$\hat{\theta}_{m_1} = [B, \tau_{p,b}, \tau_{p,r}, \tau_s, H_{p,b}, H_s]^T. \qquad (6.40)$$

with $H_{p,r}$ held at its nominal value. Table 6.3 summarizes the optimized parameters for the full model and each reduced model with asterisks denoting parameters held at their nominal value.

Fixing $s_{p,b}$: We ran the GSA using limited-memory Sobol' indices for the model in equation (6.38) and determined that $s_{p,b}$ remains below the threshold η_2 (not shown). Since $s_{p,b}$ is a half-saturation of a sigmoid curve, removing this parameter is not feasible. Therefore, we set $s_{p,b}$ at its nominal value, which is calculated from data.

Table 6.3 Estimated parameter values.

Symbol	Model			
	m_0	m_1	m_2	m_3
B	0.46	0.90	$0^{\dagger}$	$1^{\dagger}$
$\tau_{p,b}$	4.80	5.90	3.53	4.58
$\tau_{p,r}$	3.01	1.50	2.75	3.29
τ_s	8.62	12.36	14.04	11.46
$H_{p,b}$	0.44	0.29	0.46*	0.46*
$H_{p,r}$	0.53	0.20	0.54*	0.54*
H_s	0.27	0.23	0.25	0.56

†The B parameter was held constant at this value and not included as a part of the subset. *Parameter was held constant at its nominal value as it could not be included in the identifiable subset in the reduced model.

Table 6.4 Statistical analysis for model selection.

Model	Cost (J)	Parameters (p)	AICc	BIC
m_0	0.0039	7	-3100	-3093
m_1	0.0039	6	-3102	-3096
m_2	0.0045	4	**-3068**	**-3063**
m_3	0.0048	4	**-3052**	**-3047**

AICc - Akaike Information Criterion with correction in equation (6.21).
BIC - Bayesian Information Criterion in equation (6.22) .
Bold indicates the lowest value.
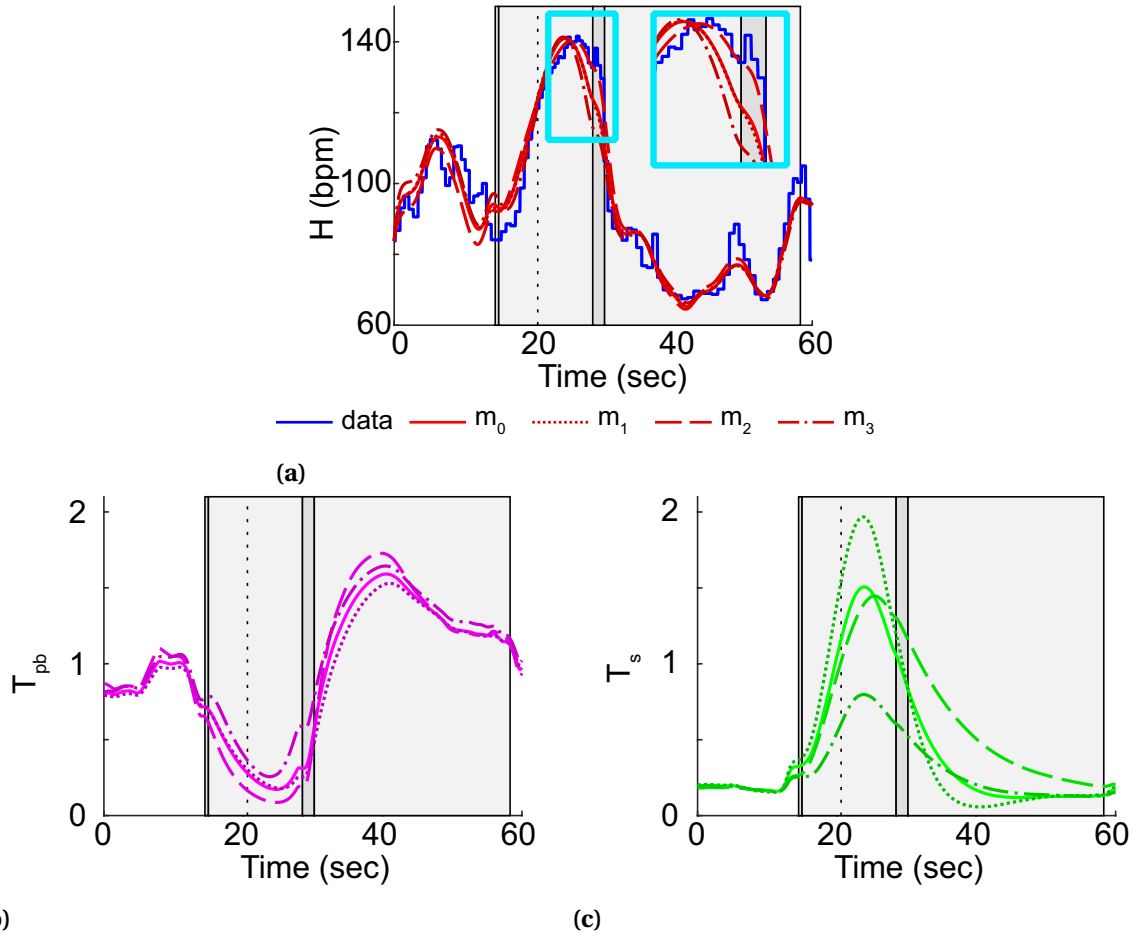
Figure 6.6 Plots of full (solid) and reduced models. Reduced model 1 (m_1 dotted) - removed 2 states and two parameters with parameter B estimated. Reduced model 2 (m_2, dashed) - same as m_1 except with $B = 0$. Reduced model 3 (m_3, dash-dotted) - same as m_1 except with $B = 1$. (a) Model fits (red) to the heart rate data (blue). Insert shows a zoom of the heart rate fit in late phase II and phase III of the Valsalva maneuver. (b) Model predictions of the efferent baroreflex-mediated parasympathetic ($T_{p,b}$, magenta) for the full and reduced models. (c) Model predictions of the efferent baroreflex-mediated sympathetic (T_s, green) for the full and reduced models.

6.3.3 Carotid versus aortic baroreceptors

In Figure 6.4f, we observe parameter, B, (purple curve) that has zero influence for most of the interval I_T except during the VM. This section analyzes the importance of B and determines the necessity of including the convex combination given in equation (4.5). Clinically, the analysis of signaling from the baroreceptors of the aortic arch versus the carotid sinus is important during the baroreflex. It is unknown how these signals are integrated in the medulla and not clear whether it is sufficient to model only one of these regions. At rest, B is noninfluential but gains prominence during the VM, becoming moderately influential after having approximately zero influence at baseline. It can be shown analytically that B is eliminated at rest. Let $\bar{\cdot}$ denote the system at steady-state. Then,

$$
\begin{aligned}
\bar{n} &= B(\bar{\varepsilon}_{w,c} - \bar{\varepsilon}_{b,c}) + (1 - B)(\bar{\varepsilon}_{w,a} - \bar{\varepsilon}_{b,a}) \\
&= B(\bar{\varepsilon}_{w,c} - \bar{\varepsilon}_{b,c}) + (1 - B)(\bar{\varepsilon}_{w,c} - \bar{\varepsilon}_{b,c}) \\
&= (B + 1 - B)(\bar{\varepsilon}_{w,c} - \bar{\varepsilon}_{b,c}) \\
&= \bar{\varepsilon}_{w,c} - \bar{\varepsilon}_{b,c}.
\end{aligned}
\tag{6.41}
$$

However, during tests that dynamically change one of these signals in relation to the other, such as the Valsalva maneuver, it is prudent to assess the necessity of modeling each region separately and together. The aim of the following analysis is to determine whether modeling of both regions is necessary with regard to this model and its purpose in predicting the response to the VM.

Using m_1 derived in the previous section, we can delineate between models containing the aortic only, carotid only, or both signals via equation (4.5). m_1 includes the estimated B parameter, where 6 of the 7 parameters from $\hat{\theta}$ can be estimated. Reduced model 2 (m_2) is the model containing the aortic baroreceptor signal only, that is, $B = 0$. After structured correlation analysis, 4 of the 7 parameters could be optimized, *i.e.*,

$$
\hat{\theta}_{m_2} = [\tau_{p,b}, \tau_{p,r}, \tau_s, H_s]^T,
\tag{6.42}
$$

where B was held constant at 0. Reduced model 3 (m_3) was obtained when $B = 1$, that is, only the carotid signal influences the output. The same parameter set estimated for m_2 was also an identifiable subset for m_3, that is $\hat{\theta}_{m_2} = \hat{\theta}_{m_3}$. All parameters removed from $\hat{\theta}$ were held at their nominal values. Table 6.3 tabulates the estimated parameters for each model and their values as determined via nonlinear least squares using the Levenberg-Marquardt algorithm [57].

The structured correlation analysis determined that there certain parameters we could not optimize in the reduced models. This is most likely due to the fact that removing model components can change the relationship between the remaining components. One such parameter is $H_{p,b}$, which was not estimable for m_2 or m_3. However, the nominal value ($H_{p,b} = 0.46$) is close to the optimized

value for m_0 and m_1 ($H_{p,b} = 0.44$). $H_{p,r}$ was not estimable for any of the reduced models, but the nominal value ($H_{p,r} = 0.54$) is close to the optimized value for m_0 ($H_{p,r} = 0.53$). This implies that the nominal values for $H_{p,b}$ and $H_{p,r}$ are close to the optimal values.

6.3.4   Model selection

We conduct the model selection protocol both quantitatively and qualitatively. The quantitative approach involves computing the Akaike Information Criterion with correction (AICc) and the Bayesian Information Criterion (BIC), assessing the model fit to the data. Qualitatively, we assess the behavior of the model predicted quantities, $T_{p,b}$ and T_s, as they evolve in time. A goal of this model is not only to fit the data but also to predict the neural tones in a physiologically relevant manner. Thus, we compare the reduced model neural signal trajectories to m_0.

6.3.4.1   Goodness of fit analysis

For the goodness of fit analysis, we computed AICc and BIC values for each of the models assuming the residuals are independent and identically distributed. Though there are methods to compute the covariance matrix to account for the nonconstant covariance structure of the residuals, they are very computationally expensive [103]. From Table 6.4, we observe that m_2 and m_3 have the lowest AICC and BIC values. Since they are highly dependent on the data set used, we computed the AICc and BIC values for other control subjects from Chapter 4 and saw that the values for m_2 and m_3 were similar, with m_2 the best fit in some cases and m_3 in others. Therefore, the AICc and BIC prefer m_2 and m_3. This is not surprising, however, since these criteria favor estimating fewer model parameters [137].

6.3.4.2   Qualitative assessment

Figure 6.6 shows the effect of using either m_2 (dashed curve) or m_3 (dash-dotted curve). The model fits to heart rate data (Figure 6.6a) are all very similar, which is to be expected since the model is calibrated to this representative data set. The least squares costs of the fits are of the same magnitude as m_0 and m_1 (Table 6.4). There is some variation in the steady-state region before phase I, but overall the traces have a similar morphology. Interestingly, m_2 is the only model that is able to fit phase III of the data (Figure 6.6a insert), suggesting from a qualitative standpoint that m_2 captures the most features of the heart rate data. Figure 6.6b displays the predicted $T_{p,b}$ trace for the models. m_1 is very similar to the full model, except for a slightly lower overshoot in phase IV. m_2 has a more oscillatory trajectory than the full model and m_1, decreasing late phase II and increasing phase IV more substantially. m_3 has less of an effect in phase II than the other models and agrees with m_0 in phase IV. Figure 6.6c shows the trajectories for T_s, exhibiting the greatest deviation from m_0. m_1 has a similar morphology to m_0 but increases sharply in late phase II and undershoots in phase IV. m_2

coincides with the full model through phase III and has a delayed return back to baseline in phase IV. m_3 also has a similar morphology as the others but has a maximum peak about half of m_0 and m_2.

Since traces for heart rate and $T_{p,b}$ for all four models are similar, we use T_s to compare the reduced models to the full model. In particular, we want to ensure the reduced model produces a similar amount of sympathetic stimulation. Using the infinity norm, we define the metric

$$\arg\min_i \|m_0 - m_i\|_\infty \quad i = 1, 2, 3, \tag{6.43}$$

which yields m_2 as the model of choice, as shown in Figure 6.6c. This result gives credence to the assertion that the aortic baroreceptors play a role in the prediction of heart rate in conjunction with the carotid sinus. Therefore, in regard to the sympathetic components, modeling the aortic arch baroreceptors only is sufficient.

In summary, we conclude that m_2 is the best model for the biological questions investigated here. The AICc and BIC values were relatively small, the model can fit the heart rate data in phase II when others cannot, and the sympathetic output has the closest resemblance to the original model.

6.4   Discussion

This study performs model reduction and selection using a global sensitivity analysis (GSA). Following the workflow in Figure 6.1, we have used a neural model predicting parasympathetic ($T_{p,b}$) and sympathetic (T_s) nervous outflow and heart rate (H) in response to the Valsalva maneuver as an example. We used Sobol' indices, conducting our analysis with respect to a scalar output (the Euclidean norm of the heart rate residual, $\|\mathbf{r}\|_2$) and a time-varying output (the vector $\mathbf{r}$). Computation for the scalar Sobol indices [110] was with respect to $\|\mathbf{r}\|_2$ and the time-varying pointwise [3], generalized [4], and limited-memory Sobol indices to $\mathbf{r}$. We introduced limited-memory Sobol' indictes using a moving integration window of width Δ motivated by the transient process analyzed with the neural model. The scalar Sobol' indices determined a ranking of parameter influence on the model output averaged over the entire time interval. Furthermore, we were able to categorize parameters based on their influence on the model output into three groups: most influential, moderately influential, and noninfluential. The limited-memory Sobol' indices informed a model reduction protocol that generated three reduced models, m_1, m_2, and m_3, which were included in the model selection procedure. We analyzed the performance of these models both qualitatively, comparing the model predicted signals to the original model m_0, and quantitatively, calculating the Akaike Information Criterion with correction (AICc) and the Bayesian Information Criterion (BIC) for each model. Statistically, either m_2 or m_3 are the better models, while qualitative comparison to the predicted signals $T_{p,b}$ and T_s show that m_2 is the best performing reduced model.

6.4.1 Local versus global sensitivity analysis

This study has focused on the use of a GSA to analyze the sensitivity of the model output to the input parameters. However, these methods are computationally expensive, whereas a local sensitivity analysis (LSA) method may suffice. In Chapter 4, we performed a LSA on the neural model presented here. LSA is useful in its relative ease in computation, especially using approximations of derivatives with forward or central differences [57], and in its ability to calculate time-varying sensitivities. In steady-state with nominal parameters close to their optimal value, LSA is very useful in ranking parameter influence as shown in our previous work [28, 71, 74, 87]. For comparison, the parameter ranking generated by calculating the sensitivity matrix with respect to $||\mathbf{r}||_2$ and evaluating the derivatives at the nominal values is very similar to the ranking generated with Sobol' indices in Figure 6.2. This is surprising since the GSA explores the entire parameter space Ω_p. Others have also found agreement in the calculation of the local and global parameter sensitivities [67]. However, there exist a number of issues complicating the interpretation of a time-varying parameter sensitivities calculated from LSA: (i) choosing a specific point in the parameter space to evaluate the model, (ii) performing LSA one parameter at a time without varying all parameters or a subset of parameters simultaneously, and (iii) interpreting traces with negative sensitivity values. Some of these issues can be circumvented, such as (i) by evaluating the LSA at various points within the parameter space and (iii) by taking the absolute value of the signals. Others are inherently challenging to overcome, such as issue (ii), but a benefit of our GSA method of choice is the ability to vary many parameters simultaneously.

6.4.2 Time-dependent Sobol' indices

In this study, we have chosen to use Sobol' indices for our GSA. Though there are many other methods that explore the parameter space, such as Morris screening [86] and derivative-based GSA methods [120], we use this approach due to its broad applications. Furthermore, we developed limited-memory Sobol' indices for the analysis of this model by including a moving window of width Δ, since the VM induces fast, transient changes in the steady-state behavior. Moving windows have been used in signal processing for decades and relatively recently in sensitivity analysis for graphical analysis of parameter sensitivities throughout the space [49, 123]. However, these methods have difficulty capturing the effects between parameters. The limited-memory Sobol' indices mitigate this issue by incorporating both parameter interactions and the history of the variance in the model output. Furthermore, these techniques can be used for virtually any modeling effort for which the analysis of parameter sensitivity over time. One such study is that of Calvo *et al.* [22], which calculated Sobol' indices at specific times for parameters of a cardiovascular model studying head-up tilt at rest and during the tilt. This study would have benefited from using our time-varying analysis to determine how parameter influence changes over time. Another is a study using insulin

signaling model by Sumner *et al.* [124], which claims to analyze time-dependent sensitivities with Sobol' indices. However, QoI for this model is the state involving glycogen synthase kinase evaluated when $t = 60$, which is a scalar value. For the sensitivity analysis protocol to be time-dependent, we propose using limited-memory Sobol' indices to quantify parameter influence as it changes over the entire time span. The clear advantage of using limited-memory Sobol indices is its inherent adaptive nature as time evolves, particularly for processes with negative feedback control mechanisms.

6.4.3 Parameter space

This analysis is highly dependent on the choice of the parameter space. Parameter sampling distributions are typically uniform if little is known about the parameter [3]. Upper and lower bounds for uniform distributions may be determined from literature, physiological intuition, or empirical studies. If there is no information about the bounds of the parameter value, it is standard to vary the nominal parameter value by ±20%. Table 6.1 lists the upper and lower bounds for the parameters analyzed. In this study, we perform the GSA on the logarithm of the parameter since the parameters vary widely in magnitude, which is similar to other approaches done previously [87, 92]. Therefore, for parameters without a physiological range, such as the parameters calculated from data, we choose upper and lower bounds by varying the nominal values by ±50%.

6.4.4 Model reduction

Mathematical representations of biological systems tend to be highly overparameterized with many states. Due to the overall complexity of such models, understanding the biological implications of the results and parameter interactions can be difficult. Therefore, model reduction can simplify these interactions and still retain its inherent predictive power. Many model reduction techniques exist from engineering and control theory [13], aiming to reduce large numbers of state variables with many nonlinearities by attempting to mitigate the same inherent problem we address here: to what extent do the input parameters affect the output. Our method of using GSA to inform an analytical model reduction uses this idea to make appropriate choices for the exclusion of certain model components, as opposed to other model reductions methods, such as balanced truncation [117], that solely approximate the input-output relationship without considering the other predicted model quantities. To our knowledge, there are no previous studies who inform a model reduction based on GSA methods for physiological models. Though we acknowledge that the Sobol' indices may be impractical for very large differential equation systems with hundreds of state variables and parameters, such as pharmacokinetics models, we suggest using a different GSA method such as Morris screening [86], to determine influential versus noninfluential model parameters. Analyzing the noninfluential model components can help determine which components may be removed and which can remain constant. In the model reduction formulation proposed by Snowden *et al.*

[117], we propose our GSA-informed model reduction methodology as an alternative approach to the balanced truncation method using Morris screening.

6.4.5 Model selection

To our knowledge, no previous studies have performed a model selection protocol for cardiovascular or neurological models in response to the Valsalva maneuver. In this study, we employ AICc and BIC scores to compare the model fits to data. However, we must also consider the effect of reducing the full model on the other predicted quantities for which data is difficult to acquire. Therefore, we combine quantitative and qualitative approaches to select whether the delineation between the baroreceptors of the carotid sinus and the aortic arch is necessary to model, and, if not, which pathway should be modeled. Along with Chapter 4, a recent study supports modeling both regions [61]. We perform our analysis by considering the parameter B, which dictates the convex combination of the aortic and carotid signals. Let $\mathcal{M} = \{m_0, m_1, m_2, m_3\}$ be the set of models where m_0 is the original model, m_1 optimizes B, m_2 sets $B = 0$ considering the aortic contribution only, and m_3 sets $B = 1$ considering the carotid contribution only. The statistical analysis shows m_3 fit the data best with the lowest AICc and BIC scores compared to the other models. However, the AICc and BIC values for m_2 are very close to m_3. Since these indices are data-dependent, it is important to assess other data sets to see if this value changes, from which we determined m_2 or m_3 suffice. This implies that it is necessary to only model either the carotid or the aortic baroreceptors to predict heart rate but not both. For the predicted states, $T_{p,b}$ and T_s, we used the infinity norm to compare model performance to the T_s trace m_0, since the traces for $T_{p,b}$ are similar for all models. Ultimately, we conclude that m_2 is the best model to fit the data and to predict the modeled quantities. Though our previous work supports the inclusion of both the carotid and aortic bodies, the added model complexity may not be as essential for certain problems. Previous studies have modeled stimulation of only the carotid region with useful results [64, 69]; however, our model selection protocol supports eliminating the carotid pathway in favor of the simpler aortic-only model.

6.4.6 Limitations

We would like to emphasize certain limitations of this analysis. The global sensitivity analysis method of choice is highly dependent on the model formulation and the quantity of interest (QoI). Choosing a computationally expensive GSA may not be feasible for models with long evaluation times, and the GSA results will differ based on the choice of QoI. Since model reduction was the focus of this study, we chose to take the analytical reduction approach, though we could have fixed τ_b at a constant value. Furthermore, analytical model reduction may also be impractical for very large systems with many parameters. In this case, setting the parameters to their nominal values may be more reasonable. Lastly, the results of the statistical analysis using AICc and BIC scores is highly

dependent on the available data. If a very different heart data set had been used, there is a possibility that the outcome of the model selection protocol could have been different. However, we conducted this analysis on three representative control subjects and achieved similar results as those produced in Section 6.3.

6.5   Conclusions

In this study, we have performed a model reduction and selection process informed by global sensitivity analysis on a neurological model predicting heart rate and autonomic nervous function in response to the Valsalva maneuver. This analysis employed Sobol' indices, which apportion the variance in the model input to the variance of the output. The main mathematical contribution of this study is the development of limited-memory Sobol' indices for time-dependent processes, incorporating a moving window, which takes into the account the transient nature of the Valsalva maneuver. Moreover, we analyzed the performance of the Sobol' indices, ranking parameter influence and determining the least influential parameters. This lead to an analytical model reduction, where we compared the incorporation of carotid, aortic, or both baroreceptor regions. Our selection procedure determined that modeling the aortic baroreceptors only is sufficient to achieve the appropriate dynamics of the Valsalva maneuver.

CHAPTER

7

COUPLED CARDIOVASUCLAR-NEUROLOGICAL CONTROL MODEL

The primary focus of this dissertation up to this point has been the regulation of heart rate in response to changes in blood pressure accounting for the baroreflex and respiratory sinus arrhythmia. The mathematical model in Chapter 4 provides an open-loop formulation that we used to analyze data from both healthy subjects and patients with autonomic dysfunction. Physiologically, the baroreflex operates via a negative feedback responding to changes in respiration, blood volume, and blood pressure modulating heart rate, vascular resistance and compliance, and cardiac contractility, which in turn impact blood pressure and volume. The open-loop model is able to predict heart rate and indirectly account for changes in peripheral resistance and contractility as it uses the blood pressure as an input. However, it does not model this negative feedback loop, since it cannot influence the blood pressure. To remedy this limitation, we develop a closed-loop cardiovascular model which we then couple to the open-loop model, simultaneously predicting both heart rate and blood pressure.

This chapter develops and parameterizes an 8-compartment lumped parameter cardiovascular model, which is coupled to the neurological control model modulating heart rate developed and analyzed in Chapters 4-6. The sympathetic branch of the neurological model is expanded to include control of peripheral resistance and compliance and cardiac contractility.

7.1 Introduction

Precision medicine provides a patient-specific approach addressing the etiology of disease, treatment, and prevention by taking into account individual patient health. This is in contrast to more universal protocols which focus on developing treatment regimes that target the average person. Though providing patient-specific care is a relatively common practice clinically, there are various physiological quantities that are difficult to measure without costly and invasive medical procedures. In the cardiovascular system, arterial blood pressure and heart rate can be measured noninvasively, while atrial pressure and venous volume can only be measured invasively with right heart catheterization [35]. To reduce patient discomfort and expense, mathematical modeling can be used in precision medicine to predict hemodynamic responses that are otherwise unmeasurable without these invasive techniques.

Mathematical modeling of the cardiovascular system and its control has been extensively studied using a range of approaches from highly complex systems of ordinary differential equations with hundreds of state variables [38] to more simplified lumped parameter compartment models focusing on either the systemic or pulmonary circulations [74, 100] or the entire cardiovascular system [28, 64, 69, 88]. Localized studies have been conducted analyzing the fluid dynamics of blood in the vasculature, typically involving one- or three-dimensional partial differential equation models [103, 112]. However, in this study, we use ordinary differential equation (ODE) models to model systemic effects. Cardiovascular ODE models are typically formulated using an electrical circuit analog where current is analogous to flow, voltage to pressure, and charge to volume. Most models rely on RCL-circuits where R denotes resistance, C denotes compliance (analogous to capacitance), and L denotes inertance (analogous to inductance) (as detailed in Table 2.1). While ODE models are easy to solve and couple with control models, a disadvantage is that they typically are overparameterized.

Cardiovascular control models of the baroreceptor reflex (*baroreflex*), the Bainbridge reflex, and respiratory sinus arrhythmia (RSA) accompany cardiovascular compartment models. The baroreflex has been modeled extensively, especially in response to respiratory and postural challenges [64, 69, 89, 133, 136]. Though these models offer valuable insight into cardiovascular dynamics, they are not patient-specific. In Chapter 4, we analyzed the baroreflex response of heart rate to the Valsalva maneuver (VM), a clinical test inducing an increase in intrathoracic pressure to elicit parasympathetic and sympathetic nervous responses. However, due to the nature of the open-loop model with systolic blood pressure and intrathoracic pressure data as inputs and heart rate as an output, the sympathetic effects on vasomotor control and cardiac contractility were ignored. These effects include an increase in resistance and cardiac contractility and a decrease in compliance [16]. The control of these quantities requires coupling to a closed-loop cardiovascular model, which can elicit the system-wide effects of fluctuations in cardiovascular dynamics. Therefore, mathematical modeling of both heart rate and blood pressure simultaneously can provide critical insight into

potential individual responses to treatment protocols.

In this study, the simplified neurological model from Chapter 6 has been integrated with a closed-loop cardiovascular model, predicting pressure, volume, and heart rate. This integrative modeling approach has been used previously to study the response to posture changes [88] and the VM [64, 69]. We also include the sympathetic control of the vascular in a similar manner as [2, 69, 101]. A major difference of this work from these theoretical models is the careful attention paid to the calculation of nominal parameter to ensure the model output is patient-specific. With this model, we analyze one control response and three types of pathological responses to the VM designated as the M, N, and V responses as posed by Palamarchuk *et al.* [94] (shown in Figure 3.2).

7.2   Methods and materials

This section develops an 8-compartment lumped parameter cardiovascular model predicting blood pressure and heart rate in response to the Valsalva maneuver (VM). The baroreflex response has been implemented to account for modulation of heart rate, resistance, compliance, and cardiac contractility. This model operates via a negative feedback loop, working to maintain homeostasis. Due to the large number of model components, this section is divided into subsections describing the cardiovascular model and the neurological model components.

Table 7.1 Subscripts for the cardiovascular model.

	Subscript	Description	Notes
Pressures	lh	Left heart	Left ventricle
& Volumes	ao	Aorta	Thoracic aorta and large arteries inside the thorax
	sa	Systemic arteries	Distal aorta, large and small arteries outside the thorax, arterioles, and capillaries
	sv	Systemic veins	Venules, small and large veins outside the thorax
	vc	Vena cava	Superior and inferior vena cava and right atrium
	rh	Right heart	Right ventricle
	pua	Pulmonary arteries	Large and small pulmonary arteries and pulmonary capillaries
	puv	Pulmonary veins	Large and small pulmonary veins and left atrium
Resistances	mv	Mitral valve	
& Flows	av	Aortic valve	
	ao	Aorta	Flow from inside the thorax to outside
	sa	Systemic arterioles	
	sv	Systemic veins	Flow from outside the thorax to inside
	tv	Tricuspid valve	
	pv	Pulmonary valve	
	pa	Pulmonary arterioles	
	th	Thoracic arterioles	
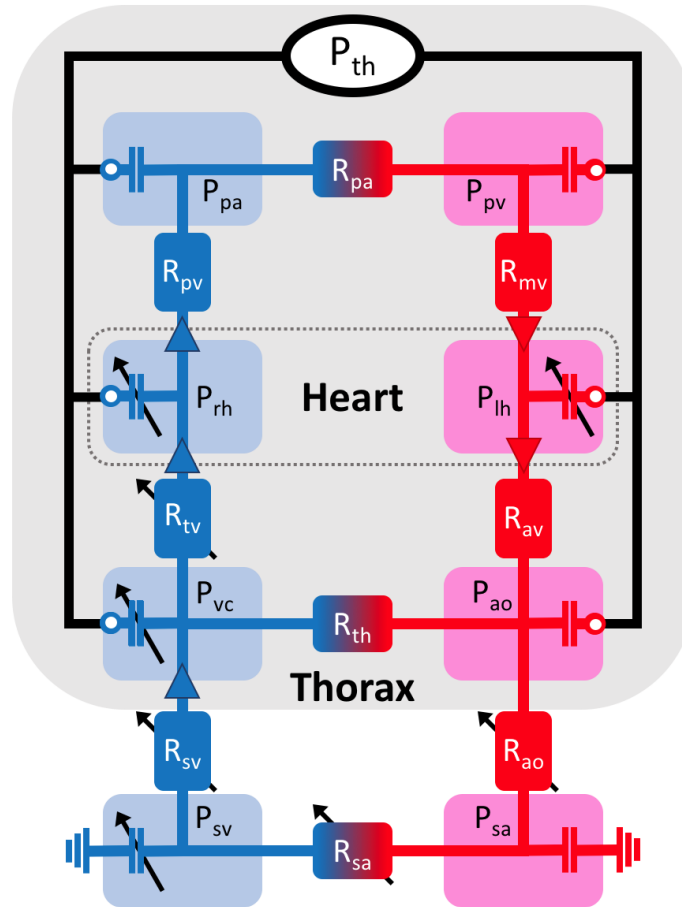
Figure 7.1 Schematic of the 8-compartment cardiovascular model formulated using an analog to an electrical circuit predicting pressure (P, mmHg) and volume (V, mL). All subscripts are summarized in Table 7.1. Six compartments are inside the thorax, the pulmonary arteries (pa) and veins (pv), left (lh) and right (rh) heart, aorta (ao), and vena cava (vc), which experience an external compressive force P_{th} as the thorax inflates. The two compartments outside the thorax, the systemic arteries (sa) and veins (sv), are connected to ground, that is, an exterior pressure of zero. Nonlinear resistances (R) and compliances are denoted with arrows. Heart and venous valves are given as triangles, denoting their function as diodes.

7.2.1 Cardiovascular model development

Figure 7.1 displays a schematic of the cardiovascular model, which is formulated using an RC electrical circuit analogy, where pressure (P, mmHg) is analogous to voltage, flow (F, mL sec^{-1}) to current, volume (V, mL) to charge, and compliance (C mL mmHg^{-1}) to capacitance. Resistance (R, mmHg sec mL^{-1}) is the same in both formulations. Table 2.1 gives a summary of the relationship between the cardiovascular system and analogous electrical circuit. Each compartment consists of a pressure and a volume with a capacitor in parallel (compliance). Since the volume V_i inside a compartment i exacts a pressure P_i on the vessel wall, the pressure and volume are related as

$$P_i - P_{ext} = f_i(V_i - V_{i,u}) = f_i(V_{i,str}), \qquad (7.1)$$

where P_{ext} is an external pressure exerting a force on the compartment (at rest $P_{ext} = 0$), $V_{i,u}$ is the unstressed volume (*i.e.*, the volume at which $P_i = 0$), $V_{i,str}$ is the stressed volume, and $f_i : \mathbb{R} \to \mathbb{R}$ is a one-to-one function relating $V_{i,str}$ to P_i. Table 7.1 summarizes the subscripts used in the cardiovascular model. The flow F from one compartment to the next is proportional to the pressure gradient between compartments given by Ohm's Law as

$$R_j = \frac{\Delta P}{F_j} = \frac{P_{in} - P_{out}}{F_j}, \qquad (7.2)$$

where R_j is the resistance of the vessels and F_j is the flow across resistance R_j. Since the cardiovascular model forms a closed system, the total volume (V_{tot}) is conserved, *i.e.*,

$$V_{tot} = V_{lh} + V_{ao} + V_{sa} + V_{sv} + V_{vc} + V_{rh} + V_{pa} + V_{pv} \qquad (7.3)$$

and from Kirchoff's Law

$$\frac{dV_i}{dt} = \sum F_{in} - \sum F_{out}. \qquad (7.4)$$

For an average human of ~70 kg, $V_{tot} = 5$ L [16].

The atrioventricular and semilunar valves operate as diodes, restricting blood flow when the valve is closed and ensuring there is no "negative" or reverse flow. There are also valves in the veins of the lower extremities preventing backflow [16]. The flow across a valve either in the heart or in the systemic veins is given by

$$F_v = \begin{cases} \dfrac{P_{in} - P_{out}}{R_v} & \text{if } P_{in} > P_{out} \\[2mm] 0 & \text{otherwise,} \end{cases} \qquad (7.5)$$

where the subscript $v = sv, mv, av, tv,$ or pv for systemic veins, mitral valve, aortic valve, tricuspid valve, and pulmonary valve, respectively.

Lastly, we assume that the resistances in the aorta, systemic veins, and vena cava (via the tricuspid valve) are volume-dependent. The aorta is highly elastic, able to accommodate the large fluctuations in arterial volume pumped by the heart. On the other hand, the systemic veins and vena cava operate at low pressures. These highly compliant vessels deform as volume decreases, increasing resistance. If we assume these vessels are rigid tubes (which they are not), we take advantage of Poiseuille's law

$$R = \frac{8\eta l}{\pi r^4},$$ (7.6)

where η is the viscosity of blood, l is the length of the vessel, and r is the radius. Thus, the resistance is proportional to the radius, *i.e.*,

$$R \propto \frac{1}{r^4} \propto \frac{1}{V^2}.$$ (7.7)

Since R is proportional to the square of the volume, the volume-dependent resistances are

$$R_i = \frac{\kappa_i}{V_i^2} + R_{i,0},$$ (7.8)

where $i = ao, sv$ and tv, κ_i is a scaling parameter, and $R_{i,0}$ is an offset parameter. It should be noted that all vessel resistances are volume-dependent; for simplicity, we assume that the resistances of the pulmonary circulation are constant.

The schematic in Figure 7.1 results in a system of 8 ordinary differential equations (ODEs). Beginning with the left heart, we have

$$\frac{dV_{lh}}{dt} = F_{mv} - F_{av},$$ (7.9)

$$\frac{dV_{ao}}{dt} = F_{av} - F_{ao} - F_{th},$$ (7.10)

$$\frac{dV_{sa}}{dt} = F_{ao} - F_{sa},$$ (7.11)

$$\frac{dV_{sv}}{dt} = F_{sa} - F_{sv},$$ (7.12)

$$\frac{dV_{vc}}{dt} = F_{sv} - F_{tv} + F_{th},$$ (7.13)

$$\frac{dV_{rh}}{dt} = F_{tv} - F_{pv},$$ (7.14)

$$\frac{dV_{pa}}{dt} = F_{pv} - F_{pa}, \text{ and}$$ (7.15)

$$\frac{dV_{pv}}{dt} = F_{pa} - F_{mv}.$$ (7.16)

The 9 flows in this model beginning with the mitral valve are

$$F_{mv} = \begin{cases} \dfrac{P_{pv} - P_{lh}}{R_{mv}} & \text{if } P_{pv} > P_{lh} \\ 0 & \text{otherwise,} \end{cases} \tag{7.17}$$

$$F_{av} = \begin{cases} \dfrac{P_{lh} - P_{ao}}{R_{av}} & \text{if } P_{lh} > P_{ao} \\ 0 & \text{otherwise,} \end{cases} \tag{7.18}$$

$$F_{ao} = \dfrac{P_{ao} - P_{sa}}{R_{ao}}, \tag{7.19}$$

$$F_{sa} = \dfrac{P_{sa} - P_{sv}}{R_{sv}}, \tag{7.20}$$

$$F_{sv} = \dfrac{P_{sv} - P_{vc}}{R_{vc}}, \tag{7.21}$$

$$F_{tv} = \begin{cases} \dfrac{P_{vc} - P_{rh}}{R_{tv}} & \text{if } P_{vc} > P_{rh} \\ 0 & \text{otherwise,} \end{cases} \tag{7.22}$$

$$F_{pv} = \begin{cases} \dfrac{P_{rh} - P_{pa}}{R_{pv}} & \text{if } P_{rh} > P_{pa} \\ 0 & \text{otherwise,} \end{cases} \tag{7.23}$$

$$F_{pa} = \dfrac{P_{pa} - P_{pv}}{R_{pa}}, \text{ and} \tag{7.24}$$

$$F_{th} = \dfrac{P_{ao} - P_{vc}}{R_{th}}. \tag{7.25}$$

The 3 nonlinear, time-varying resistances are

$$R_{ao} = \dfrac{\kappa_{ao}}{V_{ao}^2} + R_{ao,0}, \tag{7.26}$$

$$R_{sv} = \dfrac{\kappa_{sv}}{V_{sv}^2} + R_{sv,0}, \text{ and} \tag{7.27}$$

$$R_{tv} = \dfrac{\kappa_{tv}}{V_{vc}^2} + R_{tv,0}. \tag{7.28}$$

7.2.1.1 Thoracic pressure

Since intrathoracic pressure data was not collected for the autonomic dysfunction (AD) patients exhibiting M, N, and V behaviors, we chose to artificially induce the maneuver in all four subjects.
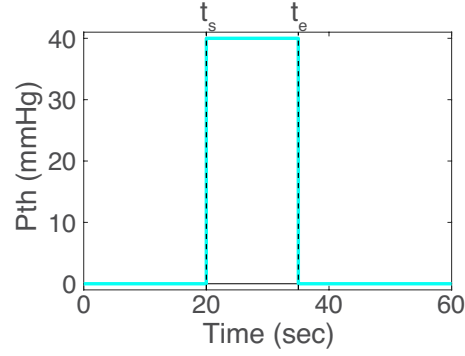
Figure 7.2 Plot of the thoracic pressure (P_{th}, blue) with the start (t_s) and end (t_e) times for the Valsalva maneuver indicated by the vertical dashed lines.

We define the thoracic pressure as the square function

$$P_{th} = \begin{cases} 40 & \text{if } t_s \leq t \leq t_e \\ 0 & \text{otherwise,} \end{cases} \tag{7.29}$$

where t_s and t_e are the start and end times of the VM, respectively, determined from the data as shown in Figure 7.2. It should be noted that respiratory input is not superimposed on P_{th} in this study, and therefore, $P_{th} = 0$ at rest. This limitation will be included in future studies.

7.2.1.2   Pressure-volume relations

To close the system of equations, we relate pressure P and V via linear and nonlinear relationships. Linear pressure-volume relationships are of the form

$$P_i - P_{ext} = \frac{V_{i,str}}{C_i}, \tag{7.30}$$

where C_i is the constant compliance of the compartment. For this model, $P_{ext} = P_{th}$ given in Section 7.2.1.1. The linear P-V relations in terms of the stressed volume are given by

$$P_{ao} = \frac{V_{ao,str}}{C_{ao}} + P_{th}, \tag{7.31}$$

$$P_{sa} = \frac{V_{sa,str}}{C_{sa}}, \tag{7.32}$$

$$P_{pa} = \frac{V_{pa,str}}{C_{pa}} + P_{th}, \quad \text{and} \tag{7.33}$$

$$P_{pv} = \frac{V_{pv,str}}{C_{pv}} + P_{th}. \tag{7.34}$$

131

The compartments of the systemic veins, vena cava, and heart have nonlinear P-V relations discussed in more detail below.

Due to the high compliance of the systemic veins and the large fluctuations in compliance within physiological pressure ranges, we model these compartments with nonlinear relationships. Following [42, 101], we assume that the vessel compliance decreases linearly as total vessel volume increases, that is

$$\frac{\mathrm{d}V_{sv}}{\mathrm{d}P_{sv}} = C_{sv} = \gamma_{sv}(V_{sv,M} - V_{sv}),$$
(7.35)

where $V_{i,M}$ is the maximal volume of the compartment and γ_{sv} is a constant. To formulate equation (7.35) in terms of stressed volume, consider

$$
\begin{aligned}
V_{sv,M} - V_{sv} &= V_{sv,M} - V_{sv,u} + V_{sv,u} - V_{sv} \\
&= (V_{sv,M} - V_{sv,u}) - (V_{sv} - V_{sv,u}) \\
&= V_{sv,M,str} - V_{sv,str},
\end{aligned}
$$
(7.36)

where $V_{sv,u}$ is the unstressed volume of the compartment and $V_{sv,M,str}$ is the maximal stressed volume. Inserting equation (7.36) into equation (7.35), we obtain

$$\frac{\mathrm{d}V_{sv,str}}{\mathrm{d}P_{sv}} = \gamma_{sv}(V_{sv,M,str} - V_{sv,str}).$$
(7.37)

We integrate (7.37) using separation of variables, giving

$$\frac{1}{\gamma_{sv}} \int \frac{1}{V_{sv,M,str} - V_{sv,str}} \, \mathrm{d}V_{sv,str} = \int \mathrm{d}P_{sv}$$

$$\Rightarrow \frac{1}{\gamma_{sv}}\left(-\ln(V_{sv,M,str} - V_{sv,str}) + \ln(V_{sv,M,str} - \tilde{V})\right) = P_{sv} - \tilde{P}$$

$$\Rightarrow \frac{1}{\gamma_{sv}} \ln\left(\frac{V_{sv,M,str} - \tilde{V}}{V_{sv,M,str} - V_{sv,str}}\right) = P_{sv} - \tilde{P},$$
(7.38)

where $\tilde{V}$ and $\tilde{P}$ are integration constants. When the volume reaches the unstressed volume, the pressure is zero, that is, when $V_{sv,str} = 0$, $P_{sv} = 0$. Therefore,

$$\frac{1}{\gamma_{sv}} \ln\left(\frac{V_{sv,M,str} - \tilde{V}}{V_{sv,M,str}}\right) = -\tilde{P}.$$
(7.39)

Substituting (7.39) into (7.38), we obtain the pressure-volume relation for the systemic veins in terms of the stressed volume given by

$$P_{sv} = \frac{1}{\gamma_{sv}} \ln\left(\frac{V_{sv,M,str}}{V_{sv,M,str} - V_{sv,str}}\right).$$
(7.40)

Under resting conditions, the vena cava operates similarly to the systemic veins. Hence, the P-V relation for the vena cava is similar to equation (7.40) when $V_{vc,str} \geq 0$. However, during the Valsalva maneuver, increased intrathoracic pressure can cause vessel collapse as the volume of the compartment drops below the unstressed volume, that is, when $V_{vc,str} < 0$. In a similar manner as Pstras *et al.* [101], we assume that the vena cava attains its maximal compliance ($C_{vc,M}$) when $V_{vc,str} = 0$. For most of the volume range below the unstressed volume, we assume the vena cava maintains $C_{vc,M}$. When the volume reaches its minimal volume ($V_{vc,m}$), the volume drops steeply to a near-zero value. We model the compliance of the vena cava under negative stressed pressures with an increasing sigmoidal relationship as

$$\frac{\mathrm{d}V_{vc,str}}{\mathrm{d}P_{vc}} = C_{vc} = \frac{C_{vc,M}}{1 + e^{-(V_{vc,str}-s_{vc})}}, \tag{7.41}$$

where s_{vc} is the half-saturation value. For simplicity, the steepness of the sigmoid was set to 1. Using separation of variables, we obtain

$$\int 1 + e^{-(V_{vc,str}-s_{vc})} \, \mathrm{d}V_{vc,str} = \int C_{vc,M} \, \mathrm{d}P_{vc}$$
$$\Rightarrow (V_{vc,str} - \tilde{V}) - \left(e^{-(V_{vc,str}-s_{vc})} - e^{-(\tilde{V}-s_{vc})}\right) = C_{vc,M}(P_{vc} - \tilde{P}), \tag{7.42}$$

where $\tilde{P}$ and $\tilde{V}$ are integration constants. Using the condition that $P_{vc} = 0$ when $V_{vc,str} = 0$, we obtain

$$\tilde{P} = \frac{1}{C_{vc,M}}\left(\tilde{V} + \left(e^{s_{vc}} - e^{-(\tilde{V}-s_{vc})}\right)\right). \tag{7.43}$$

Substituting equation (7.43) into (7.42), we obtain

$$P_{vc} = \frac{1}{C_{vc,M}}\left(V_{vc,str} + e^{s_{vc}}\left(1 - e^{-V_{vc,str}}\right)\right), \quad V_{vc,str} < 0. \tag{7.44}$$

Therefore, since the vena cava compartment is inside the thorax, the pressure volume relation for the vena cava is

$$P_{vc} = \begin{cases} \dfrac{1}{\gamma_{vc}} \ln\left(\dfrac{V_{vc,M,str}}{V_{vc,M,str} - V_{vc,str}}\right) + P_{th} & \text{if } V_{vc,str} \geq 0 \\[4mm] \dfrac{1}{C_{vc,M}}\left(V_{vc,str} + e^{s_{vc}}\left(1 - e^{-V_{vc,str}}\right)\right) + P_{th} & \text{if } V_{vc,str} < 0. \end{cases} \tag{7.45}$$

7.2.1.3 Time-varying elastance model

To model the beating heart, we use an asymmetric elastance function similar to previous studies [28, 45, 74]. As noted in Table 2.1, elastance is the inverse of compliance, that is, $E_i = 1/C_i$. Using
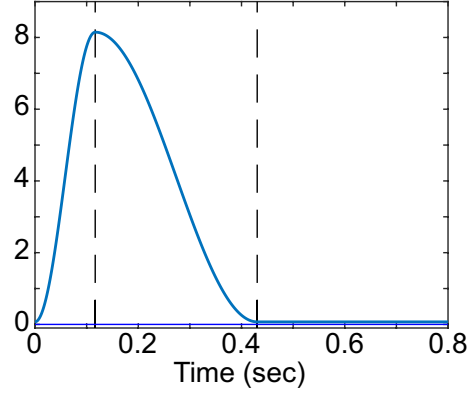
Figure 7.3 Plot of nonlinear elastance function defined in equation (7.47). Vertical lines indicate the times for end-systole, T_S, and end-diastole, T_R.

this terminology, we model the pressure-volume relation of the left and right heart as

$$P_i - P_{ext} = E_i V_{i,str}, \qquad (7.46)$$

for $i = lh$ and rh, where the elastance E_i for a heart with time-varying heart period T is given as

$$E_i = \begin{cases} E_{i,m} + \dfrac{E_{i,M} - E_{i,m}}{2}\left(1 - \cos\left(\dfrac{\pi t}{T_M}\right)\right) & \text{if } 0 \le t \le k_{T_M} T \\[2ex] E_{i,m} + \dfrac{E_{i,M} - E_{i,m}}{2}\left(1 - \cos\left(\dfrac{\pi(t - T_M)}{T_R - T_M}\right)\right) & \text{if } k_{T_M} T < t \le k_{T_R} T \\[2ex] E_{i,m} & \text{otherwise,} \end{cases} \qquad (7.47)$$

where $E_{i,M}$ and $E_{i,m}$ are the maximal and minimal elastances, respectively. $k_{T_M} = T_M/\bar{H}$ and $k_{T_R} = T_R/\bar{H}$, where $\bar{H}$ is the baseline heart rate and T_M and T_R are the times for the maximal systolic elastance and end of isovolumetric relaxation, respectively. Figure 7.3 shows the elastance function for one heart period.

7.2.1.4 Summary

In summary, the closed-loop cardiovascular model can be formulated as a system of ordinary differential equations of the form

$$\frac{d\mathbf{x}_c}{dt} = f_c(t, \mathbf{x}_c; \theta_c), \quad \mathbf{x}_c(0) = \mathbf{x}_0 \qquad (7.48)$$

$$y_c = g_c(\mathbf{x}_c; \theta_c), \qquad (7.49)$$

where $\mathbf{x}_c \in \mathbb{R}^8$ denotes the vector of states for the cardiovascular model, f_c denotes the right hand side of the ODE system, $\theta_c \in \mathbb{R}^{28}$ is a vector of parameters, and g_c relates the states to the observable y_c. The states are formulated as stressed volumes and from here on we will suppress the str subscript. The state and parameter vectors are

$$\mathbf{x}_c = [V_{lh}, V_{ao}, V_{sa}, V_{sv}, V_{vc}, V_{rh}, V_{pa}, V_{pv}]^T \text{ and} \tag{7.50}$$

$$\theta_c = [E_{lh,M}, E_{lh,m}, E_{rh,M}, E_{rh,m}, C_{ao}, C_{sa}, C_{pa}, C_{pv}, C_{vc,M} \ldots$$

$$\ldots R_{mv}, R_{av}, R_{sa}, R_{pv}, R_{pa}, R_{th}, R_{ao,0}, \kappa_{ao}, R_{sv,0}, \kappa_{sv}, R_{tv,0}, \kappa_{tv} \ldots$$

$$\ldots \gamma_{sv}, V_{sv,M}, \gamma_{vc}, V_{vc,M}, s_{vc}, k_{T_M}, k_{T_R}]^T, \tag{7.51}$$

respectively. The observable y_c of the cardiovascular model is the prediction of systemic arterial blood pressure, P_{sa}.

7.2.1.5 Initial conditions

The initial conditions of the cardiovascular model are calculated such that the model begins at end-diastole to coincide with the initialization of the elastance function in equation (7.47). Hence, V_{lv} and V_{rv} are maximal. Since the equations are formulated in terms of stressed volumes, Beneken and DeWit [11] determined that the stressed volumes for the arterial and venous components were ~30% and ~10%, respectively, of the total volume for that compartment. Table 7.2 tabulates the volume distribution for the cardiovascular model, assuming the subject has a total blood volume $V_{tot} = 5000$ mL [16]. Therefore, the initial conditions for the stressed volumes of each compartment are

$$V_{i,0} = d_i V_{tot}, \tag{7.52}$$

where d_i is a percentage calculated by multiplying across the rows in Table 7.2.

Table 7.2 Stressed volume distribution percentages at end-diastole.

Compartment	V_{tot} % [16]	V_{str} % [11]	d_i
V_{lh}	2.5		0.025
V_{ao}	5	30	0.015
V_{sa}	8	30	0.024
V_{sv}	65	10	0.065
V_{vc}	5	10	0.005
V_{rh}	2.5		0.025
V_{pa}	5	30	0.015
V_{pv}	5	10	0.005

Table 7.3 Calculations for parameters associated with the pressure-volume relations for the systemic veins and vena cava.

Systemic Veins		Vena Cava	
Parameter	**Calculation**	**Parameter**	**Calculation**
$V_{sv,m}$	$1.01\ V_{sv,0}$	$V_{vc,m}$	$1.01\ V_{vc,0}$
γ_{sv}	$\dfrac{C_{sv,n}}{V_{sv,M} - V_{sv,0}}$	γ_{vc}	$\dfrac{C_{vc,n}}{V_{vc,M} - V_{vc,0}}$
		$C_{vc,M}$	$\gamma_{vc}\ V_{v,M}$
		$V_{vc,m}$	$0.02(0.9)(0.05)\ V_{tot}$
		s_{vc}	$V_{vc,m} + \ln\left(\dfrac{C_{vc,M}}{C_{vc,0}} - 1\right)$

$C_{sv,n}$ and $C_{vc,n}$ are taken from literature [101].

Table 7.4 Pressure scaling factors for baseline mean, systolic, and diastolic pressure values for each compartment, where applicable.

Reference						Compartment			
Pressure		P_{lh}	P_{ao}	P_{sa}	P_{sv}	P_{vc}	P_{rh}	P_{pa}	P_{pv}
Mean	95		$k_{ao}=\dfrac{98}{95}$	$k_{sa}=1$	$k_{sv}=\dfrac{6}{95}$	$k_{vc}=\dfrac{4}{95}$		$k_{pa}=\dfrac{15}{95}$	$k_{pv}=\dfrac{6}{95}$
Systolic	120	$k_{lh,s}=\dfrac{125}{120}$	$k_{ao,s}=\dfrac{125}{120}$	$k_{sa,s}=1$			$k_{rh,s}=\dfrac{30}{120}$	$k_{pa,s}=\dfrac{25}{120}$	
Diastolic	80	$k_{lh,d}=\dfrac{10}{80}$	$k_{ao,d}=\dfrac{85}{80}$	$k_{sa,d}=1$			$k_{rh,d}=\dfrac{6}{80}$	$k_{pa,d}=\dfrac{3}{80}$	

Table 7.5 Pressure scaling factors for baseline mean, systolic, and diastolic pressure values for each compartment, where applicable.

Parameter	Calculation	Parameter	Calculation	Parameter	Calculation
R_{ao}^*	$\dfrac{\bar{P}_{ao} - \bar{P}_{sa}}{.9\ \text{CO}} = \dfrac{k_{ao} - k_{sa}}{.9\ \text{CO}}\bar{P}$	C_{ao}	$\dfrac{V_{ao,0}}{\bar{P}_{ao}} = \dfrac{V_{ao,0}}{k_{ao}\bar{P}}$	$E_{lh,M}$	$\dfrac{P_{lh,M}}{0.1\ V_{lh,0}} = \dfrac{k_{lh,s}}{0.1\ V_{lh,0}}\bar{P}_s$
R_{sa}^*	$\dfrac{\bar{P}_{sa} - \bar{P}_{sv}}{.9\ \text{CO}} = \dfrac{k_{sa} - k_{sv}}{.9\ \text{CO}}\bar{P}$	C_{sa}^*	$\dfrac{V_{sa,0}}{\bar{P}_{sa}} = \dfrac{V_{sa,0}}{k_{sa}\bar{P}}$	$E_{lh,m}^*$	$\dfrac{P_{lh,m}}{V_{lh,0}} = \dfrac{k_{lh,d}}{V_{lh,0}}\bar{P}_d$
R_{sv}^*	$\dfrac{\bar{P}_{sv} - \bar{P}_{vc}}{.9\ \text{CO}} = \dfrac{k_{sv} - k_{vc}}{.9\ \text{CO}}\bar{P}$	C_{pa}	$\dfrac{V_{pa,0}}{\bar{P}_{pa}} = \dfrac{V_{pa,0}}{k_{pa}\bar{P}}$	$E_{rh,M}$	$\dfrac{P_{rh,M}}{0.1\ V_{rh,0}} = \dfrac{k_{rh,s}}{0.1\ V_{rh,0}}\bar{P}_s$
R_{pa}	$\dfrac{\bar{P}_{pa} - \bar{P}_{pv}}{\text{CO}} = \dfrac{k_{pa} - k_{pv}}{\text{CO}}\bar{P}$	C_{pv}	$\dfrac{V_{pv,0}}{\bar{P}_{pv}} = \dfrac{V_{pv,0}}{k_{pv}\bar{P}}$	$E_{rh,m}$	$\dfrac{P_{rh,m}}{V_{rh,0}} = \dfrac{k_{rh,d}}{V_{rh,0}}\bar{P}_d$
R_{th}	$\dfrac{\bar{P}_{ao} - \bar{P}_{vc}}{.1\ \text{CO}} = \dfrac{k_{ao} - k_{vc}}{.1\ \text{CO}}\bar{P}$				

CO - cardiac output. Values for k_i can be found in Table 7.4. Values for $V_{i,0}$ can be found in Table 7.2.

$\bar{P}$, $\bar{P}_s$, and $\bar{P}_d$ are the mean, mean systolic, and mean diastolic blood pressures, respectively.

An asterisk indicates this value is not used in the model, but used to calculate other nominal parameter values or initial conditions.

7.2.1.6 Nominal parameter values

To ensure the model output is patient-specific, careful attention is paid to the assignment of nominal parameter values. In this section, we discuss assumptions associated with calculating the nominal parameter values from data using baseline mean blood pressure ($\bar{P}$), mean systolic blood pressure ($\bar{P}_s$), and mean diastolic blood pressure ($\bar{P}_d$). The compartment pressures are scaled from the data using the reference pressures MBP = 95, SBP = 120, and DBP = 80, as shown in Table 7.4. The numerators for every scaling factor k_i was taken as the population blood pressure value given in [16].

The nominal parameter values associated with the the P-V relation of the systemic veins are calculated under the assumption that under unphysiologically high pressures the veins have a relatively small compliance [16]. Therefore, we assume the maximal stressed volume of the systemic veins is marginally larger than the initial value, that is,

$$V_{sv,M} = 1.01 \; V_{sv,0}. \tag{7.53}$$

Furthermore, the compliance of the systemic veins is taken from literature. The literature compliance value of the systemic veins $C_{sv,n} = 70$ ml mmHg^{-1} [102]. Then, from equation (7.35), we have

$$\gamma_{sv} = \frac{C_{sv,n}}{V_{sv,M} - V_{sv,0}}. \tag{7.54}$$

The parameters for the P-V relation of the veins where $V_{vc,str} \geq 0$ can be found in a similar manner with $C_{vc,n} = 32$ ml mmHg^{-1} [101]. For the vena cava where $V_{vc,str} < 0$, there are two parameters. $C_{vc,M}$, the maximal compliance that occurs when $V_{vc,str} = 0$, is calculated from equation (7.35) as

$$C_{vc,M} = \gamma_{vc} V_{vc,M}. \tag{7.55}$$

The sigmoid half-saturation value s_{vc} is determined from the assumption that when $V_{vc,str} = V_{vc,m} < 0$ where $V_{vc,m}$ is the minimal volume of the vena cava compartment, the compliance decreases to zero. We assume a near zero value is $C_{vc,0} = 0.01$. Then,

$$C_{vc,0} = \frac{C_{vc,M}}{1 + e^{-(V_{vc,m}-s)}} \;\Rightarrow\; s = V_m + \ln\left(\frac{C_{vc,M}}{C_{vc,0}} - 1\right). \tag{7.56}$$

In the same manner as [101], we assume $V_{vc,m}$ is 20% of the unstressed volume. From Beneken and DeWit [11], the unstressed volume of the vena cava is 90% of the total volume of the vena cava. Hence, from Table 7.2,

$$V_{vc,m} = 0.02(0.9)(0.05)V_{tot}. \tag{7.57}$$

For the parameters associated with the time-varying elastance function, T_M and T_R are calculated

directly from data. T_M is the time to maximal systolic elastance, which corresponds to the time it takes for the blood pressure data to reach its maximal systolic pressure. T_R is the time of end isovolumetric relaxations, which corresponds to the time it takes for the blood pressure to drop below $\bar{P}$ from the systolic pressure. These time parameters are calculated for and averaged over 10 cardiac cycles. Hence, the scaling factors k_{T_M} and k_{T_R} are calculated as described in Section 7.2.1.3. The maximum elastance occurs when the blood pressure is maximal and the volume is minimal and the minimal elastance when the blood pressure is minimal but the volume is maximal. Maximum and minimum pressures of the left and right heart are scaled from $\bar{P}_s$ and $\bar{P}_d$, respectively. We assume that the minimal volume of the heart compartment is 10% of the end-diastolic volume. Hence,

$$E_{i,M} = \frac{P_{i,M}}{0.1 V_{i,0}} \quad \text{and} \quad E_{i,m} = \frac{P_{i,m}}{V_{i,0}}, \tag{7.58}$$

where $P_{i,M} = k_{i,s} \bar{P}_s$ and $P_{i,m} = k_{i,d} \bar{P}_d$ for k_i a scaling factor given in Table 7.4. The nominal compliances are calculated as

$$C_i = \frac{V_{i,0}}{\bar{P}_i} = \frac{V_{i,0}}{k_i \bar{P}}. \tag{7.59}$$

The compliance values and elastance function parameter calculations are given in Table 7.5.

For the nominal resistance parameters, we calculate based on Ohm's Law using average pressure values, that is,

$$R_j = \frac{\bar{P}_{in} - \bar{P}_{out}}{F_j}, \tag{7.60}$$

where the mean pressures are determined using the ratios k_i given in Table 7.4 and F_j is a percentage of the cardiac output (CO). For the systemic circulation, we assume that 90% of the CO is distributed to the systemic arteries and 10% through the thoracic arteries to the vena cava. The pulmonary circulation receives 100% of the CO. These calculations are tabulated in Table 7.5. The nominal parameter values for the heart valves is set to 10^{-4} for all valves except the tricuspid valve, which will be discussed next.

The parameters associated with the nonlinear resistances are calculated in the following manner. From Table 7.5, the average resistance of the aorta is given as R_{ao}^*, i.e.,

$$\frac{\bar{P}_{ao} - \bar{P}_{sa}}{.9\,\text{CO}} = R_{ao}^* = \frac{\kappa_{ao}}{V_{ao}^{*2}} + R_{ao,0}, \tag{7.61}$$

where V_{ao}^* is the corresponding blood volume when pressure is an average, that is, $V_{ao}^* = C_{ao} \bar{P}_{ao} = C_{ao} k_{ao} \bar{P}$. Similarly, we also have a relation at the systolic and diastolic pressures; however, for this study, we use the diastolic pressure-volume relation, that is,

$$\frac{\bar{P}_{ao,d} - \bar{P}_{sa,d}}{.9\,\text{CO}} = R_{ao,d} = \frac{\kappa_{ao}}{V_{ao,d}^{2}} + R_{ao,0}, \tag{7.62}$$

140

where $V_{ao,d} = C_{ao}\bar{P}_{ao,d} = C_{ao}k_{ao,d}\bar{P}_d$. Solving the system in equations (7.61) and (7.62) for κ_{ao} and $R_{ao,0}$ yields

$$\kappa_{ao} = (R_{ao}^* - R_{ao,d})\frac{V_{ao}^{*\,2}V_{ao,d}^{\,2}}{V_{ao,d}^{\,2} - V_{ao}^{*\,2}} \tag{7.63}$$

and

$$R_{ao,0} = R_{ao}^* - \frac{\kappa_{ao}}{V_{ao}^{*\,2}}. \tag{7.64}$$

Similar calculations can be made for the venous nonlinear resistance relations. For the systemic venous resistance R_{sv}, we have

$$\frac{\bar{P}_{sv} - \bar{P}_{vc}}{0.9\,\text{CO}} = R_{vc}^* = \frac{\kappa_{sv}}{V_{sv}^{*\,2}} + R_{sv,0}, \tag{7.65}$$

where $\bar{P}_{sv} = k_{sv}\bar{P}$. To determine V_{sv}^*, we use equation (7.40) to obtain

$$\bar{P}_{sv} = \frac{1}{\gamma_{sv}}\ln\left(\frac{V_{sv,M}}{V_{sv,M} - V_{sv}^*}\right) \Rightarrow V_{sv}^* = V_{sv,M}(1 - e^{-\gamma_{sv}\bar{P}_{sv}}) = V_{sv,M}(1 - e^{-\gamma_{sv}k_{sv}\bar{P}}). \tag{7.66}$$

Since we do not have a suitable diastolic pressure and volume relationship as with the aortic compartment, we assume that at 90% of the mean pressure of the systemic veins compartment, we have a corresponding reduction in resistance and, hence, volume. Therefore,

$$0.9\frac{\bar{P}_{sv} - \bar{P}_{vc}}{0.9\,\text{CO}} = 0.9R_{vc}^* = R_{vc}^{**} = \frac{\kappa_{sv}}{V_{sv}^{**2}} + R_{sv,0}. \tag{7.67}$$

Using (7.40) again, we obtain

$$V_{sv}^{**} = V_{sv,M}(1 - e^{-0.9\gamma_{vc}k_{sv}\bar{P}}). \tag{7.68}$$

Solving the system given in equations (7.65) and (7.67) gives

$$\begin{aligned}\kappa_{sv} &= (R_{sv}^* - R_{sv}^{**})\frac{V_{sv}^{*\,2}V_{sv}^{**2}}{V_{sv}^{**2} - V_{sv}^{*\,2}} \\ &= 0.1R_{sv}^*\frac{V_{sv}^{*\,2}V_{sv}^{**2}}{V_{sv}^{**2} - V_{sv}^{*\,2}}\end{aligned} \tag{7.69}$$

and

$$R_{sv,0} = R_{sv}^* - \frac{\kappa_{sv}}{V_{sv}^{*\,2}}. \tag{7.70}$$

The parameters for the nonlinear resistance of the tricuspid valve dependent on the volume of the

vena cava are calculated in a similarly, giving

$$\kappa_{tv} = 0.1 R_{tv}^* \frac{V_{vc}^{*\,2} V_{vc}^{**2}}{V_{vc}^{**2} - V_{vc}^{*\,2}}, \tag{7.71}$$

$$R_{tv,0} = R_{tv}^* - \frac{\kappa_{tv}}{V_{vc}^{*\,2}}, \tag{7.72}$$

$$V_{vc}^* = V_{vc,M}(1 - e^{\gamma_{vc} k_{vc} \bar{P}}), \quad \text{and} \tag{7.73}$$

$$V_{vc}^{**} = V_{vc,M}(1 - e^{0.9\gamma_{vc} k_{vc} \bar{P}}). \tag{7.74}$$

7.2.2 Neurological model development

The neurological model implemented in this study is the reduced heart rate control model from Chapter 6. We omit the respiratory sinus arrhythmia model, that is, the model solely responds to baroreflex stimulation. The arterial wall strain of the aorta deforms due to the mean blood pressure. We approximate the mean arterial blood pressure (MAP) of the aorta as a differential equation of the form

$$\frac{\mathrm{d}}{\mathrm{d}t}\mathrm{MAP} = \frac{-\mathrm{MAP} + P_{ao}}{\tau_P} \tag{7.75}$$

for time-scale τ_P and P_{ao} from equation (7.31). Then, the the arterial wall stain in the aorta is

$$\varepsilon_w = 1 - \sqrt{\frac{1 + e^{-q_w(\mathrm{MAP} - s_w)}}{A + e^{-q_w(\mathrm{MAP} - s_w)}}}, \tag{7.76}$$

which stimulates the baroreflex-mediated parasympathetic ($T_{p,H}$) and sympathetic ($T_{p,H}$) heart rate responses modeled as solutions to the differential equations

$$\frac{\mathrm{d}T_{p,H}}{\mathrm{d}t} = \frac{-T_{p,H} + K_{p,H} G_{p,H}}{\tau_{p,H}} \quad \text{and} \quad \frac{\mathrm{d}T_{s,H}}{\mathrm{d}t} = \frac{-T_{s,H}(t - D_H) + K_{s,H} G_{s,H}}{\tau_{s,H}}, \tag{7.77}$$

where $K_{l,H}$ and $\tau_{l,H}$ are the gain and time-scale, respectively, for $l = p$ or s for parasympathetic and sympathetic, respectively, The $G_{l,H}$ are the sigmoidal functions

$$G_{p,H} = \frac{1}{1 + e^{-q_{p,H}(\varepsilon_w - s_{p,H})}} \quad \text{and} \quad G_{s,H} = \frac{1}{1 + e^{q_{s,H}(\varepsilon_w - s_{s,H})}}, \tag{7.78}$$

where $q_{l,H}$ and $s_{l,H}$ are the sigmoid steepness and half-saturation values, respectively. The heart rate is modeled as a linear differential equation of the form

$$\frac{\mathrm{d}H}{\mathrm{d}t} = \frac{-H + \tilde{H}}{\tau_H} \tag{7.79}$$

for heart rate time-scale τ_H where

$$\tilde{H} = H_I(1 - H_p T_{p,H} + H_s T_{s,H}) \tag{7.80}$$

for scaling parameters H_p and H_s. H_I denotes the intrinsic heart rate, the heart rate when the sinoatrial node is denervated, calculated from the age of the subject [52].

During the Valsalva maneuver, stimulation of the sympathetic nervous system causes an increase in peripheral resistance, an increase in cardiac contractility, and a decrease in compliance. The baroreflex decreases venous compliance; however, since the cardiovascular model is a closedcircuit, we can mode any of the compliances dynamically. In this study, we choose to model the compliance of the systemic arteries with a delay differential equation to coincide with the blood pressure data. When the baroreflex activates, vasoconstriction of the vascular smooth muscle surrounding the systemic arterioles overrides the elastic properties of the vessels. We model this relation in a similar manner to the heart rate response model given above. Sympathetically mediated changes in systemic arteriolar resistance and compliance are given as solutions to delay differential equations

$$\frac{\mathrm{d}R_{sa}}{\mathrm{d}t} = \frac{-R_{sa}(t - D_R) + \tilde{R}}{\tau_R} \quad \text{and} \quad \frac{\mathrm{d}C_{sa}}{\mathrm{d}t} = \frac{-C_{sa}(t - D_C) + \tilde{C}}{\tau_C} \tag{7.81}$$

for time-scale τ_m and discrete delay D_m for $m = R$ or C for resistance or compliance, respectively, and

$$\tilde{R} = a_R G_R + b_R \quad \text{and} \quad \tilde{C} = a_C G_C + b_C, \tag{7.82}$$

where a_m and b_m are the scaling factor and offset parameters of the sigmoid curve G_m given as

$$G_R = \frac{1}{1 + e^{q_R(\varepsilon_w - s_R)}} \quad \text{and} \quad G_C = \frac{1}{1 + e^{-q_C(\varepsilon_w - s_C)}} \tag{7.83}$$

for steepness parameter q_m and half-saturation value s_m where ε_w is as in equation (7.76).

Similarly, cardiac contractility increases as sympathetic activity increases due to a decrease in pressure. We model an increase in contractility as a decrease in the minimal elastance of the left heart, $E_{lh,m}$, which is held constant in the cardiovascular model. It should be noted that we could have chosen to model $E_{lh,M}$ instead, which is equivalent. The minimal left heart elastance is the solution to the delay differential equation

$$\frac{\mathrm{d}E_{lh,m}}{\mathrm{d}t} = \frac{-E_{lh,m}(t - D_E) + \tilde{E}}{\tau_E} \tag{7.84}$$

for time-scale τ_E and discrete delay D_E, where

$$\tilde{E} = a_E G_E + b_E \tag{7.85}$$

143

for scaling factor a_E and offset parameter b_E. As pressure decreases, $E_{lh,m}$ decreases, and hence, arterial wall strain and minimal elastance have an increasing sigmoidal relationship, that is,

$$G_E = \frac{1}{1 + e^{-q_E(\varepsilon_w - s_E)}} \tag{7.86}$$

for steepness q_E and half-saturation value s_E.

7.2.2.1 Initial conditions

The initial conditions of the parasympathetic and sympathetic tones controlling heart rate are based on the assumption that at rest parasympathetic activity contributes to 80% of the neural control of heart rate and sympathetic contributes 20% [60]. Hence, the initial condition for $T_{p,H}$ and the constant history function for $T_{s,H}$ are given as

$$T_{p,H}(0) = T_{p,H,0} = 0.8 \qquad \text{and} \tag{7.87}$$

$$T_{s,H}(t) = T_{s,H,0} = 0.2, \qquad t \in [-D_H, 0]. \tag{7.88}$$

The initial condition for heart rate and mean aortic blood pressure are set as functions of the the mean heart rate and blood pressure values from the data, that is,

$$H(0) = \bar{H} \quad \text{and} \tag{7.89}$$

$$\text{MAP}(0) = k_{ao}\bar{P}. \tag{7.90}$$

The initial conditions of the systemic arteriolar resistance and compliance and minimal left heart elastance are calculated such that at rest they sustain the average value given in Table 7.5, that is, the constant history function for each is

$$R_{sa}(t) = R_{sa,0} = \frac{k_{sa} - k_{sv}}{0.9 \, \text{CO}} \bar{P}, \qquad t \in [-D_R, 0], \tag{7.91}$$

$$C_{sa}(t) = C_{sa,0} = \frac{V_{sa,0}}{k_{sa}\bar{P}}, \qquad t \in [-D_C, 0], \quad \text{and} \tag{7.92}$$

$$E_{lh,m}(t) = E_{lh,m,0} = \frac{k_{lh,d}}{V_{lh,0}} \bar{P}, \qquad t \in [-D_E, 0]. \tag{7.93}$$

Table 7.6 Nominal parameter values for the heart rate model.

Parasympathetic		Sympathetic		Heart Rate	
Parameter	**Value**	**Parameter**	**Value**	**Parameter**	**Value**
$K_{p,H}$	5	$K_{s,H}$	5	τ_H	0.5
$\tau_{p,H}$	1.8	$\tau_{s,H}$	10	H_I	$118 - 0.57\text{age}$
H_p	$\dfrac{1 - \bar{H}/H_I + H_s T_{s,H,0}}{T_{p,H,0}}$	H_s	$(H_M/H_I - 1)/K_{s,H}$	H_M	$208 - 0.7\text{age}$
$q_{p,H}$	9	$q_{s,H}$	9		
$s_{p,H}$	$\varepsilon_w(0) + \ln(K_{p,H}/T_{p,H,0} - 1)$	$s_{p,H}$	$\varepsilon_w(0) - \ln(K_{p,H}/T_{p,H,0} - 1)$		
		D_H	3		

Table 7.7 Nominal parameter values for sympathetic effectors.

	Resistance		Compliance		Elastance
Parameter	**Value**	**Parameter**	**Value**	**Parameter**	**Value**
q_R	$\dfrac{2}{\bar{\varepsilon}_w - \varepsilon_{w,m}} \ln\left(\dfrac{1}{G_{C,0}} - 1\right)$	q_C	$\dfrac{2}{\bar{\varepsilon}_w - \varepsilon_{w,m}} \ln\left(\dfrac{1}{G_{C,0}} - 1\right)$	q_E	$\dfrac{2}{\bar{\varepsilon}_w - \varepsilon_{w,m}} \ln\left(\dfrac{1}{G_{C,0}} - 1\right)$
s_R	$\dfrac{1}{2}(\bar{\varepsilon}_w + \varepsilon_{w,m})$	s_C	$\dfrac{1}{2}(\bar{\varepsilon}_w + \varepsilon_{w,m})$	s_E	$\dfrac{1}{2}(\bar{\varepsilon}_w + \varepsilon_{w,m})$
a_R	$\dfrac{R_{sa,0} - R_{sa,M}}{G_{R,0} - G_{R,M}}$	a_C	$\dfrac{C_{sa,0} - C_{sa,m}}{G_{C,0} - G_{C,m}}$	a_E	$\dfrac{E_{lh,m,0} - E_{lh,m,m}}{G_{E,0} - G_{E,m}}$
b_R	$R_{sa,0} - a_R G_{R,0}$	b_C	$C_{sa,0} - a_C G_{C,0}$	b_E	$E_{lh,m,0} - a_E G_{E,0}$
τ_R	6	τ_C	6	τ_E	10
D_R	3	D_C	3	D_E	3

$\bar{\varepsilon}_w = \varepsilon_w(\bar{P})$ and $\varepsilon_{w,m} = \varepsilon_w(\bar{P}_m)$.

7.2.2.2 Nominal parameter values

Nominal parameter values for the heart rate response are given in Chapter 4. Table 7.6 lists the nominal parameter values and calculations based on the assumptions given above. For the sympathetic effectors, R_{sa}, C_{sa}, and $E_{lh,m}$, the time-scales and delay parameter values are from Lu *et al.* [69].

Arterial compliance influences the width of the oscillations of the arterial pulse pressure (PP) defined as the difference in systolic and diastolic pressures. The mean pulse pressure is

$$\bar{PP} = \bar{P}_s - \bar{P}_d. \tag{7.94}$$

$\bar{PP}$ and C_{sa} are inversely proportional, *i.e.*,

$$C_{sa,0}\bar{PP} = C_{sa,m}PP_m \quad \Rightarrow \quad C_{sa,m} = \frac{\bar{PP}}{PP_m}C_{sa_0}, \tag{7.95}$$

where $C_{sa,0}$ is as in equation (7.92) and PP_m is the minimal pulse pressure calculated directly from the data. To determine the nominal parameter values for a_C, b_C, q_C, and s_C, at rest we have the mean blood pressure $\bar{P}$ from the data the baseline compliance $C_{sa,0}$ and we assume that this point is sufficiently high on the increasing sigmoidal curve in equation (7.83) so that a drop in pressure induces a significant decrease in compliance. For this study, we assign a value of 80% to denote "sufficiently high", that is,

$$G_{C,0} = \frac{1}{1 + e^{-q_C(\bar{\varepsilon}_w - s_C)}}, \tag{7.96}$$

where $G_{c,0} = 0.8$ and

$$\bar{\varepsilon}_w = \varepsilon_w(\bar{P}). \tag{7.97}$$

The minimal compliance $C_{sa,m}$ occurs approximately when the mean blood pressure is minimal. Furthermore, we assume this minimal value occurs at 20% of the curve in equation (7.83). For $\varepsilon_{w,m} = \varepsilon_w(\bar{P}_m)$, we have

$$G_{C,m} = \frac{1}{1 + e^{-q_C(\varepsilon_{w,m} - s_C)}}, \tag{7.98}$$

where $G_{C,m} = 0.2$. Solving the system given by equations (7.96) and (7.98) for q_C and s_C yields

$$s_C = \frac{1}{2}(\bar{\varepsilon}_w + \varepsilon_{w,m}) \text{ and} \tag{7.99}$$

$$q_C = \frac{2}{\bar{\varepsilon}_w - \varepsilon_{w,m}} \ln\left(\frac{1}{G_{C,0}} - 1\right). \tag{7.100}$$

Using these assumptions, we can set up the system

$$C_{sa,0} = a_C G_{C,0} + b_C \quad \text{and} \tag{7.101}$$

$$C_{sa,m} = a_C G_{C,m} + b_C. \tag{7.102}$$

Solving this system for a_C and b_C gives

$$a_C = \frac{C_{sa,0} - C_{sa,m}}{G_{c,0} - C_{c,m}} \quad \text{and} \tag{7.103}$$

$$b_C = C_{sa,0} - a_C G_{C,0}. \tag{7.104}$$

Calculation of the minimal left heart elastance parameters follows a similar methodology with the points $(\bar{\varepsilon}, E_{lh,m,0})$ for $G_{E,0} = 0.8$ and $(\varepsilon_{w,m}, E_{lh,m,m})$ for $G_{E,m} = 0.2$, where $E_{lh,m,m}$ is the minimal value the minimal left heart elastance can attain. We assume $E_{lh,m,m} = 0.5 E_{lh,m,0}$. Since the arteriolar resistance involves an increasing sigmoid, we have the points $(\bar{\varepsilon}, R_{sa,0})$ for $G_{R,0} = 0.2$ and $(\varepsilon_{w,m}, R_{sa,M})$ for $G_{R,M} = 0.8$ to ensure a dramatic increase in resistance as pressure drops. We assume $R_{sa,m} = 2R_{sa,0}$. Calculations for the sympathetic effector nominal parameter values are listed in Table 7.7.

7.2.3 Summary

In summary, the coupled cardiovascular-neurological control model incorporating the parasympathetic and sympathetic effects of the baroreflex is a system of ordinary and delay differential equations of the form

$$\frac{d\mathbf{x}}{dt} = f(t, \mathbf{x}, \mathbf{x}(t - D_H), \mathbf{x}(t - D_R), \mathbf{x}(t - D_C), \mathbf{x}(t - D_E); \theta) \tag{7.105}$$

$$y = g(\mathbf{x}, \mathbf{x}(t - D_H), \mathbf{x}(t - D_R), \mathbf{x}(t - D_C), \mathbf{x}(t - D_E); \theta), \tag{7.106}$$

where $\mathbf{x} \in \mathbb{R}^{15}$ denotes the vector of states for the cardiovascular model, f denotes the right hand side of the system, $\theta \in \mathbb{R}^{57}$ is a vector of parameters, and g relates the states to the observable y. The state vector is given as

$$\mathbf{x} = [V_{lh}, V_{ao}, V_{sa}, V_{sv}, V_{vc}, V_{rh}, V_{pa}, V_{pv}, \dots$$

$$\dots H, \text{MAP}, T_{p,H}, T_{s,H}, R_{sa}, C_{sa}, E_{lh,m}]^T \tag{7.107}$$

and the parameter vector as

$$\theta = [E_{lh,M}, E_{rh,M}, E_{rh,m}, C_{ao}, C_{pa}, C_{pv}, C_{vc,M} \ldots$$
$$\ldots R_{mv}, R_{av}, R_{pv}, R_{pa}, R_{th}, R_{ao,0}, \kappa_{ao}, R_{sv,0}, \kappa_{sv}, R_{tv,0}, \kappa_{tv} \ldots$$
$$\ldots \gamma_{sv}, V_{sv,M}, \gamma_{vc}, V_{vc,M}, s_{vc}, T_M, T_R, \ldots$$
$$\ldots A, K_{p,H}, K_{s,H}, \tau_{p,H}, \tau_{s,H}, \tau_H, \tau_R, \tau_C, \tau_E \ldots$$
$$\ldots q_{p,H}, q_{s,H}, q_R, q_C, q_E, s_{p,H}, s_{s,H}, s_R, s_C, s_E, \ldots$$
$$\ldots H_I, H_{p,H}, H_{s,H}, a_R, a_C, a_E, b_R, b_C, b_E, \ldots$$
$$\ldots D_H, D_R, D_C, D_E]^T. \tag{7.108}$$

The observable y of the cardiovascular model is the prediction of systemic arterial blood pressure, P_{sa}, and heart rate H.

Table 7.8 Assumptions for pathological subjects.

| Behavior	System	Assumption	Effector	Implementation
M	Parasympathetic	Increased	Heart rate	$\tau_{p,H} \approx 0$
	Sympathetic	Increased	Heart rate	$\uparrow q_{s,H}$
			Resistance	$\uparrow R_{sa}$
			Compliance	$\downarrow C_{sa}$
			Contractility	$\downarrow E_{lh,m}$
N	Parasympathetic	No change	Heart rate	
	Sympathetic	Delayed	Heart rate	$\uparrow D_H$
			Resistance	$\uparrow R_{sa}$ and $\uparrow D_R$
			Compliance	$\uparrow D_E$
			Contractility	$\uparrow D_E$
V	Parasympathetic	Diminished	Heart rate	$\downarrow q_{p,H}$
	Sympathetic	Diminished	Heart rate	$\dfrac{\mathrm{d}T_{s,H}}{\mathrm{d}t} = 0$
			Resistance	$\dfrac{\mathrm{d}R_{sa}}{\mathrm{d}t} = 0$
			Compliance	$\dfrac{\mathrm{d}C_{sa}}{\mathrm{d}t} = 0$
			Contractility	$\dfrac{\mathrm{d}E_{lh,m}}{\mathrm{d}t} = 0$
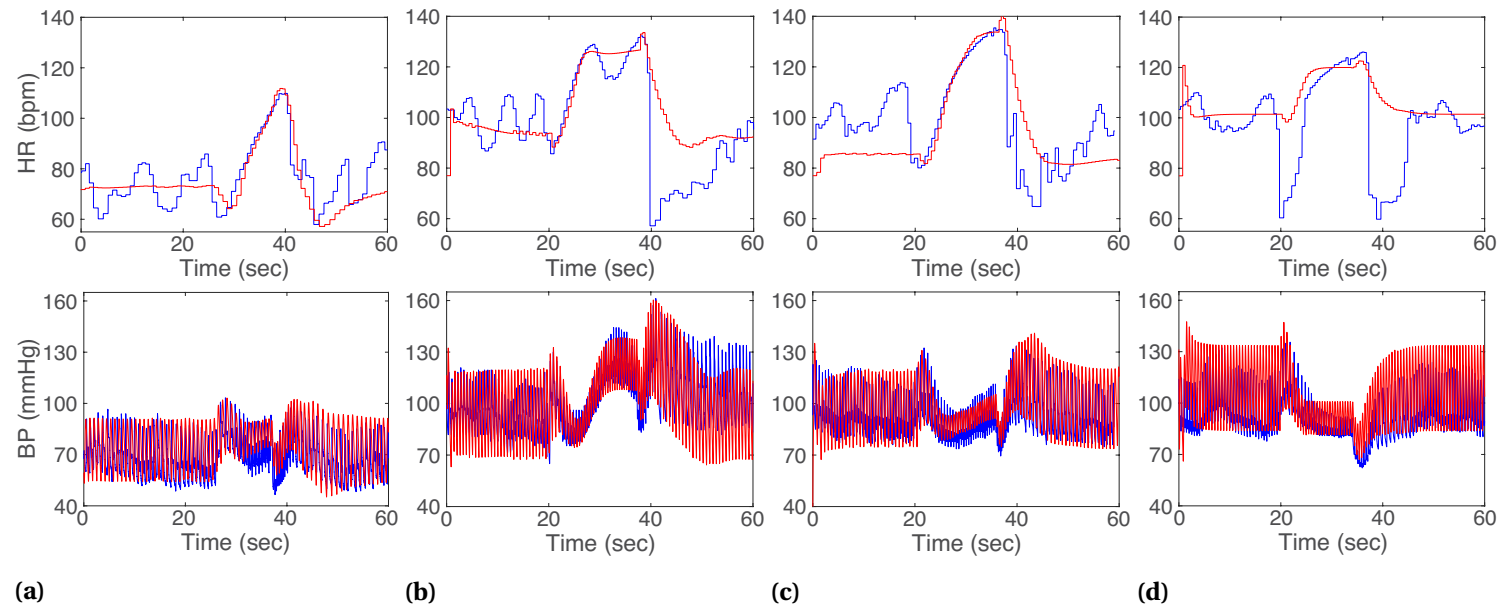
Figure 7.4 Heart rate (top row) and blood pressure (bottom row) data (blue) and model fits (red) in response to a Valsalva maneuver with different etiologies: (a) control. (b) M pattern. (c) N pattern. (d) V pattern.

7.3   Results and discussion

The results from the methodology presented in Section 7.2 are presented in Figure 7.4. The upper and lower traces display heart rate and blood pressure responses to the Valsalva maneuver (VM) for a control subject and three AD patients exhibiting M, N, and V responses. The nominal model parameter values and initial conditions were calculated to ensure a patient-specific model output. It should be noted that careful consideration of nominal parameter values allow us to predict qualitative behavior of heart rate response without optimization. We develop a qualitative model for each case of the data presented in Figure 3.2 by changing the assumptions on the model. Section 2.4 discusses the hypotheses for the M, N, and V patients, and we adjusted each model accordingly.

7.3.1   Control model

The nominal model outputs for the heart rate and blood pressure (Figure 7.4a) of the healthy subject fits the baseline values and the regions controlled by the baroreflex well. For the heart rate, this is due to the effort expended in calculating nominal parameter values for the baroreflex effectors. For blood pressure control, P_{sa} fits the blood pressure data in phases I, III, and IV of the VM. However, in late phase II, the diastolic pressure of the model output rises quicker than the data. This could be due to an effect of too much stimulation from the sympathetically-mediated cardiac contractility component controlling the minimal elastance.

7.3.2   Pathophysiological models

To predict dynamics for the POTS patients, we modified the model according to the hypotheses associated with the pathophysiology for each subject as described in Section 2.4.1. The assumptions regarding the M, N, and V patterns are summarized in Table 7.8.

7.3.2.1   M model

The M pattern has two SBP overshoots, one in late phase II and another during phase IV, and the overshoot in phase IV rapidly declines to baseline within 5 seconds [94]. We hypothesize that the M pattern is generated by *increased sympathetic and parasympathetic activity*. To model this pathophysiology, we

- increase the effect of the parasympathetic tone on heart rate by decreasing the time-scale $\tau_{p,H}$ to near zero ($\tau_{p,H} = 0.01$), which resulted in a faster parasympathetic withdrawal in early phase II and a sharper increase in heart rate.

- double the sigmoid steepness for the sympathetic heart rate effects, inducing a further increase in heart rate.

- increase arteriolar resistance by increasing nominal pressure-resistance relationship from 20% to 30% of the sigmoid curve.

- decrease C_{sa} and $E_{lh,m}$ by reducing the nominal sigmoidal relationship from 80% to 70% of the sigmoid curve.

These nominal assumption adjustments yield the resulting M behavior seen in the data (Figure 7.4b). Though the baseline oscillations are slightly broader than the data, the VM region of the signal fits the blood pressure well. In phase IV, fast parasympathetic recovery causes a sharper decrease in blood pressure than in the data.

7.3.2.2 N model

The N pattern has a delayed increase in SBP in late phase II and a sustained SBP overshoot in phase IV for longer than 10 seconds [94]. We hypothesize that the N pattern is a result of a *delayed sympathetic response*, causing an prolonged increase in peripheral resistance. To model this behavior we

- multiply the delay parameters by a scaling factor ξ. The effect seen in Figure 7.4c is a result of multiplying all of the delays by $\xi = 1.5$ except for D_E ($\xi_E = 2$).

- increase arteriolar resistance by increasing nominal pressure-resistance relationship from 20% to 30% of the sigmoid curve.

This effectively produced the expected outcome for both heart rate and blood pressure. However, in phase II in Figure 7.4c, the diastolic blood pressure is higher in the model than the data. This may be due to increased cardiac contractility, as seen in the healthy control subject.

7.3.2.3 V model

The V pattern has an absent increase in SBP in late phase II causing a prolonged decrease in SBP, an altered phase III, and an absent SBP overshoot in phase IV [94]. It has been hypothesized that the V pattern is a result of sympathetic dysfunction, as adrenergic activity contributes to late phase II and phase IV of the VM. However, we showed that it may be more likely that the V behavior is a result of *diminished sympathetic and parasympathetic activity* in Chapter 4. To decrease the parasympathetic response, we

- halve the sigmoid steepness parameter $q_{p,H}$.

- set all of the differential equations for the systemic effectors to zero to simulate complete sympathetic blockade.

The result is the V behavior that fits the data both at baseline and during the VM. The large heart rate drops before and after the maneuver are due to deep breaths, which are not modeled in this study.
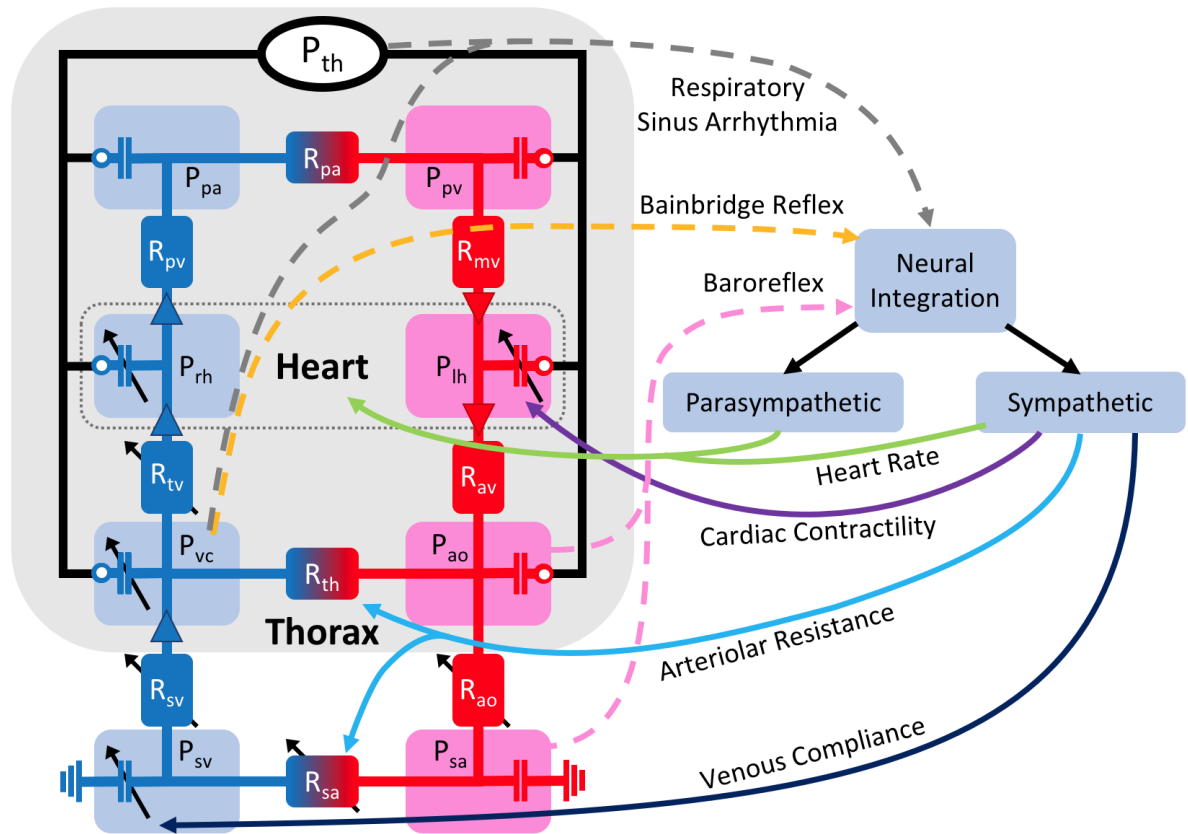
Figure 7.5 Schematic of the neurological control model coupled to the lumped parameter compartment cardiovascular model from Figure 7.1. Dashed curves represent afferent signals from the cardiovascular system stimulating the appropriate control mechanism: respiratory sinus arrhythmia (gray), the Bainbridge reflex (orange), and the baroreflex (pink). Efferent parasympathetic response affects heart rate (light green). Efferent sympathetic response affects heart rate (light green), cardiac contractility (purple), arteriolar resistance (light blue), and venous compliance (dark blue).

7.3.3 Limitations and future work

Without the implementation of other control mechanisms, such as the cardiopulmonary reflex and respiratory sinus arrhythmia (RSA), the model currently provides an incomplete depiction. Figure 7.5 shows a schematic of the future modeling efforts incorporating the effects of RSA and the Bainbridge reflex that are both influenced by the cardiopulmonary receptors. At baseline, the clearly oscillatory behavior of both the heart rate and blood pressure is due to respiration. The dramatic drops in heart rate in the M (Figure 7.4b) and V (Figure 7.4d) patients are due to large breaths, which the model cannot fit without a respiratory component. The incorporation of RSA would provide better predictions at baseline and during phase I of the VM (as determined in Chapter 4 that RSA may play a slight role in the early VM phases).

Implementation of control mechanisms influenced by the cardiopulmonary receptors could be achieved in a variety of ways. The Bainbridge reflex can be implemented using the volume of the vena cava compartment as the input to the negative feedback submodel, as shown in Figure 7.5. V_{vc} could also be one of the inputs for respiratory sinus arrhythmia. We can impose RSA by altering the baseline of the thoracic pressure as well. Some suggestions for future studies include:

- using an ECG-derived respiratory signal as an input similar to the open-loop approach of Chapter 4 in which the model would no longer be closed-loop but more patient-specific.

- defining an explicit oscillatory respiratory signal analytically and integrating it with the thoracic pressure, P_{th} in which the model may or may not oscillate with the same frequency as the data.

- fitting an analytical oscillatory function to the respiratory data first and then incorporating this signal into P_{th}, which has the potential to maintain the closed-loop and be patient-specific.

- developing or adapting a physiologically-motivated submodel accounting for the reflex, such as the model developed by Ben-Tal *et al.* [10].

7.4 Conclusions

From the present preliminary analysis, this model has great potential. The baroreflex modeling component performs admirably and the methodology used to calculate nominal parameter values provides patient-specific outcomes. The M, N, and V patterns are characteristics of blood pressure. In Chapter 4, we were able to characterize the V pattern, but by coupling the neurological model to a cardiovascular model, we were able to support the clinical hypotheses posed for all three patterns.

CHAPTER

8

CONCLUDING REMARKS

In this study, we have developed and analyzed models of the autonomic response to the Valsalva maneuver (VM), a clinical test that elicits both a parasympathetic and sympathetic response. The open-loop model incorporates cardiovascular control mechanisms of the baroreceptor reflex (*baroreflex*) and the respiratory sinus arrhythmia, analyzing their contribution to the control of HR during the VM. We have validated this model against control subject data and assessed its effectiveness in predicting heart for patients with autonomic dysfunction characterized by a V behavior from Palamarchuk *et al.* [94].

Development of physiologically models

Open-loop model: We have developed an open-loop model motivated by the physiological mechanisms and clinical hypotheses to predict the parasympathetic and sympathetic nervous system responses, which cannot be measured (a) without costly or invasive techniques which fundamentally comprise the autonomic system or (b) without anesthetization which also blunts the nervous response. The model predicts baroreflex-mediated parasympathetic and sympathetic function and respiratory-mediated parasympathetic function to control heart rate. In conjunction with parameter estimation in an inverse problem framework., we showed that this open-loop approach can explore dysfunction of the VM arising in the V response [94]. We determined that the V pattern hypothesis is incomplete and subcategories should be used to classify different etiologies.

A limitation of this model is its restriction to using the blood pressure as an input, which assumes that blood pressure changes stimulating the baroreflex and respiratory sinus arrhythmia are the only contributors to heart rate control. However, heart rate regulation is governed by many factors, including the cardiopulmonary receptors that respond to changes in blood volume. The model does not incorporate the Bainbridge reflex initiated by the cardiopulmonary receptors since blood volume data was not available. Coupling the neurological model to a cardiovascular model can elicit the volume changes necessary to model the Bainbridge reflex effectively. Future studies should explore the contributions of these receptors.

Closed-loop model: We have developed a lumped parameter compartment model of the cardiovascular system and coupled this model with the open-loop neurological control model. Though this work is preliminary, the outlook is promising given that the development of a control submodel and submodels for each of the M, N, and V patterns nominally fit the morphology of the data. A limitation of using a zero-dimensional lumped parameter model is the assumption that the compartments are homogeneous and the flow is steady. At rest, these assumptions may be valid, but it is not unlikely that patients suffering from autonomic dysfunction violate these assumptions more readily than healthy control subjects.

Patient-specific modeling

To ensure the model output was patient-specific, we calculated nominal parameter values from data and analytical initial conditions so that the model was in steady-state. We implemented various physiological assumptions in regard to the M, N, and V patterns, which supported their clinical hypotheses. We used subset selection and parameter estimation to identify a subset of parameters to optimize, fitting the model heart rate output to data. Using parameter estimation, we conducted a model-based data analysis for 34 healthy control subjects and 5 patients with AD. We also developed an algorithm for patient-specific respiratory sinus arrhythmia derived from an electrocardiogram.

Model analysis

Several mathematical techniques were applied to this model, analyzing the influence of the parameters on the model output via local and global sensitivity analysis and analyzing the stability of the system with bifurcation analysis. The stability analysis showed that defining an appropriate parameter regime can ensure the model's resting state is asymptotically stable. The extent to which instability, including dampened oscillations, limit cycles, and unstable modes, persists in the model solution after deviating from the critical point may be related to diseased outcomes, such as the M patient, due to overstimulation of the system.

Local and global sensitivity analyses were conducted to assess the influence of the model's param-

eters on the output. We used global sensitivity analysis to motivate a model reduction and selection protocol. This analysis required the development of a new metric that we call limited-memory Sobol' indices, which incorporate the time-dependent variance within a moving window centered about a time point t. These indices were found to be useful for interpreting the time-dependent parameter influence on the model output, as the dynamic changes in parameter influence were averaged out by other methods.

In conclusion, the modeling efforts in this study provide a mathematical framework for the analysis of autonomic control of blood pressure and heart rate. Furthermore, this approach combined many different mathematical techniques for analysis of both the model and data. This work has shown to provide important insight clinically by supporting hypotheses of how autonomic dysfunction impacts the cardiovascular system.

Future work

There is still much work to be done investigating these areas. Mathematically, a more rigorous derivation of the limited-memory Sobol' indices and time-dependent GSA in general is necessary. Determining the "yardstick" by which to measure is still an open and active area of research. Moreover, it would be useful to investigate these indices on smaller problems to ensure we obtain useful and interpretable results overall. However, it should be noted that these small problems must exhibit similar properties to this model, that is, they must also have fast transient behavior for the results to be meaningful.

In regard to the modeling efforts, parameter subset selection and optimization is the natural next step to from Chapter 7. The submodels for the disease patients should also be included in these efforts, as it would be interesting to see if the optimization scheme can determine disease parameter regimes that correspond to the type of dysfunction response. Furthermore, implementation of the cardiopulmonary receptors and RSA in the coupled cardiovascular is an immediate follow-up to this work. The cardiopulmonary response to blood volume has been modeled previous [69, 133], but these models are not patient-specific and the cardiopulmonary feedback loops are not physiologically-motivated (but rather by transfer functions in the frequency domain).

BIBLIOGRAPHY

[1] Airaksinen, K. E. J. et al. "Valsalva manoeuvre in the assessment of baroreflex sensitivity in patients with coronary artery disease". *Eur Heart J* **14** (1993), pp. 1519–1523.

[2] Albanese, A. et al. "An integrated mathematical model of the human cardiopulmonary system: model development". *Am J Physiol Heart Circ Physiol* **310** (2016), H899–H921.

[3] Alexandarian, A. et al. "Global sensitivity analysis in an ocean general circulation model: a sparse spectral projection approach". *Comput Geosci* **16** (2012), pp. 757–778.

[4] Alexanderian, A. et al. *Variance-based sensitivity analysis for time-dependent processes*. 2017.

[5] Arndt, J. O. et al. "The physiologically relevant information regarding systemic blood pressure encoded in the carotid sinus baroreceptor discharge pattern". *J Physiol* **268** (1977), pp. 775–791.

[6] Bai, J. et al. "Optimization and mechanism of step-leap respiration exercise in treating of cor pulmonale". *Comput Biol Med* **28** (1998), pp. 289–307.

[7] Banks, H. T. et al. "The complex-step method for sensitivity analysis of non-smooth problems arising in biology". *Eurasian J Math Comp Appl* **3** (2015), pp. 16–68.

[8] Banks, H. T. et al. "Modeling bumble bee population dynamics with delay differential equations". *Ecol Model* **351** (2017), pp. 14–23.

[9] Bellman, R. & Cooke, K. L. *Differential-Difference Equations*. 1963.

[10] Ben-Tal, A. et al. "Central regulation of heart rate and the appearance of respiratory sinus arrhythmia: new insights from mathematical modeling". *Math Biosci* **255**.1 (2014), pp. 71–82.

[11] Beneken, J. E. W. & DeWit, B. "A physical approach to hemodynamic aspects of the human cardiovascular system". *Physical bases of circulatory transport, regulation and exchange*. Ed. by Saunders, W. B. Philadelphia, PA, 1967, pp. 1–45.

[12] Berger, R. D. et al. "Transfer function analysis of autonomic regulation. I. Canine atrial rate response". *Am J Physiol Heart Circ Physiol* **25** (1989), H142–H152.

[13] Besselink, B et al. "A comparison of model reduction techniques from structural dynamics, numerical mathematics, and systems and control". *J Sound Vib* **332** (2013), pp. 4403–4422.

[14] Bevan, J. A. & Verity, A. "Postganglionic sympathetic delay in vascular smooth muscle". *J Pharmacol and Exp Ther* **152**.2 (1966), pp. 221–230.

[15] Bi, P. & Ruan, S. "Bifurcations in delay differential equations and applications to tumor and immune system interaction models". *SIAM J Appl Dyn Sys* **12** (2013), pp. 1847–1888.

[16] Boron, W. F. & Boulpaep, E. L. *Medical Physiology: A Cellular and Molecular Approach*. 3rd ed. Elsevier Inc., 2017.

[17] Braunwald, E. "The circulatory response of patients with idiopathic hypertrophic subaortic stenosis to nitroglycerin and to the Valsalva maneuver". *Circ Res* **29** (1964), pp. 422–431.

[18] Brinth, L. et al. "Suspected side effects to the quadrivalent human papilloma vaccine". *Dan Med J* **62**.4 (2015), pp. 1–5.

[19] Brown, T. P. "Pure autonomic failure". *Pract Neurol* **17**.5 (2017), pp. 341–348.

[20] Bugenhagen, S. M. et al. "Identifying physiological origins of baroreflex dysfunction in salt-sensitive hypertension in the Dahl SS rat". *Physiol Genomics* **42**.1 (2010), pp. 23–41.

[21] Burnham, K. P. & Anderson, D. R. *Model selection and multimodel inference: a practical information-theoretic approach*. 2nd edition. New York: Springer-Verlag, 2002.

[22] Calvo, M. et al. "Global sensitivity analysis of a cardiovascular model for the study of the autonomic response to head-up tilt testing". *Eng Med Biol Soc*. 2018, pp. 5458–5461.

[23] Campagna, J. A. & Carter, C. "Clinical relevance of the Bezold-Jarisch reflex". *Anesthesiology* **98** (2003), pp. 1250–1260.

[24] Cheng, L. et al. "Two-parameter bifurcation analysis of limit cycles of a simplified railway wheel set model". *Nonlinear Dyn* **93** (2018), pp. 2415–2431.

[25] Craft, N. & Schwartz, J. B. "Effects of age on intrinsic heat rate, heart rate variability, and AV conduction in healthy humans". *Am J Physiol Heart Circ Physiol* **268**.4 (1995), H1441–H1452.

[26] DeBoer, R. W. et al. "Hemodynamic fluctuations and baroreflex sensitivity in humans: a beat-to-beat model". *Am J Physiol Heart Circ Physiol* **253**.22 (1987), pp. 680–689.

[27] d'Onofrio, A. et al. "Delay-induced oscillatory dynamics of tumour-immune system interaction". *Math Comput Model* **51** (2010), pp. 572–591.

[28] Ellwein, L. M. et al. "Sensitivity analysis and model assessment: mathematical models for arterial blood flow and blood pressure". *Cardiovasc Eng* **8**.2 (2008), pp. 94–108.

[29] Engelborghs, K et al. "Numerical bifurcation analysis of delay differential equations using DDE-BIFTOOL". *ACM Trans Math Softw* **28** (2002), pp. 1–21.

[30] Eslami, M. *Theory of Sensitivity in Dynamic Systems: An Introduction*. Springer Verlag, 1994.

[31] Freeman, R. & Chapleau, M. W. "Testing the autonomic nervous system". *Handbook of Clinical Neurology*. Ed. by Said, G. & Krarup, C. Vol. 115. Elsevier B.V., 2013, pp. 115–136.

[32] Fritsch, F. N. & Carlson, R. E. "Monotone piecewise cubic interpolation". *SIAM J Numer Anal* **17**.2 (1980), pp. 238–246.

[33] Fung, Y. C. *Biomechanics: Circulation*. 2nd ed. Springer Verlag, 1996.

[34] Garcia-Lledo, A. et al. "Prognostic value of Valsalva maneuver-induced change Doppler-detected ventricular filling in patients with systolic dysfunction". *Rev Esp Cardiol* **58**.9 (2005), pp. 1029–36.

[35] Grymuza, M. et al. "Right heart catheterization procedures in patients with suspicion of pulmonary hypertension - experiences of a tertiary center". *Adv Interv Cardiol* **13**.4 (2017), pp. 295–301.

[36] Guglielmi, N & Hairer, E. "Implementing Radau IIA methods for stiff delay differential equations". *Computing* **67**.1 (2001).

[37] Gunter, F. N. "Nonlinear rate sensitivity of the carotid sinus reflex as a consequence of static and dynamic nonlinearities in baroreceptor behavior". *Ann NY Acad Sci* **156**.2 (1969), pp. 811–824.

[38] Guyton, A. C. et al. "Circulation: overall regulation". *Ann Rev Physiol* **34** (1972), pp. 13–44.

[39] Haario, H. et al. "DRAM: Efficient adaptive MCMC". *Statistics and Computing* **16**.4 (2006), pp. 339–354.

[40] Hall, J. E. *Guyton and Hall Textbook of Medical Physiology*. Thirteenth. Philadelphia, PA: Elsevier, Inc., 2016.

[41] Hamilton, W. F. et al. "Arterial, cerebrospinal, and venous pressures in man during cough and strain". *Am Heart J* **27**.6 (1943), p. 871.

[42] Hardy, H. H. & Collins, R. E. "On the pressure-volume relationship in circulatory elements". *Med Biol Eng Comput* (1982), pp. 565–570.

[43] Harris, F. J. "On the use of windows for harmonic analysis with the discrete Fourier transform". *Proc IEEE* **66**.1 (1978), pp. 51–83.

[44] Hart, J. L. "Extensions of global sensitivity analysis: theory, computation, and applications". PhD thesis. North Carolina State University, 2018.

[45] Heldt, T. et al. "Computational modeling of cardiovascular response to orthostatic stress". *J Appl Physiol* **92**.8750-7587 (Print) (2002), pp. 1239–1254.

[46] Helfenbein, E. et al. "Development of three methods for extracting respiration from the surface ECG: A review". *J Electrocardiol* **47** (2014), pp. 819–825.

[47] Hemalatha, K & Manivannan, M. "Valsalva maneuver for the analysis of interaction hemodynamic - model study". *ITC 2010 - 2010 International Conference on Recent Trends in Information, Telecommunication, and Computing*. Vol. 28. 2010, pp. 28–32.

[48] Hilz, M. J. & Dutsch, M. "Quantitative studies of autonomic function". *Muscle Nerve* **33** (2006), pp. 6–20.

[49] Iooss, B. & Lemaitre, P. "A review on global sensitivity analysis methods". *Uncertainty Management in Simulation-Optimization of Complex Systems: Algorithms and Applications*. Ed. by Dellino, G. Boston, MA: Springer US, 2015, pp. 101–122.

[50] Iwase, S. et al. "Role of sympathetic nerve activity in the process of fainting". *Front Physiol* **5** (2014), pp. 1–8.

[51] Jennings, G. L. et al. "Accentuated hypotensive effect of sodium nitroprusside in man after captopril". *Clin Sci* **61** (1981), pp. 521–526.

[52] Jose, A. D. & Collison, D. "The normal range and determinants of the intrinsic heart rate in man". *Cardiovasc Res* **4**.2 (1970), pp. 160–167.

[53] Kana, M. & Holcik, J. "Mathematical model-based markers of autonomic nervous activity during the Valsalva Maneuver and comparison to heart rate variability". *Biomed Signal Process Control* **6**.3 (2011), pp. 251–260.

[54] Kappel, F. & Munir, M. "Generalized sensitivity functions for multiple output systems". *J Inverse Ill-Posed Probl* **25**.4 (2017), pp. 499–519.

[55] Kautzner, J. et al. "Arterial baroreflex sensitivity assessed from Phase IV of the Valsalva Maneuver". *Am J Cardiol* **78**.5 (1996), pp. 575–579.

[56] Keane, A. et al. "Climate models with delay differential equations". *Chaos* **27** (2017), p. 114309.

[57] Kelley, C. T. *Iterative Methods for Optimization*. Philadelphia, PA: Society for Industrial and Applied Mathematics, 1996.

[58] Kiparissides, A et al. "Global sensitivity analysis challenges in biological systems modeling". *Ind Eng Chem Res* **48** (2009), pp. 7168–7180.

[59] Kobayashi, H. "Normalization of respiratory sinus arrhythmia by factoring in tidal volume". *Appl Human Sci* **17**.5 (1998), pp. 207–213.

[60] Korner, P. I. et al. "Reflex and mechanical circulatory effects of graded Valsalva maneuvers in normal man". *J Appl Physiol* **40**.3 (1976), pp. 434–40.

[61] Kosinski, S. A. et al. "Computational model-based assessment of baroreflex function from response to Valsalva maneuver". *J Appl Physiol* (2018).

[62] Krauskopf, B. & Sieber, J. "Bifurcation analysis of delay-induced resonances of the El Nino Southern Oscillation". *Proc Math Phys Eng Sci* **420**.2169 (2014), pp. 1–18.

[63] Le Rolle, V et al. "Recursive identification of an arterial baroreflex model for the evaluation of cardiovascular autonomic modulation". *Comput Biol Med* **66** (2015), pp. 287–294.

[64] Le Rolle, V. et al. "An autonomic nervous system model applied to the analysis of orthostatic tests". *Model Simul Eng* **2008** (2008), pp. 1–15.

[65] Le Rolle, V. et al. "A model-based approach for the evaluation of vagal and sympathetic activities in a newborn lamb". *Conf Proc IEEE Eng Med Biol Soc.* 2013, pp. 3881–3884.

[66] Lin, J. et al. "Development of a cardiopulmonary mathematical model incorporating a baro-chemoreceptor reflex control system". *Proc Inst Mech Eng H* **226**.10 (2012), pp. 787–803.

[67] Link, K. G. et al. "A local and global sensitivity analysis of a mathematical model of coagulation and platelet deposition under flow". *PLoS One* **13**.7 (2018).

[68] Loushin, M. K. et al. "Mechanical Aspects of Cardiac Performance". *Handbook of Cardiac Anatomy, Physiology, and Devices.* Ed. by Iaizzo, P. A. Cham: Springer International Publishing, 2015.

[69] Lu, K et al. "A human cardiopulmonary system model applied to the analysis of the Valsalva maneuver." *Am J Physiol Heart Circ Physiol* **281**.6 (2001), H2661–H2679.

[70] Luzyanina, T. et al. "Numerical bifurcation analysis of immunological models with time delays". *J Comp Appl Math* **184** (2005), pp. 165–176.

[71] Mader, G. et al. "Modeling cerebral blood flow velocity during orthostatic stress". *Ann Biomed Eng* **43**.8 (2015), pp. 1748–1758.

[72] Mahdi, A. et al. "Modeling the afferent dynamics of the baroreflex control system". *PLoS Comput Biol* **9**.12 (2013), pp. 1–18.

[73] Makroglou, A. et al. "Mathematical models and software tools for the glucose-insulin regulatory system and diabetes: an overview". *Apl Num Math* **56** (2006), pp. 559–573.

[74] Marquis, A. D. et al. "Practical identifiability and uncertainty quantification of a pulsatile cardiovascular model". *Math Biosci* **304** (2018), pp. 9–24.

[75] Mathias, C. J. "Autonomic diseases: clinical features and laboratory evaluation". *J Neurol Neurosurg Psychiatry* **74** (2003), pp. iii31–iii41.

[76] Michail, M. & Brown, A. J. "Physiology of the normal heart". *Medicine* **46**.8 (2018), pp. 427–430.

[77] MIki, K. et al. "Acute shifts of baroreflex control of renal sympathetic nerve activity induced by treadmill exercise in rats". *J Physiol* **548.1** (2003), pp. 313–322.

[78] MIki, K. et al. "Role of cardiopulmonary and carotid sinus baroreceptors in regulating renal sympathetic nerve activity during water immersion in conscious dogs". *Am J Physiol Regul Integr Comp Physiol* **296** (2009), R:1807–R1812.

[79] Monahan, K. D. "Effect of aging on baroreflex function in humans". *Am J Physiol Regul Integr Comp Physiol* **293** (2007), R3–R12.

[80] Nelson, P. & Perelson, A. S. "Mathematical analysis of delay differential equation models of HIV-1 infection". *Math Biosci* **179** (2002), pp. 73–94.

[81] Nichols, W. W. & Edwards, D. G. "Arterial elastance and wave reflection augmentation of systolic blood pressure: deleterious effects and implications for therapy". *J Cardiovasc Pharmacol Therapeut* **6**.1 (2001), pp. 5–21.

[82] Novak, P. "Assessment of sympathetic index from the Valsalva maneuver". *Neurology* **76**.23 (2011), pp. 2010–2016.

[83] Novak, P. "Quantitative autonomic testing". *J Vis Exp* **53** (2011).

[84] OLeary, D. D. et al. "Differential effect of head-up tilt on cardiovagal and sympathetic baroreflex sensitivity in humans". *Exp Physiol* **88**.6 (2003), pp. 769–774.

[85] Olsen, C. H. "Modeling Heart Rate Regulation by the Baroreflex". PhD thesis. North Carolina State University, 2014.

[86] Olsen, C. H. et al. "Parameter subset selection techniques for problems in mathematical and biology". *Biol Cybern* **113** (2019), pp. 121–138.

[87] Olufsen, M. S. & Ottesen, J. T. "A practical approach to parameter estimation applied to model predicting heart rate regulation". *J Math Biol* **67**.1 (2013), pp. 39–68.

[88] Olufsen, M. S. et al. "Blood pressure and blood flow variation during postural change from sitting to standing: model development and validation". *J Appl Physiol* **99**.4 (2005), pp. 1523–1537.

[89] Olufsen, M. S. et al. "Modeling baroreflex regulation of heart rate during orthostatic stress". *Am J Physiol Regul Integr Comp Physiol* **291**.5 (2006), R1355–R1368.

[90] Ottesen, J. T. "Modelling of the baroreflex-feedback mechanism with time-delay". *J Math Biol* **36**.1 (1997), pp. 41–63.

[91] Ottesen, J. T. "Modelling the dynamical baroreflex-feedback control". *Math Comput Model* **31**.4-5 (2000), pp. 167–173.

[92] Ottesen, J. T. et al. "Structural correlation method for model reduction and practical estimation of patient specific parameters illustrated on heart rate regulation". *Math Biosci* **257** (2014), pp. 50–59.

[93] Palamarchuk, I. S. et al. "Non-invasive measurement of adrenergic baroreflex during Valsalva maneuver reveals three distinct patterns in healthy subjects". *Clin Neurophysiol* **127** (2016), pp. 858–863.

[94] Palamarchuk, I. S. et al. "The utility of Valsalva maneuver in the diagnoses of orthostatic disorders". *Am J Physiol Regul Integr Comp Physiol* **310**.3 (2016), R243–252.

[95] Palma, J.-A. & Kaufmann, H. "Autonomic disorders predicting Parkinson disease". *Parkinsonism Relat Disord* **20** (2014), S94–S98.

[96] Parashar, R. et al. "Age related changes in autonomic functions". *J Clin Diagn Res* **10**.3 (2016), pp. CC11–CC15.

[97] Petersen, M. E. V. et al. "The normal response to prolonged passive head up tilt testing". *Heart* **84** (2000), pp. 509–514.

[98] Piccirillo, G. et al. "Influence of aging on cardiac baroreflex sensitivity determined non-invasively by power spectral analysis". *Clin Sci* **100** (2001), pp. 267–274.

[99] Pomeranz, B. et al. "Assessment of autonomic function in humans by heart rate spectral analysis". *Am J Physiol Heart Circ Physiol* **248** (1985), H151–H153.

[100] Pope, S. R. et al. "Estimation and identification of parameters in a lumped cerebrovascular model". *Math Biosci Eng* **6**.1 (2009), pp. 93–115.

[101] Pstras, L. et al. "Mathematical modelling of cardiovascular response to the Valsalva manoeuvre". *Math Med Biol* (2016).

[102] Pstras, L. et al. "The Valsalva manoeuvre: physiology and clinical examples". *Acta Physiol* **217**.2 (2016), pp. 103–119.

[103] Qureshi, M. U. et al. "Hemodynamic assessment of pulmonary hypertension in mice: a model-based analysis of the disease mechanism". *Biomech Model Mechanobiol* **18**.1 (2019), pp. 219–243.

[104] Rall, L. B. *Automatic differentiation*. Lecture notes in computer science. Berlin Heidelberg: Springer-Verlag, 1981.

[105] Ramya, K & Rajkumar, K. "Respiration rate diagnosis using single lead ECG in real time". *Global J Med Res* **13**.1 (2013).

[106] Rao, F. et al. "Dynamics of a diffusion reaction prey-predator model with delay in prey: effects of delay and spatial components". *J Math Anal Appl* **461** (2018), pp. 1177–1214.

[107] Robinson, B. F. et al. "Control of heart rate by the autonomic nervous system". *Circ Res* **19**.2 (1966), pp. 400–411.

[108] Roose, D. & Szalai, R. "Continuation and bifurcation analysis of delay differential equations". *Numerical Continuation Methods for Dynamical Systems: Understanding Complex Systems*. Ed. by Krauskopf, B et al. Dordrecht: Springer, 2007.

[109] Ruan, S. & Wei, J. "On the zeros of transcendental functions with applications to stability of delay differential equations with two delays". *Dyn Cont Disc Imp Syst* **10** (2003), pp. 863–874.

[110] Saltelli, A. et al. "Variance based sensitivity analysis of model output. Design and estimator for total sensitivity index". *Comput Phys Commun* **181** (2010), pp. 259–270.

[111] Schrezenmaier, C. et al. "Adrenergic and vagal baroreflex sensitivity in autonomic failure". *Arch Neurol* **64** (2007), pp. 381–386.

[112] Shi, Y. et al. "Review of Zero-D and 1-D models of blood flow in the cardiovascular system". *BioMedical Eng Online* **10**.33 (2011).

[113] Sipahi, R. et al. "Stability and stabilization of systems with time delay". *IEEE Contr Syst Mag* **31** (2011), pp. 38–65.

[114] Smith, M. L. et al. "Valsalva's maneuver revisited: a quantitative method yielding insights into human autonomic control". *Am J Physiol* **271**.3 Pt 2 (1996), H1240–9.

[115] Smith, R. C. *Uncertainty quantification: theory, implementation, and applications*. Philadelphia: SIAM, 2014.

[116] Smith, S. A. "Reduced sinus arrhythmia in diabetic autonomic neuropathy: diagnostic value of an age-related normal range". *Br Med J* **285** (1982), pp. 1599–1601.

[117] Snowden, T. J. et al. "Model reduction in mathematical pharmacology". *J Pharmacokinet Pharmacodyn* **45** (2018), pp. 537–555.

[118] Sobol, I. M. "Sensitivity estimates for nonlinear mathematical models". *Math Mod Comp Exp* **1** (1993), pp. 407–414.

[119] Sobol, I. M. "Global sensitivity indices for nonlinear mathematical models and their Monte Carlo estimates". *Math Comput Simul* **55** (2001), pp. 271–280.

[120] Sobol, I. M. & Kucherenko, S. S. "Derivative based global sensitivity measures". *Procedia Soc Behav Sci* **2** (2010), pp. 7745–7746.

[121] Sobol, I. M. et al. "Estimating the approximation error when fisxing unessential factors in global sensitivity analysis". *Reliab Eng Syst Safe* **92** (2007), pp. 957–960.

[122] Spickler, J. W. et al. "Transfer characteristics of the carotid sinus pressure control system." *Baroreceptors and Hypertension*. Ed. by Kezdi, P. Pergamon Press, 1967, pp. 31–40.

[123] Storlie, C. & Helton, J. C. "Multiple predictor smoothing methods for sensitivity analysis: description of techniques". *Reliab Eng Syst Safe* **93** (2008), pp. 28–54.

[124] Sumner, T et al. "A methodology for global sensitivity analysis of time-dependent outputs in systems biology modelling". *J R Soc Interface* **9** (2012), pp. 2156–2166.

[125] Swenne, C. A. "Baroreflex sensitivity: mechanisms and measurement". *Neth Heart J* **21** (2013), pp. 58–60.

[126] Szalai, R. et al. "Continuation of bifucations in periodic delay-differential equations using characteristic matrices". *SIAM J Sci Comput* **28**.4 (2006), pp. 1301–1317.

[127] Tanaka, H. et al. "Age-predicted maximal heart rate revisited". *J Am Coll Cardiol* **37**.1 (2001), pp. 153–156.

[128] Thomas, J. R. et al. "An electrocardiogram-based technique to assess cardiopulmonary coupling during sleep". *SLEEP* **28**.9 (2005), pp. 1151–1161.

[129] Valdez-Jasso, D. "Modeling and Identification of Vascular Biomechanical Properties in Large Arteries". PhD thesis. North Carolina State University, 2010.

[130] Vielle, B. & Chauvet, G. "Delay equation analysis of human respiratory stability". *Math Biosci* **152** (1998), pp. 105–122.

[131] Wang, Z et al. "Simultaneous beat-by-beat investigation of the effects of the Valsalva maneuver on left and right ventricular filling and the possible mechanism". *PLoS One* **8**.1 (2013), e53917.

[132] Weimer, L. H. "Autonomic testing: common techniques and clinical applications". *The Neurologist* **16**.4 (2010), pp. 215–222.

[133] Wesseling, K. H. & Settels, J. J. "Circulatory model of baro- and cardio-pulmonary reflexes". *Blood Pressure and Heart Rate Variability*. Ed. by Di Rienzi, M. & Mancia, G. Vol. 4. Amsterdam, The Netherlands: IOS Press, 1993.

[134] Widjaja, D. et al. "ECG-derived respiration: comparison and new measures for respiratory variability". *Comput Cardiol* **37** (2010), pp. 149–152.

[135] Wilhelm, T. "The smallest chemical reaction system with bistability". *BMC Syst Biol* **9** (2009).

[136] Williams, N. D. et al. "Patient-specific modelling of head-up tilt". *Math Med Biol* **31**.4 (2014), pp. 365–92.

[137] Wit, E. et al. "'All models are wrong ...': an introduction to model uncertainty". *Stat Neerl* **66** (2012), pp. 217–236.

[138] Yasuma, F. & Hayano, J.-i. "Respiratory sinus arrhythmia - why does the heartbeat synchronize with respiratory rhythm?" *Chest* **125**.2 (2004), pp. 683–690.

[139] Zygmunt, A. & Stanczyk, J. "Methods of evaluation of autonomic nervous system function". *Arch Med Sci* **6**.1 (2010), pp. 11–18.